THÈSE

Pour l'obtention du titre de

DOCTEUR de L'UNIVERSITÉ DE LORRAINE

Spécialité: Science des Matériaux

Présentée par

Christy FADEL

Influence of the Al content on the structure, optoelectronic properties and electronic structure of AZO transparent electrodes deposited by HiPIMS for solar energy conversion

Soutenance publique prévue le 13 Juillet 2022 à Nancy devant le jury composé de :

Patrick CHOQUET	Rapporteur	Directeur de recherche, Luxembourg Institute of Science and Technology, Luxembourg
Nicolas MARTIN	Rapporteur	Professeur des universités, FEMTO ST, Université de Franche-Comté, Besançon
Marie-Paule BESLAND	Examinatrice	Directrice de recherche, Institut des Matériaux de Nantes, Nantes Université, Nantes
Angélique BOUSQUET	Examinatrice	Maître de Conférences, Institut de Chimie de Clermont-Ferrand, Université Clermont Auvergne, Aubière
Jean-François PIERSON	Examinateur	Professeur des universités, Institut Jean Lamour, Université de Lorraine, Nancy
Christian MOTZ	Examinateur	Professeur, Lehrstuhl für Experimentelle Methodik der Werkstoffwissenschaften, Universität des Saarlandes, Saarbrücken
Frank MÜCKLICH	Co-directeur de thèse	Professeur, Lehrstuhl für Funktionswerkstoffe, Universität des Saarlandes, Saarbrücken
David HORWAT	Directeur de thèse	Professeur des universités, Institut Jean Lamour, Université de Lorraine, Nancy
Stéphane CUYNET	Invité, Co-encadrant de thèse	Chargé de recherche, Institut Jean Lamour, Université de Lorraine, Nancy

Institut Jean Lamour, UMR 7198, ARTEM - CS 50840-54011 Nancy Cedex
Université de Lorraine – Ecole doctorale : Chimie - Mécanique - Matériaux- Physique (C2MP)

Influence of the Al content on the structure, optoelectronic properties and electronic structure of AZO transparent electrodes deposited by HiPIMS for solar energy conversion

DISSERTATION

zur Erlangung des Grades des
Doktors der Ingenieurwissenschaften
der Naturwissenschaftlich-
Technischen Fakultät der Universität
des Saarlandes

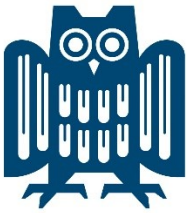

UNIVERSITÄT
DES
SAARLANDES

Von

Christy Fadel

Saarbrücken / Nancy - 2022

Tag des Kolloquiums: 13.07.2022

Dekan: Univ.-Prof. Dr. rer. nat. Jörn Walter

Berichterstatter: Prof. Dr.-Ing. Frank Mücklich
Prof. Dr. Christian Motz
Pr. Nicolas Martin
Dr. Patrick Choquet

Vorsitz: Dr. Marie-Paule Besland

Akad. Mitarbeiter: Pr. David Horwat
Dr. Stéphane Cuynet
Pr. Jean-François Pierson
Dr. Angélique Bousquet

Abstract

In this work, the influence of Al (Aluminum) dopant concentration on the properties of Al-doped ZnO (AZO) films synthesized by reactive High Power Impulse Magnetron Sputtering (HiPIMS), and deposited from Zn/Al targets with 1, 2, 5, 10 or 15 at.% Al is studied. It is observed that the Al content has a strong influence on the reactive sputtering process, as it is easier to sputter-deposit at high rates from targets containing lower Al contents. This is explained by the high reactivity of Al towards oxygen, which easily poisons the target surface with Al oxide more difficult to etch upon bombardment by ions from the plasma phase. Films have been synthesized in the 0.56-14.71 at.% Al range, where the film structure and microstructure evolves from nanocrystalline columnar films towards ultrafine nanocrystalline films of wurtzite ZnO structure upon increasing the Al content. The electrical properties revealed that effective doping may be achieved up to 3 at.% Al by using HiPIMS. And most importantly, it is found that electronic structure measurements contain signatures of dopant activation and segregation that may serve to investigate on the origin of electrical properties degradation and to optimize the electrical properties of AZO films. Finally, flat or structured glass/AZO/ZnO/Cu_2O/Au thin film stacks were made. The patterning was done by ultrashort pulsed direct laser interference patterning, and the morphology and microstructure are presented together with possible strategies to improve the preliminary electrical results.

Résumé

Dans cette thèse, l'influence de la concentration en dopant Al (Aluminium) sur les propriétés de films d'oxyde de zinc (ZnO) dopés par Al (AZO – Al-doped zinc oxide) synthétisés par pulvérisation magnétron impulsionnelle à haute puissance réactive (HiPIMS) est étudiée. Pour cela, des cibles de pulvérisation d'alliages Zn/Al à 1, 2, 5, 10 ou 15 at.% Al sont utilisées. Il est observé que la teneur en Al a une forte influence sur le processus de pulvérisation réactive, car il est plus facile de pulvériser et de déposer à des vitesses de dépôts élevées à partir de cibles contenant des teneurs en Al plus faibles. Cela s'explique par la forte réactivité de l'Al vis-à-vis de l'oxygène qui facilite la formation d'un oxyde d'aluminium en surface des cibles, et rend plus difficile la pulvérisation lors du bombardement par les ions de la phase plasma. Des films ont été synthétisés dans la gamme 0,56-14,71 at.% Al, où la structure et la microstructure du film évoluent de films colonnaires nanocristallins vers des films nanocristallins ultrafins lors de l'augmentation de la teneur en Al. La structure hexagonale wurtzite de ZnO est conservée pour toutes les conditions. Les mesures électriques réalisées sur les films élaborés ont révélé qu'un dopage efficace peut être atteint jusqu'à 3 at.% Al en utilisant la pulvérisation HiPIMS réactive. Plus important encore, on constate que les mesures de structure électronique montrent des indices d'activation et de ségrégation de dopants qui peuvent servir à chercher l'origine de la dégradation des propriétés électriques et à optimiser les propriétés électriques des films AZO. Enfin, des empilements de couches minces visant à fabriquer des cellules photovoltaïques ont été réalisés selon la séquence verre plat ou structuré/AZO/ZnO/Cu_2O/Au. La structuration a été réalisée par interférence laser directe à pulses ultracourts, et la morphologie et la microstructure obtenues sont présentées ainsi que des stratégies possibles pour permettre le développement de cellules efficaces.

Zusammenfassung

In dieser Arbeit wird der Einfluss der Al-Dotierungskonzentration (Al = Aluminium) auf die Eigenschaften von Al-dotierten ZnO (AZO)-Filmen untersucht, die durch reaktives Hochleistungs-Impuls-Magnetron-Sputtern (HiPIMS) synthetisiert und von Zn/Al-Targets mit 1, 2, 5, 10 oder 15 at.% Al abgeschieden wurden. Es wird beobachtet, dass dieser Al-Gehalt einen starken Einfluss auf den reaktiven Sputterprozess hat, da sich hohe Abscheideraten mit Targets, die niedrigere Al-Gehalte aufweisen, besser realisieren lassen. Dies erklärt sich durch die hohe Reaktivität von Al gegenüber Sauerstoff, was zur Kontamination der Target Oberfläche mit Al-Oxid führt, das beim Beschuss mit Ionen aus der Plasmaphase schwieriger abzutragen ist. Filme wurden im Bereich von 0,56–14,71 Atom-% Al synthetisiert, wobei sich die Filmstruktur und Mikrostruktur von nanokristallinen säulenförmigen Filmen zu ultrafeinen nanokristallinen Filmen mit Wurtzit-ZnO-Struktur entwickelt, wenn der Al-Gehalt erhöht wird. Die elektrischen Eigenschaften zeigten, dass mit HiPIMS eine effektive Dotierung bis zu 3 at.% Al erreicht werden kann. Ein weiteres wichtiges Ergebnis bilden ist, dass elektronische Strukturmessungen Signaturen der Dotierstoffaktivierung und -segregation enthalten, die dazu dienen können, den Ursprung der Verschlechterung der elektrischen Eigenschaften zu untersuchen und die elektrischen Eigenschaften von AZO-Filmen zu optimieren. Schließlich wurden flache oder strukturierte Glas/AZO/ZnO/Cu_2O/Au-Dünnschichtstapel hergestellt. Die Strukturierung erfolgte durch ultrakurz gepulste direkte Laserinterferenzstrukturierung. Die Morphologie und Mikrostruktur werden zusammen mit möglichen Strategien zur Verbesserung der vorläufigen elektrischen Ergebnisse präsentiert.

Résumé étendu

Les oxides transparents et conducteurs (TCOs en anglais) sont des matériaux semi-conducteurs connus pour leur propriétés de bonne transparence optique et leur conductivité électrique élevée. Ils sont utilisés dans de nombreux domaines tels que les écrans LCD, les photodétecteurs, les appareils électroluminescents, les cellules solaires, etc. L'importance clé de ces matériaux réside dans leur capacité à réaliser un compromis entre les propriétés électriques et optiques. Parmi les TCOs les plus connus et utilisés, on cite l'oxyde d'étain (SnO_2), l'oxyde d'indium (In_2O_3), l'oxyde d'indium et d'étain (ITO) et l'oxyde de zinc (ZnO). ITO est en principe le plus performant parmi les TCOs à cause de ces propriétés électriques et optiques exceptionnelles, i.e. c'est un film à la fois très transparent et très conducteur, lui permettant de jouer le rôle d'une électrode transparente très performante dans les cellules solaires. Cependant, les constituants de ce matériau, c'est-à-dire l'indium et l'étain, mais surtout l'indium, sont des métaux rares au coût élevé et fluctuant, toxiques et néfastes pour l'environnement. Pour cette raison, les chercheurs ont été amenés à développer des matériaux de remplacement à l'ITO dans ces divers applications. Le défi est de trouver un matériau présentant des propriétés équivalentes à celles d'ITO. L'oxyde de zinc dopé par l'aluminium (AZO), a été considéré comme un très bon remplaçant. D'une part, ses constituants (Al et Zn) sont des métaux abondants dans la croute terrestre, non-toxiques et non néfastes pour l'environnement. Il est possible, en fonction des conditions de synthèse, d'obtenir des propriétés optiques et électriques comptabible avec une utilisation comme électrode transparente. Plusieurs méthodes ont été utilisées pour le dépôt des couches minces d'AZO, parmi lesquelles l'électrodéposition, le procédé sol-gel, l'épitaxie par jet moléculaire, le dépôt par ablation laser pulsée, la pulvérisation cathodique magnétron, etc. Les films AZO ont été largement étudiés dans la littérature afin d'optimiser leurs conditions d'élaboration en pulvérisation cathodique conventionnelle: certaines études ont montré l'effet de la température du substrat, l'influence de la nature du substrat, de la pression de dépôt, du type de matériau de départ (cible, précurseur, solution …), etc. Dans cette thèse, la pulvérisation cathodique magnétron à impulsions de haute puissance (HiPIMS en anglais) est choisie comme méthode de dépôt pour les films AZO au regard de sa capacité, démontrée lors de précédents travaux, à produire des propriétés homogènes et performantes sur de larges surface sans faire appel à une assistance thermique. Notre approche vient compléter les travaux précédents par la synthèse et caractérisation de films AZO par HiPIMS réactif dans une gamme étendue de teneurs en aluminium. Pour cela, des cibles d'alliages Zn/Al contenant 1,

2, 5, 10 et 15 at.% d'aluminium ont été utilisées. Le cœur de ce travail concerne l'étude de l'influence de la composition en aluminium des cibles et des films sur les propriétés électriques, optiques, structurales et la structure électronique des films élaborés.

Les conditions environnementales de nos jours, ainsi que l'épuisement de certaines ressources naturelles nécessaires pour la croissance de la population, ont amené les chercheurs à trouver des solutions de remplacements pour ces ressources. Parmi les solutions possibles, les cellules photovoltaïques apparaissent comme une solution séduisante compte tenu de l'abondance et de la gratuité de l'énergie solaire. Ceci permet d'envisager la production d'électricité avec un minimum d'impact environnemental si des matériaux et procédés à faible impact environnemental sont utilisés. En plus de l'étude de l'influence des paramètres d'élaboration sur les propriétés de films minces d'AZO, cette thèse vise également à fabriquer des cellules photovoltaïques basées sur des hétérojonctions de type n-ZnO/p-Cu_2O en combinant la pulvérisation cathodique réactive en mode HiPIMS pour l'élaboration d'électrodes transparentes d'AZO, en mode continu (DC) pour la synthèse de films de ZnO et la croissance de films Cu_2O par ALD (Atomic Layer Deposition) sélective. Dans la perspective d'améliorer le rendement de telles cellules en réalisant le piégeage des photons, des substrats structurés par méthode d'interférence laser ont été utilisés comme support de croissance pour les cellules. Ce manuscrit est divisé en 6 chapitres dont quatre chapitres consacrés pour montrer les résultats obtenus suite à l'optimisation des films AZO (**Chapitres 3, 4 et 5**) et l'élaboration et la caractérisation des cellules solaires ou des dispositifs pour cellules solaires (**Chapitre 6**).

Le premier chapitre est constitué de deux parties. Dans la première partie, les applications des TCOs et leur caractéristiques générales sont tout d'abord introduites en détaillant en particulier les mécanismes de dopage et le lien avec la réalisation d'un compromis entre les propriétés optiques et électriques au sein de ces matériaux. Cela permet ensuite de présenter les propriétés des trois différents TCOs utilisés dans ce travail à savoir l'oxyde de zinc (ZnO), l'oxyde de zinc dopé à l'aluminium (AZO) et l'oxyde de cuivre cuprite (Cu_2O). À chaque fois, l'intérêt de sélectionner une méthode de dépôt particulière est motivé. La deuxième partie de ce chapitre est dédiée aux cellules solaires en focalisant sur les informations utiles pour les deux points traités dans ce travail: les caractéristiques des cellules solaires à base d'hétérojonction de type ZnO/Cu_2O, et les principes de la structuration du substrat par texturation par interference laser directe à pulses ultracourts USP-DLIP (UltraShort Pulsed-Direct Laser Interference Patterning) spécifiquement.

Le deuxième chapitre est consacré aux méthodes expérimentales utilisées. Une première partie de ce chapitre est consacrée à la description des méthodes de dépôt et de traitement utilisées:

- le dépôt de couches minces par pulvérisation cathodique magnétron réactive en régimes DC et HiPIMS. Les principes, le dispositif expérimental et les conditions expérimentales pour la réalisation de films minces de ZnO et d'or par pulvérisation DC, et d'AZO par HiPIMS sont présentés.
- D'une manière similaire, le principe, le dispositif expérimental et les conditions utiles pour la synthèse de films minces de Cu_2O par la méthode d'ALD sont présentés.
- La méthode de structuration du substrat, spécifiquement par USP-DLIP est détaillée et expliquée. Ensuite, les principes de la méthode de modélisation utilisée pour prévoir les conditions de texturation idéales, ainsi que la méthode expérimentale de structuration sont décrites.
- Cette première partie se termine par une présentation des conditions de fabrication des dispositifs de test pour la réalisation de futures cellules solaires texturées.

Dans la deuxième partie de ce chapitre, sont présentées les méthodes de caractérisations employées pour étudier les propriétés électriques, optiques, structurales et la structure électronique des différentes couches ainsi que pour la caractérisation du verre structuré et les dispositifs de cellules solaires.

Le troisième chapitre est dédié à l'étude de l'influence de la concentration en Al dans les cibles de Zn/Al sur le processus de dépôt HiPIMS réactif, la composition chimique, la structure et la microstructure des films. Tout d'abord, il est observé que le courant de décharge et la vitesse de dépôt des films sont fortement influencés par la teneur en aluminium dans les cibles. En effet, pour un même état d'usure des cibles la vitesse de dépôt diminue fortement avec la teneur en aluminium alors que le courant de décharge augmente fortement. Ces résultats ont été interprétés par l'augmentation de la réactivité des cibles vis-à-vis de l'oxygène présent dans la phase gazeuse lorsque la teneur en aluminium augmente. Ensuite, l'étude des propriétés des films AZO obtenus a débuté par leur analyse chimique. La distribution du zinc, de l'aluminium et de l'oxygène au sein des films est relativement homogène avec la confirmation que la concentration en Al dans les films augmente avec celle des cibles. Ensuite, la structure et la microstructure des films ont été caractérisées par diffraction des rayons X (DRX) et microscopie électronique en transmission pour deux positions caractéristiques, face à l'axe de la cible. Les résultats de diffraction des rayons X ont

montré que la structure cristalline de type hexagonale wurtzite des films se dégradent au fur et à mesure que la composition en Al est augmentée jusqu'à devenir amorphe ou très finement nanocristallisée pour les films déposés à partir de la cible contenant 15 at.% en Al. Alors que les films déposés à partir des cibles contenant 5 et 10 at.% en Al sont préférentiellement orientés selon l'axe *c* de la structure wurtzite, les films déposés à partir des cibles contenant 1 et 2 at.% d'Al possèdent plusieurs orientations et sont probablement sous-stœchiométriques. À partir des données de DRX, la taille des cristallites et l'indice de cristallinité ont été calculés pour les films les mieux cristallisés et il a été observé que les valeurs de ces deux paramètres diminuent avec l'augmentation de la teneur en Al. Cette étude a été complétée par la Microscopie Electronique en Transmission (MET) qui a confirmé la dégradation de la cristallinité et la transition d'une croissance colonnaire vers une croissance avec des grains fins et équiaxes pour les films déposés à partir des cibles contenant 10 et 15 at.% en Al. Ces derniers sont nanocristallisés et conservent la structure wurtzite.

Dans le quatrième chapitre, l'étude de l'évolution des propriétés des films AZO en fonction de la composition en Al a été poursuivie en portant notre intérêt sur les propriétés optiques et les propriétés électriques. Il a été observé que la transmittance des films augmente avec l'augmentation de la composition en Al dans les films. L'évolution des courbes de distribution du coefficient d'absorption avec la longueur d'onde pour les différents films a permis de montrer que plus les films contiennent une teneur élevée en aluminium, plus ils tendent à être transparents. Ces résultats corroborent l'hypothèse de la présence d'une sous-stœchiométrie en oxygène dans les films synthétisés à partir de cibles présentant une faible teneur en aluminium. L'extraction des valeurs du band gap par la méthode de Tauc montre une augmentation progressive de ce paramètre avec la teneur en aluminium dans les films. Pour des teneurs inférieures ou égales à 3 at.% Al, l'augmentation est expliquée par l'effet Burstein-Moss lié à l'augmentation de la densité d'électrons libres. Pour les teneurs plus élevées, l'augmentation n'est pas cohérente avec l'effet Burstein-Moss et suggère un changement de type de liaisons au sein du matériau. L'étude des propriétés électriques des films AZO, montre une augmentation de la résistivité avec la composition en Al, avec une valeur de résistivité systématiquement plus élevée en face à l'axe des cibles qui a été attribuée à une possible désactivation du dopant par formation de phase secondaires. Pour montrer le compromis entre la transmittance et la résistivité, la figure de mérite dépendant de façon inversement proportionnelle à la résistivité et à l'absorption, a été calculée et présentée. Ce paramètre voit sa valeur diminuer avec l'augmentation de la composition en Al, avec des valeurs plus faibles en *in-axis* (position en face de l'axe de la cible). La résistivité électrique

mesurée pendant des recuits séquentiels sous air à 100, 150, 200 et 225 °C pendant 1h diminue dans un premier temps avant d'augmenter. Cette augmentation de la résistivité qui est susceptible de caractériser une oxydation sous air intervient d'autant plus tôt que la composition en Al diminue. Ces mesures pourraient, après certaines validations, servir à comparer qualitativement des niveaux de sous-stœchiométrie en oxygène. Pour terminer ce chapitre, une étude extensive des propriétés électriques des films à faibles teneurs en Al a été réalisée en considérant la teneur en aluminium, la tension de décharge et l'état de vieillissement des cibles. Cette étude indique la présence de mécanismes complexes au niveau des interactions plasma-cible qui influencent indirectement les propriétés de conduction des films en agissant sur la sous-stœchiométrie en oxygène et les mécanismes de désactivation du dopant aluminium.

Dans le cinquième chapitre, pour tenter d'expliquer l'origine de la dégradation des propriétés des films AZO à composition élevée en Al, l'activation/la désactivation du dopant Al au sein des films AZO a été étudiée par spectroscopie de perte d'énergie des électron à proximité des seuils (ELNES - Energy Loss Near Edge Structure) Zn-L_3, Al-K, Al-$L_{2,3}$ et O-K. Le résultat principal de cette étude est la possibilité de détecter au niveau du seuil Al-$L_{2,3}$ deux signatures indépendantes :

- La présence d'états électroniques délocalisés issus du dopant Al au niveau du bas de bande
  de conduction. Ceci est corrélé à une densité d'électrons élevée telle que mesurée par effet
  Hall et caractérise l'activation du dopant.
- Le positionnement du dopant Al en conformation octaédrique, au lieu de tétraédrique. Ceci caractérise la désactivation du dopant Al.

Il est montré qu'il est possible de simuler des spectres ELNES expérimentaux au seuil Al-$L_{2,3}$ à partir de spectres de références caractérisant ces deux états et d'en déduire leurs proportions respectives. Nous pensons que cette approche pourra être utilisée dans de futurs travaux pour mieux comprendre les mécanismes d'activation/désactivation du dopant et, ainsi, tenter d'optimiser les propriétés des films AZO.

Dans le sixième chapitre, des prototypes de cellules basés sur des empilements verre/AZO/ZnO/Cu_2O/Au ont été fabriqués puis testés pour définir les voies d'amélioration permettant d'aller vers la fabrication de cellules solaires texturées efficaces. Des substrats de verre plat ou structuré à différentes périodicités, une électrode transparente d'AZO déposée à

partir d'une cible à 1 ou 2 at.% en Al, une hétérojonction ZnO/Cu_2O et un contact en or (Au) ont été élaborés et caractérisés. Des simulations de photo-courant et de pertes optiques ont été réalisées dans le cadre d'une collaboration avec Dr. Marcos Soldera **[1]** pour permettre de choisir les paramètres de structuration convenables. Les résultats ont montré qu'une épaisseur élevée de la couche Cu_2O allant jusqu'à 500 nm, une profondeur élevée de structure et une faible périodicité de 1 µm sont nécessaires pour atteindre des valeurs maximales de photo-courant. Par contre, la réalisation expérimentale n'était possible que pour 70 nm de Cu_2O déposé par ALD et pour une périodicité de 1.5 µm comme minimum. À partir des données obtenues en DRX, en plus de la confirmation de la croissance de la phase Cu_2O par ALD, il a été observé que le film de ZnO croît bien selon la structure cristalline de type wurtzite mais son orientation préférentielle est déterminée par le type de substrat (verre ou Si), la position de ce dernier par rapport à l'axe du porte-substrat pendant la phase de dépôt par pulvérisation cathodique DC et le flux d'oxygène utilisé pendant le dépôt. Les observations au MET ont montré que les films d'AZO déposés à partir d'une cible contenant 1 at.% Al et de ZnO déposé dessus sont colonnaires et cristallisés dans la structure wurtzite, avec le premier présentant plusieurs directions cristallines alignées selon la direction de croissance du film et le deuxième fortement orienté préférentiellement selon l'axe *c*. La comparaison entre une hétérojonction ZnO/Cu_2O déposée sur un substrat de silicium placé à 2 ou à 8 cm de l'axe du porte-substrat, a montré que le film de ZnO croît toujours avec les plans (002) parallèles à la surface du substrat alors que le film de Cu_2O croît en suivant des orientations différentes selon la position. Enfin, les observations au Microscope électronique à balayage ont montré que la croissance de l'AZO sur verre structuré a besoin d'optimisation que ce soit au niveau de la structuration du verre ou au niveau du processus de déposition. L'analyse chimique des dispositifs a permis d'améliorer l'homogénéité de la couche de Cu_2O par ALD et de confirmer, via l'ELNES aux seuils Cu-$L_{2,3}$ et O-K, les observations en DRX qui ont montré que c'est bien la phase Cuprite Cu_2O qui a été déposée et non la phase Ténorite CuO. Des cellules solaires complètes ont été élaborées et des mesures I-V (Courant-Tension) ont bien montré un comportement redresseur d'une jonction p-n. Cependant, le photo-courant mesuré était excessivement faible montrant la nécessité d'optimiser les caractéristiques des films de ZnO et Cu_2O.

L'étude extensive réalisée sur les films d'AZO dans ce travail a permis de mettre en relation l'effet de la composition en Al et l'évolution des propriétés électriques et optiques des films, afin de trouver un compromis convenable pour utilisation comme électrode transparente dans les cellules solaires. L'analyse ELNES a permis de mieux comprendre les relations entre la

structure électronique, les propriétés électriques, structurales et chimiques des films en fonction de la composition en Al. En ce qui concerne l'élaboration et la caractérisation des échantillons pour cellules solaires, les résultats ont montré un bon établissement de l'hétérojonction de ZnO/Cu_2O au sein de la cellule, mais des optimisations sur plusieurs niveaux restent nécessaires pour élaborer une cellule solaire à photo-courant élevé.

Ausführliche Zusammenfassung

Transparente leitende Oxide (TCOs) sind Halbleitermaterialien, die für ihre hohe optische Transparenz und elektrische Leitfähigkeit bekannt sind. Sie werden in vielen Bereichen wie LCD-Anzeigen, Fotodetektoren, lichtemittierenden Geräten, Solarzellen usw. verwendet. Die Schlüsselbedeutung dieser Materialien liegt in ihrer Fähigkeit, einen Kompromiss zwischen elektrischen und optischen Eigenschaften zu erzielen. Zu den bekanntesten und am häufigsten verwendeten TCOs gehören Zinnoxid (SnO_2), Indiumoxid (In_2O_3), Indium Zinnoxid (ITO) und Zinkoxid (ZnO). Das ITO ist aufgrund dieser außergewöhnlichen elektrischen und optischen Eigenschaften im Prinzip das effizienteste unter den TCOs, d. h. Folien dieses Materials sind sowohl sehr transparent als auch sehr leitfähig ist und damit geeignet, die Rolle einer sehr effizienten transparenten Elektrode in Solarzellen zu spielen. Die Bestandteile dieses Materials, also Indium und Zinn, aber insbesondere Indium, sind seltene Metalle mit hohen und schwankenden Kosten, giftig und umweltschädlich. Aus diesem Grund wurden Forscher veranlasst, Ersatzmaterialien für ITO für dessen verschiedene Anwendungen zu entwickeln. Die Herausforderung besteht darin, ein Material zu finden, dessen Eigenschaften denen von ITO entsprechen. Aluminium-dotiertes Zinkoxid (AZO) gilt als sehr guter Ersatz. Einerseits sind diese Bestandteile (Al und Zn) in der Erdkruste reichlich vorhandene Metalle, ungiftig und nicht umweltschädlich. Je nach Synthesebedingungen können optische und elektrische Eigenschaften für den Einsatz als transparente Elektrode erhalten werden. Für die Abscheidung dünner AZO-Schichten wurden mehrere Verfahren verwendet, darunter Elektroabscheidung, Sol-Gel-Verfahren, Molekularstrahlepitaxie, gepulste Laserablationsabscheidung, Magnetron-Sputtern usw. AZO-Filme wurden in der Literatur ausführlich untersucht, um ihre Herstellungsbedingungen beim herkömmlichen Sputtern zu optimieren: Bisherige Studien fokussierten sich auf die Wirkung der Temperatur des Substrats, den Einfluss der Art des Substrats, des Abscheidungsdrucks, der Art des Ausgangsmaterials (Target, Vorläufer, Lösung…), usw.. In dieser Arbeit wird das gepulste Hochleistungs-Magnetron-Kathodenzerstäuben (HiPIMS) als Abscheidungsverfahren für

AZO-Schichten gewählt, da in früheren Arbeiten die Erzeugung effizienter und homogener Eigenschaften über große Oberflächen, ohne thermische Unterstützung demonstriert werden konnte. Unser Ansatz ergänzt frühere Arbeiten durch die Synthese und Charakterisierung von AZO-Filmen durch reaktives HiPIMS in einem breiten Spektrum von Aluminiumgehalten. Dazu wurden Zn/Al-Legierungstargets verwendet, die 1, 2, 5, 10 und 15 at.% Aluminium enthielten. Das Herzstück dieser Arbeit betrifft die Untersuchung des Einflusses der Aluminiumzusammensetzung von Targets und Filmen auf die elektrischen, optischen und strukturellen Eigenschaften sowie die elektronische Struktur der hergestellten Filme.

Die heutigen Umweltbedingungen sowie die Erschöpfung bestimmter natürlicher Ressourcen, die für das Bevölkerungswachstum erforderlich sind, haben Forscher dazu veranlasst, alternative Lösungen für diese Ressourcen zu finden. Unter den möglichen Lösungen scheinen Photovoltaikzellen angesichts der Fülle und kostenlosen Sonnenenergie eine attraktive Lösung zu sein. Dadurch ist es möglich, eine Stromerzeugung mit minimaler Umweltbelastung zu realisieren, sofern Materialien und Verfahren mit geringer Umweltbelastung verwendet werden. Neben der Untersuchung des Einflusses der Ausarbeitungsparameter auf die Eigenschaften von AZO-Dünnschichten zielt diese Arbeit auch darauf ab, photovoltaische Zellen basierend auf Heteroübergängen des n-ZnO/p-Cu_2O-Typs, durch die Kombination von reaktiven Sputtern im HiPIMS-Modus zur Ausarbeitung transparenter AZO-Elektroden mit dem kontinuierlichen Modus (DC) für die Synthese von ZnO-Filmen und das Wachstum von Cu_2O-Filmen durch selektive ALD, herzustellen. Im Hinblick auf die Verbesserung der Leistung solcher Zellen durch Einfangen von Photonen wurden durch Laserinterferenzverfahren (ultrakurz gepulste direkte Laserinterferenzstrukturierung, USP-DLIP) strukturierte Substrate als Wachstumsträger für die Zellen verwendet. Dieses Manuskript ist in 6 Kapitel gegliedert, von denen vier den erzielten Ergebnissen im Hinblick auf die Optimierung von AZO-Filmen (**Kapitel 3, 4 und 5**) und die Entwicklung und Charakterisierung von Solarzellen oder Bauelementen für Zellen gewidmet sind (**Kapitel 6**).

Das erste Kapitel besteht aus zwei Teilen. Im ersten Teil werden zunächst die Anwendungen von TCOs und ihre allgemeinen Eigenschaften vorgestellt, indem insbesondere die Dotierungsmechanismen und die Verbindung mit der Realisierung eines Kompromisses zwischen den optischen und elektrischen Eigenschaften innerhalb dieser Materialien detailliert beschrieben werden. Dies ermöglicht es dann, die Eigenschaften der drei unterschiedlichen TCOs darzustellen, die in dieser Arbeit verwendet wurden, nämlich

Zinkoxid (ZnO), Aluminium-dotiertes Zinkoxid (AZO) und Cuprit-Kupfer-Oxid (Cu_2O). Jedes Mal ist das Interesse an der Auswahl einer bestimmten Einzahlungsmethode motiviert. Der zweite Teil dieses Kapitels ist Solarzellen gewidmet, indem er sich auf nützliche Informationen zu den beiden in dieser Arbeit behandelten Punkten konzentriert: die Eigenschaften von Solarzellen, die auf einem ZnO/Cu_2O-Heteroübergang basieren, und die Prinzipien der Substratstrukturierung durch DLIP (Direct Laser Interferenzmuster) speziell.

Das zweite Kapitel widmet sich den verwendeten experimentellen Methoden. Der erste Teil dieses Kapitels ist der Beschreibung der verwendeten Ablagerungs- und Behandlungsmethoden gewidmet:
- die Abscheidung dünner Schichten durch reaktives Magnetron-Sputtern im DC- und HiPIMS-Regime. Die Prinzipien, der experimentelle Aufbau und die experimentellen Bedingungen für die Realisierung von dünnen Schichten aus ZnO und Gold durch DC-Sputtern und von AZO durch HiPIMS werden vorgestellt.
- In ähnlicher Weise werden das Prinzip, die experimentelle Vorrichtung und die nützlichen Bedingungen für die Synthese von Cu_2O-Dünnschichten durch das ALD-Verfahren vorgestellt.
- Das Substratstrukturierungsverfahren, speziell durch USP-DLIP, wird detailliert erklärt. Anschließend werden die Prinzipien der Modellierungsmethode zur Vorhersage der idealen Texturierungsbedingungen sowie die experimentelle Strukturierungsmethode beschrieben.
- Dieser erste Teil endet mit einer Darstellung der Voraussetzungen zur Herstellung von Testvorrichtungen für die Produktion zukünftiger texturierter Solarzellen.
Im zweiten Teil dieses Kapitels werden die zur Untersuchung der elektrischen, optischen, strukturellen Eigenschaften und der elektronischen Struktur der verschiedenen Schichten verwendeten Charakterisierungsmethoden vorgestellt; sowie für die Charakterisierung von strukturierten Glas- und Solarzellengeräten.

Das dritte Kapitel widmet sich der Untersuchung des Einflusses der Al-Konzentration in den Zn/Al-Targets auf den reaktiven HiPIMS-Abscheidungsprozess, die chemische Zusammensetzung, die Struktur und die Mikrostruktur der Schichten. Zunächst wird beobachtet, dass der Entladestrom und die Filmabscheidungsrate stark vom Aluminiumgehalt in den Targets beeinflusst werden. Tatsächlich nimmt bei gleichem Verschleißzustand der Targets die Abscheidungsrate mit dem Aluminiumgehalt stark ab, während der Entladungsstrom stark ansteigt. Diese Ergebnisse wurden durch die Zunahme der Reaktivität der Targets gegenüber dem in der Gasphase vorhandenen Sauerstoff bei steigendem

Aluminiumgehalt interpretiert. Dann begann die Untersuchung der Eigenschaften der erhaltenen AZO-Filme mit ihrer chemischen Analyse. Die Verteilung von Zink, Aluminium und Sauerstoff innerhalb der Filme ist relativ homogen, wobei die Konzentration von Al in den Filmen mit der der Targets wie erwartet zunimmt. Im Anschluss wurden die Struktur und Mikrostruktur der Filme durch Röntgenbeugung und Transmissionselektronenmikroskopie für zwei charakteristische Positionen charakterisiert, die der Achse des Targets zugewandt sind. Die Ergebnisse der Röntgenbeugung (XRD) zeigten, dass die kristalline Struktur des Wurtzit-Typs der Filme sich verschlechtert, wenn die Al-Zusammensetzung erhöht wird, bis sie amorph oder sehr fein nanokristallin für den Film wird, der von dem Target abgeschieden wird, das 15 Atom-% Al enthält. Die Filme, die von Targets abgeschieden werden, die 5 und 10 Atom-% Al enthalten, sind vorzugsweise entlang der *c*-Achse der Wurtzitstruktur orientiert. Die Filme, die von Targets abgeschieden sind, die 1 und 2 Atom-% Al enthalten, haben mehrere Orientierungen und sind wahrscheinlich substöchiometrisch. Aus den XRD-Daten wurden die Kristallitgröße und der Kristallinitätsindex für die am besten kristallisierten Filme berechnet und es wurde beobachtet, dass die Werte dieser beiden Parameter mit zunehmendem Al-Gehalt abnehmen. Diese Studie wurde durch Transmissionselektronenmikroskopie (TEM) vervollständigt, wodurch dieVerschlechterung der Kristallinität und der Übergang von säulenförmigem Wachstum zu Wachstum mit feinen und gleichachsigen Körnern für die Filme, die von den Targets mit 10 und 15 Atom-% Al abgeschieden werden, bestätigt werden konnte. Letztere sind nanokristallisiert und behalten die Wurtzitstruktur bei.

Das vierte Kapitel wurde die Untersuchung der Entwicklung der Eigenschaften von AZO-Filmen gemäß der Al-Zusammensetzung fortgesetzt, indem das Interesse auf die optischen Eigenschaften und die elektrischen Eigenschaften konzentriert wurde. Es wurde beobachtet, dass die Durchlässigkeit der Filme mit zunehmender Al-Konzentration zunimmt. Die Entwicklung der Verteilungskurven des Absorptionskoeffizienten mit der Wellenlänge für die verschiedenen Filme ermöglichte es zu zeigen, dass die Filme mit steigendem Aluminiumgehalt transparenter werden. Diese Ergebnisse unterstützen die Hypothese des Vorhandenseins von Sauerstoffunterstöchiometrie in Filmen, die aus Targets mit niedrigem Aluminiumgehalt synthetisiert wurden. Die Extraktion der Bandlückenwerte nach der Tauc-Methode zeigt eine quasi-progressive Zunahme dieses Parameters mit dem Aluminiumgehalt in den Folien. Bei Gehalten kleiner oder gleich 3 Atom-% erklärt sich die Zunahme durch den Burstein-Moss-Effekt, der mit der Zunahme der Dichte freier Elektronen verbunden ist. Bei höheren Gehalten stimmt der Anstieg nicht mit dem Burstein-Moss-Effekt überein und deutet

auf eine Änderung des Bindungstyps innerhalb des Materials hin. Die Untersuchung der elektrischen Eigenschaften der AZO-Filme zeigt eine Erhöhung des spezifischen Widerstands mit der Al-Konzentration mit einem systematisch höheren Widerstandswert in axialer Richtung, was einer möglichen Deaktivierung der Dotierung durch Bildung sekundärer Phasen zugeschrieben wurde. Um den Kompromiss zwischen Durchlässigkeit und spezifischem Widerstand zu zeigen, wurde die Gütezahl, die umgekehrt abhängig von spezifischem Widerstand und Absorption ist, berechnet und dargestellt. Dieser Parameter nimmt mit zunehmender Al-Zusammensetzung ab, mit niedrigeren Werten entlang der in-Achse (Position gegenüber der Achse des Ziels). Der elektrische Widerstand, gemessen während des sequentiellen Glühens in Luft bei 100, 150, 200 und 225°C für 1 Stunde, nimmt zuerst ab, bevor er zunimmt. Dieser Anstieg des spezifischen Widerstands, der wahrscheinlich die Oxidation an Luft charakterisiert, tritt umso früher auf, je geringer die Al-Zusammensetzung ist. Diese Messungen könnten nach bestimmten Validierungen zum qualitativen Vergleich der Sauerstoffsubstöchiometrie verwendet werden. Zum Abschluss dieses Kapitels wurde eine umfassende Untersuchung der elektrischen Eigenschaften von Filmen mit niedriger Al-Zusammensetzung durchgeführt, wobei der Aluminiumgehalt, die Entladungsspannung und der Alterungszustand der Targets berücksichtigt wurden. Diese Studie weist auf das Vorhandensein komplexer Mechanismen auf der Ebene der Plasma-Target-Wechselwirkungen hin, die indirekt die Leitungseigenschaften der Filme beeinflussen, indem sie auf die Sauerstoffsubstöchiometrie und die Deaktivierungsmechanismen des Aluminiumdotierungsmittels einwirken.

Das fünfte Kapitel wird versucht, den Ursprung der Verschlechterung der Eigenschaften von AZO-Filmen mit hoher Al-Konzentration durch die Aktivierung/Deaktivierung der Al-Dotierung innerhalb der AZO-Filme anhand von Untersuchungen via Verlustspektroskopie (ELNES - Energy Loss Near Edge Structure) Zn-L_3, Al-K, Al-$L_{2,3}$ und O-K zu erklären. Das Hauptergebnis dieser Studie ist die Möglichkeit, zwei unabhängige Signaturen an der Al-$L_{2,3}$-Schwelle zu erkennen:

- Das Vorhandensein delokalisierter elektronischer Zustände vom Al-Dotierstoff am unteren Rand des Leitungsbandes. Dies korreliert mit einer durch den Hall-Effekt gemessenen hohen Elektronendichte und charakterisiert die Aktivierung des Dotierstoffs.
- Die Positionierung der Al-Dotierung in oktaedrischer Konformation statt in tetraedrischer. Dies charakterisiert die Deaktivierung der Al-Dotierung.

Es wird gezeigt, dass es möglich ist, experimentelle ELNES-Spektren an der Al-$L_{2,3}$-Schwelle aus Referenzspektren zu simulieren, die diese beiden Zustände charakterisieren, und ihre

jeweiligen Anteile abzuleiten. Wir glauben, dass dieser Ansatz in zukünftigen Arbeiten verwendet werden kann, um die Mechanismen der Aktivierung/Deaktivierung der Dotierung besser zu verstehen und somit zu versuchen, die Eigenschaften von AZO-Filmen zu optimieren.

Das sechste Kapitel wurden Zellprototypen basierend auf Glas/AZO/ZnO/Cu_2O/Au-Stapeln hergestellt und dann getestet, um Verbesserungsmöglichkeiten für die Herstellung von Solarzellen oder effizienten texturierten Solarzellen zu definieren. Insgesamt wurden flache oder via USP-DLIP strukturierte Glassubstrate mit unterschiedlichen Periodizitäten, eine transparente AZO-Elektrode, abgeschieden von einem 1 oder 2 at.% Al-Target, ein ZnO/Cu_2O-Heteroübergang und ein Goldkontakt entwickelt und charakterisiert. Die Photostrom- und optischen Verlustsimulationen wurden in Zusammenarbeit mit Marcos Soldera **[1]** durchgeführt, um bei der Auswahl der geeigneten Strukturierungsparameter zu helfen. Die Ergebnisse zeigten, dass eine hohe Dicke der Cu_2O-Schicht bis zu 500 nm, eine hohe Strukturtiefe und eine geringe Periodizität von 1 µm notwendig sind, um maximale Werte des Photostroms zu erreichen. Andererseits war die experimentelle Durchführung nur für 70 nm Cu_2O, abgeschieden durch ALD, und für eine Periodizität von mindestens 1,5 µm möglich. Aus den in XRD erhaltenen Daten wurde zusätzlich zur Bestätigung des Wachstums der Cu_2O-Phase durch ALD beobachtet, dass der ZnO-Film gemäß der kristallinen Struktur vom Wurtzit-Typ gut wächst, aber seine bevorzugte Orientierung durch die Art des Substrats (Glas oder Si), die Position des letzteren in Bezug auf die Achse des Substrathalters während der DC-Sputter-Abscheidungsphase und der während der Abscheidung verwendete Sauerstofffluss bestimmt wird. TEM-Beobachtungen zeigten, dass AZO-Filme, die von einem Target mit 1 Atom-% Al und darauf abgeschiedenem ZnO abgeschieden wurden, säulenförmig und in der Wurtzitstruktur kristallisiert sind, wobei der erstere mehrere Kristallrichtungen aufweist, die entlang der Wachstumsrichtung des Films ausgerichtet sind, und der zweite hoch orientiert ist vorzugsweise entlang der *c*-Achse. Der Vergleich zwischen einem ZnO/Cu_2O-Heteroübergang, der auf einem Siliziumsubstrat abgeschieden wurde, das 2 oder 8 cm von der Achse des Substrathalters entfernt platziert wurde, zeigte, dass ZnO immer in der (002)-Richtung wächst, während Cu_2O je nach Position unterschiedlichen Orientierungen folgt. Schließlich haben rasterelektronenmikroskopische Beobachtungen gezeigt, dass das Wachstum von AZO auf strukturiertem Glas optimiert werden muss, sei es auf Glasebene oder auf der Ebene des Abscheidungsprozesses. Die chemische Analyse der Geräte ermöglichte es, die Homogenität der Cu_2O-Schicht durch ALD zu verbessern und über

ELNES bei den Cu-$L_{2,3}$- und O-K-Schwellenwerten die XRD-Beobachtungen zu bestätigen, die zeigten, dass es sich um die Cuprit-Cu_2O-Phase handelt, die abgeschieden wurde und nicht die Tenorite-CuO-Phase. Es wurden komplette Solarzellen entwickelt und I-V-Messungen (Current-Voltage-Messungen) haben eindeutig ein gleichrichtendes Verhalten eines p-n-Übergangs gezeigt. Der gemessene Photostrom war jedoch übermäßig niedrig, was die Notwendigkeit zeigt, die Eigenschaften von ZnO- und Cu_2O-Filmen zu optimieren.

Die umfangreiche Studie, die in dieser Arbeit an den AZO-Filmen durchgeführt wurde, ermöglichte es, die Wirkung der Al-Zusammensetzung und die Entwicklung der elektrischen und optischen Eigenschaften der Filme in Beziehung zu setzen, um einen geeigneten Kompromiss für die Verwendung als transparente Elektrode in Solarzellen zu finden. Die ELNES-Analyse hat ein besseres Verständnis der Zusammenhänge zwischen der elektronischen Struktur, den elektrischen, strukturellen und chemischen Eigenschaften der Schichten in Abhängigkeit von der Al-Zusammensetzung ermöglicht. Bezüglich der Ausarbeitung und Charakterisierung der Proben für Solarzellen zeigten die Ergebnisse eine gute Etablierung des ZnO/Cu_2O-Heteroübergangs innerhalb der Zelle, aber Optimierungen auf mehreren Ebenen bleiben notwendig, um eine Solarzelle mit hohem Photostrom zu entwickeln.

Acknowledgements

While personal hard work is undeniable for the success of a doctoral thesis, the support and help of others on all sorts of levels is without a doubt indispensable.

Firstly, I would like to thank my supervisor David Horwat for accepting my doctoral thesis application and giving me the opportunity to realize my dream of becoming a doctor in the materials science field. Also, I thank you for giving me the opportunity to teach at the EEIGM university for three years of my thesis which provided me with a lot of teaching experience. One could not ask for a better supervisor than David; he is always there and ready to answer all sorts of questions and help when I get frustrated with an experiment or a result interpretation. Outside of lab work, he was also ready to help with me with job and post-doc applications, as well as doing his best to make sure I don't go into financial trouble. Finally and most importantly, I thank David for being there for me, encouraging me and supporting me during the hard times I went through with the pandemic and with personal life problems. I wouldn't have been able to be writing this exact page from my manuscript, i.e. been able to reach the end of my thesis, without your patience, help and support. I have learned from you so much and I always keep in mind your "Il y a toujours une solution" (There is always a solution) reassuring sentence. I apply this to my daily life now, because much like how you taught me, there is not only a plan B and C, but even a plan D, E, F, and so on.

While I was happy and lucky to have such an amazing supervisor, I discovered I was even more lucky to have an equally amazing co-supervisor, Stéphane Cuynet. Much like David, Stéphane was always there to help me figure out the problems I was having with my PVD deposition, explain them to me, and we would solve them together. He was always there and

excited to see my results after each deposition, that we follow with discussion and plans for the next one. Other than that, Stéphane was also very supportive during the hard times I went through with the pandemic and with personal life problems. He was always there to listen to me when I was feeling tired and discouraged, always reminded me of what I am able to accomplish in times when I forgot my own strength and value, and kept on pushing me and pushing me to the very end. I wouldn't have been able to be writing this page right now without your support either.

I will also not forget to thank Pr. Frank Mücklich for giving me the opportunity of realizing this work in co-mentorship with Saarland University. He was very supportive during my stay in Germany and I was very lucky to be able to learn laser patterning in his lab; attend seminars, workshops and summer schools organized by the lab members.

Of course, some characterization measurements performed in this work wouldn't have been possible without the help and contribution of the expert members. Firstly I thank Sylvie Migot for the preparation of the TEM lamellae and for the time you sacrificed to provide me with the SEM cross-section images that I needed to perform on my structured samples. A special thanks to Jaafar Ghanbaja for realizing the TEM measurements on my samples for all three years of my thesis; we have worked a lot together to be able to show great results for my samples. Jaafar was always ready to help me analyze the data afterwards and understand the results. And when he was not available, Hiba Kabbara and Stéphanie Bruyère were more than happy to assist me with the data treatment, especially the FFT images that were not easy to index. I thank you for your patience and expertise that helped me analyze and understand the results. For the XRD measurements, I give my thanks to Pascal Boulet and Ghouti Medjahdi for conducting the measurements and answering my questions when needed. On the ALD experiments level, I am grateful for Claudia de Melo for the times she sacrificed to train me on the ALD machine and perform the Cu_2O films deposition together. And finally for the I-V measurements performed in Metz, I thank Sidi Hamadi for welcoming me in his laboratory and accompanying me during those measurements. I also thank Sourav Bose for his warm welcome and help when I was in Metz.

I won't forget to thank Juliette Barbat, Christine Sartori, Georges Billant and Marc Dalaut from the doctoral school office; Valérie Madeline, Martine Tailleur and Amandine Reiter from the human resources office, for their help with the administrative papers and aspects that needed to be done during this thesis.

I was lucky to have great colleagues from two different laboratories. From the Institut Jean Lamour lab, I thank my office partners Daria, Agathe and Adrian for their help when I had some questions and the small laughs that we shared. I also won't forget my colleagues of the (202) team: Joseph, Christophe, Benjamin, Zil, Quentin, Alejandro, Claudia, Fahad, Osama, Alexis and Vitalis; as well as the scientific discussions that I shared with Silvère Barrat, David Pilloud and Jean-François Pierson. From the Lehrstuhl für Funktionswerkstoffe lab, I thank Dr. Flavio Soldera, Dr. Claudia Hess and Dr. Jiaqi Luo for their help with the administrative aspects as well as the transportation and living accommodations in Saarbrücken. For their help with the laser patterning experiments, I thank Daniel Müller and Tobias Fox for the time they took to train me to use the lasers and perform the experiments while I was staying in Saarbrücken. But I especially thank them for providing me with patterned samples during the difficult pandemic times when travelling was quite hard, allowing me to continue doing my experiments in France on patterned substrates. I also won't forget to thank Dr. Marcos Soldera for the simulations run he has done on my samples in order to narrow down the right parameters for the substrate structuring.

I am happy to have completed by PhD within the PULSATEC-Interreg project that grouped partners from different universities and regions, working to bring new technologies to the surface treatment field by using pulsed plasma deposition. I have learned so much from our scientific meetings and discussions with our partners in Nancy (Dimitri Boivin, Ludovic de Poucques, Jean-François Pierson), Liège (Antoine Merlo, Grégoire Leonard, Daniel Alain) Luxembourg (Emmanuel Bidaine, Patrick Choquet, Marta Ferreira) and Saarbrücken (Dr. Flavio Soldera, Daniel Müller). I thank the PULSATEC project, the "Erasmus Mundus" within the DocMASE project, the UFA (Université Franco-Allemande) and the CNRS for the financial support of this thesis and especially Jean-François Pierson for the coordination of this project and financial support.

On a personal level, I would like to thank my family (my mother Randa, my father Joseph and my brother Christ) for their love, sacrifice and support that got me to this point in life.

A special thanks to my friends, back home in Lebanon or in Nancy, for the good times that we shared and for their great friendship. I think of Chirine, Ghenwa, Rami, Inas, Ossama, Farah, Anthony, Georges and Jenny. To my best friends Youssef Berro and Tony Srour, I appreciate your special daily support and advice on a personal and professional level. To Abir Nachawaty and Ossama El Hamouly, I will never forget you being there for me during the difficult times of the pandemic, among other times.

And finally, I dedicate this work to the two most important women in my life. My mom, for being my rock during these years and being a phone call away, day or night, to help me when I needed her and was worried about something. I don’t know what I would have done without you on those sleepless nights. And to my best friend, Joêlle (Jija), my life savior in all sense of the word. I don’t know what I would have done without you by my side, feeling things exactly how I felt them (the good and the bad), advising me and guiding me every single day of this long journey and until the very end. I could go on for pages about how much I love you, appreciate you, and cannot imagine losing you or finding someone as amazing as you are. I wish to always be the friend that you deserve, as I am lucky to have you as mine.

Table of contents

Motivation

While metals are very conductive due to their high free carrier density, the latter causes plasmonic reflections which makes them also very light absorbent; when considering very transparent materials with wide band gaps, they are usually also very resistive. For this reason, thin films of metal oxides called Transparent Conductive Oxides (TCO)s are drawing a lot of attention due to their simultaneous good transparency and electrical conductivity **[2]**. Sn:In_2O_3 or (ITO: Indium Tin Oxide) is known to be the most famous TCOs material due to its exceptionally high transparency and conductivity in the order of 10^{-5} Ω.cm. However, the toxic, expensive and rare metals used in ITO lead researchers to seek other metal oxides with similar properties **[3]**. Among those materials, Al-doped zinc oxide, or AZO, can nearly compete with those of ITO. Other than the zinc and aluminum being cheap, non-toxic and abundant, its optical and electrical properties were very interesting. In fact, over the years researchers took it upon themselves to obtain better and higher electrical and optical properties of AZO films by testing different deposition methods, and various conditions within these methods **[4-6]**. In this thesis, we adopted Reactive High Power Impulse Magnetron Sputtering (R-HiPIMS) as deposition method of the AZO films and chose to study the influence of the Al content in the alloyed Zn/Al targets on the optical, electrical, structural and chemical properties of the film. We also performed electronic structure measurements to try to explain the results obtained from the previous properties study.

The repercussions of the human activities on the environment and the depletion of the natural resources such as gas and petrol, led scientific researchers to find more environmentally friendly alternatives that are at the same time respondent to our basic needs. The conversion of sunlight into electricity appears as a good idea since natural sunlight is free, clean and abundant depending on the region; and thus solar cells and photovoltaics became very popular. However, one needs to fabricate easily processable solar cells that are scalable to large volumes and low cost. Many materials have been employed for the fabrication of solar cells, silicon based ones being the most common; however, they require a large amount of silicon and are expensive and complicated to make. Other materials like Copper Indium Gallium Selenide (CIGS)-based cells are also used but the toxicity of selenium and scarcity of indium are major issues. That’s why oxide thin film solar cells have been put into the light due to the abundance of their constituting elements, non-toxicity and low cost in terms of raw materials and fabrication costs. Among the considered oxides, ZnO and Cu_2O thin films are seen as promising due to their ease of deposition, good electrical and optical properties and

excellent photoconductivity. On the one hand, ZnO is a n-type semiconductor with a ≈ 3.3 eV direct band gap and 60 meV of exciton binding energy at room temperature. On the other hand, Cu_2O is a p-type semiconductor with a 2.2-2.9 eV band gap and suitable optical absorption and photoelectric properties for photovoltaics applications. Combining the optical transparency and electrical conductivity of n-ZnO with the high optical absorption in the visible region of p-Cu_2O makes up for a ZnO/Cu_2O heterojunction of interest for optoelectronic and sensor applications, as well as for solar cells **[2,7-11]**. In this thesis, we based the fabrication of the solar devices on the optimized AZO electrode obtained from the study described in the previous paragraph, and on the ZnO/Cu_2O heterojunction.

Solar cell structuring has been introduced as means of improving their efficiency. In fact, when a solar cell is structured, whether on the active layers level or the substrate, the photocurrent is found to be higher than that of a flat cell. However, substrate patterning was found to be better because it allows thickness reduction of the active layer without impairing the photoconversion, which is not possible if this layer is structured. Patterning in general allows the solar cell device to trap the light longer after it hits the substrate surface via multiple reflections on the facets of the structure before leaving the cell **[1,12]**. Different methods and structure shapes were tested out over the years, with the envisaged application being the deciding factor of the structure type and dimensions. In this thesis, we chose to pattern the glass substrate of our solar cell device by UltraShort Pulsed-Direct Laser Interference Patterning (USP-DLIP) method with a picosecond laser in order to make sinusoidal structures on the glass surface. We also collaborated with Dr. Marcos Soldera from the Institut für Fertigungstechnik of the Technische Universität Dresden **[1]** to model beforehand the possible texturing parameters that need to be applied in order to maximize the photocurrent of our solar cells.

On the whole, the goal of this thesis is to firstly optimize the transparent electrode AZO film deposited by reactive high power impulse magnetron sputtering mode without thermal assistance and from Zn/Al alloyed targets with 1, 2, 5, 10 and 15 at.% of Al. Once the films properties were studied and the optimized film was chosen, the next step was to fabricate a structured solar cell device based on a ZnO/Cu_2O heterojunction. For this, samples based on some parts of the solar cell and others consisting of a full solar cell device were subjected to electrical, structural and chemical analysis in order to evaluate their efficiency. This thesis is presented in the form of 6 chapters followed by a Conclusion and Outlook chapter.

In **Chapter 1**, a literature review of the different materials used in this work for the solar cells fabrication will be presented. In a first section, the importance and interest of TCOs in general will be introduced and then the three main thin films used in this study will be detailed: ZnO, AZO which is an Al-doped ZnO and the Cu_2O films. In each of the sections are listed their applications, properties, structures, deposition methods and of course their particular role in this work. In a second section, a view on the solar cell domain especially that based on ZnO/Cu_2O heterojunctions and substrate patterning will be detailed.

In **Chapter 2**, the different experimental techniques employed in this work will be presented and detailed from a bibliography approach, and then the experimental setups and conditions employed in this work will be shown. This will be followed by a description of the various characterization techniques used to study the thin films and the solar cells setups.

In **Chapter 3**, the optimization process of the AZO films will start with the study of the effect of the Al content in the Zn/Al targets on the properties of the resulting films. The deposition process will firstly be studied through the deposition rate and discharge current waveforms. Then, the results of the chemical analysis of the films performed by Energy Dispersive Spectroscopy of X-rays (EDS) mapping and cartography will be presented in order to follow the evolution of the Zn, Al and O species in the films. This will be followed by the structural and microstructural analysis of the films by means of X-Ray Diffraction (XRD), from which the crystallite size and crystallinity index were calculated, and by means of Transmission Electron Microscopy (TEM) to further extend the structural analysis.

In **Chapter 4**, the study of the AZO films properties will be pursued with the optical and electrical properties. In the optical properties section, the transmittance curves measured by (UltraViolet-Visible) UV-VIS spectroscopy will be presented and analyzed and then used to calculate the band-gap of the AZO films. Next, in the electrical properties section, the evolution of resistivity of the films as a function of the Al content will be shown and explained. While the values were obtained from the resistance measurements performed with the four point probe setup, the Hall effect measurement for some films will also be shown to support those results. Additionally in another experiment, the films were heated while performing the four point probe method in order to follow the evolution of their electrical properties with the temperature increase. To conclude this section, a study on the low content AZO films will be presented to highlight their different behavior from that of the higher Al content films.

In **Chapter 5**, the results of electronic structure measurements performed by the Energy Loss Near Edge Structure (ELNES) on the Zn-L_3, O-K, Al-K and Al-$L_{2,3}$ edges will be presented and interpreted to explain the evolution of the properties of the AZO films with the Al content. This chapter will be concluded by using a model that we developed from our data and that could serve future works for the study of the evolution of electronic structure and electrical properties of AZO.

In **Chapter 6**, the study of fabricated structured solar cells based on ZnO/Cu_2O heterojunctions will be developed. The first part will be dedicated to the glass structuring by USP-DLIP via the picosecond laser, where the modeling and the actual patterning of the substrate results are shown and explained. Next, the morphology observed from scanning electron microscopy and the structure/microstructure analysis done with XRD and TEM will be shown for the samples fabricated to be tested for use in the final solar cells setup. The chemical analysis of these samples obtained from the EDS and ELNES will also be conducted. To conclude this chapter, the I-V measurements done on two solar cells series will be presented and commented.

Chapter 1

General Introduction

In this work, zinc oxide films doped by aluminum (AZO: Al-doped zinc oxide) were deposited from Zn/Al targets with different at.% of Al by reactive magnetron sputtering in HiPIMS mode. The optical, electrical, structural and chemical properties were studied in order to understand the effect of the Al content in the targets, and eventually in the AZO films, on their performance. The goal of this was to optimize the AZO films to be used as a transparent electrode in solar cells. Next, based on the works of William Chamarro **[34]** and Claudia de Melo **[14]**, we deposited ZnO films by reactive DC sputtering and Cu_2O films by Area Selective-ALD (AS-ALD). For this reason, from **Sections 1.1 to 1.4**, we extensively detail the structure, properties, applications, deposition methods, etc. of the three main layers utilized in this work; them being the AZO, ZnO and Cu_2O films. Those different layers were used in this thesis for the elaboration, or for testing towards the elaboration, of structured solar cells based on a n-ZnO/p-Cu_2O heterojunction: patterned glass is used as substrate, AZO is the transparent electrode, ZnO and Cu_2O form the heterojunction and a final gold layer is deposited on top to play the role of the contact. Accordingly, the last section of this chapter (**Section 1.5**) is dedicated to the fabrication of patterned solar cells based on ZnO/Cu_2O heterojunctions specifically. The choice of patterned substrate, specifically via UltraShort Pulsed-Direct Laser Interference Patterning (USP-DLIP), instead of a conventional flat one and the importance of a ZnO/Cu_2O heterojunction are detailed.

1.1. Transparent Conducting Oxides (TCO)s

Here we start by giving some general considerations on TCOs. TCOs are compound semiconductors often represented by A_xB_y, with A being a metal or metal combinations and B the oxygen. They have specific opto-electrical behaviors that can be altered by doping with a dopant D being a metal, metalloid or nonmetal (A_xB_y:D). A TCO material is basically a wide band-gap semiconductor with intrinsic defects in the material or extrinsic defects from dopants. Some applications of TCOs include

opto-electrical apparatuses, interfaces and circuits like photodetectors, flat panel displays and light emitting diodes (due to TCO's good spectral transmittance), photovoltaic cells and modules, transparent electrodes for electrochromic cells, Liquid Crystal Display devices (LCDs) and electroluminescent devices. Some TCOs can also be used in aircraft windshields to prevent surface icing. All these applications employ TCO's in a thin films form, which is a great alternative to periodic or irregular metal grids or nanowires prepared by lithography or direct deposition from solutions because their patterning introduces an additional processing step. Also, there are huge contact resistances between the wires and tubes as well as an intrinsic percolation problem. To this day, the most known and employed TCOs are tin oxide (SnO_2), indium oxide (In_2O_3), indium tin oxide (ITO) and zinc oxide (ZnO). ITO is a solid solution of ≈ 90 wt.% In_2O_3 and ≈ 10 wt.% SnO_2. ITO finds its applications in touchscreens, organic solar cells and Copper Indium Gallium Selenide (CIGS) solar cells because it can exhibit, simultaneously, very low electrical resistivity values, in the 10^{-5} .cm range, and high optical transparency in the visible range. However, ITO has several drawbacks. First, indium is scarcely found in the earth crust, making its cost volatile and high. Second, indium and tin are heavy and hard to recycle metals. Finally, the production of ITO films can release cytotoxic ITO nanoparticles **[15,16]**. Hence, alternative n-type transparent conductive materials exhibiting similar performance without the drawbacks of ITO are highly sought. Among these alternatives are metal nanogrids, arrays of nanowires, conductive polymers, graphene and other TCOs **[17]**. Another TCO, Al-doped zinc oxide (AZO) is a very serious candidate given the abundance of zinc and aluminum, their low cost and low toxicity and good recyclability, but also its compatibility with the semiconductor industry technologies. AZO films were the semiconductor of choice in this work to be optimized then used as the transparent electrode in the final solar cells. The long term objective of our research group, whose this work is a building block, is to develop a textured all-oxide solar cell based on Cu_2O/ZnO junctions and an AZO transparent electrode. In the following paragraphs, we review the main properties of TCOs in general followed by detailed descriptions of the three types of wide bandgap semiconductors/TCOs involved: ZnO, AZO and Cu_2O.

1.1.1. Types and doping of TCOs

As for semiconductors in general, n-type or p-type TCOs exist. A n-type TCO is a semiconductor doped with an element holding an extra electron compared to the host; this electron has nothing to bond with and so roams freely in the host crystalline structure which leads to an electric current in the structure if an electric field in applied. For example Sn-doped InO_2, ZnO doped with group III

elements, SnO_2 doped with group V elements are n-type TCO. The conduction paths of electrons at the bottom of the Conduction Band (CB) are ensured by the ns^0 orbitals of the metal ions, like Zn^{2+}, In^{3+} and Sn^{4+}.

A p-type TCO is a semiconductor doped with an element missing an electron compared to the host; this produces a hole in the Valance Band (VB) of the host. The conduction paths of holes at the top of the VB are ensured by the hybridization of the oxygen's $2p^6$ orbital and the metal's orbitals such as Cu $3d^{10}$, Sn $5s^2$ and S $3p^6$.

1.1.2. Relationships between electrical and optical properties

The typical electrical conductivity of n-type TCOs is shown in **Figure 1 a)**, where we can see that it is usually between that of semiconductors and metals and is in the 10^3 – 10^4 S/cm range. From **Figure 1 b)**, we can see that metals have very high carrier concentration *n* but mediocre carrier mobility μ, whereas doped semiconductors have high μ but low *n*. TCOs are in between those two types of materials and they are degenerate semiconductors. They have similar μ as some typical metals like copper (Cu) and silver (Ag) and so are regarded as metals with low *n*. Much like metals, they don't need a thermal activation energy to generate carriers **[18-21]**.

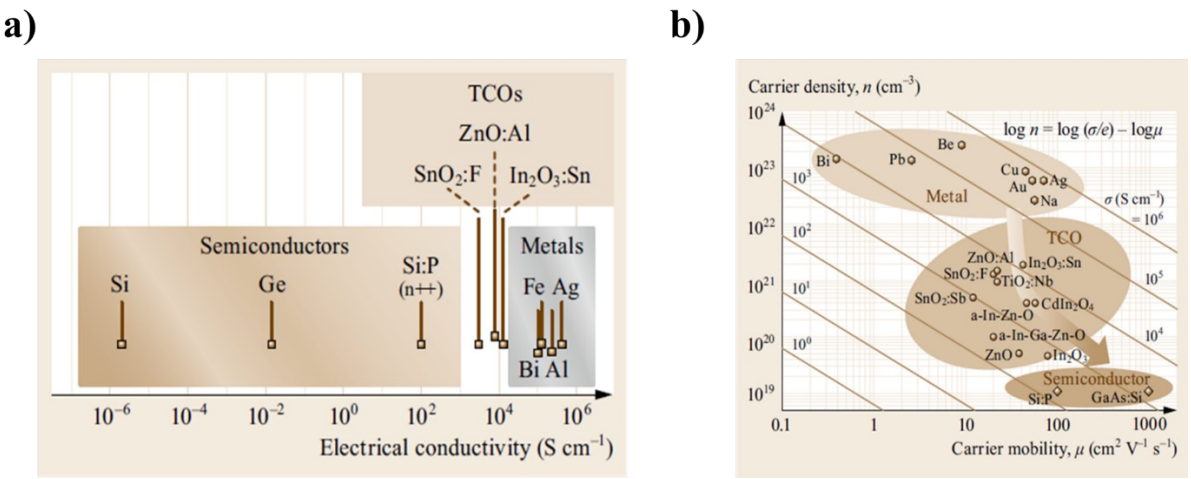

Figure 1: **a)** Electrical conductivity (S/cm) ranking and **b)** carrier density *n* (cm^{-3}) and carrier mobility μ ($cm^2V^{-1}s^{-1}$) of some semiconductors, TCOs and metals **[20]**.

Intrinsic or extrinsic doping of n-type TCOs provides their CB with free electrons (expressed with *n* as in electron carrier concentration) since the defects' levels lie near the CB. However, a high value of *n* means a higher absorption of light in the visible and infra-red regions of the solar spectrum which decreases the material's transparency (300 nm–10 µm range for typical oxides). For this reason, it is not easy to fabricate TCO's that are both transparent (Band gap (E_g) > 3,3 eV to be

transparent in the whole visible spectral range) and electrically conductive without having some sort of compromise between the properties or parameters. In fact, transparent materials are normally insulators (SiO_2) and highly conductive materials are usually of a reflective metallic appearance (Ag and Al) or of dark color ($YBa_2Cu_3O_7$ black superconductor). Let's consider the following **Equation 1**:

$$\rho = \frac{1}{\sigma} = \frac{1}{ne\mu} \qquad \textbf{(Eq. 1)}$$

With ρ the electrical resistivity, σ the electrical conductivity and e the elementary charge. In order to have low resistivity ρ (inversely proportional to the conductivity σ), we can have either high n or high mobility μ; but since the absorption of light in the infra-red region is favored by a high carrier concentration as well as a high defect density in the band gap, and since the electron mobility increase does not have any side effects, it can be preferred to work on increasing the latter to improve both the electrical conductivity and optical transparency range, in particular if applications using the infra-red range are targeted **[18-22]**.

The transmittance curve for a typical oxide is plotted in **Figure 2 a)**; one can see that the TCO is transparent in the visible region and has two absorption edges in the infra-red and ultraviolet regions due to respectively the lattice vibration and the fundamental absorption following the electron transition from the VB to the CB **[20]**.

a) **b)**

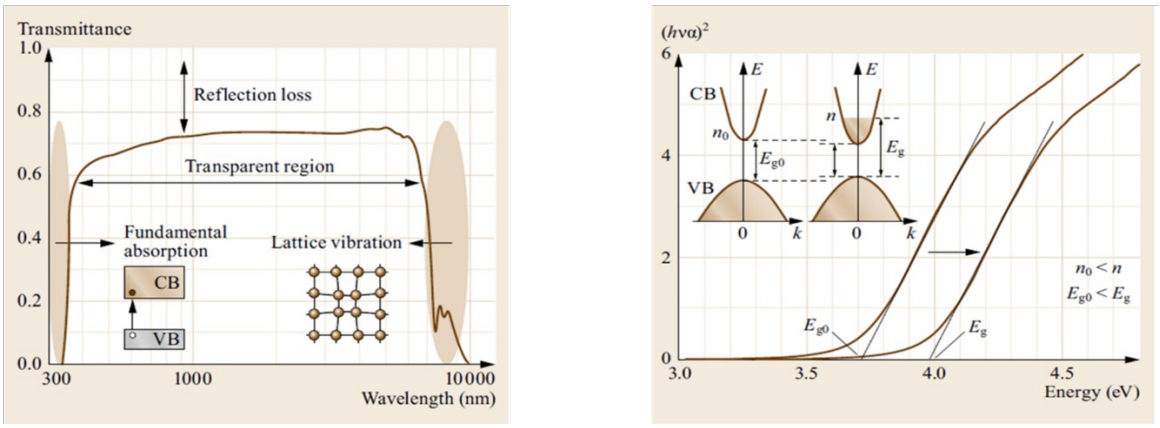

Figure 2: **a)** Transmittance of a typical oxide and **b)** Tauc plot to show the blue shift of fundamental absorption due to band filling **[20]**.

Carriers in TCO introduce light absorption and reflection; in fact, when light illuminates the conductors, the carriers oscillate with the light's frequency (plasma oscillation) and the light is reflected. But if the frequency is too high, the light goes directly through the conductors without any

plasma oscillation or reflection. Hence, there is a maximum threshold frequency ω_p or wavelength λ_p that permits plasma oscillation and they are expressed as follows (**Equation 2**):

$$\omega_p = \frac{n e^2}{\varepsilon_0 m} \text{ and } \lambda_p = \frac{2\pi c}{e}\sqrt{\frac{\varepsilon_0 m}{n}} \quad \textbf{(Eq. 2)}$$

With n the carrier concentration, e the elementary electron charge, ε_0 the permittivity, m the electron rest mass and c the speed of light in vacuum.

For example, ITO's n is 10 times smaller than that of Al which means that λ_p moves to the infra-red region and ITO is then transparent in the visible region especially that its band gap is high enough (> 3,5 eV) to transmit visible light. Hence, for applications involving infra-red light such as solar cells, we aim to have $n < 10^{21}$ cm^{-3} for TCOs because a greater value implicates a significant absorption of light by the free carriers.

Doping introduces additional energy levels, i.e. increased n, next to the VB for p-type semiconductors and next to the CB for n-type semiconductors. For the latter, the Fermi level is shifted according to the following **Equation 3**:

$$E_C - E_F = k_B T \ln\left(\frac{n_C}{n_D}\right) \quad \textbf{(Eq. 3)}$$

With E_C the CB's energy level, E_F the Fermi's level energy level, k_B Boltzmann's constant, T the temperature, n_C the effective density of states in the CB and n_D the density of donor defects.

In non-degenerate semiconductors, the Fermi level increases with doping. But if the dopant concentration > n_C, the Fermi level goes up into the CB yielding a degenerate semiconductor and the **Equation 3** becomes:

$$E_C - E_F = \frac{\hbar^2}{2 m_e^*}(3\pi^2 n_e)^{\frac{2}{3}} \quad \textbf{(Eq. 4)}$$

With $\hbar$ the reduced Planck's constant, m_e^* the effective mass of an electron and n_e the electron's concentration.

Since the Fermi level is inside the CB, the latter's bottom states are filled and the E_g is shifted to higher energies as can be seen in **Figure 2 b)** representing Tauc's plot detailed further in this work. We can see that when n increases the absorption edge shifts to higher energies indicating higher band gaps and wider optical windows in the UV region. In fact, as shown in the inset of **Figure 2 b)**, when carriers occupy the CB, the band gap energy necessary to the transition from VB to an unoccupied CB becomes larger. This change is called band filling or Burstein-Moss effect with the shift (ΔE_{BM}) being expressed by the following **Equation 5**:

$$\Delta E_{BM} = \frac{\hbar^2}{2}(3\pi^2 n_e)^{\frac{2}{3}}\left(\frac{1}{m_e^*} + \frac{1}{m_h^*}\right) \qquad \textbf{(Eq. 5)}$$

With m_h^* the hole effective mass **[13,20,22]**.

p-type conductors include almost all copper oxide-based, high-temperature superconductors derived from semiconductors like La_2CuO_4 ($E_g \approx 2$ eV); however they are correlated electron insulators. This means that vibrational, magnetic, and excitonic transitions occur and cause sub-band-gap optical excitation; doping increases their light absorption. For this reason, p-type conductors are not good compromised transparent and conductive TCOs. Nevertheless, some p-type conductors include Cu_2O, CuO, $CuAlO_2$ and $SrCu_2O_2$ with Cu^{1+} $[Ar]3d^{10}4s^0$. They are filled d-band insulators and are suitable transparent/conductive TCOs. One must note however that even though Cu^{2+} can be accommodated in p-type conductors, it still means that a hole is added to the d orbital, which increases the light absorption. Nevertheless, $CuAlO_2$ is transparent, probably because either the doping level is so low that the light absorption is not high enough to cause coloration or the optical excitations are altered due to hole doping after the Cu-O hybridization **[18,20,22-25]**.

1.2. Properties of ZnO films

ZnO is a direct wide band gap compound semiconductor from the II-VI group with an ionicity between that of the covalent semiconductors and the ionic semiconductors. ZnO has a bandgap of ≈ 3.3 eV at room temperature which provides this material with a very high transmittance in the visible region. Additionally, one important property of ZnO is its large exciton binding energy of 60 meV, which makes it useful for optical emission in the UV region under harsh conditions. In fact, if a photon has an energy higher than E_g, the electrons go from the VB to the CB leaving a hole in the VB. The excited electron then needs to return to its stable ground state emitting a photon with lower energy than the absorption step and that can be observed at room temperature for such a high value of 60 meV. This photon is emitted due to the formation of the electron-pair or exciton which is a neutral quasiparticle that moves freely inside the crystal carrying energy not mass. These properties make ZnO very interesting for many optoelectronic devices.

ZnO's morphology is a determining factor of the material's properties: ZnO can be fabricated in form of grains, fibers, thick or thin films, biocompatible nanostructures like nanowires, nanobelts, nanocrystals, nanorods and nanocombs. ZnO is used for gas sensing, modification of biosensing surfaces, biomolecules immobilization, as well as in solar cells and LCDs. ZnO nanostructures have excellent properties and are easily fabricated with inexpensive methods. ZnO is also used in

photocatalysis, catalysis, varistors, biosensors, transparent electrodes, optical sensors, UV absorption, sunscreen lotions, light emitters and antibacterials. For example, in solar cells with the absorber layer being a-Si:H or $Cu(In,Ga)Se(S)_2$, ZnO makes a great contact and window layer; the latter being also useful in display devices. Additionally, ZnO's piezoelectric properties makes it a good choice as a thin layer for surface acoustic wave devices. ZnO is even used by the food industry in breakfast cereals, food supplements and animal feedstuffs as a source of zinc necessary for humans and animals **[9,13,14,17,26-34]**.

Since oxygen (O) has the highest ionization energy among all the elements of the sixth group of the periodic table, a strong bond can be established between the 3d orbital of Zn and the 2p orbital of O. The VB maximum, given by the O^{2-} 2p orbital, and the CB minimum, given by the Zn^{2+} 4s orbital, are located at the same Γ point in the Brillouin zone at $k = 0$ with the Γ point being the center of the Brillouin zone; this makes ZnO a direct band gap semiconductor. In the band diagram of **Figure 3 a)**, we can see 10 bands near -9 eV corresponding to Zn 3d, 6 bands in the -5-0 eV range corresponding to O 2p bonding states representing VB and 2 bands in the 3-10 eV range corresponding to delocalized Zn 3s. As for the O 2p orbitals, due to crystal-field and spin-orbit interactions, they are degenerated into three sub-bands as seen in **Figure 3 b)**, each responsible for producing an exciton: A and C with a Γ_7 symmetry and B with a Γ_9 symmetry **[13,14,30,34]**.

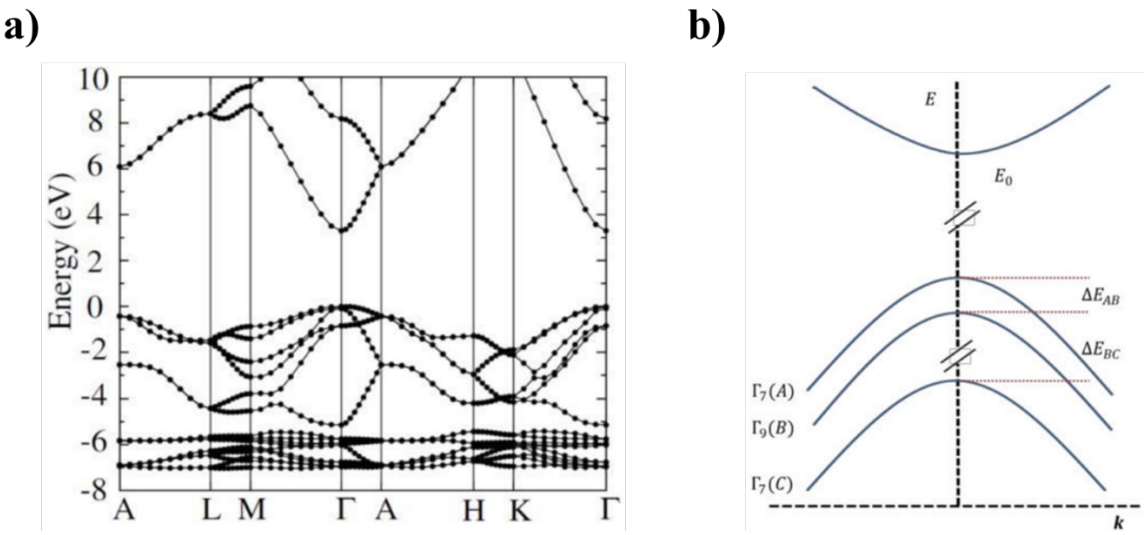

Figure 3: **a)** Graph showing the band structure of ZnO calculated with the HSE hybrid functional from the density functional theory. At 0 eV, the energy of the VB maximum was set **[35]**; **b)** Schematic representation of the VB and CB levels of ZnO with a direct transition **[34]**.

ZnO can crystallize into three types of structures presented in **Figure 4 a)**: hexagonal wurtzite known as the thermodynamically stable phase under normal conditions, cubic zinc blende which can be stabilized only if ZnO is grown on cubic substrates and cubic rocksalt or Rochelle salt obtained at

high pressures with a structure similar to salt (NaCl). In the wurtzite structure of ZnO (**Figure 4 b)**) belonging to the space group $P6_3mc$, the zinc ions (Z = 4, cation linked to four anions of a tetrahedron) occupy half of the tetrahedral sites *(T)* while the oxygen ions (Z = 4, anion linked to four cations of a tetrahedron) are hexagonally close-packed in the structure with the lattice parameters *a* and *c* being 3.2501 Å and 5.2071 Å, respectively. ZnO thin films are often oriented with the *c*-axis along the growth direction, especially the ones resulting from sputtering. ZnO has polar planes with the (0001) and $(000\bar{1})$ planes terminated respectively by Zn and O; this signifies that ZnO has no inversion symmetry and hosts piezoelectric properties. Due to the large size difference, Zn and O ions fill ≈ 44% of the ZnO crystal leaving a lot of open space **[13,29-31,36]**.

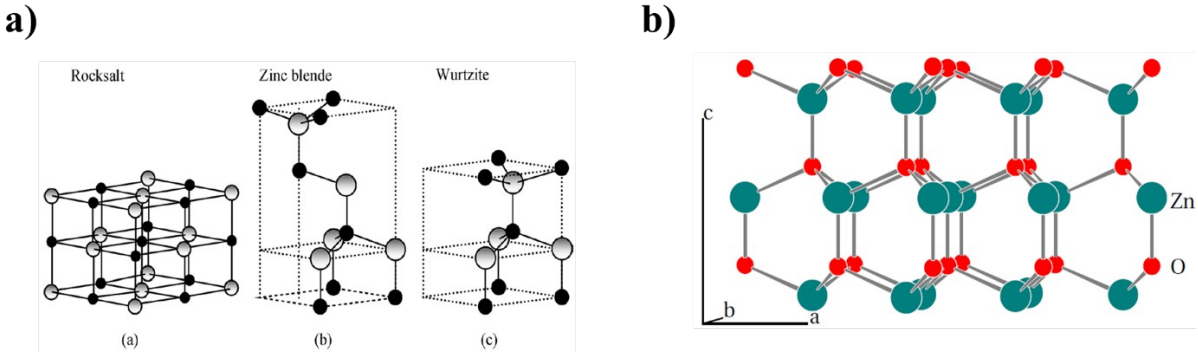

Figure 4: a) Schematic representation of ZnO's three crystal structures: (a) Rocksalt, (b) Zinc blende and (c) Wurtzite; Zn is presented by black spheres and O by the shaded grey spheres **[29]**; **b)** Another schematic representation of the wurtzite structure showing the superimposition of two hexagonal close packed Zn and O **[13]**.

ZnO's native defects comprise the following vacancies, interstitials and anti-sites of Zn and O, with the energy position of the vacancies and interstitials presented inside the band diagram of **Figure 5**:

Oxygen vacancy (O_v), zinc interstitial (Zn_i) and Zn anti-site due to O deficiency or Zn excess are donor defects; O_v and Zn_i are responsible for the intrinsic n-type conductivity of ZnO.

Zinc vacancy (Zn_v), Oxygen interstitial (O_i) and O anti-site due to Zn deficiency or O excess are acceptor defects; Zn_v and O_i are the dominant compensating defect in n-type ZnO.

Most studies agree that: O_i is a shallow acceptor that has the lowest formation energy among all intrinsic defects which is why its presence is dominant in an O_2 environment. Zn_i is a shallow donor but with a high formation energy so it exists in n-type ZnO only in out-of-equilibrium conditions. O_v has the lowest formation energy among the donor defects but is a deep donor that cannot contribute significantly to the carrier density (n), which makes both Zn_i and O_v an unlikely or an insufficient source of n-type conductivity under stable thermodynamic equilibrium conditions (this is not necessarily true for out-of-equilibrium conditions). Some authors propose the intervention of

extrinsic doping by hydrogen (H) impurities in order to explain the natural n-type conductivity of ZnO **[13,37-39]**.

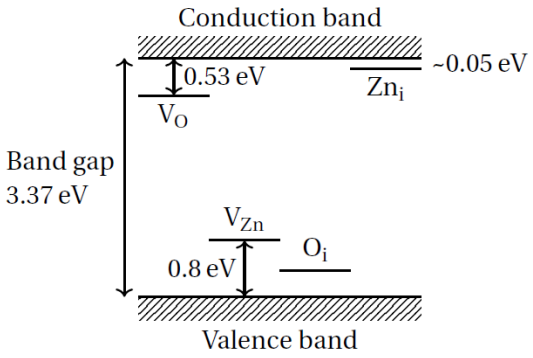

Figure 5: Schematic representation of the energy levels of the intrinsic point defects in ZnO **[13]**.

The interstitial defects in ZnO can occupy the octahedral *(O)* sites seen in the center of the 6-ring channels in the *c*-direction and tetrahedral *(T)* sites present on the lines of the Zn-O bonds that connect the hexagonal sheets like shown in **Figure 6 b)**. Zn_i at the (T) sites are thermodynamically unstable **[38,39]**.

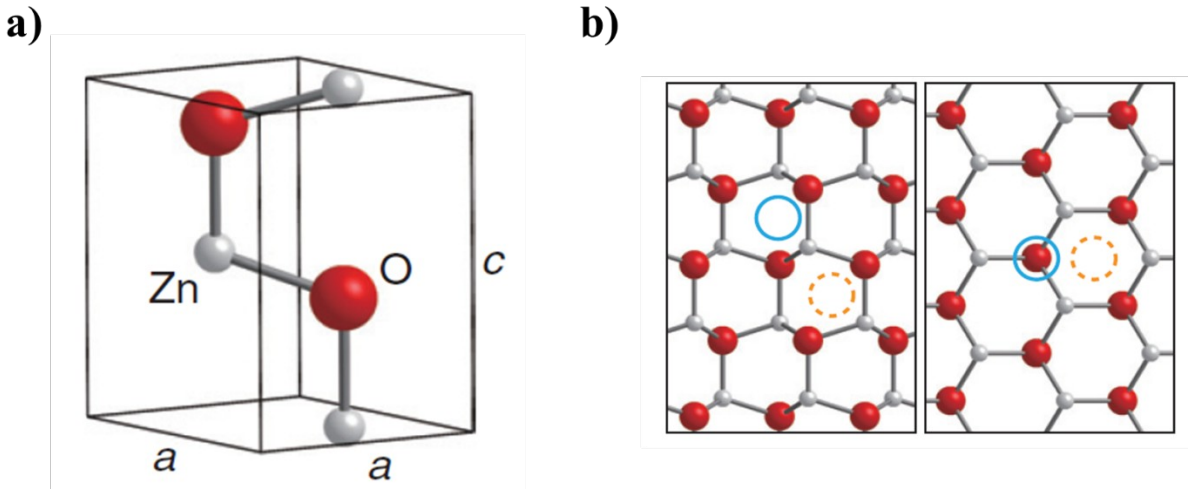

Figure 6: Schematic representation of **a)** the wurtzite structure unit cell of ZnO; and **b)** the same crystal structure but viewed in the [$\bar{1}\bar{1}$00] direction (left) and in the [0001] direction (right); the solid blue circle indicates the *(T)* sites while the dashed orange circle points to the *(O)* sites **[38]**.

ZnO is a great replacement for ITO due to the better availability and non-toxicity of Zn compared to Sn and In; ZnO is also highly transparent with good electrical conductivity. However, the properties may not always be homogeneous on the material's surface for many reasons, one of them being the oxygen sub- or over-stoichiometry **[7,32,40]**. An excess of oxygen in ZnO increases the concentration of the deep acceptors, O_i and Zn_v, which reduces the film's carrier density. But a lack of oxygen stimulates the introduction of the shallow donor Zn_i and the deep donor O_v.

ZnO can be deposited by various methods, under vacuum or not, such as spray pyrolysis, sol-gel, electrochemical deposition, thermal evaporation, Chemical Vapor Deposition (CVD), Metal-Organic CVD (MOCVD), Molecular Beam Epitaxy (MBE) and Pulsed Laser Deposition (PLD). Direct Current (DC), RadioFrequency (RF) or High Power Impulse Magnetron Sputtering (HiPIMS) are also widely used and the latter is the deposition of choice in this work for the AZO films deposition. In order to obtain very high electrical conductivities, the films usually require post-treatment methods. For example, while the sol-gel process (spin coating) is simple, flexible, scalable to large area coating and not so expensive; the ZnO films obtained are of poor conductivity, crystallinity and uniformity. Even though sputtering at low temperatures yields ZnO thin films with high conductivities ($\approx 10^2$ S/cm) and transmittance scalable to large area substrates, some applications require some additional changes to obtain even better properties. ZnO is a n-type TCO due to the excited electrons coming from the ionized Zn_i; increasing the latter contributes to decreasing it's electrical resistivity ($\rho \approx 0.01$ Ω.cm) by means of quenching, by heat treatment or sputtering in a (Ar + H_2) gas mixture. **[9,14,26,27,32,33,36]**.

ZnO films can be n-doped with excess Zn or with Al, Cu, Ag, Ga, Mg, Cd, In, Sn, Sc, Y, Co, Mn, Cr and B **[21,41]**. It exhibits a resistivity of 2-4 x 10^{-4} Ω.cm, with optimum extrinsic doping, which are medium values between those of ITO and SnO_2 and can be suitable for various applications. For instance, Y. Hagiwara et al. **[42]**compared the CIGS solar cells' performance using AZO or boron doped ZnO (ZnO:B) window layers deposited by RadioFrequency Magnetron Sputtering (RFMS). Both were deposited by RFMS at room temperature but a 2 wt.% ZnO:Al_2O_3 target in an Ar gas was used for the AZO film and a ZnO target in a B_2H_6-Ar gas mixture was used for the ZnO:B film. The short-current density (J_{SC}) was higher for ZnO:B with the same resistivity as AZO because it has higher electron mobility (μ_e) and so is more transparent in the near-Infra-Red (near-IR) region which gives it a higher quantum efficiency. The resulting MgF_2/ZnO:B/i-ZnO/CdS/CIGS/Mo solar cell had an active area efficiency of 18%, an Open-current voltage (V_{OC}) of 0.645 V, a J_{SC} of 36.8 mA/cm^2 and a Fill Factor (FF) of 0.76. In another example, highly conductive ($\rho \approx 10^{-4}$ Ω.cm) and transparent (T > 85%) ZnO:Sc and ZnO:Y films were deposited by DCMS from a powder target. Up to a maximum of 2 wt.% of Sc_2O_3 and 4 wt.% of Y_2O_3, the resistivity of the films decreased and so for the ZnO:Sc thin film with 2 wt.% of Sc_2O_3 and for the ZnO:Y film with 4 wt.% of Y_2O_3 both deposited on glass at 200 °C, the resistivity was 3.1 x 10^{-4} Ω.cm and 7.9 x 10^{-4} Ω.cm, respectively **[43]**.

In this work, the ZnO:Al (AZO) film was the doped ZnO film of choice to be optimized and used as a transparent electrode for solar cells; its properties will be detailed in the next section.

1.3. Properties of AZO films

1.3.1. General properties

Doping ZnO with group-III elements for instance B, Al, Ga and In yields materials that are alternatives to ITO because they are abundant, inexpensive (**Figure 7 a)**), non-toxic and environmentally friendly (**Figure 7 b)**) and could provide good transmittance and conductivity. The latter is due to the dopants that provide singly-charged donors supplying the CB with an excess of charged carriers. In the case of Al dopant (ZnO:Al, AZO or $Al_xZn_yO_z$), it can lead to an increased conductivity by several orders of magnitude **[5,7,21,44-48]**.

a)

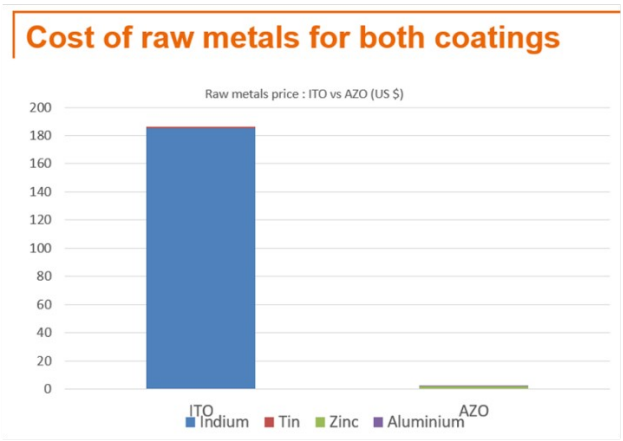

b)

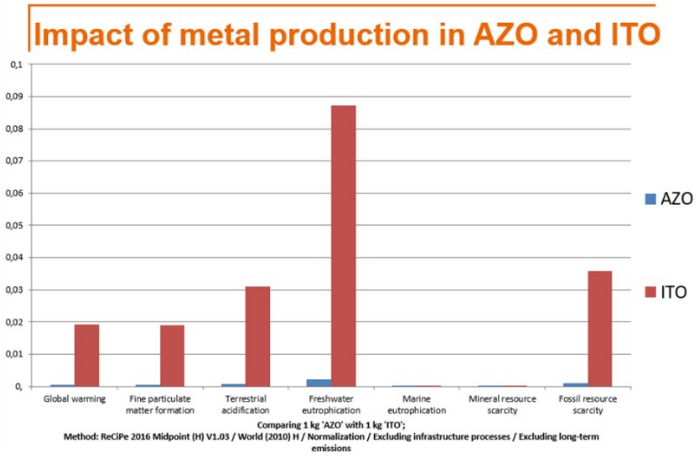

Figure 7: Statistic graphs showing **a)** the raw price (dollars) of the metals used to deposit ITO (indium and tin) and AZO (zinc and aluminum) films; and **b)** the environmental effect of the metal produced to be used in the ITO and AZO films **[Analysis of raw materials for ITO and CZO films, Antoine Merlo, Uliège, 2020]**.

Intrinsic defects produce compensating charge carriers determining the conductivity of ZnO; the equation representing this is established in **Figure 8 a)**. It represents the fact that the density of free electrons results from these compensations and in order to reach high performances one must optimize the intrinsic and extrinsic doping. Since the electrons generally compensate the holes in ZnO, the material is of n-type intrinsic conductivity but is still insufficient for use as a transparent electrode which is the role required in this thesis; this is where extrinsic doping is introduced, with Ga^{3+} and Al^{3+} being the most used dopants. In AZO films, the predominant donor Al replaces or substitutes Zn in the presented wurtzite structure of ZnO: The Al^{3+} ion replaces the Zn^{2+} ion in the structure forming a Al_{Zn}^{+} state and induces the release of a free electron (**Figure 8 B)**). The previous equation is maintained with the added $[Al_{Zn}^{\circ}]$ factor like shown in the equation of **Figure 8 b)** based on neutrality and omitting the influence of defect complexes. V_o, Zn_i and Al_{Zn} should highly dominate over O_i and V_{Zn} to ensure a high electron conductivity **[3,47,49]**.

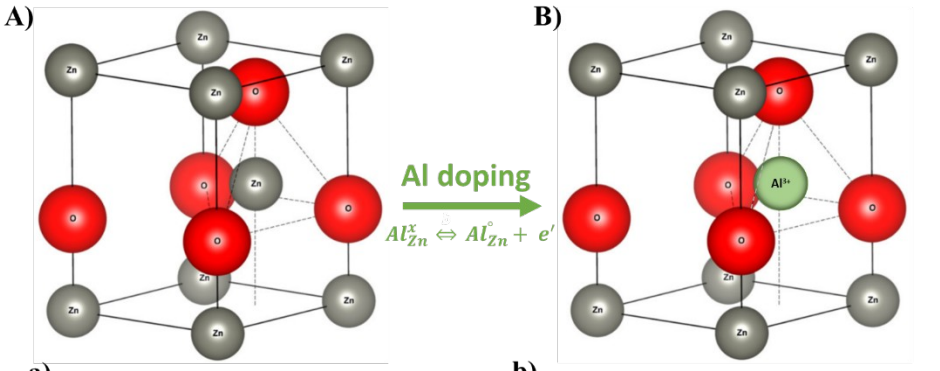

Figure 8: Graphic representation of the wurtzite structure of **A)** ZnO and **B)** AZO after doping ZnO with Al as well as the balanced equation for **a)** the intrinsic conductivity of ZnO and **b)** the extrinsic conductivity after doping with Al **[Modified from 3 and 50]**.

1.3.2. Deposition methods

AZO films can be deposited by sol gel, spray pyrolysis, vapor phase deposition, electro deposition, DCMS/RFMS or a combination of both as well as HiPIMS. Spray pyrolysis and sol-gel are simple methods (due to the lack of vacuum) that can control the film's composition, but they demand high process temperatures to reach good film properties. Pulsed filtered cathodic arc deposition, MOCVD, Plasma Enhanced CVD (PECVD), Atmospheric Pressure CVD (APCVD), ALD and thermal evaporation can ensure resistivities in the order of 10^{-4} Ω.cm for the AZO films. MOCVD needs high process temperatures; PECVD can reduce this temperature by using a plasma. APCVD does not

require vacuum and ALD deposits films with great conformity but at lower deposition rates and with a high sensitivity to the chemical nature of the substrate.

High quality deposition methods using plasma include Low Pressure CVD, MOCVD, PECVD, PLD, ALD and electron beam evaporation. PLD produces great quality AZO films but it requires high deposition temperatures and is only suitable to laboratory scale. Y. Liu et al. **[45]** deposited AZO films on quartz glass substrates by PLD at 150 °C under 11 Pa of oxygen pressure, from Zn/Al targets with 0-8 wt.% of Al. Their optimized film contained 1.37 wt.% of Al (from a Zn/Al 2 wt.% target) and presented the smallest resistivity and a strong UV photoluminescence.

AZO films with electron mobilities greater than 40 $cm^2V^{-1}s^{-1}$ can be deposited by pulsed filtered cathodic arc which in DC mode can reach high growth rates. The resulting AZO films are highly crystalline with impressive crystallographic alignment of the grains even for room temperature depositions. However, since the cathode-substrate distance is needed to be quite long in order to ensure a thin films free of macroscopic particles by making enough space for the magnetic plasma filter, the ion flux is majorly reduced.

Therefore, we need to use other non-equilibrium methods like Physical Vapor Deposition (PVD) in order to deposit AZO films with high dopant concentration of Al because the solubility limit under stable equilibrium of Al in ZnO is around 0.3 at.%. The opto-electronic properties determined by the aforementioned deposition methods could also be influenced by the nature of the substrate: amorphous, crystalline or organic. They can as well be altered via surface and interface states by post-process annealing in an inert or reactive gas atmosphere **[5-7,13,21,44,45,51]**.

The AZO films used in this study are aimed for use in solar cells as transparent electrodes; but they also have many other applications such as transparent electrodes in flat panel displays where a very low resistivity is required. AZO films deposited on flexible (polymer) substrates are also interesting for touch screens, electronic maps, smart cards and LCDs **[27,47,52,53].**

In order for AZO and ZnO:Ga (GZO) to replace ITO as transparent electrodes in LCDs, we need to find the proper deposition methods and the means to ensure the stability of the films under different conditions. The deposition technique must occur at less than 200 °C in order to comply with the limits of eventual organic substrate or thermally degrading layers to be contacted with it, while ensuring a resulting film resistivity in the order of 10^{-4} Ω.cm.

Magnetron Sputtering (MS) is a good deposition method for AZO due to its scalability to industrial scale. For example, S. Rahmane et al. **[6]** deposited polycrystalline AZO films on glass and Si substrates by RFMS at room temperature. The films deposited at 200 W and under a pressure of 0.2 Pa have an average transmittance > 90% in the visible range, an optical band gap of 3.33-3.47 eV

and a resistivity of ~ 1.25 x 10^{-3} Ω.cm. Additionally, DCMS is a good deposition method for scalability, electron mobility and carrier concentration. Nevertheless, films deposited by DCMS are normally inhomogeneous: A maximum resistivity is observed on the AZO films in the position where the substrate was placed facing the target axis, especially in the presence of an oxygen reactive gas (**Figure 9 a)**) **[3-7,37,40,44,45,47,49,52]**.

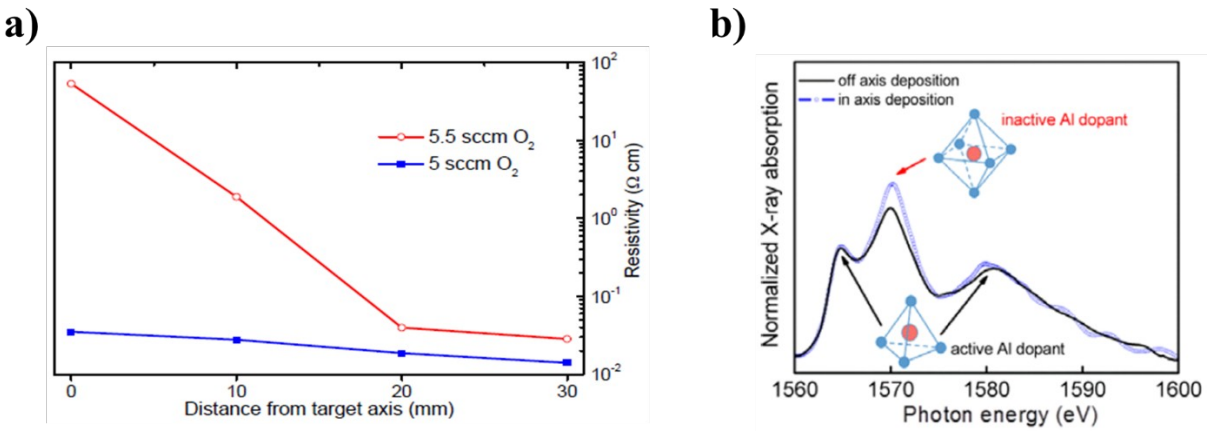

Figure 9: **a)** Resistivity (Ω.cm) of AZO films deposited by reactive DCMS under 5 and 5.5 sccm flow of oxygen as a function of the distance to the target axis (mm) and **b)** Al-K edge XANES spectra of the AZO films deposited at 0 mm (facing the target axis) and 30 mm from the target axis **[3].**

The origin of the maximum resistivity was interpreted to be due to the highly energetic oxygen ions that incorporate point defects into the AZO films like V_{Zn}, V_o, O_i and oxygen at grain boundaries (O_{GB}) which reduces the conductivity and transparency, as well as captures the free electrons and deactivates Al. Those oxygen ions come from the oxide layer formed on the target's surface and accelerated towards the substrate. D. Horwat et al. **[3]** determined the Al dopant deactivation from the Al-K edge X-ray Absorption Near Edge Structure (XANES) spectra of AZO films with 1.5 at.% of Al shown in **Figure 9 b)**; three main contributions can be distinguished: Two contributions at the lowest and highest energy corresponding to the electrically active $Al_{(T)}$ where Al substitutes Zn in a tetrahedral position, and the middle contribution assigned to the electrically inactive $Al_{(O)}$ due to the oxygen excess that stops Al from freeing electrons by plawing them in an inactive octahedral position. The higher intensity of the latter contribution in the position facing the target axis, depicting an inactive dopant correlates with the higher resistivity in this position. Annealing the films in H_2 gas at ≈ 500 °C is able to remove or convert the O_i and $O_{GB,}$ reactivating Al which increases n, μ and the transmittance in the visible range. However above 550 °C, the Al dopants are deactivated by V_{Zn} due to dominant hydrogen etching effect even though the dislocations and stacking faults are removed; Al dopants can be deactivated due to the excess of Zn_v because nAl_{Zn}-V_{Zn} complexes (n = 1 or 2) can form.

Other possible reasons for dopant deactivation is the precipitation of a secondary Al_2O_3 phase or the formation of a Al_2O_3(ZnO) homologous phase since their formation energy is lower than that of Zn_v. In fact, the Al dopant is found in the insulating Al_2O_3 and the Al_2O_3(ZnO) homologous phase to be $Al_{(O)}$; which explains why some $Al_{(O)}$ dopants in the AZO films are deactivated thus decreasing the film's conductivity. The deactivated Al dopant is present in nano-laminates of poorly doped ZnO blocks that alternate with Al_2O_3-like monolayers in the direction of the *c*-axis controlled by the "m" value. The homologous phase expands the *c*-axis parameter in AZO compared to ZnO; although a similar expansion can be observed in ZnO due to the bombardment by energetic oxygen ions that induce compressive stress in the ZnO film. D. Horwat et al. **[3]** observed a value of the *c*-axis parameter 0.35 to 1.48% higher in their AZO films than that of ZnO (c = 0.5205 nm) accompanied by improved crystalline quality while the conductivity is degraded. They interpreted these changes in structure and the change in Al-K XANES to the formation of the homologous phase induced by the high energy brought by the fast oxygen particles. Yet, there is no direct evidence of homologous phase formation to date.

The portion of deactivated Al dopants increases when placing the substrate closer to the magnetron axis, which yields heterogenous films, as well as when increasing the flow of oxygen gas and the at. % of Al present in the target. This means that optimizing AZO films should be based on choosing the right position of the substrate in reference to the magnetron's axis, as well as finding the right amount of Al and flow of oxygen **[3-5,7,37,40,44,45,47,49,52]**.

While stability is a very important property for a transparent electrode, ZnO, AZO and GZO are less electrically and chemically stable or resilient than In_2O_3 and ITO, i.e. the etching rate increases in acid and alkaline environments and the resistivity increases in presence of oxygen at high temperatures. The latter was tested by T. Minami et al. **[40]** where they observed that the resistivity of AZO and GZO (20-200 nm) deposited on glass at < 200 °C increased with their exposure time in high humidity (90% humidity at 60 °C). Nevertheless, this stability can be improved either by enhanced crystallinity or controlled chemical composition by changing the type and quantity of dopant or even adding another dopant. T. Minami et al. **[40]** deposited very good transparent and conducting doped ZnO films using RF and DCMS with or without H_2 gas. These solutions make GZO and especially AZO the best substitutes for ITO as the transparent electrode in LCDs as long as the thickness is greater than 30 nm **[21,51]**.

Moreover, AZO films are not stable in humid environments due to the water intake thus forming the $Zn(OH)_2$ compound which is a wide band semiconductor (E_g = 5.645 eV) with a high resistivity. The hydroxyl groups are trap states for charge carriers at the grain boundaries thus increasing the

potential barrier; this leads to a reduced mobility of the charge carriers. In fact, $R_{film} = R_{grains} + R_{grain\ boundaries}$ (with *R* representing the resistance); trapping the charge carrier increases $R_{grain\ boundaries}$ which increases the overall resistance of the film. However, one solution for this is post-deposition annealing to remove these hydroxyl groups that decompose at 150 °C and molecular H_2O actually diffuses out of the grain boundaries, this regains the high *n* and μ values of the charge carriers. Studies showed that an annealing of AZO films at 650 °C in vacuum stabilized the films under humidity **[44,53]**.

HiPIMS consists of high amplitude impulses with a low duty cycle leading to high ionization of sputtered atoms and near-target process gas. Deposition of Al-doped ZnO using HiPIMS, in particular in reactive mode (R-HiPIMS), was studied by Rezek et al **[37]** and by Zubkins et al. **[5]** for the rather high average power typical for HiPIMS operations. It yielded best resistivity values in the low 10^{-3} .cm range. In our group, we prefer to use lower discharge powers, that are below the usual powers used for HiPIMS operations, because zinc is a low melting point metal and that too high discharge power can lead to target melting and unintentional transition to evaporation during deposition **[44,52,53]**. This yields sub-stochiometric films with good homogeneity across the substrates and highly conductive (in the low 10^{-4} .cm range) and transparent films on large (possibly flexible) surfaces at low temperature (≈ 45 °C self-established temperature).

In an attempt to understand why R-HiPIMS yields more homogeneous AZO films (**Figure 10 a)**), the Al-K edge XANES spectra of optimized AZO films deposited in the same reactor at the target axis, and 30 mm from it in DC, HiPIMS and RF modes was reported in D. Horwat et al.'s study **[3]** (**Figure 10 b)**). It showed obvious film electrical heterogeneity in the DC and RF modes but barely any in the reactive HiPIMS (R-HiPIMS) mode if proper oxygen partial pressure is used. Additionally, if we consider the AZO films' resistivity in **Figure 10 c)**, we can see that a lower resistivity and a better homogeneity is obtained for films deposited by HiPIMS rather than by DC or Medium Frequency (MF) sputtering. In fact, R-HiPIMS is supposed to be useful to reduce the oxygen ion bombardment effect compared to DCMS or MFMS due to the effect of target cleaning during HiPIMS pulses. In his thesis, M. Mickan **[13]** has calculated that a 100 μs repetition pulse of R-HiPIMS with 3A peak current is sufficient to clean the Zn-Al target surface from the oxide layer formed during the off-time of 900 μs between consecutive pulses.

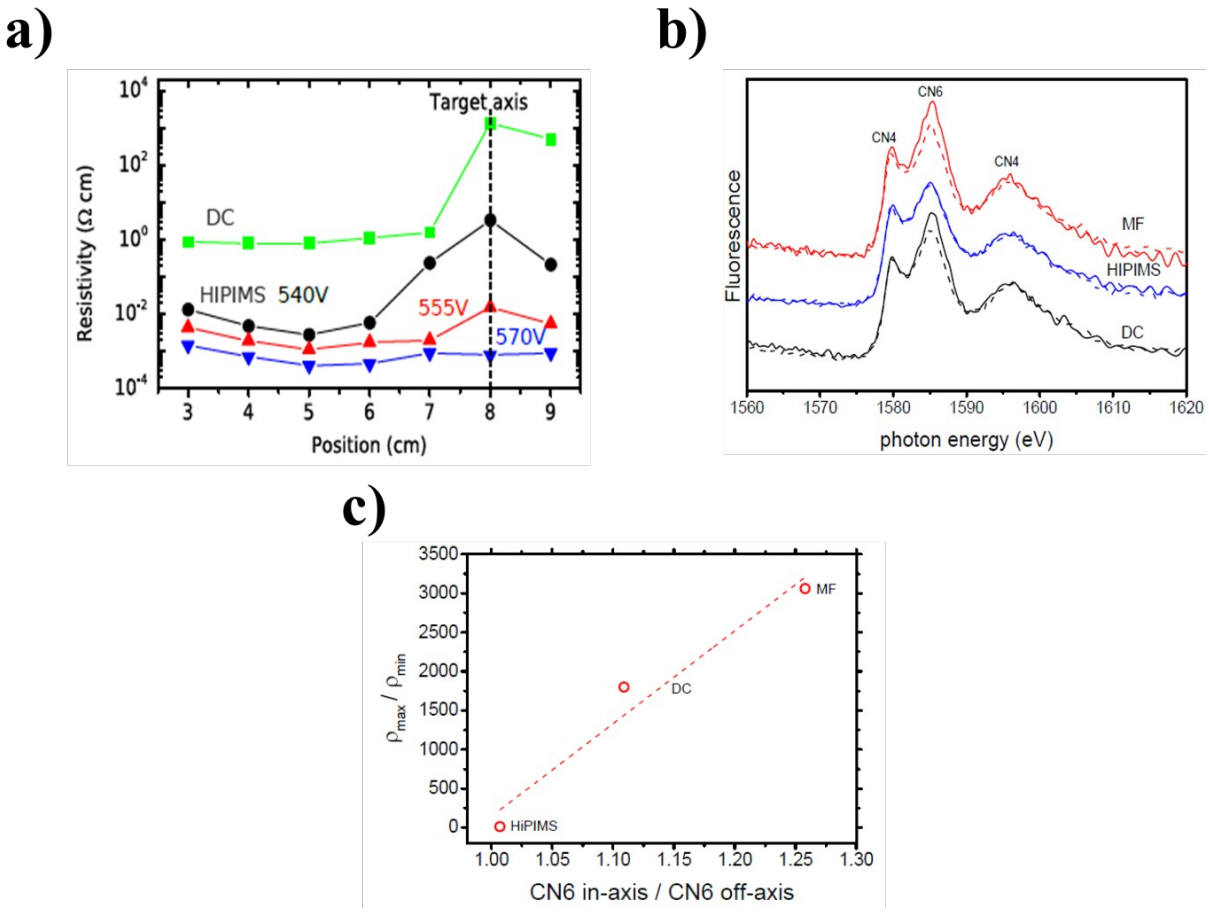

Figure 10: **a)** Resistivity of AZO films deposited by DC and HiPIMS at different applied voltages as a function of the position (cm) **[52]**, **b)** Al-K edge XANES spectra of the AZO films deposited at 0 mm (solid lines) and 30 mm (dashed lines) from the target axis by reactive DC, MF and HiPIMS **[3]** and **c)** Graph of the intensity ratio of maximum (30 mm) to minimum (0 mm) resistivity as a function of the intensity ratio of aluminum (Coordination Number 6) CN6 at 0 mm to CN6 at 30 mm **[3]**.

Finally, Mickan et al. **[53]** showed that AZO films deposited by R-HiPIMS at 200 °C are relatively stable to humid environment. Therefore, R-HiPIMS appears to be a suitable method to produce homogeneous AZO transparent electrodes without thermal assistance. It seems also to activate efficiently the Al dopant. Therefore, we selected it as a platform to investigate the influence of Al incorporation into ZnO and study the influence of the Al content. While our previous studies were limited to the use of targets containing up to 4 at.% Al, here we extend it to up to 15 at.% in order to detect possible structural/microstructural changes and changes in dopant activation/deactivation. We characterized the film properties in terms of resistivity, optical transparency, crystal structure for various sample positions into the deposition chamber.

The electrical and optical properties of AZO films are affected by many aspects such as the deposition or substrate temperature, the deposition pressure, the deposition rate and eventually the

film thickness, the type of process gas and its flow rate, the type of substrate, the target-substrate distance, the post-deposition annealing, the applied power, the dopant concentration, etc. **[54,55]**. Deposition temperatures of 100 °C or higher are often required for AZO films deposition in order to obtain high quality films, i.e. high electrical conductivity and optical transmittance as well as a homogeneous distribution of those properties on the whole film's area. However working without thermal assistance is possible if one understands the relationship between the process parameters and the films properties **[56]**. For example, the gas flow rate, depending on the type of gas, controls the dopant incorporation and crystallinity, it also has an effect on the electronic structure of the films **[54]**. Moreover, the post-deposition annealing controls the absorption/desorption of oxygen, the activation/deactivation of dopants as well as their distribution in the film **[54,57]**. In the following, we show some works that studied the effect of some of those aspects on the electrical and optical properties of the AZO films.

E. Chitanu **[56]** deposited AZO films on glass by RF sputtering from a doped ceramic Zn/Al_2O_3 target (98:2 wt.%) under three different RF powers; 100, 150 and 200 W. The RF power controlled the structural properties that subsequently had an effect on the electrical and optical properties; the best ones were obtained for the highest RF power. E. Krawczak et al. **[55]** deposited AZO films with 2.3 wt.% of Al by magnetron sputtering with a deposition rate ranging from 8.8 to 18 nm/min depending on the applied power and the deposition time. They observed a lower refractive index for thicker films, and a lower resistivity for higher applied power (2.5 W/cm^2 yielded less than 500 Ω/sq of sheet resistance).

The concentration of the dopant has a direct effect on the electronic structure which is inflicted on the electrical properties **[54]**. B. Swatowska et al. **[57]** deposited ZnO and AZO films on silicon and glass substrates by ALD using diethylzinc (DEZ), deionized water and trimethylaluminum (TMA) as the zinc, oxygen and aluminum dopant precursors, respectively. The fraction of TMA was varied in order to study the effect of the Al content on the properties of the AZO films. While ALD is able to precisely control the Al content in the growing films for up to 3% of Al fractions, the resulting films properties strongly depended on the Al content. For AZO films with Al fractions greater than ≈ 3%, the films structure became disordered, the classic columnar structure of ZnO no longer appeared, and the films electrical resistivity as well as the optical band gap increased. While the Burstein-Moss effect explains the latter result for low Al content, inefficient doping or alloying of the ZnO films might be the probable reason for the band gap increase when large Al fractions are involved. The authors found that only the AZO films with 2-3% of Al showed the suitable optical and electrical properties of a transparent electrode. In this work, we aimed to study ourselves the effect of the Al

concentration on the AZO films properties by depositing AZO films from Zn/Al targets with 1, 2, 5, 10 and 15 at.% Al via R-HiPIMS magnetron sputtering.

1.4. Properties of Cu_2O films

Copper metal (Cu) is used in integrated microelectronics due do its excellent electrical conductivity. Copper can form two types of p-type transition metal oxide semiconductors with high optical absorption that can be used as superconductors, absorber materials in gas sensors, magnetic storage media as well as in batterie and catalysis applications:

a) Tenorite or cupric oxide (CuO – Cu^{2+}) with E_g of 1.21-1.51 eV, a low thermal emittance and a high absorption (> 105 cm^{-1}) in the visible region which is effective for the role of selective solar absorber; also CuO/ZnO, CuO/Cu_2O and CuO/SnO_2 are used in humidity and gas sensors;

b) Cuprite or cuprous oxide (Cu_2O – Cu^+) with a band gap as low as E_g of 2.1-2.6 eV for the bulk material due to the interactions between the $3d^{10}$ electrons of the Cu^+ ions. Normally super-lattice or low-dimension crystal structures annihilate these interactions which results into an increased band gap to form a more transparent material.

In **Figure 11 a)**, we present the band structure of Cu_2O at the Γ-point of the Brillouin zone: The highest VB is noted Γ_7^+ and corresponds to the 3d orbital of Cu and the lowest CB noted Γ_6^+ corresponds to the 4s orbitals of Cu. Also, the possible transitions from VB to CB are represented (**Figure 11 b)**) in blue and violet for the lowest optical transitions and in yellow and green if a phonon excitation occurs; these transitions explain the value range of the band gap of Cu_2O.

Cu_2O is a green, abundant, non-toxic, stable, non-expensive and a non-stoichiometric direct band gap p-type semiconductor that can be easily prepared and employed in the industry. It is used in optoelectronics, photodiodes, photoconductors, (photo)catalysis, and photoelectrochemical devices (water-splitting), it is also used as an absorber layer in homojunction and heterojunction photovoltaics, as a channel material in thin film transistors and as a negative electrode for Li-ion batteries and, finally, Cu_2O can be employed for resistive switching in non-volatile memory devices.

The non-stoichiometry characteristic is necessary to ensure a p-type conductivity; it is done by the oxidation of the stoichiometric Cu_2O acting as insulator, by means of Cu atoms removal as presented in the following **Equation 6**:

$$Cu_{lattice} \xrightarrow{(I)\ a} V_{Cu}^{0} + h^{+} \quad \textbf{(Eq. 6)}$$

The V_{Cu}^{0} is a Cu vacancy with no charge and the hole h^+ can be localized and acts as a trap impairing conduction, or it can delocalized which leads to potential p-type conductivity.

Cu_2O has a high hole mobility (40-120 $cm^2/(V.s)$, 50 $cm^2/(V.s)$ at room temperature), a high optical absorption coefficient and a large minority carrier diffusion length (≈ 1 µm); these properties fit the absorber layer profile in solar cells at low cost with a maximum theoretical solar conversion efficiency of ≈ 20%. Cu_2O also has an electron diffusion length of up to 5 µm and a high excitonic binding energy of 140-150 meV. This provides excitonic features at low temperature in the absorption and luminescence spectrum, suitable for a Bose-Einstein condensate generation which can occur when a pulsed laser uses the high density excitation **[8,10,14,58-75]**.

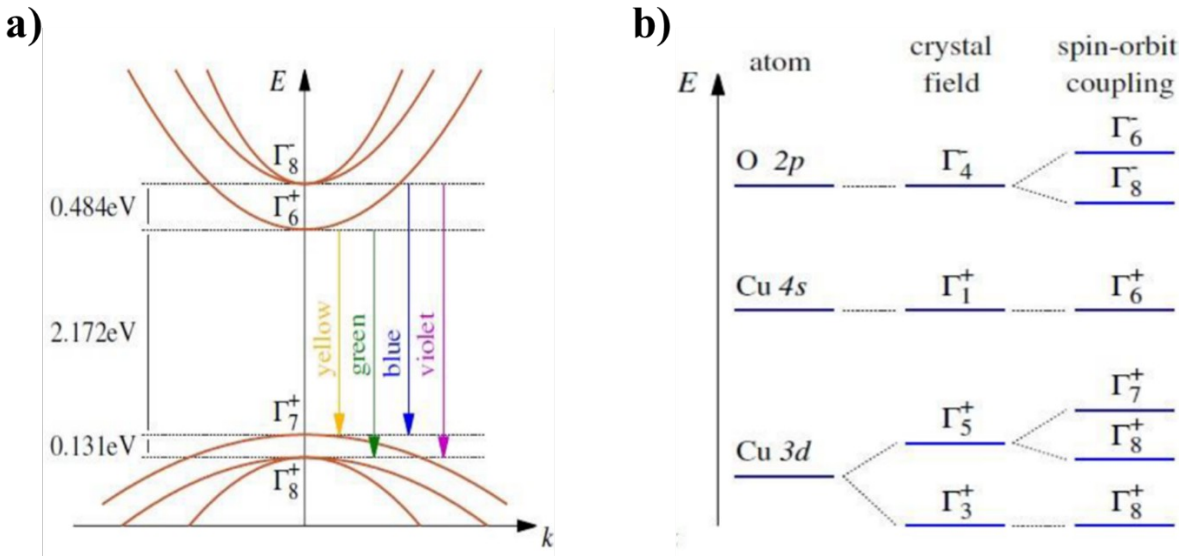

Figure 11: Schematic of **a)** the band structure of Cu_2O at the Γ-point of the Brillouin zone and **b)** the atomic orbitals of the Cu and O atoms responsible for the VBs and CBs as well as the band splitting considering the crystal field and the spin-orbit coupling **[14]**.

While CuO grows in a monoclinic structure, Cu_2O grows in a cuprite cubic structure like shown in **Figure 12 a)** (224^{th} space group O_h^4 $Pn\bar{3}m$, $CN_O = 2$ and $CN_{Cu} = 4$) with the oxygen atoms O having a tetrahedral T_d site symmetry and positioned at (0,0,0) in a body centered cubic structure and the copper atoms Cu having a D_{3d} site symmetry and positioned at $(\frac{1}{4}, \frac{1}{4}, \frac{1}{4})$ alternating interstitials in a face centered cubic structure; each O atom is in a tetrahedral position between four Cu atoms while each Cu atom is linked to two oxygen atoms (Cu-O = 1.848 Å, Cu-Cu = 3.017 Å and O-O = 3.695 Å). Each Cu atom is surrounded by 12 other Cu atoms which can be divided into O-linked and non O-linked: the first one concerns 3 Cu atoms linked to one neighboring O atom and other 3 Cu atoms bonded to the remaining neighboring O atoms; the second one is the remaining 6 Cu atoms not bonded to anything. The optimized and ideal lattice constant and bulk modulus are respectively 4.32 Å and 103.7 GPa. The Cu_2O (111) surface is presented in **Figure 12 b)**; the unit cell contains twice the number of atoms as the cubic unit cell and in hexagonal coordinates is defined by a hexagonal

base of length of a $= \sqrt{2}a_0$ and a height of c $= \sqrt{3}a_0$. Its diffraction pattern belongs to a cubic pattern with three-fold symmetry about the [111] perpendicular axis. Other than Cu_v, there exist a split vacancy where a copper interstitial (Cu_i) in a D_2 site symmetry separates two Cu_v. We show in **Figure 12 c)** two possible high symmetry Cu_i with the largest emptiness around them, denoted "c" with D_{3d} site symmetry and "d" with D_{2d} site symmetry **[59,62,65,74,76,77]**.

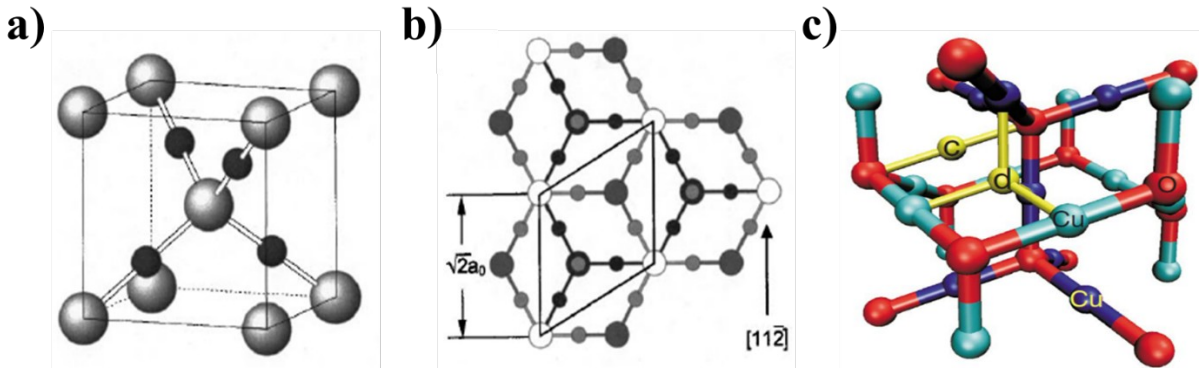

Figure 12: Schematic representation of **a)** the Cu_2O cuprite structure with the solid balls representing the Cu ions and the shaded balls the O ions **[76]**; **b)** the top view of the (111) surface after performing a cross-section containing three O atoms, all the Cu atoms at $(\frac{1}{4},\frac{1}{4},\frac{1}{4})$ are removed so that the image is clear **[76]** and **c)** the possible interstitial sites "c" and "d" in the cuprite structure consisting of two interpenetrating cristobalite lattices differentiated by a light blue and a dark blue of Cu atoms **[77]**.

While it is possible to produce n-type photo-responsive Cu_2O films in faintly acidic solution, Cu_2O's p-type conductivity remains the most desired electrical property. The solvothermal approach is used to fabricate 1D Cu_2O nanostructures but p-type Cu_2O thin films can be deposited by electrodeposition, thermal, chemical or anodic oxidation, chemical conversion spraying, (reactive) magnetron sputtering, (reactive) plasma evaporation, vacuum evaporation, sol-gel, reactive laser ablation, pulsed excimer laser ablation, MBE, PLD, CVD and in alkaline electrolytes. The resulting physical properties of the Cu_2O films depend on the deposition method and its conditions.

Thermal oxidation of Cu films yields Cu_2O films with high mobilities (30-40 $cm^2/(V.s)$). With no expensive additional heat treatment, higher deposition rates and atmosphere control, electrodeposition can produce highly crystalline and uniform Cu_2O films in a controllable growth direction, thickness and morphology on simple or complex metal or TCO glass coated substrates, which makes it a simple, convenient and effective deposition technique. S. Laidoudi et al. **[78]** electrodeposited from a Cu(II) sulfate solution with $C_6H_8O_7$ chelating agent Cu_2O films on a FTO coated glass substrate. The obtained films were in a well crystallized cubic structure and of p-type conductivity with E_g = 2.07-2.49 eV and n = 2.41 x 10^{18}-5.38 x 10^{18} cm^{-3} (doping level) with their

exact values depending on the deposition potential. In fact, when the deposition potential increased, the stoichiometric defects of the films as well as the homogeneity of the films increased but the average size of crystallites decreased. A sol-gel based electrochemical deposition method also exists and it has many advantages such as low cost, simplicity, accessibility, scalability to large areas as well as being environmental-friendly.

PLD can grow single phase Cu_2O with good electrical, structural and morphological properties easily controlled by the deposition parameters related to the laser (wavelength, energy, pulse rate), the gas pressure and the substrate temperature. The physical and chemical interaction of the ablated material with the process gas while traveling towards the substrate determines the film's properties. But, temperatures ≥ 600 °C and oxygen partial pressure >1.29 x 10^{-4} Pa are needed to achieve a pure equilibrium phase of Cu_2O, which makes PLD in this case quite costly.

Sputtering, mainly in DC or RF modes (13.56 MHz), is an easy deposition method that produces high quality uniform thin films on large area substrates with controlled properties. In the copper oxide case, simply changing the oxygen flow rate determines the ultimate growth of a Cu_2O film or a CuO film. Y. Wang et al. **[80]** selectively deposited CuO, Cu_2O or Cu_4O_3 films on glass and silicon substrates by reactive magnetron sputtering from a copper target at room temperature, while oxygen was used as the reactive gas. Single and two-phased of copper oxide films were obtained depending on the oxygen flow rate and deposition pressure; the conditions are schemed in **Figure 13**. Also, these parameters controlled the preferential orientation of the films: the Cu_2O and Cu_4O_3 grew in the (100) and (101) directions respectively at low total pressure while at high total pressure they grew in the (111) and (100) direction respectively. The pressure also determined the texture and morphology of the Cu_2O and Cu_4O_3 films. As for the CuO film, its preferred orientation was controlled by the oxygen flow rate where the films were oriented in the (111) direction at low flow rate and ($\bar{1}11$¿ at high flow rate **[10,58,61,62,64-67,69-75,78-80]**.

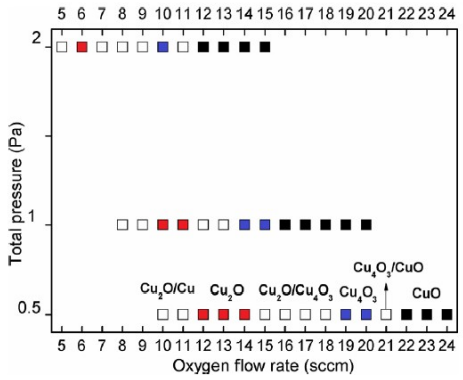

Figure 13: Diagram of the deposition conditions (total pressure and oxygen flow rate) used for the growth of the different phases of copper oxide **[80]**.

However, electrical properties of Cu_2O films deposited by reactive sputtering without thermal assistance are generally mediocre with low Hall mobility in the order of < 1 $cm^2/(V.s)$. In RFMS, one can control the properties of those films by varying the parameters such as the gas flow rate which controls the total pressure, the substrate temperature if substrate heating is required, the applied voltage and the target-substrate distance. So by controlling the oxygen flow rate and performing the deposition at 500 °C by RFMS, the electrical, optical and structural properties of the Cu_2O were majorly improved; the Hall mobility went up to 60 $cm^2/(V.s)$.

However sputtering, and PVD methods in general, are not apt to produce conformal films when the substrate presents complex surfaces like deep trenches and thus leave uncovered voids on the substrate. For this reason, ALD was introduced due to its capability to deposit, after cycling repetition of at least two self-limited chemical reactions separated by the injection of gas precursors in the chamber, conformal, homogeneous, pure and pin-hole free ultrathin films on large and complex 3D substrates with very high aspect ratios which is of great use in the microelectronics field. Additionally, the fabrication of nanolaminates and the flexible introduction of dopants is also an important characteristic of ALD. T. Iivonen et al. **[74]** deposited high quality and conformal Cu_2O thin films with photoconductivity and photoresponsivity in the visible region by ALD at 180-220 °C from a copper (II) acetate ($Cu(OAc)_2$) copper precursor and water vapor co-reactant on trench structures (AR 2:1). ALD is able to accurately control the overall thickness of the film on a sub-nanometer level as well as achieve saturated growth characteristics. The Cu_2O films deposited at 200 °C were pure, polycrystalline, and almost stoichiometric with little impurities. One should mention that the photoconductivity could hinder or slow the film's performance in photodetection, however the existence of the Cu_2O films in thin films form rather than bulk crystals fights this negative effect **[10,58,61,62,64-67,69-75,78-80]**. In another study, Claudia de Melo et al. **[14,81]** fabricated p-Cu_2O/n-ZnO nanoscale heterojunctions with high crystalline and optical quality in the visible region, as well as a local epitaxial relation between the layers. Under 1 Sun illumination, these heterojunctions were photoconductive and had a stable and quick self-powered photo-response. The Cu_2O films were of relatively high carrier concentration ($\approx 10^{16}$ cm^{-3}), very low resistivity (9-150 Ω.cm) and high carrier mobility (19 cm^2/Vs). Following the recipe developed during the PhD thesis of Claudia de Melo, we have used $cu(hfac)_2$ and water as precursors for the deposition of our Cu_2O on ZnO by ALD in order to fabricate similar heterojunctions for our patterned solar cells.

1.5. Structured solar cells based on ZnO/Cu_2O heterojunctions

In the previous sections, we introduced the three main layers used in this work for the elaboration of the final structured solar cells based on a ZnO/Cu_2O heterojunction. Here, we will show the interest in patterned cells instead of flat cells, as well as the importance of the ZnO/Cu_2O heterojunctions.

Fossil fuel combustion is one of the main causes for global warming that has serious environmental and economic consequences. Solar photovoltaics (PV) is considered as one of the cleanest and safest technologies used to generate electricity. Solar cells are the main components of PV systems; it's an electrical device that converts the energy of photons into DC electricity. Photons with energy exceeding the bandgap energy of the absorber material in the cell material are absorbed, causing excitation of charge-carriers **[82]**. The solar cell industry aims to produce large areas at a reasonable cost, and since silicon wafer technology is complex and expensive, one would rather use glass as substrates in combination with thin films as functional layers. In this case we get economical in-line process, less material consumption and competition with other energy sources **[83]**.

Structured solar cells have gained much attention these recent years due to their higher efficiency compared to flat cells, i.e. higher obtained photocurrents by means of light trapping. While some works pattern the front surface of the layer stack, in this work we fabricated structured solar cells by means of substrate patterning. Using an absorber layer with reduced thickness facilitates the transport of photo-exited electrons and holes to the contacting layers via the absorber layer; however this is associated to lower absorption and photoelectron conversion. Instead, using a structured substrate leads to a possibility of reduction of the thickness of the absorber layer without degradation of the photoconversion, because structured substrates tend to increase the optical path within the solar cell and thus enhance the optical absorbance **[84]**. In fact, when light is in contact with a structured surface, the radiation enters the cell at an oblique angle and the light, trapped inside the structure, performs internal reflections where the rays bounce between the facets several times before being reflected back and out of the cell **[12].** This scattering into multiple directions is what increases the optical path. The light diffraction mode however depends on the chosen structure period; if the latter is in the same order as the incoming light's wavelength, the light might be diffracted into different modes with various propagation angles thus prolonging the optical path **[85]**. While patterning may be realized by several methods such as wet-chemical etching, nanoimprint or optical or ion beam lithography, etc **[12]**; the method of choice in this work is UltraShort-Direct Laser Interference Patterning (USP-DLIP). In USP-DLIP, two or more laser beams are interfered on a substrate surface to efficiently and rapidly ablate the material thus creating the desired patterns; this method is detailed

in **Section 2.3.1 of Chapter 2**. It employs ultrafast lasers that emit very short laser pulses with an average power of 1-100 W creating micron-sized spot on the substrate. Nano- and picosecond lasers, the latter being the laser type used for the USP-DLIP in this work, reduce the material damage, the thermal load and they increase the micromachining accuracy. They have a pulse duration of 10 femtoseconds-10 picoseconds which limits material heating. Non thermal ultrashort pulses have high peak intensities leading to multiphoton absorption mechanisms ablating any material leaving a clean cut spot while avoiding ridges, since the short pulses rapid heating leads to earlier ablation and reduced melt pool which re-solidifies at the boundaries of the removed area. Other negative secondary effects are avoided such as high costs and toxic wastes. Additionally, the ultrashort pulse laser is a high fluence, high precision and versatile tool for structuring substrates in extreme detail and low roughness (less than 1 µm) by laser ablation to change its optical, aesthetic and haptic properties. **[86-89]**.

The solar cells in this work are based on a n-ZnO/p-Cu_2O heterojunction where the ZnO layer holds an excess of free electrons and the Cu_2O layer holds an excess of free holes and plays the role of the absorber layer due to its high absorption coefficient **[90,91]**. This type of heterojunction was realized to achieve high efficiency of Cu_2O based solar cells by inserting a suitable n-type semiconductor. ZnO is a good choice due to the favorable alignment of the conduction band edges of ZnO and Cu_2O **[92-96]**. When the ZnO and Cu_2O layers are in contact, the electrons and the holes diffuse across the interface to the area less filled with electrons and holes, respectively cancelling each other out like shown in **Figure 14**. Thus in the proximity of the interface, remain the fixed positive charges of the *n* layer and fixed negative charges of the *p* layer generating a built-in electric field or a built-in voltage stopping the free charge diffusion; this zone is named the depletion zone **[90,91]**.

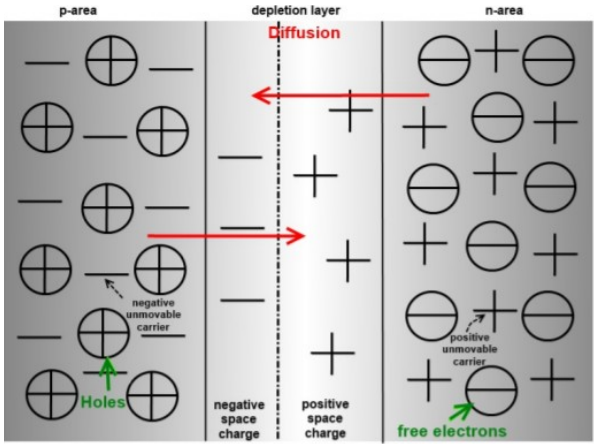

Figure 14: Representation of the charge carrier diffusion when a n-type and a p-type semi-conductors are put in contact **[97]**.

When a positive voltage is applied on the p-Cu_2O side, the built-in voltage is reduced and the carriers can again diffuse across the interface, which generates a large current that exponentially increases with the applied voltage; this is the case of the forward bias (**Figure 15 c)**). When a negative voltage is applied on the p-Cu_2O side, the built-in voltage is enhanced and the carriers cannot diffuse much across the interface which generates a low current; this is the case of the reverse bias (**Figure 15 a)**). This behavior can easily be seen on the I-V curve following the I-V measurement in dark mode (**Figure 15 d)**) **[90]**. Illuminating the junction with photons of energy higher than the bandgap of the absorber (Cu_2O in our case) generate electron-hole pairs that contribute to the increase of the current flowing through the junction.

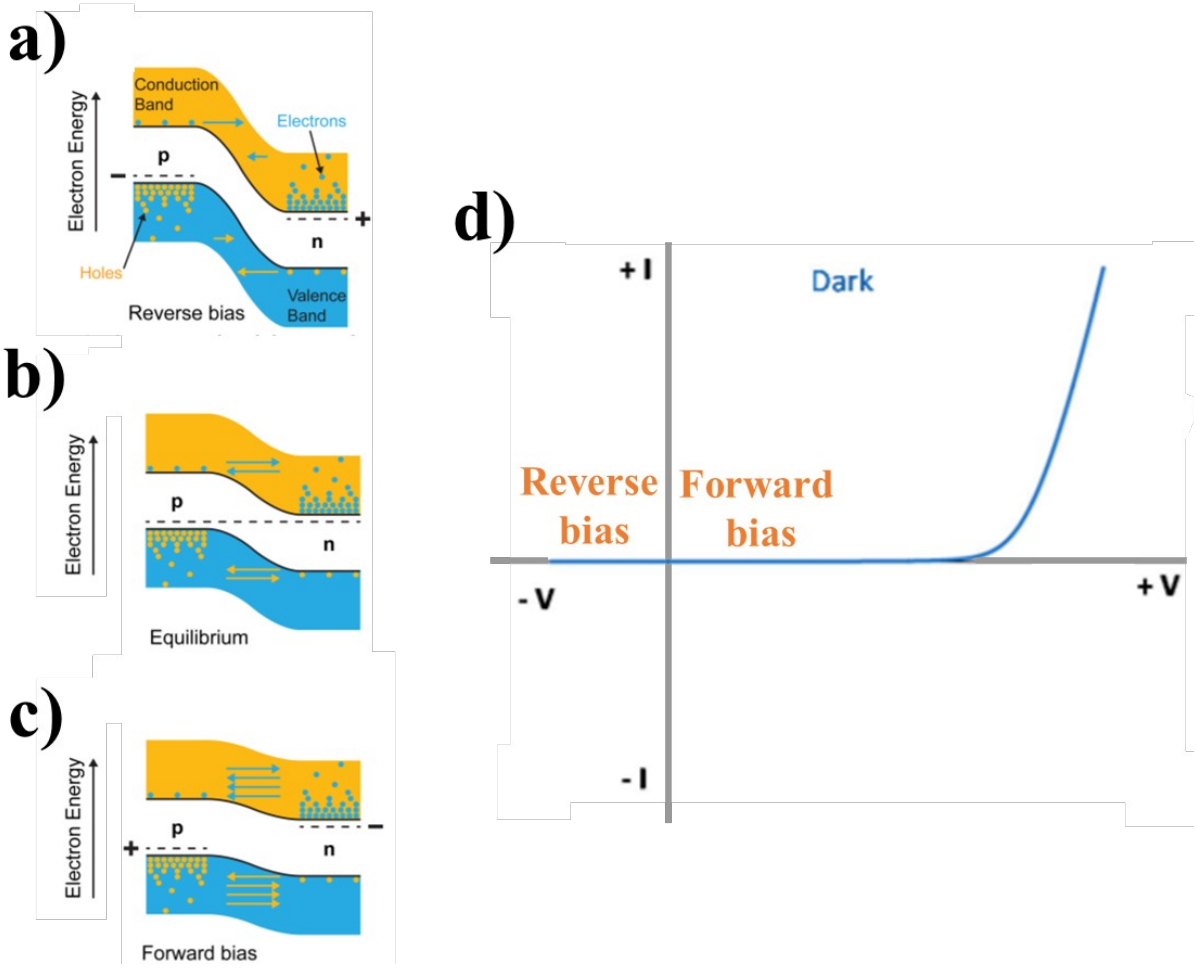

Figure 15: Representation of the energy band diagram of a p-n junction in dark mode during **a)** reverse bias, **b)** equilibrium and **c)** forward bias with **d)** being the corresponding I-V curve for the reverse and forward biases **[Adapted from 90 and 98]**.

Chapter 2

Experimental techniques

2.1. Introduction

This chapter represents and details the experimental techniques and characterization methods employed in order to fabricate and characterize the thin films and the desired ZnO/Cu_2O heterojunction-based solar cells. Three thin films deposition methods were used: 1) Reactive High Power Impulse Magnetron Sputtering (R-HiPIMS) to optimize Al-doped ZnO (AZO) films to serve as transparent electrode, 2) Direct Current (DC) reactive magnetron sputtering to deposit the n-type semiconductor ZnO and Au thin film metallic electrode and 3) Atomic Layer Deposition (ALD) to obtain the Cu_2O layer. UltrasShort Pulsed-Direct Laser Interference Patterning method (USP-DLIP) via the picosecond laser was used for structuring soda-lime glass substrates. This was based on the optical modelling of ZnO/Cu_2O solar cells deposited on patterned glass. In this chapter, we present the fundamentals of USP-DLIP and modelling of patterned solar cells. Throughout this work in terms of film characterization, the electrical properties were studied by the 4 point probe method, Hall effect and the Current-Voltage measurements, the optical properties via UV Visible Near-Infra-Red spectrophotometry, morphological and structural analysis by X-ray Diffraction (XRD), Scanning Electron Microscopy (SEM), Transmission Electron Microscopy (TEM) and Confocal Laser Scanning Microscopy (CLSM) and, finally, chemical analysis by Energy Dispersive Spectroscopy (EDS) and electron Energy Loss Near Edge Structure (ELNES).

2.2. Thin films deposition

Thin film deposition is the act of forming and then depositing a thin layer of metals, oxides or compounds on a substrate material; the films' thickness ranges between the nanometer and the micrometer scales. Unlike bulk materials, thin films are interesting because they offer the opportunity of miniaturizing some technological devices which then contributes to cost and material use reduction; also, their functional properties can be tuned in order to achieve the desired properties: optical properties such as transparency, absorption or reflection, electrical properties such as conductivity or resistivity, mechanical and chemical properties such as durability, hardness, abrasion or corrosion resistance. Thin films are used e.g. in opto-electronics such as in solar panels, semiconductor and fiber lasers, LED screens, CDs, optical filters, medical implants, etc.

Thin film vapor deposition methods can be divided into two major categories: Chemical Vapor Deposition (CVD) and Physical Vapor Deposition (PVD), which gather the deposition methods employed in this work **[99-101]**.

PVD is when a film is deposited by using a physical interaction with a source material under vacuum leading to its vaporization, the transport of the vapor phase and the condensation of the vapor phase on a substrate to form the film. PVD is a group of very clean and flexible deposition methods that allow the deposition of, in a relatively short time, thin layers of almost any inorganic material, pure or alloys and, in some cases, organic materials. The deposition conditions can be tuned in order to obtain the desired properties such as conductive or resistive films, optically transparent or absorbent films, high hardness etc. **[102,103]**. Nevertheless, PVD are usually costly methods that have some difficulties in coating structured or patterned shapes depending on the method **[104]**. Different PVD techniques exist such as sputtering, Pulsed Laser Deposition (PLD), ion plating, Electron Beam Evaporation (EBE), thermal evaporation, cathodic arc evaporation, magnetron sputtering, etc.

In the following section, we will provide in more details, the process and mechanisms of the PVD deposition method we used: magnetron sputtering deposition, in the DC and HiPIMS mode.

2.2.1. Magnetron sputtering process

Sputtering deposition is a thin film deposition method that consists on bombarding a target material by negative ions originating from a noble and/or reactive gas in a PVD chamber under reduced pressure. The ionization of the gas, usually argon (Ar), is done by a potential difference and forms a plasma state containing Ar^+ ions. Plasma is considered as the fourth state of matter and consists of ions, molecules and atoms, all in quasi-neutral equilibrium. Electrons and ions can influence charged particles at a distance of a radius called Debye radius making all plasma elements move at the same time under the influence of an electromagnetic field. The Ar^+ ions, once at the surface of the target, transfer their energy to the target atoms that are ejected and condensated at the substrate surface where they form the thin film **[13,105,106]**. A schematic representation of the sputtering process is presented in **Figure 16**.

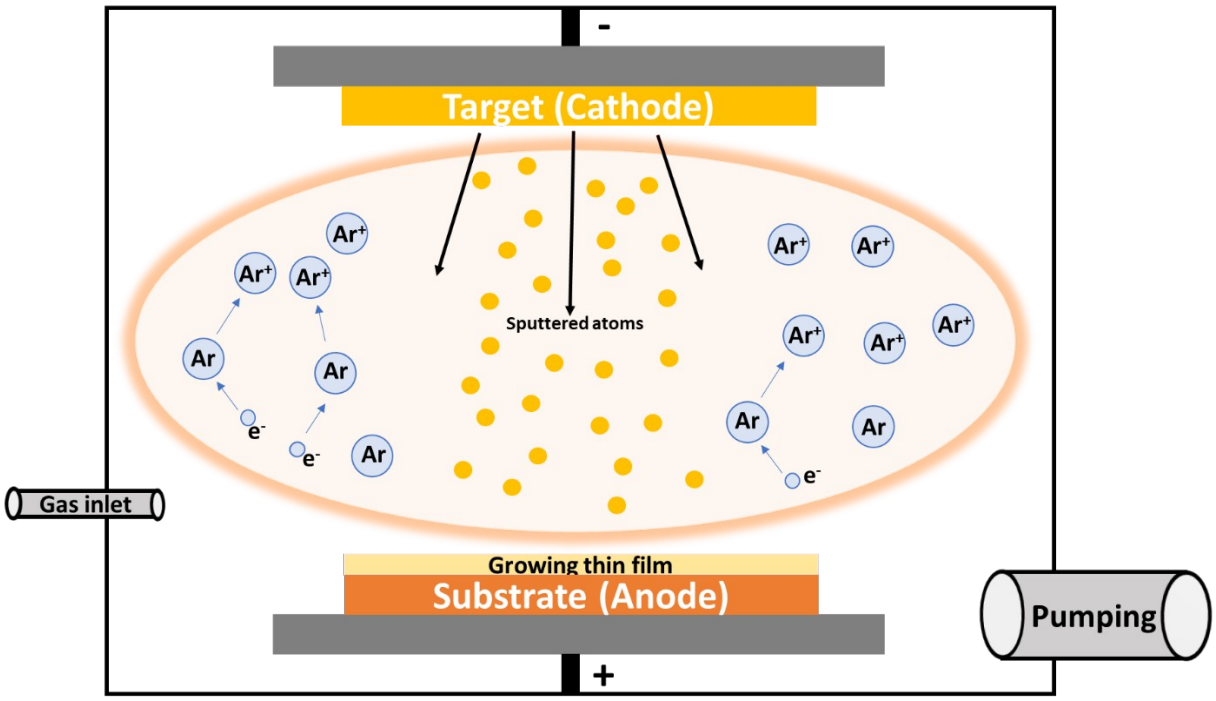

Figure 16: Representation of a general sputtering process experimental setup.

To ignite a plasma, we need a diode setup composed of a cathode from which electrons are accelerated towards an anode while colliding with ions and neutral elements and molecules present and transferring energy towards their electrons. However, the voltage must be carefully minded because a too low or too high voltage means a too slow or too fast movement of the free electrons, preventing them from performing this collision crucial to the plasma ignition. When the electric field is high enough, electrons are ejected from the elements or molecules and thus the number of electrons and ions increases inside the chamber, igniting the plasma **[105]**.

Magnetron sputtering is one of the most used deposition methods. In the general sputtering process already detailed above, some disadvantages to the method are not to be denied; such as low deposition rates and ionization efficiencies. Here comes the role of the magnetron device to overcome these difficulties. A magnetron consists on two concentric magnets of opposite poles and separated by a gap placed below the target. With this configuration, a magnetic field over the target is formed constraining the secondary electrons near the target surface to ensure the more efficient ionization of the Ar atoms, visually interpreted as a dense plasma. This means that the Ar^+ ions bombardment of the target increases, yielding higher sputtering and deposition rates. It also means that lower discharge voltages and gas pressures are needed, as opposed to the classical diode setup sputtering process, to perform thin film depositions.

2.2.1.1. Magnetron configurations

There are two types of magnetrons: balanced and unbalanced magnetrons, the first one is depicted in **Figure 17 a)** and the second one is of two types shown in **Figures 17 b) and c)**.

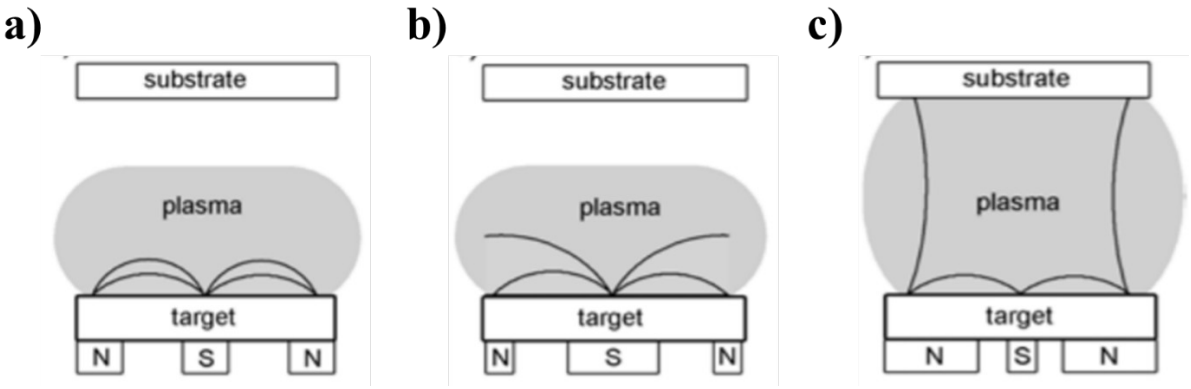

Figure 17: Schematic representation of the three magnetron types: **a)** Balanced magnetron, **b)** Unbalanced magnetron type I and **c)** Unbalanced magnetron type II **[107]**.

The balanced magnetron is most commonly used, and it has the role of keeping the plasma close to the target. In the area where the plasma is closest to the target and the secondary electrons are highly present, this zone is more efficiently bombarded by the Ar^+ ions and, so, more eroded; this forms an erosion zone labelled as the racetrack. Even though this zone leads to a higher deposition rate, it also means that the films deposited directly opposite to this region may be subjected to high ion bombardment, e.g. Ar^+ ions neutralized and reflected by the target, that can change the structure and properties of the films, while the films deposited outside this region are nearly safe from this effect **[110-112]**. The racetrack of the balanced magnetron is presented in **Figure 18 a)** with the corresponding erosion profile shown in **Figure 18 B)**, while the racetracks of the unbalanced magnetrons are shown in **Figures 18 b) and c)** with the corresponding erosion profile shown in **Figure 18 A)**. This will be discussed in more detail further on in this section.

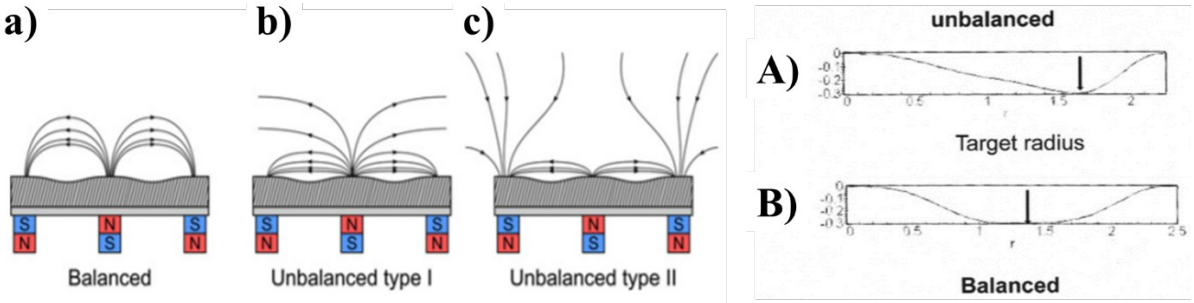

Figure 18: On the left, a representation of the racetrack for all three types of magnetron: **a)** Balanced, **b)** Unbalanced type 1 and **c)** Unbalanced type II **[108]**. On the right, the target erosion profile for **A)** an unbalanced and **B)** an balanced magnetron **[109]**.

Unbalanced magnetrons are of two types. Type I where the central pole of the magnet is stronger than the side opposite pole of the magnets; this means that the electric field can reach the chamber walls but the plasma near the substrate is low yielding low ion density. Obviously, this means that this type of unbalanced magnetron is unpopular for the deposition of dense thin films; however, it was used successfully for the deposition of porous thin films for catalysis applications.
Type II where the side south pole of the magnets are stronger than the central north pole of the magnet; this means that the secondary electrons and the plasma are not confined to the target but can even reach the substrate **[110-112]**.

2.2.1.2. Reactive Magnetron sputtering

In general, thin film deposition from a metallic target by magnetron sputtering is quite common. However, some compound films such as oxide, nitride, carbide, fluoride and even arsenide films are interesting; but their deposition process is more complicated. It is possible to use the corresponding compound target and deposit using RF sputtering since DC sputtering requires conductive cathodes. However, this method is more expensive because compound targets and RF supplies are costly. Moreover, the deposition rate in RF is low and the voltage and current are difficult to control **[13,14]**. Also, the chemical transfer between compound target and deposited film is not perfect requiring in most cases the use of reactive gas to adjust the final composition.
One alternative to RF sputtering of compound targets is reactive magnetron sputtering that consists on sputtering metal targets while a chemically-reactive gas is present in the chamber. This gas interacts with both the sputtered target atoms that eventually land on the film surface and the surface of the target. In this way, at high deposition rates and low substrate temperatures, high-purity compound thin films of controlled stoichiometry and composition are obtained. Also, the electrical conductivity of targets allows the application of DC sputtering instead of RF and its thermal conductivity makes it possible to apply higher discharge power **[113]**.
There are three modes of reactive magnetron sputtering: metallic, transition and compound (or poisoned). As one can see from **Figure 19 a)**, the deposition rate of compound film produced in reactive mode is lower than that of metal or alloy films produced in metallic mode; the difference between the two however is dependent on the target material and the reactive gas. The reason for that is the formation of a compound of higher bond strength on the target surface due to the reaction between the reactive gas and the target material; this is called target poisoning. The compound may cover the erosion zone but also the less sputtered areas of the target. If it is resistive, it could lead to

electrical charge built up and induce arcing during deposition. It can also cover the substrate and chamber wall, preventing it from being the anode. Finally, it is responsible for the drop in the sputtering yield Y by production of stronger bonds, a change in the discharge voltage induced by change in secondary electron emission and it allows the taking place of the hysteresis effect **[114]**.

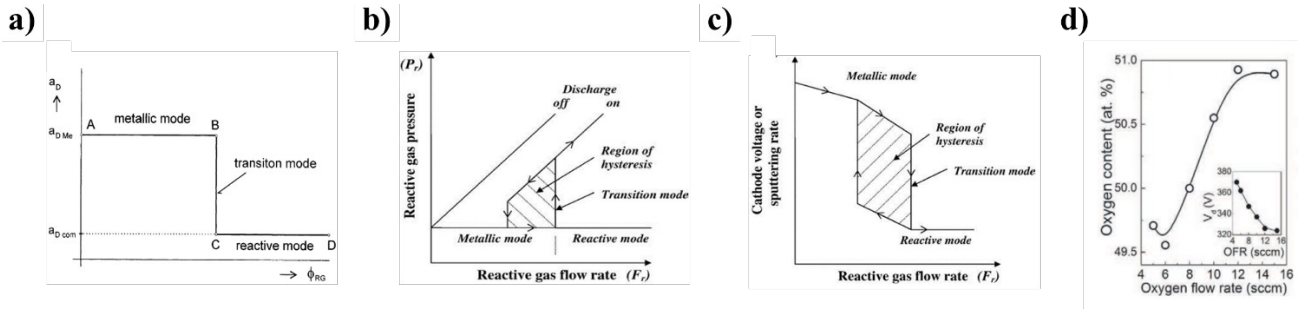

Figure 19: a) Illustration of the deposition rate of thin films a_D as a function of the reactive gas flow rate φ_{RG} in metallic, transition and reactive modes **[114]**; Illustration of the hysteresis effect of the reactive gas pressure P_r in **b)** and of the cathode voltage or sputtering rate in **c)** as a function of the reactive gas flow rate F_r in metallic, transition and reactive modes. The hysteresis loop is represented by the shaded area **[115]**; and **d)** Graph of the oxygen content and discharge voltage V_d (insert) as a function of the oxygen flow rate for ZnO films deposited by DC sputtering **[117]**.

The discharge voltage decreases in the compound mode for some metals like Al and Zn but it increases for others like Ti. In the first case, the secondary electron emission coefficient, γ_{eff}, of the compound is greater than that of the metal, the discharge voltage decreases because the plasma impedance decreases. In the second case, γ_{eff} of the compound is smaller than that of the metal meaning an increase in the discharge voltage **[13]**.

The hysteresis effect is the result of two inevitable conditions that occur during deposition: i) the sputter yield Y of the metal is much higher than the sputter yield of the compound formed on the target except for few compounds and ii) the reactive gas getter capacity of the metal is proportional to the vacuum pumping capacity defined by its speed. Note that the reactive gas getter capacity is the reaction of the reactive gas with the sputtered metal and freshly etched target surface that introduces gas atoms and molecules inside the deposited film and at the target surface **[116]**. The hysteresis loop can be seen in two ways, either by plotting the reactive gas pressure as a function of the reactive gas flow rate or by plotting the target voltage/sputtering rate as a function of the reactive gas flow rate. As seen in **Figure 19 b)**, almost all the reactive gas reacts with the sputtered metal at low reactive gas flow rate; this is the metallic mode characterized by a stable reactive gas pressure and target voltage. When the flow rate reaches a certain critical value, the partial pressure of the reactive gas suddenly increases because the reactive gas flow rate fed in the chamber is higher than the rate of the gas reacting with the sputtered metals; the target poisoning step is reached and this is the reactive

mode yielding a gas-rich deposited film. In this mode, the partial pressure of the gas will continue to increase with the increasing flow rate. However, if the flow rate is decreased, the reactive gas pressure will still remain high because the compound layer on the target must be removed so the metal can be ready again for sputtering. Once that is done, the reactive gas is consumed by the sputtered metal and the reactive gas pressure can decrease again and the metal mode is re-established. This delay in the decrease of the partial pressure of the gas is responsible for the hysteresis loop. As for the second representation of the hysteresis loop plotted in **Figures 19 c) and d)**, the target voltage decreases with the increase of the flow rate until dropping sharply at the critical point at which target poisoning occurs (reactive mode). Even if the flow rate is reduced, the target voltage will not increase again until all the compound layer is removed from the target metal and the metallic mode is slowly re-established after forming the hysteresis loop **[115]**. Ideally, it is interesting to run the deposition process in the transition mode where stoichiometric compound films are deposited but with higher deposition rate than the compound mode. However, for metals that are highly reactive towards the reactive gas, it is hard to stay in the transition mode without an active feedback control that monitors the deposition parameters such as the partial pressure and flow rate of the reactive gas or the discharge voltage **[13]**. Fortunately, for the zinc-oxygen system used within this study, the hysteresis usually does not establish because smoother transition is observed with each value of the oxygen flow rate leading to a single working point **[117]**. This is due to the low reactivity of zinc towards oxygen ensuring that the pumping rate of oxygen is always higher than the feeding rate into the reactor. Despite this, it has been shown that the film properties are strongly varying with minute changes of the oxygen flow rate when reactive DC sputtering is used **[118,119]**.

Magnetron sputtering includes many deposition methods of choice but we are interested in DC and HiPIMS sputtering, both of which are utilized in this work to deposit and optimize different layers of the desired solar cell. Detailed information on both these deposition methods are presented in the following sections.

2.2.1.3. DC regime

In DC magnetron sputtering, the cathode is under a constant negative voltage. This attracts the Ar^+ ions that bombard the target surface and induce atom sputtering. The Ar atoms are ionized mainly by Penning ionization which is the electron-Ar collision, however the degree of ionization is low (≤ 0,1%). The secondary electrons are accelerated by the potential difference between the cathode and the plasma. The density of sputtered atoms is much lower than that of the noble gas and the mean

free path of sputtered atoms with respect to electron impact ionization is over 50 cm; therefore, sputtered atoms remain neutral. However, the deposition rate is 1,5-2 factors higher than that of RF sputtering and DC magnetron sputtering is of very high productivity and is applied in industry **[110,113,120-122]**.

2.2.1.4. HiPIMS regime

High Power Impulse Magnetron Sputtering (HiPIMS) is a PVD magnetron sputtering deposition regime that, unlike DC sputtering, uses and controls short pulses of high density of current as schemed in **Figure 20**. The result is a denser plasma (≈ 10^{12} ions/cm^3) with no droplets and an up to 90% higher ionization of the sputtered atoms without overheating the target in contrast to conventional sputtering methods such as DC and/or RF (< 1%). This makes HiPIMS deposition ideal for coating car parts, cutting tools and decorative materials. HiPIMS could offer many advantages :

i) It combines the advantages of high electronic density plasma, as arc technology, with magnetron sputtering by simply adding a HiPIMS supply to any existing magnetron sputtering system, which is economically interesting.

ii) It offers the opportunity to deposit dense, hard, smooth, highly transparent and conductive thin films with good adhesion on large and complex substrates such as cutting tools (drills), without heating.

iii) It cleans the substrate surface from an already present oxide layer prior to deposition; but most importantly, it has the advantage of reducing the hysteresis effect during deposition especially in presence of a reactive gas due to the rarefaction effect, and due to the decrease of the compound formation on the target after the high instantaneous sputtering rate that removes the oxide layer during pulses and brings the system to a metallic or transition mode **[5,44,123]**. Hence, the transition to the poisoned target mode is less abrupt, and the deposition rate is higher than in the DC mode for the same initial metal rate. However if the gas flow is not regulated, deposition instability may occur and the chemical composition of the thin films is not constant. In fact, R. Ganesan et al. **[124]** deposited transparent, stoichiometric and amorphous hafnium oxide from a hafnium target by reactive HiPIMS with oxygen as the reactive gas, and they found that regulating the pulse length eliminates the need to regulate the gas flow. They studied the effect of the pulse length on the properties of the films; and it was found that increasing the pulse length produces a smooth transition from the compound mode to the quasi-metallic mode. The compound mode occurs due to short pulses and stoichiometric films are obtained for pulse durations (τ_P) ⩽ 140µs, whereas the metallic

mode appears for long pulses and sub-stoichiometric films are grown. In the last case, higher proportions of hafnium ions is present in the plasma discharge, and this translated in the observation of spokes or dense ionization zones in the erosion zone of the target, similarly to non-reactive HiPIMS **[13,124,125]**.

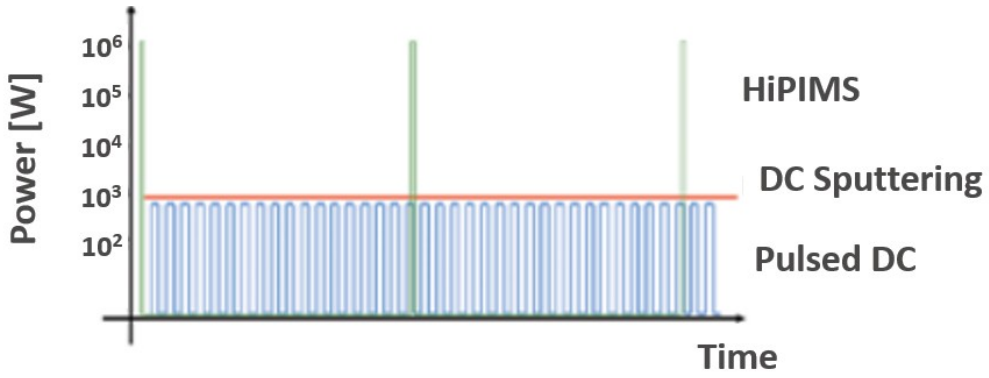

Figure 20: Schematic representation of the power (W) as a function of time to demonstrate the importance of HIPIMS compared to DC and pulsed-DC sputtering **[Modified from 126]**.

In fact, when performing sputter deposition in the presence of a reactive gas such as oxygen, an oxide layer is formed on the cathode surface (compound mode). The problem is that this layer too is bombarded by the Ar^+ ions releasing oxygen atoms that can react with secondary electrons leading to the formation of fast negative oxygen ions (O^-). These ions are then accelerated towards the substrate in a perpendicular direction to the target surface, while passing through the cathodic sheath and gaining kinetic energy; the flux of the O^- ions can be expressed as follows (**Equation 7**) :

$$\gamma_{O^-} = a.N_O.e^{\frac{1}{V_d}} \qquad \textbf{(Eq. 7)}$$

with γ_O- the flux of negative oxygen ions, a a constant, N_O the flux of sputtered oxygen atoms and V_d the discharge voltage measured in the compound sputtering regime during a reactive DC experiment using different 50 mm diameter metallic targets sputtered with 0.25 A; γ_O- is proportional to N_O but inversely proportional to V_d. The logarithm of γ_O- is found proportional to the secondary electron emission yield **[127]**.

If the growing semiconducting film is doped in order to improve its electrical properties, for example in the case of AZO films, a lateral inhomogeneity of the properties of the films is detected: the resistivity is at a maximum in the position facing the target (*in-axis*) due to the bombardment of the film by the negative oxygen ions. In fact, when the target to substrate distance is more than 2.5 times greater than the racetrack diameter, the target could be considered as a punctual source. If we consider that the sputtered flux is separated by an angle θ from the target normal, the distribution law

can be approximated by a $Cos^n(\theta)$ evolution as shown in **Figure 21 (Top)**. Hence a substrate placed far from the target axis will receive sputtered atoms in a solid angle that is glancing from the target surface and, therefore the received flux of atoms is small. This is accentuated by the fact that the sputtered flux propagates and the farther is the substrate, the more the sputtered atoms will have dispersed during their drift, and the smaller will be the received flux (**Figure 21 (Bottom)**). Hence a sample placed on the circumference in front of the target axis receives an intense flux of sputtered particles as it passes above the target, and a very small amount of matter, including O^- ions, at its farthest distance from the target axis, i.e. after half a turn. The variation of received sputtered flux is inexistent for a substrate placed on the substrate holder axis; it receives a constant sputtered flux that is intermediate to the two extreme positions discussed above.

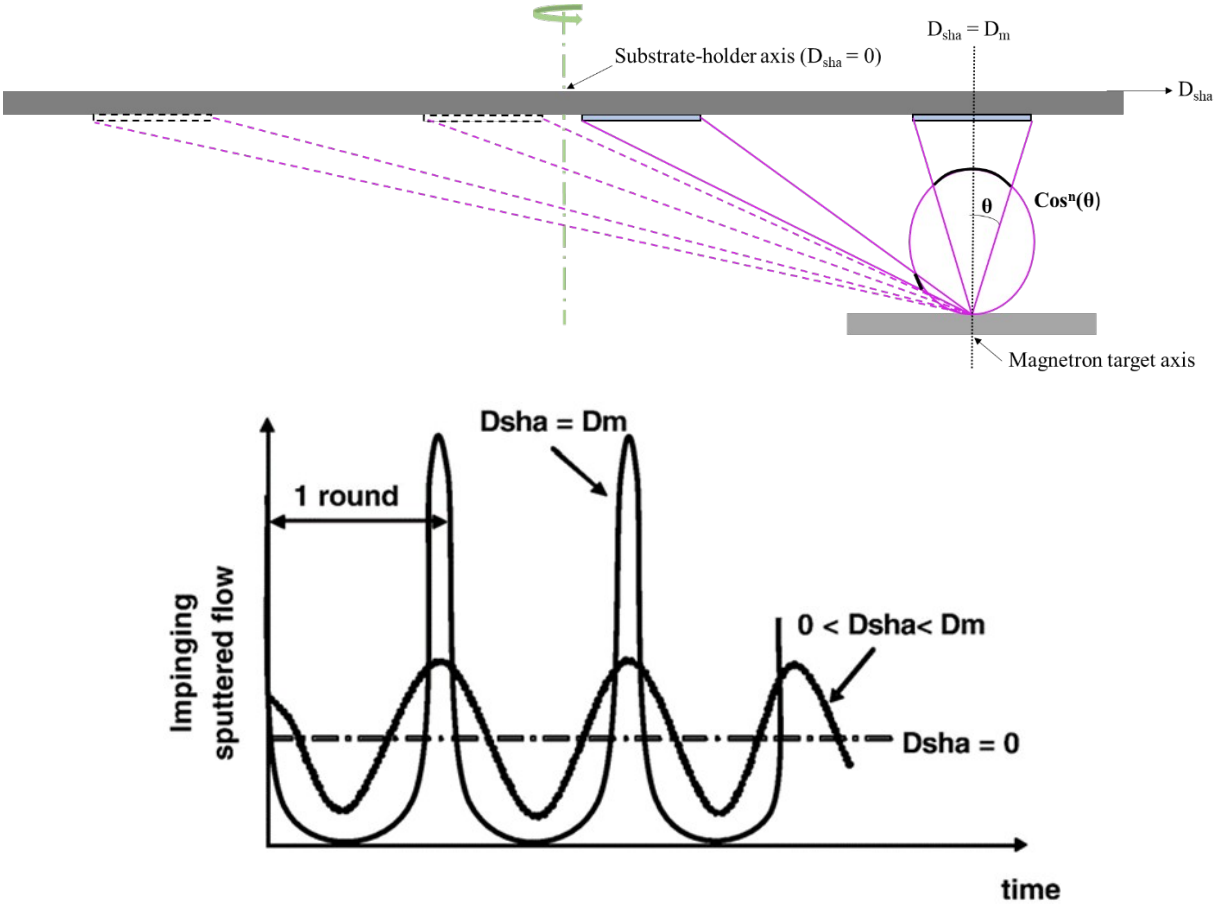

Figure 21: **(Top)** Illustration of the sputtering flux propagation from a target surface towards a rotatable substrate-holder holding a glass sample; and **(Bottom)** Graphic demonstration of the impinging sputtered flow as a function of time for the different possible positions of the sample in reference to the magnetron axis **[118]**.

This higher bombardment of the forming AZO film by the O^- ions when the substrate is placed in front of the target axis may explain the resulting higher resistivity. The consequence of that is the

introduction of acceptor defects like O_i decreasing the charge carrier concentration n; and/or the formation of secondary phases. Evidently this means that the flow of oxygen inside the chamber has a major effect on the properties of the deposited films. Mickan et al. **[13,44]** proposed that reactive HiPIMS of Zn-Al target limits this effect by enabling during pulses the cleaning of the target surface from the compounds formed between pulses. Additionally, Mickan et al. **[13,44]** have reported that the amount of oxygen in the gas mixture modifies dramatically the pulse shape during the reactive deposition of AZO by HiPIMS from a Zn/Al 3 at.% Al target. The pulse shape evolves from flat under pure argon towards a more peaked shape as the oxygen flow rate is increased; moreover the peak current is strongly increased upon increasing the oxygen flow rate (**Figure 22 a)**). When comparing the relative evolution of the plasma impedance during reactive HiPIMS and reactive DC both shown in **Figure 22 b)**, it has been observed that the plasma impedance decays much faster in HiPIMS. Different mechanisms among which the emission of energetic electrons, easier dissociation and ionization of molecular oxygen have been proposed in order to explain this difference **[52]**.

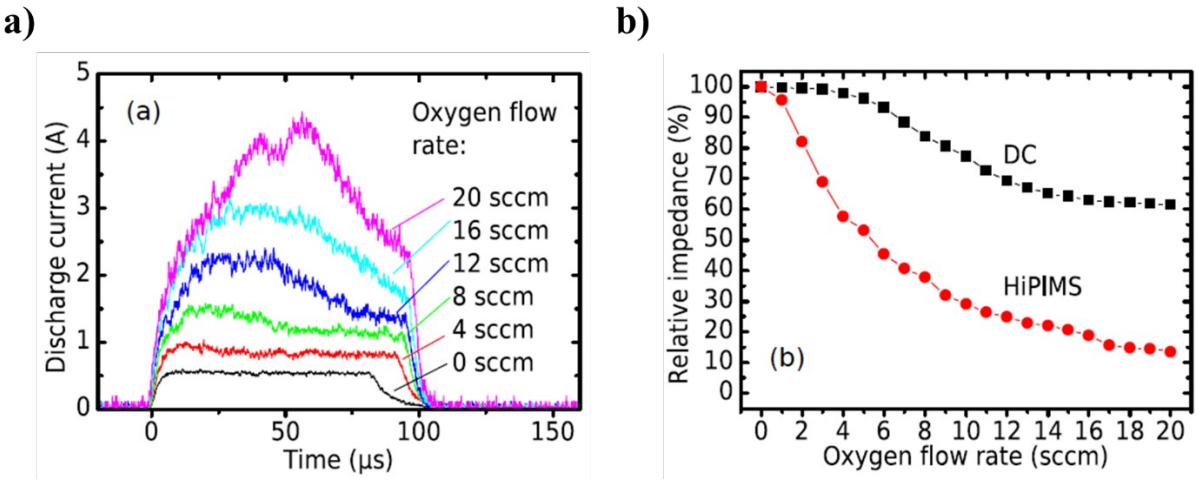

Figure 22: a) Discharge current waveforms of AZO films deposited by HiPIMS sputtering under a constant applied voltage of 570 V, for different oxygen flow rates; and **b)** Graph of the normalized relative impedance as a function of the oxygen flow rate for AZO films deposited by sputtering in a DC (black) or in a HiPIMS (red) regime. The graphs were extracted from **[supplementary material of ref. 52]**.

Another parameter to consider in relation to the oxygen ion bombardment, is the target utilization. If we consider that O^- ions are formed at the target surface and accelerated throughout the cathodic sheath, they are essentially emitted perpendicular to the target surface from the racetrack because sputtering and secondary electron emission are most intense; this has been verified by Weltzel and Ellmer in the case of DC reactive sputtering of zinc at 0.5 Pa **[128]**. As the surface of a new target is flat (**Figure 23)Left)**), a coherent beam of fast O^- particles is emitted parallel to the target axis. In

the case of a used target (**Figure 23 (Right)**), the grove of the racetrack originating from inhomogeneous sputtering, would lead to a more dispersive beam of O^- energetic particles. Therefore positions on circumference farther from target axis could be bombarded more easily by energetic O^- particles when a used target is employed.

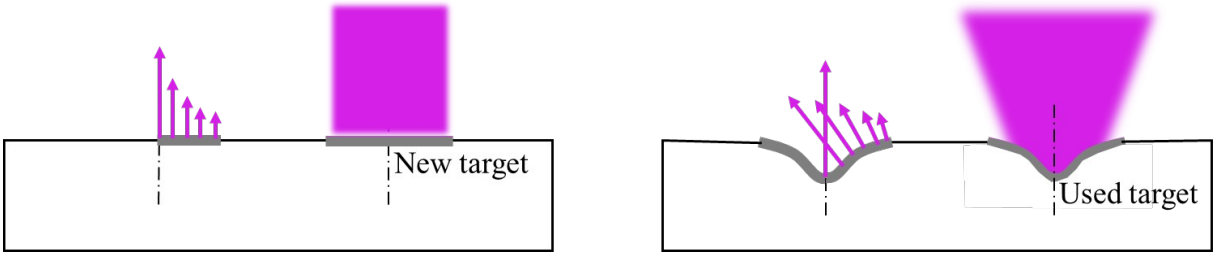

Figure 23: Illustration of the sputtering flux emerging from a **(Left)** new target compared to **(Right)** a used one. Dotted dashed lines represent the radius of the racetrack and arrows represent the sputtered flux.

Other than the oxygen ion bombardment, the Al content in the AZO films has a major effect on the films properties. Many authors studied the effect of the Al content on the structure and electronic structure of AZO films deposited by HiPIMS, which in their turn affected the electrical and optical properties of the films. Some authors used either XANES or ELNES most commonly on the Al-$L_{2,3}$, O-K and Zn-$L_{2,3}$ edges, in order to study the evolution of the spectral shape where they deduced structural modifications as a function of the Al content. Depending on the deposition conditions and the Al content used, and specifically in oxygen-rich conditions, it was commonly proposed that for high Al contents the dopant was deactivated through different mechanisms such as the formation of a $Al_2O_3(ZnO)$ homologous phase, a Al_{Zn}-V_{Zn} and/or $2Al_{Zn}$-V_{Zn} complexes, a α-Al_2O_3 phase, etc. **[4,5,7,44,52,129]**. In this work, we are interested in studying the effect of the Al content on the properties of the AZO films deposited by HiPIMS magnetron sputtering from a Zn/Al target with different at.% of Al. We studied the optical, electrical, chemical, structural and electronic structure properties of the films in hopes of understanding the relation between the structure of the AZO films and their optical and electrical properties.

2.2.1.5. Deposition of AZO films

In this study, magnetron sputtering is used as the deposition method for the elaboration of AZO films; a schematic representation of the PVD chamber and parameters is depicted in **Figure 24**. The deposition was realized in an home-built PVD chamber attached to a primary and a secondary pump in order to establish the proper vacuum for the AZO films deposition. The primary pump is an oil-sealed rotary vane Leybold GmbH TRIVAC B D40B pump with a pumping speed of 40 m^3/h and an

ultimate partial pressure of ≤ 0.01 Pa. A water cooled Pfeiffer vacuum Adixen ATP400 turbo-molecular pump was used as the secondary pump at a rotation speed of 27 000 rpm. This pumping system amounts to a pressure in the order of 10^{-3} Pa suitable for AZO films depositions. The pressure is monitored by two pressure gauges: a Leybold PENNINGVAC PTR 90 N vacuum probe with a measuring range (in N_2 and air) of $1x10^{-6}$-10 Pa; it is used to monitor the proper vacuum of the chamber before deposition; and a Leybold CERAVAC CTR100N vacuum transmitter with a measurement range of 0.1 – 1000 Torr and an insensitivity to gas compositions. The latter is more sensitive, accurate and is more reliable for checking the vacuum pressure in the PVD chamber as well as the pressure during deposition when the gases are injected in the chamber.

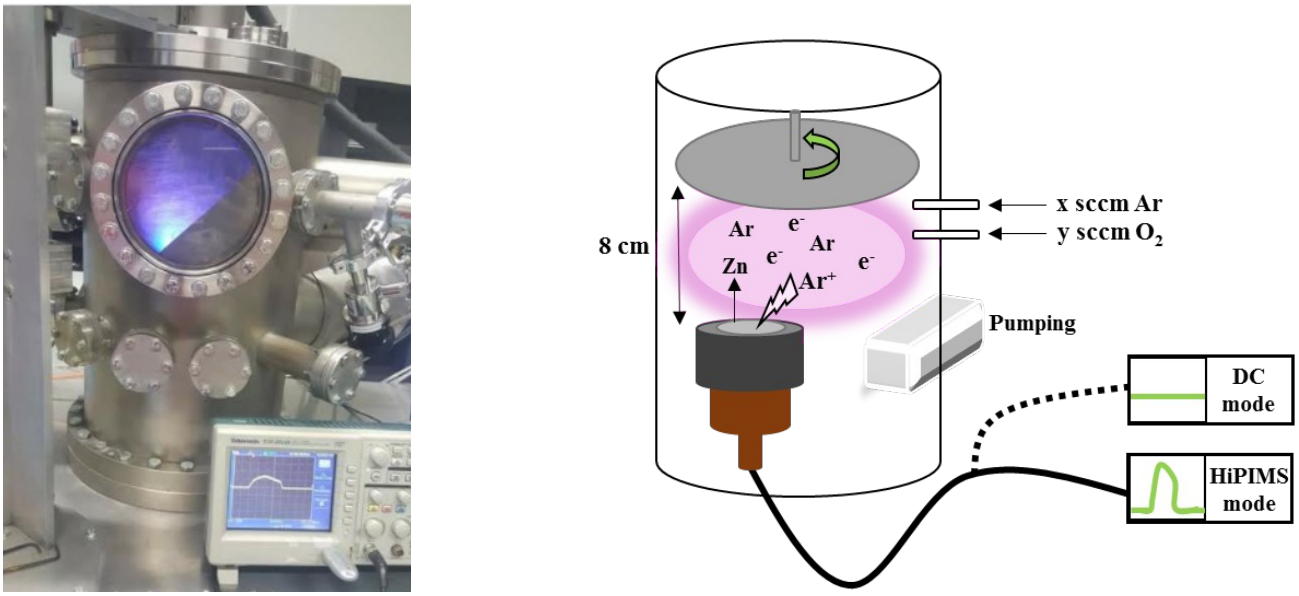

Figure 24: (Left) Picture of the PVD chamber used in this work during an AZO film HiPIMS deposition; and **(Right)** Schematic representation of the PVD chamber used for the AZO films deposition in this study, as well as a portrayal of the deposition parameters and conditions. The black cable represents the possibility to plug the magnetron to a DC or to a HiPIMS generator.

Reactive HiPIMS depositions were performed with argon for plasma initiation and oxygen as the reactive gas. The gas administration was done via the Bronkhorst FlowView 2V1.23 software and a Bronkhorst High-Tech flowmeter used to monitor the argon and oxygen flow rates injected in the chamber. A polarizable substrate-holder (diameter = 25 cm and thickness = 0.4 cm) situated at the top lid of the chamber is connected to a motor allowing it's rotation at 3.5 rpm to improve the homogeneity of the chemical composition and thickness of the AZO films.

The chamber is equipped with 3 magnetrons allowing users to perform co-sputtering depositions; all magnetrons are located with their axis parallel and at 8 cm from the rotation axis of the substrate-

holder. For our study only one magnetron was used. The magnetrons are a type II NdFeB unbalanced magnetrons with an equilibrium factor of K = 3.37, a central magnet with a maximum magnetic field of 640 mT, and an outer magnet with a minimum magnetic field of -430 mT. The magnetrons are suited to fit a target of 50,8 mm diameter and 3 mm thickness **[130]**.VFive HMW Hauner GmbH & Co.KG Zn/Al circular targets (99.99% purity) with different Al at.% (1, 2, 5, 10 and 15 at.%) were used. The distance from the target surface to the substrate-holder was maintained at 8 cm for all deposition runs.

Prior to HiPIMS deposition, the magnetron was supplied with an Advanced Energy® MDX 500 DC power supply for target etching; the applied current was 0.1 A for all targets, 50 sccm of Argon were injected and the etching time varied between 15 and 30 mins and considered completed after the target voltage reached an asymptotic trend. Once the etching was done, the chamber was opened to install the substrates and perform the deposition. The magnetron was disconnected from the DC source and connected to a MELEC GmbH SPIK 2000A HiPIMS generator which was itself supplied by an Advanced Energy® Pinnacle Plus DC power supply that enables applying a high constant voltage of up to 600 V. This HiPIMS generator was used to apply the discharge voltage which varied between 400 and 590 V depending on the deposition conditions; the average current and the power were then displayed during deposition. The HiPIMS generator was set to a negative unipolar mode with a 100 µs ON time and 900 µs OFF time (10% duty cycle). The resulting current was monitored by a Pearson™ Current Monitor probe (output V/A= 0.1) and the applied voltage to the target was monitored by a Cal Test CT4028 High Voltage divider probe with an accuracy of ≤ 3%; the pulse current and the voltage were observed on a Tektronix TDS 2024B oscilloscope (200 Mhz bandwidth and 2 GS/s maximum sample rate). All depositions lasted 40 mins and the flow rate of Argon was always set to 80 sccm. For all depositions, Knittel soda lime glass slides with ground edges (76 x 26 cm, thickness ≈ 1 mm) were used as substrates and were placed radially at ≈ 2.6 cm from the center of the rotatable substrate-holder axis, as represented in **Figure 25**. The glass slides were cleaned using simply water and ethanol; when in the chamber under vaccum and before each deposition, the substrates were etched for 1 min using an Advanced Energy® Cesar RF power generator in order to remove all impurities still present on the substrate surface as well as ease the adhesion of the deposited film to the substrate. The deposition conditions for the optimized AZO films deposited from Zn/Al targets with 1, 2, 5, 10 and 15 at.% Al are shown in **Table 1**.

Table 1: Table representing the deposition parameters for each AZO film deposited from the Zn/Al 1, 2, 5, 10 and 15 at.% Al targets respectively: O_2 flow rate (sccm), deposition pressure (Pa), applied voltage (V) and peak current (A).

Conditions / Target	O_2 flow rate (sccm)	Deposition pressure (Pa)	Applied voltage (V)	Peak current (A)
Zn/Al 1 at.%	20	1.18	560	2.844
Zn/Al 2 at.%	20	1.19	555	3.008
Zn/Al 5 at.%	10	0.921	450	1.472
Zn/Al 10 at.%	10	0.876	450	2.864
Zn/Al 15 at.%	10	0.678	450	3.488

After completing the deposition step, the AZO films were then subjected to various characterizations that will be discussed further on in this chapter. Whereas some characterizations were performed every cm, such as thickness measurements, others were only performed in specific positions. **Figure 25** shows exactly where the characterization of the AZO films occurred. It's important to remember the *in-axis* and the *off-axis* terms as the position of the surface substrate placed on a circumference of the substrate-holder crossing the magnetron axis and the position of the surface substrate furthest away from it, respectively. It's on these points that most of the characterization was conducted and the results presented in order to conduct a comparative analysis.

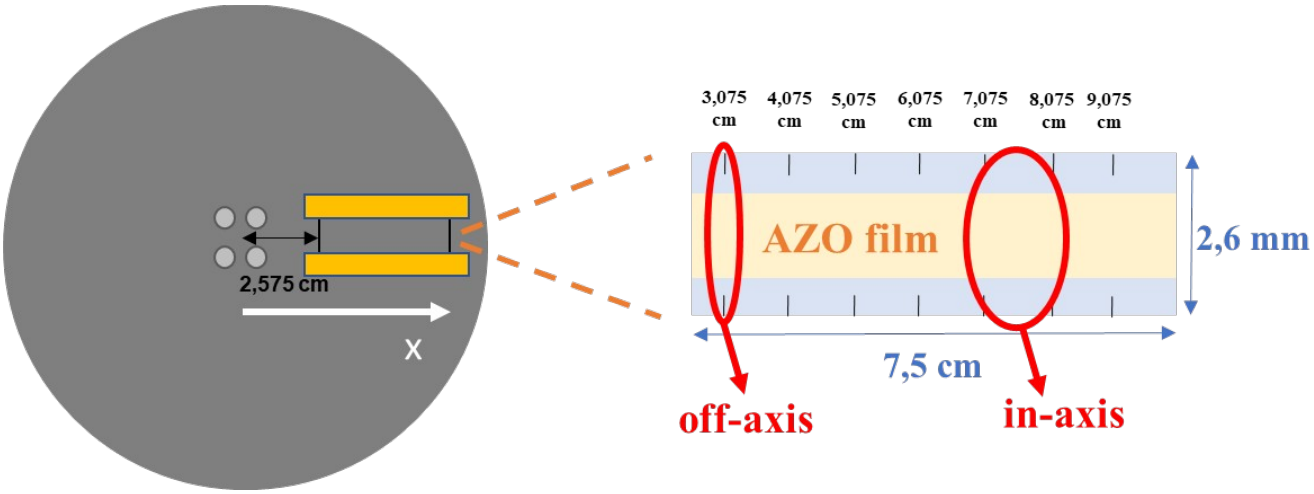

Figure 25: Schematic representation of the substrate-holder and the glass slide substrate positioned at 2.575 cm from the center of the substrate holder. The enlarged image shows in detail the 7 different positions on which all the characterisations were performed, as well as a highlight of the *in-axis* and *off-axis* positions.

2.2.1.6. Deposition of ZnO and Au films

The ZnO layer, intended to serve as n-type semiconductor in the targeted ZnO/Cu_2O junction, was deposited by reactive DC sputtering using an Advanced Energy® MDX 500 DC power supply. The target-substrate distance was fixed to 5 cm after putting in place the HMW Hauner GmbH & Co.KG Zn circular target (99.99% purity). For etching, 50 sccm of Ar and 8 sccm of O_2 were injected leading to a total pressure of ≈0.325 Pa. The applied current used for cleaning the target was 0,07 A and the etching time was 30 mins. Then, the substrates were cleaned and placed on the rotating substrate-holder to deposit the ZnO layer under the same conditions as the etching.

The gold layer plays the role of the front contact for the solar cells and is thus realized as the last step of the solar cell fabrication. In order to deposit this last one, the target-substrate distance was fixed at 5 cm and the deposition was performed by DC magnetron sputtering from a gold 99.99% purity target using an Advanced Energy® MDX 500 DC power supply. Since gold is not subjected to a natural oxide layer, the target etching step is not necessary. Prior to re-initiating the vacuum, the substrates were cleaned and placed on the rotatable substrate-holder to be introduced in the chamber. RF etching of 1 min is applied to clean the substrates before starting the DC deposition. For the deposition step, the discharge current was set to 0.06 A and 68 sccm of Ar were injected in the chamber leading to a background pressure of 0.5 Pa. Depositions lasted 20 mins to obtain a gold layer of approximately 150 nm-thickness.

2.2.2. ALD deposition process

TCOs can be obtained either from PVD deposition techniques such as thermal evaporation, magnetron sputtering, Molecular Beam Epitaxy (MBE) or Pulsed Laser Ablation (PLA), but also from CVD deposition techniques such as high temperature CVD, MOCVD or Atomic Layer Deposition (ALD). However, the latter is only used for specific films like buffer layers or protection films because of its very low deposition rate compared to other methods like MS, MOCVD, spin coating, solution processing and ion-layer gas reaction **[17]**. Nevertheless, it was observed in AZO, ZnO and other crystalline films studies that the crystalline quality of the film is inversely proportional to the growth rate. R.J. Mendelsberg et al. **[51]** set the decreasing following order of deposition methods leading to very high crystal quality films but with very low growth rate: ALD >

MBE > PLD > RFMS > Reactive Sputtering > Ultra-high rates techniques like atmospheric plasma torches. ALD is hence a very interesting method for the deposition of high quality thin films.

2.2.2.1. ALD setup

ALD is a reproducible deposition technique from the vapor phase with a sub-nm precision based on a cyclic self-limiting growth mechanism that yields high quality thin films with sharp interfaces and conformity on high aspect ratio and nano-porous structures. It has also the flexibility quality because it can modify the surface properties of a material by depositing very thin films on top and form chemical and size gradients. But maybe the most important ALD quality is the excellent surface coverage and thickness control at the Angstrom scale even on structured substrates.
In fact, in CVD and PVD, the gas flow is an important deposition parameter. If the substrate is patterned by narrow trenches, the flow of gas is larger at the entrance of the trench rather than at the bottom of it due to kinetics of gas transport which clogs the entrance. Some solutions include inhibiting growth, pulsed CVD, catalyzers. However in ALD, the higher flux at the entrance of the trenches means a faster coverage of it until saturation since ALD is self-limiting avoiding the clogging; the precursors can now go deeper into the structure and coat the whole if it **[131-135]**.
ALD is also very important in heterojunction based solar cells fabrication. In fact, in any heterojunction, defects play the role of trap density at the interface which reduces the latter's quality. In the case of ZnO/Cu_2O heterojunctions, a CuO layer on the Cu_2O surface might be formed when the deposition occurs in an oxygen enriched environment or during quenching, it's problematic because CuO has a smaller band gap (1,4 < 2 eV) and its CB is 4 eV near the vacuum level creating deep states at the interface favorizing recombination. Some solutions include wet etching, heat treatments and a catalyst layer but a nm scale CuO layer can grow later on when the surface is exposed to air **[136]**. Sputtering, CVD, electrodeposition, PLD and thermal evaporation are all good methods to deposit highly pure Cu_2O thin films in the right deposition conditions. Nevertheless, they become unreliable when complex, patterned and nanometric structures are involved which is the specialty of ALD. However, the deposition temperature and oxygen partial pressure must still be carefully chosen to avoid the formation of the Cu and CuO layers **[137]**.

The ALD's cyclic nature leads to uniform films on high aspect ratio surfaces which is not the case of CVD because of its faster surface reactions nor by PVD because of its shadowing effect. As opposed to CVD, ALD is characterized by a cyclic or alternating reaction of the precursors to deposit a thin film usually at low temperatures (< 380°C). The precursors need to be nontoxic, inexpensive, stable,

volatile if in a solid or liquid initial state, and highly and fully reactive to the substrate without bringing any harm to it and to the growing film.

The ALD process, as schematically shown in **Figure 26**, starts with the "half-reactions" where the chemical precursor is vaporized into the vacuumed chamber for some time to react with the substrate surface; one monolayer is formed after the self-limited reaction stops, i.e. the vaporized precursor reacted with all the active sites on the substrate (**Equation 8**):

$$A_g + * \underset{\Leftarrow}{\text{Reversible}} A^* \quad \textbf{(Eq. 8)}$$

where A_g is the precursor in the gas phase, * is a vacant site on the substrate, and A^* is the adsorbed precursor A **[14,133-135,138]**.

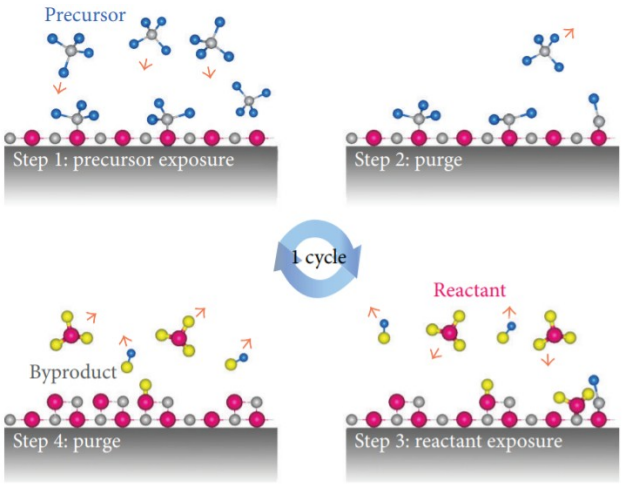

Figure 26: Schematic illustration of the ALD process **[139]**.

Then, the by-products and unused precursors are purged from the chamber via a noble carrier gas such as nitrogen or argon to avoid parasite reactions between the precursors in the gas phase. These steps are repeated (cycles) (**Equation 9**) until the desired film thickness is achieved; one monolayer is deposited per each cycle:

$$A^* + B_g \underset{\rightarrow}{\text{Irreversible}} AB^* \quad \textbf{(Eq. 9)}$$

where B_g is the second precursor in the gas phase and AB^* is the chemisorbed product of *A* and *B*. One of ALD's advantages is the relatively low temperature of deposition, in the 210-350°C range where the self-limiting reactions occur; this is called the ALD temperature window and it depends on the precursor, the substrate and the reactions taking place **[14,133,138]**.

2.2.2.2. Deposition of Cu_2O films

In this work, the p-Cu_2O layer of the solar cell was deposited by ALD on different substrates based on the method tested and optimized by Claudia de Melo **[14]**.

In **Figure 27**, a photograph and an illustration of the ALD PICOSUN™ R-200 Advanced reactor controlled by a computer system were presented, as well as the substrate holder used for this deposition.

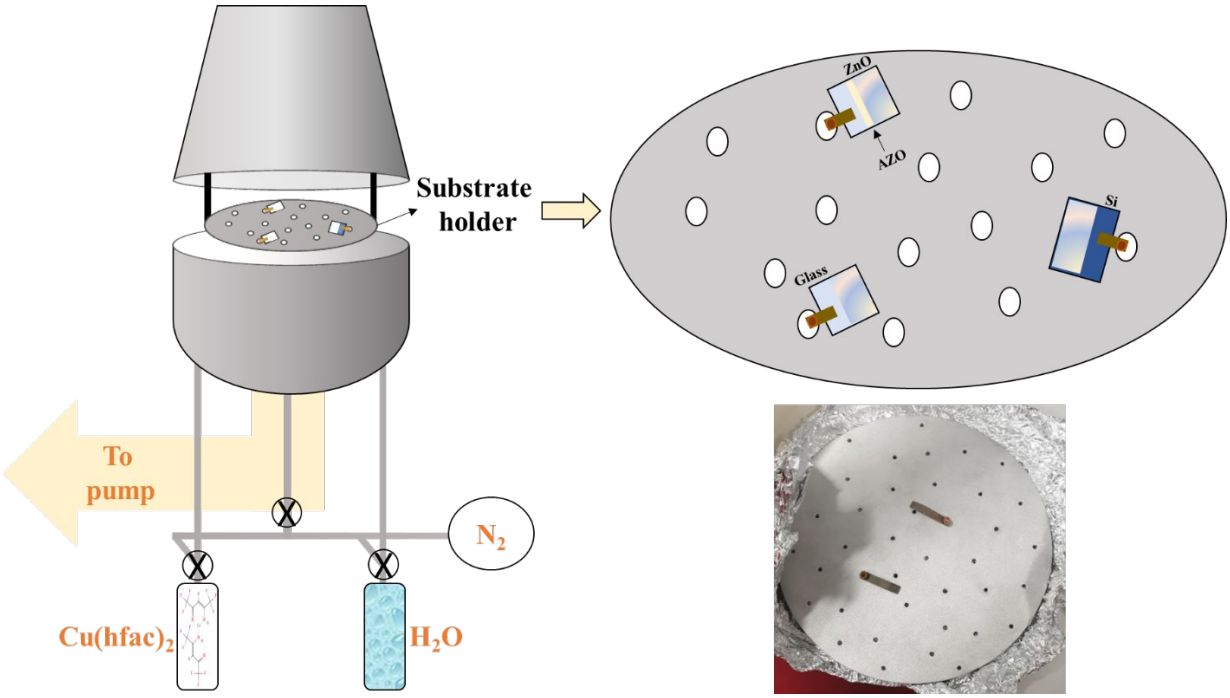

Figure 27: Schematic illustration of the ALD chamber showing the precursor $Cu(hfac)_2$, reactant H_2O and carrier gas N_2 tanks as well as an image and details of the substrate holder.

The substrates used and detailed in the solar cells fabrication section (**Section 2.4**), were covered by the AZO and then the n-ZnO layer of the p-n junction to ensure the proper deposition of the Cu_2O film instead of a metallic Cu film, which is necessary to fabricate ZnO/Cu_2O junctions. The substrates, after being cleaned in distilled water and ethanol in an ultrasound bath, are strapped on the substrates-holder with a small leather fixator while making sure that the surface is well exposed for the deposition and the substrate-holder is then placed inside the deposition chamber on a heatable substrate stage. Then, the system software is used to start the vacuum pump housed by an exterior vacuum chamber in order to reach a vacuum pressure of 10 hPa. The deposition parameters are set, controlled and monitored on the computer system. For our Cu_2O films deposition, copper (II) hexafluoro acetyl acetonate (Strem Chemicals, 99.99% purity) or $Cu(hfac)_2$ for short is used as the

Cu precursor and deionized water as reactant. They are kept in small tanks on the side of the chamber and introduced into it by gas lines. Since the precursors must be in the vapor phase, the heating temperatures for the $Cu(hfac)_2$ is set at 70 °C and that of water is set at 22 °C. Next, the pulse and purge times of the precursor and reactant are set. For that, we need to look back on the optimization of the precursors purse length done and presented by Claudia de Melo in **Figure 28**; the reaction temperature was 280 °C and the number of ALD cycles were 5000 for all cases.

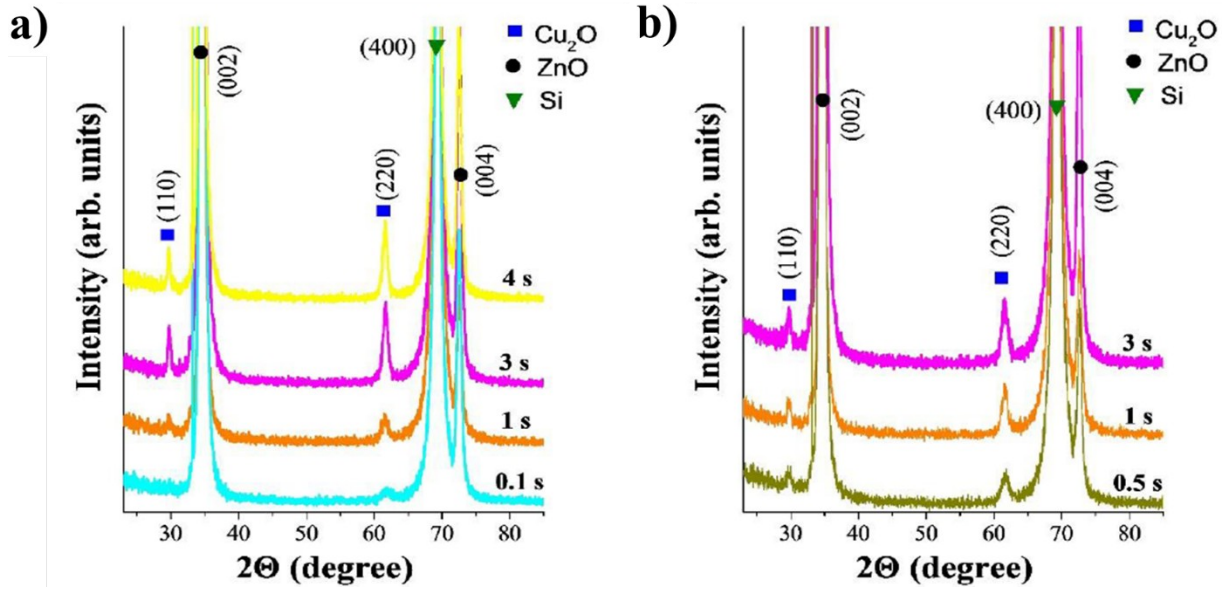

Figure 28: XRD diffractograms of a Cu_2O film deposited on ZnO when **a)** the $Cu(hfac)_2$ pulse is kept constant at 3 s while the H_2O pulse is varied from 0,1 to 4 s and when **b)** the H_2O pulse is kept constant at 3s while the $Cu(hfac)_2$ pulse is varied from 0,5 to 3 s **[14]**.

In **Figure 28 a)**, the XRD diffractograms are shown for a constant 3 s pulse of $Cu(hfac)_2$ and an H_2O pulse going from 0,1 to 4 s. One can see that the Cu_2O's characteristic peaks, (110) and (220), increase with the pulse length till reaching a maximum at 3 s. Therefore, a pulse time of 3 s for H_2O was used in our deposition. Similarly, the H_2O pulse is fixed at 3 s and the (110) and (220) peaks of the Cu_2O in the XRD diffractograms increased for an increasing $Cu(hfac)_2$ pulse going from 0,5 to 3 s in **Figure 28 b)**. Since the XRD diffractograms were quite similar for 1 and 3 s pulses, the 1 s pulse is suitable and it enables limiting the cycle period and entire deposition time. As for the purge time, 6 s is set for both the precursor and the reactant.

Next, the Nitrogen (N_2) carrier gas settings are set to ensure the proper transport of the precursor and reactant in the ALD chamber followed by the purge of the non-reacted precursors and the by-products. The N_2 flow rate was set to 120 sccm for $Cu(hfac)_2$ and 150 sccm for H_2O. Additionally, the ALD deposition system is equipped with a boosting mode used to enhance the vapor pressure of precursors when needed; in our case, it was set at 300 sccm or 500 sccm. Finally, the heating

temperature of the substrate is set to 280 °C and the number of ALD cycles to 10 000. Once all the parameters are taken care of, the deposition can be started.

2.3. Glass substrate structuring

Ideally, semiconductor layers in solar cells should only be 10-60 nm thick for the purpose of charge collection as this is the order of exciton diffusion length. However, these thicknesses are not enough to absorb light, especially in the infra-red region of the spectrum. Light trapping comes as a solution for this problem by structuring the front or back layer of the solar cell because the transport path of the charge carriers in the absorber layer is reduced and the optical path for the light is increased **[12,84].**

Light trapping in a solar cell consists on structuring the front or back surface of a layer stack so that the light is scattered into many directions, increasing its optical path inside the cell, especially if the texture has a periodic pattern in the order of the light's wavelength. In fact, the optical path is increased because light accesses the solar cell in an oblique angle, and it is also trapped inside the cell because the incoming light bounces off the different facets many times before coming out of the cell. According to M. Soldera et al. **[85]**, there are three light trapping mechanisms listed here and schemed in **Figure 29**:

i) Refraction of light at the oblique interface changes the propagation angle, which increases the optical path. This is more pronounced for shorter periods yielding steeper angles.

ii) Deep structures lead to the reflection of light hitting one facet to an adjacent one and then refracted to the following layer. These multiple reflections are the reason behind the efficient light trapping and thus the increase of absorption in the following layer. This effect is evident for structures with high aspect ratios and inexistent for aspect ratios less than 0.3.

iii) Diffraction of light by the pattern could lead to coupling of light into several modes that propagate at oblique angles thus increasing the optical path **[12,85].**

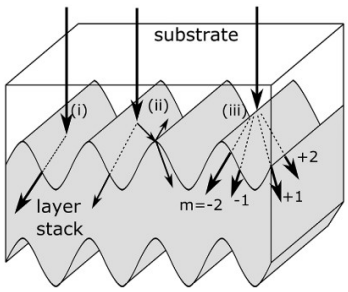

Figure 29: Schematic representation of the light trapping mechanisms on a substrate structured by USP-DLIP **[85].**

M. Soldera et al. **[12]** studied the influence of the geometry of an organic solar cell on the delivered photocurrent. They found that when the light bounces 3 times (aperture angle (φ) < 36°), the maximum photocurrent density (J_{max}) is the highest for all the periodicities and the highest value obtained is J_{max} = 16.5 mA/cm^2 for the V-grooved textured cells with periodicity = 1 µm and φ = 15°. In this case and comparing with a planar cell, the absorbance increases of 9.5% in the active layers but also an increase in parasitic absorption of 14.4% in the anode layers, which decreases the reflectance by 23.9%. Additionally, since the open-circuit voltage (V_{OC}) values for the textured cells is 5% lower than that of the planar cell and the Power Conversion Efficiency (PCE) is ≈ 22% higher, we can conclude that textured cells perform better than planar cells. J. Lim et al. **[140]** fabricated on large area glass substrates a dense, uniform and defect-free nano-dome array by UV photolithography and PVD in order to obtain antireflective coatings for solar cells, illumination and imaging optics. Nanoimprinting from a master holding the replicated mold of polymeric nanopillar array (**Figure 30 a)**) was applied on glass (**Figure 30 b)**) to reduce its Fresnel reflection yielding a 3% enhancement in transmittance compared to bare glass.

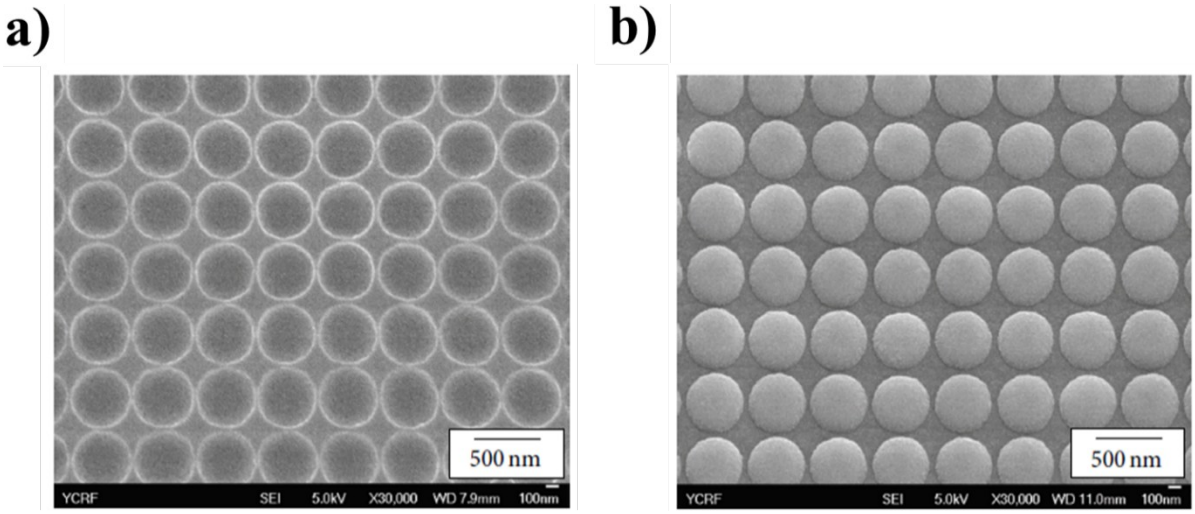

Figure 30: SEM image of **a)** a nano-dome mold of dome-shaped cavities and **b)** the replicated polymeric nano-domes on a glass substrate **[140]**.

There are many different methods for surface structuring in the microscale; among them is Liquid Phase Crystallization (LPC), wet-chemical etching, ion beam lithography yielding highly precise structures, nanoimprint and optical lithography. Lithography consists mainly on the application of a photoresist coating, exposure and transfer steps or printing, molding and embossing steps.

For instance, imprint and UV or normal photolithography was used to successfully make periodic micro-pyramids or honey-comb like textures on substrates. However, photolithography requires the use of photo-cross-linkable materials, it is a destructive method when biological materials are envisaged and it's only a 2D process that needs further steps for 3D applications.

Wet etching was employed to make random textures with root mean square roughness (S_q) of up to 300 nm in AZO films however this method could cause undercutting and reduce the adhesion of films to substrates like glass and even to other layers.

LPC deposits the absorber layer in solar cells by using a high energy density source, such as a laser or an electron beam, to locally melt a previously as-deposited Si layer on glass substrates. Once cooled down, the Si layer crystallizes to form a crystalline silicon layer of 5-30 µm thickness with a grain morphology of several centimeters length and several millimeters width. For example, D. Eisenhauer et al. **[141]** proved that LPC Si thin-film on pyramid textured solar cells gives better optical properties in terms of haze (≈ 1), transmittance (≈ 92% in a $500 < \lambda < 1100$ nm range) and absorbance. In fact, the optical losses at the glass-air interface are reduced by half and the light management in pyramid solar cells is due to their better External Quantum Efficiency (EQE) providing a higher short-circuit current density (J_{SC}). However, this method has some disadvantages such as the need to deposit an amorphous SiCx layer on top of the Si layer already deposited on glass to stabilize the crystallization in electron beam LPC, which results in high surface recombination.

Depending on the application, these methods have their advantages since they were able to enhance the photocurrent of the solar cells but they require many steps (including disposal of toxic chemicals), which makes them expensive. Moreover, they do not provide protection from surface contamination and they are not industrially interesting **[12,85,141-146]**. For these reasons, laser structuring was introduced to overcome these drawbacks and bring new advantages to the fabrication process; as will be discussed in the following section.

2.3.1. UltraShort Pulsed-Direct Laser Interference Patterning (USP-DLIP)

Substrate patterning is a very interesting step for solar cells efficiency enhancement. Laser based methods for substrate patterning, compared to plasma or chemical etching, bring many advantages to the table such as high efficiency and selectivity, highly precise production, a clean and environmental-friendly process, applicability to many materials and little to no material damage for the photovoltaics. For example, M. Soldera et al. **[12]** deposited zinc phtalocyanine (ZnPc) and fullerene (C_{60}) films onto laser patterned polyethylene therephtalate (PET) with hexagonal grid

structure of 0,7 µm period by Vacuum Thermal Evaporation (VTE). The increased light absorption in the semiconductor layer increased the J_{SC} of the textured cell by 18% compared to the planar cell **[12,147,148]**.

Within this study we used USP-DLIP to pattern the glass substrates to serve as support for the growth of textured ZnO/Cu_2O junctions in an attempt to generate photocurrent. USP-DLIP is a 1D, 2D and even 3D substrate laser structuring method used to add to the substrate various surface functions such as super-hydrophobicity, tribological, bacteria repellency and even to simply decorate the material with colorful structures. It has the advantage of directly transferring the textures to the substrate surface, in one step, without heating and with no medium needed, such as masks or solvents. USP-DLIP can produce micron and sub-micron structures on various types of surfaces such as glass, metals, thin metallic films, ceramics and even plastics (polymers) of large industrial standards areas at a processing speed of about 1 m^2/min and fabrication rates going from 10 to 100 cm^2/s. It consists on employing a high power coherent laser beam that is split in two or more sub-beams that interfere on the substrate surface to form a redistributed fringe-like intensity (**Figure 31 a)**). The structure is produced based on the fact that the surface is modified in the interference maxima positions by local melting and/or selective ablation, as shown in **Figure 31 b)**, while the regions of minimum intensity remain mostly intact with the temperature below the melting point **[85,142,149-152].**

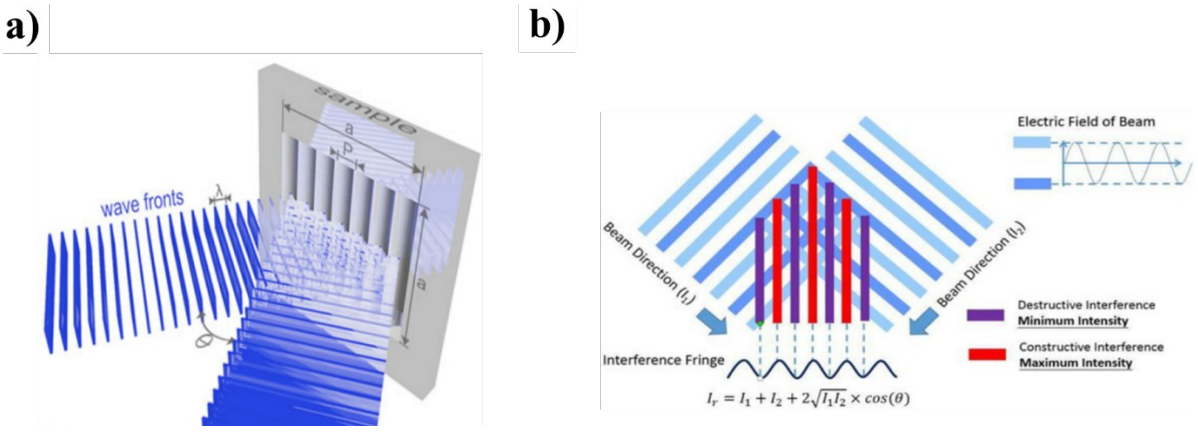

Figure 31: Schematic representation of **a)** the interference of two laser beams separated by an angle θ on a (*axa*) sample to form a structure with a *p* periodicity; and **b)** the laser interference of two beams on a surface showing the constructive and destructive interferences at maximum and minimum intensities respectively, responsible for the structure creation **[153,154]**.

The implemented surface structure depends on the laser pulses (nano-, pico- or femto-second lasers) and the laser fluency, the number of the interfering sub-beams and the angle θ separating those sub-

beams. **Figure 32** represents the possible surface structures if a two (**Figures 32 a) and d)**), three (**Figures 32 b) and e)**) or four (**Figures 32 c) and f)**) laser beam interference took place which results in line-like, dot-like and square-like geometries respectively. In some cases, six-beams interference may be used to form hexagonal-like structures **[85,142,155]**.

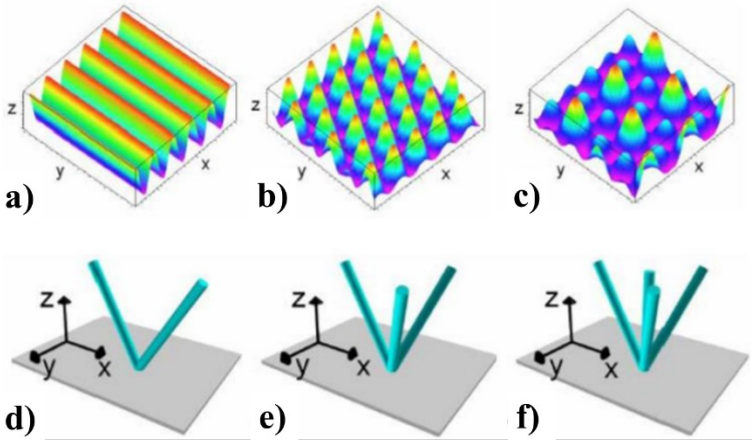

Figure 32: Representation of the calculated intensity distribution and the corresponding beam configurations for **a,d)** two-beam, **b,e)** three-beam and **c,f)** four-beam laser interference **[156]**.

The structure of interest for this work is the sinusoidal structure resulting from a two-beam interference USP-DLIP method. In this case, the spatial intensity distribution (*I*) and the periodicity (*p*) are calculated from the following **Equations 10 and 11**:

$$I(x) = 2c\varepsilon_0 E_0^2 \cos(kx\sin(\alpha_0))^2 \text{ with } k = \frac{2\pi}{\lambda} \qquad \textbf{(Eq. 10)}$$

$$p = \frac{\lambda}{2\sin\theta} \qquad \textbf{(Eq. 11)}$$

With *c* the speed of light, ε_0 the dielectric vacuum permittivity, E_0 the electric field amplitude, *k* the wave number, α_0 the angle of the interfered sub-beams with respect to the surface and λ the wavelength of the laser **[85,151,153,156,157]**.

Ultra-short laser pulses, i.e. nano-, pico- and femto-second lasers, can be used as laser sources in USP-DLIP. Nanosecond lasers are mainly used to produce high-depth/width-ratio µm structures due to the coherent length limitation with a structure height as little as a few nanometers for p < 2-3 µm as was observed for several metals. In contrast, the pico- and femtosecond lasers can go down to sub-µm structures which provides interesting surface properties such as self-cleaning, antireflection, ice and dirt repellence. The nanosecond laser can successfully locally ablate a material, however it will

leave melted zones on the metal surface. This is explained in reference to the following **Equation 12**:

$$l_T = \sqrt{\frac{\lambda_{th}\,\tau}{d\,c_p}} \qquad \textbf{(Eq. 12)}$$

with l_T the thermal diffusion length, λ_{th} the thermal conductivity, τ the pulse duration, d the density and c_p the specific heat capacity.

In fact, if the periodicity is in the same order as l_T, low thermal contrast takes place with the latter being the temperature difference between the maxima and minima intensity interference positions over the spatial periodicity. This means that the local treatment is inhibited at the maxima position and the material is melted over the whole ablated area. From **Equation 12**, one can see that when τ decreases l_T decreases as well. Therefore, if pico- or femtosecond lasers were to replace the nanosecond laser (10 ps instead of 10 ns per say), the material is only heated at the maxima position which reduces the production of melt and opens up the opportunity of creating sub-µm textures with sufficiently high ablation rates. Additionally, pico- and femtosecond lasers can be used to produce complex geometries even when employing two-beam interference USP-DLIP. For example, for a pillar-like texture, the substrate surface is submitted to several irradiation separated by a material rotation of 60 or 90°; a nanosecond USP-DLIP treatment will melt the first structure while making the second one after material rotation **[157]**.

While much more precise structures are obtained from femtosecond USP-DLIP, the picosecond USP-DLIP is still important for specific applications such as the super-hydrophobicity of surfaces useful for corrosion and ice resistance. In fact, femtosecond USP-DLIP treated surfaces are almost completely resistant to the attachments of organic components responsible for the superhydrophobic characteristic, as opposed to the picosecond USP-DLIP treated surfaces. In their study of the pico- and femtosecond four-beam USP-DLIP of Aluminum 2024, S. Milles et al. **[158]** observed that femtosecond USP-DLIP produced 3,1 µm deep structures with almost no super-hydrophobicity behavior while picosecond USP-DLIP produced 6,8 µm deep structures with constant super-hydrophobicity behavior after 16 days with water angles above 150° due to the higher structure depth and surface roughness resulting from the strong redeposition of the recast aluminum **[149,150,158]**.

Next, the realization of the structured glass by picosecond laser USP-DLIP done in the Lehrstuhl für Funktionswerkstoffe laboratory in Saarbrücken is described. The choice of picosecond laser, instead of the femtosecond laser known for its more efficient structuring abilities such as very high structure depths, is due to the fact that pretty low structure periodicities (p = 1-3 µm) are needed. In fact, finding the right laser focus for such small periodicities using a femtosecond laser was quite difficult. For this reason, the picosecond laser was adopted for the glass structuring because not only does it

facilitate finding the right laser focus for small periodicities, but it is also much easier to use than the femtosecond laser. The picosecond laser adopted was an Edgewave™ GmbH Ultrashort Pulse InnoSlab picosecond laser of the PXxxx-2 series with a maximum average power of 100 W, a maximum repetition rate of 100 kHz, a maximum pulse energy of 1000 µJ and a pulse width of 12 ps.

The experimental setup for the picosecond laser USP-DLIP is presented in the following **Figure 33**:

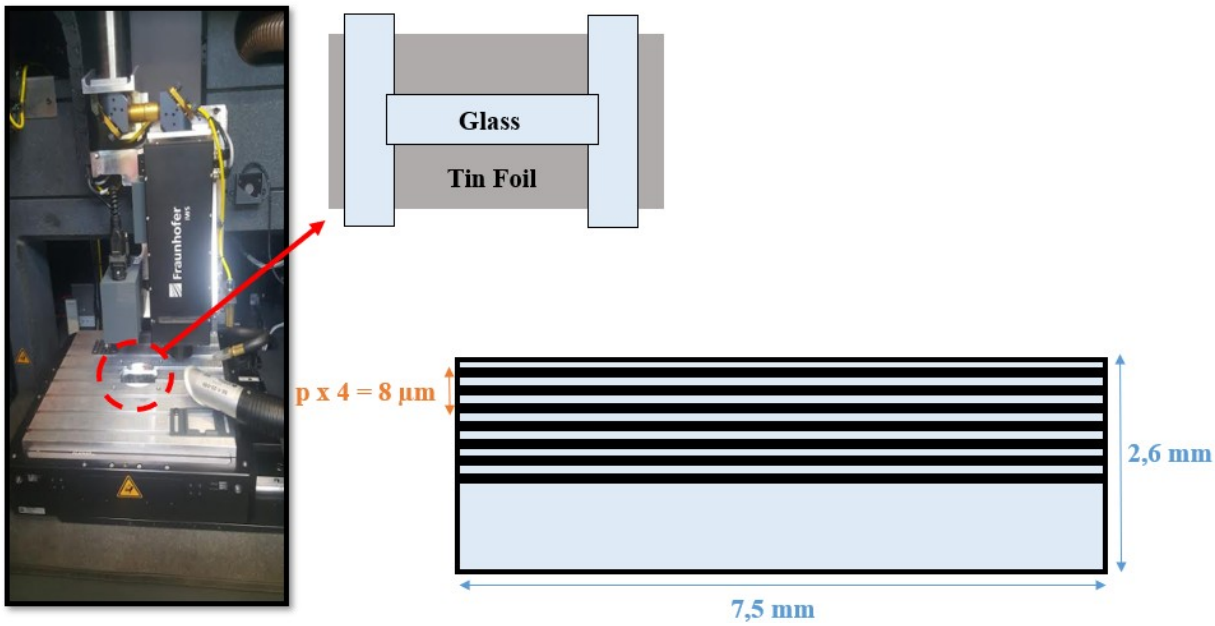

Figure 33: Photographic image of the experimental setup, and a scheme showing the to be structured sample position and the structure geometry on a glass slide.

Before placing the glass substrate, it is necessary to protect the metallic support with aluminum foil in order to prevent its contamination by projectiles resulting from the glass structuring. Moreover, the glass slide is positioned on two parallel glass slides in order to ensure a homogeneous structuring all along the surface. Then, the experimental parameters were set up on the laser's software: laser power, USP-DLIP value which presents the position of the prism in the laser head, pulse distance along the glass slide (x direction) and distance Z between the laser and top of the substrate (z direction). These values are changed in order to find the focus point of the laser as a first step and then to obtain the desired periodicity as the second step; checking the success of these steps is done by using a Confocal Laser Scanning Microscope (CLSM). The parameters used for successfully achieving respectively 1.5 and 2 µm structure periodicities tested within this study were a laser power of 77 and 80%, a pulse distance of 2.5 and 3 µm, a Z value of 267.38 and 267.45 mm and, finally, USP-DLIP values of 128 and 150 mm. Once the structuring is completed, the surface topography is measured by the CLSM in order to extract the structure periodicities and heights.

2.3.2. Solar cell modelling on patterned glass

In order to fabricate the ZnO/Cu_2O heterojunction-based structured solar cells, we need to have an idea about the proper structure properties and conditions for the glass substrate. For that, we collaborated with Dr. Marcos Soldera from the Institut für Fertigungstechnik of the Technische Universität Dresden **[1]** for the simulation of the light absorption in the textured solar cells, in order to preview and understand what conditions are needed for the glass texturing to be able to maximize the photocurrent of the solar cells and minimize the parasitic absorption losses.

To that end, a model implemented with the Finite Element Method (FEM) was used to calculate the solar cells absorption and photocurrent from an AM1,5G 100 mW/cm^2 spectrum illumination in the 300-640 nm wavelength range **[1]**. The results of the simulations also yielded the photogeneration rate as a function of the position. The three-component steady state electric field represented by complex values is obtained from solving Maxwell's equations by FEM using COMSOL Multiphysics. The simulations are used to enhance light absorption in the solar cell by studying the interaction of light with the USP-DLIP-structured glass substrate in a periodic 1D line-like sinusoidal form, which implies that a 2D domain is enough for the modeling (*z*-direction is uniform). A sinusoidal structure is very simple and fast to fabricate while also offering the least computational effort and time for the simulation. Since the conformal growth of the Cu_2O film on the textured glass substrate is only ideally realized on low aspect ratio substrates or extremely thin film, the simulations were based on a conformal growth model (isotropic growth) where the layer grows at constant thickness with the normal direction of the surface at any point on this surface **[159]**; this translates as a uniform mean electric field. If a low aspect ratio substrate and very thin films are considered, we can obtain the same layer profiles as the conformal growth. The unpolarized solar spectrum is divided into two components with the same electromagnetic energy: a Transverse Electric (TE) mode and a Transverse Magnetic (TM) mode with the electric field and the magnetic field along the structure direction respectively; note that during the simulation the results are averaged. Since the glass has a thickness much larger than the simulated wavelengths, the light propagation is incoherent in the substrate. One solution to this problem is implementing the phase elimination method that only requires two simulation runs to model the incoherent propagation of light in glass and the coherent propagation of light in the layers **[160]**. As can be seen from **Figure 34**, on top of the air domain a Perfectly Matched Layer (PML) domain with the same refractive index as air is placed to absorb all departing radiation and prevent the re-introduction of spurious reflected light **[1]**.

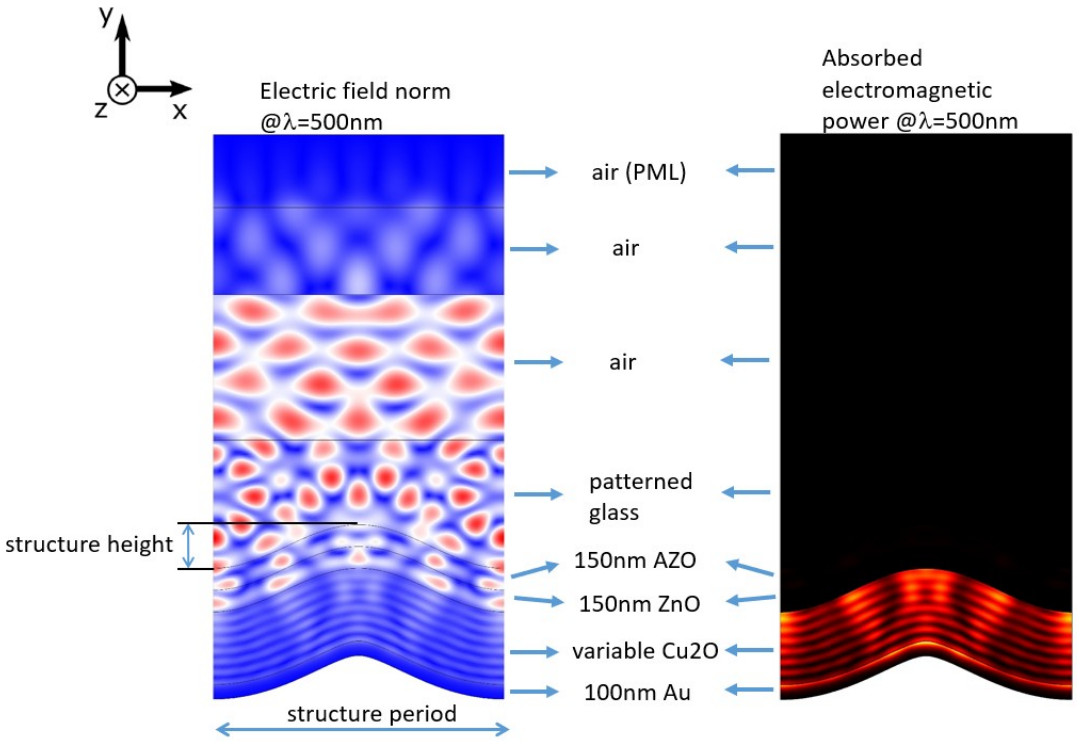

Figure 34: Simulation of the electric field norm **(Left)** and the absorbed electromagnetic power **(Right)** at 500 nm wavelength for a solar cell comprised of a patterned glass substrate with a specific structure height and period, a 150 nm AZO layer, a 150 nm ZnO layer, a Cu_2O with variable thickness and a 100 nm gold (Au) layer **[1]**.

The complex index of refraction ($\tilde{n}$), the average electromagnetic energy density absorbed in a material (Q), the free carrier photogeneration rate (G) and the maximum available photocurrent density $J_{ph,max}$ (considering all photocurrent carriers are perfectly extracted from the solar cells contacts) are calculated from the following **Equations 13 to 16**:

$$\tilde{n}(\lambda) = n(\lambda) + i\kappa(\lambda) \qquad \textbf{(Eq. 13)}$$

$$Q(x,y,\lambda) = \frac{1}{2} c \varepsilon_0 n(\lambda) \alpha(\lambda) |E(x,y,\lambda)|^2 \text{ with } \alpha = \frac{4\pi\kappa(\lambda)}{\lambda} \qquad \textbf{(Eq. 14)}$$

$$G(x,y,\lambda) = \frac{Q_{Cu_2O}(x,y,\lambda)}{\frac{hc}{\lambda}} \qquad \textbf{(Eq. 15)}$$

$$J_{ph,max} = q \int_{300\text{ nm}}^{640\text{ nm}} \int_{V}^{d} \frac{GdVd\lambda}{S} \qquad \textbf{(Eq. 16)}$$

with λ the free space wavelength of the plane electromagnetic wave, c the speed of light in vacuum, ε_0 the permittivity of free space, α the absorption coefficient, h the Planck's constant, q the elementary charge, V the volume and S the projected solar cell area in the substrate plane.

The electromagnetic model presented in **Figure 34** was implemented using the software COMSOL Multiphysics; the mesh was made from triangular elements with the consideration that the minimum effective wavelength in each subdomain is at least five times larger than the element size. This yielded typical mesh sizes of 20000-70000 elements **[1]**.

2.4. Solar cell fabrication on flat and patterned glass

The final part of this work consists on the fabrication of the ZnO/Cu_2O heterojunction based solar cells on flat and patterned substrates of different periodicities. However, some layer stack testing was done at first to ensure that we obtain the required electrical, structural and chemical properties of the layers destined to be used in the final solar cell. In this section, we present the four series towards solar cells fabrication that were done and shown in **Table 2**; one must refer to the deposition conditions of the different layers detailed in **Sections 2.2.1.5, 2.2.1.6 and 2.2.2.2**.

Table 2: Summary of the four towards solar cells series showing the substrate, transparent electrode, n-layer, p-layer and contact layer used in each sample.

Series	Sample	Substrate	Transparent electrode	n-layer	p-layer	Contact
1	A	Flat glass	X	ZnO	Cu_2O	X
	B	Flat glass	AZO 1 at.%	ZnO	Cu_2O	X
	C	Structured glass with p = 1.5 µm	AZO 1 at.%	ZnO	Cu_2O	X
2	A	Si placed at 2 cm from the substrate holder axis	X	ZnO	Cu_2O	X
	B	Si placed at 8 cm from the substrate holder axis	X	ZnO	Cu_2O	X
3	A	Flat glass	AZO 2 at.%	ZnO	Cu_2O	Au
	B	Structured glass with p = 1.5 µm	AZO 2 at.%	ZnO	Cu_2O	Au
	C	Structured glass with p = 2 µm	AZO 2 at.%	ZnO	Cu_2O	Au
	D	Structured glass with p = 3 µm	AZO 2 at.%	ZnO	Cu_2O	Au
4	A	Flat glass	AZO 2 at.% (545 V)	ZnO	Cu_2O	Au
	B	Structured glass with p = 1.5 µm	AZO 2 at.% (545 V)	ZnO	Cu_2O	Au
	C	Flat glass	AZO 2 at.% (550 V)	ZnO	Cu_2O	Au
	D	Structured glass with p = 3 µm	AZO 2 at.% (550 V)	ZnO	Cu_2O	Au

In the following, we cite the main changes in deposition parameters used to go from one sample to another; the non-mentioned parameters remain the ones presented in **Sections 2.2.1.5, 2.2.1.6 and 2.2.2.2** without any changes for the solar cells fabrication process.

In the first series, the AZO 1 at.% refers to the AZO film deposited from a Zn/Al 1 at.% target at 555 V/20 sccm of O_2. For the deposition of AZO 1 at.% by HiPIMS, the films were placed furthest away from the target axis at 3 cm from the substrate holder axis to ensure a minimum film resistivity. For the ZnO deposition by DC, the samples were placed at 2 cm from the substrate holder axis in reference to Claudia de Melo's work **[14]** and also to ensure a minimum resistivity away from target axis. As for the Cu_2O deposition by ALD, 300 sccm of N_2 were injected during the boosting mode.
The goal of this series is to test for the first time the deposition of a homogeneous Cu_2O layer.

In the second series, the ZnO deposition by DC was realized on Si substrates placed at 2 and 8 cm from the substrate holder axis to test the difference in, mainly, the structure properties of the Cu_2O grown on top by ALD this time with a boosting mode consisting of 500 sccm of N_2 gas. At 8 cm, the sample is facing the target axis and at 2 cm it is furthest away.
The goal of this series is again to test the homogeneity of the deposited Cu_2O film, but also to understand the difference in growing Cu_2O on ZnO deposited at a position facing the target axis (8 cm) or furthest away (2 cm).
In the third series, AZO 2 at.% was the AZO film deposited from a Zn/Al 2 at.% target at 555 V/20 sccm of O_2. For the deposition of AZO 2 at.% by HiPIMS and ZnO by DC, the films were placed furthest away from the target axis at 3 cm and 2 cm respectively from the substrate holder axis to ensure a minimum film resistivity.
The goal of this series is to test the performance of a full fabricated ZnO/Cu_2O heterojunction based solar cell. A schematic representation of the solar cell is presented in the following **Figure 35**:

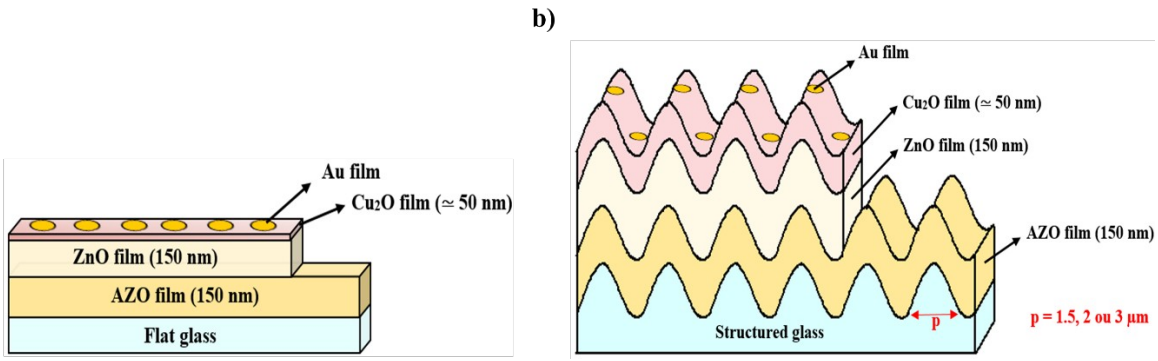

Figure 35: Scheme of the solar cell structure of the third solar cells series fabricated on four different substrates : **a)** Flat glass and **b)** Structured glass of three different periodicites p = 1.5, 2 and 3 µm.

In the fourth series, aside from the different applied voltage used to deposit the AZO 2 at.% films, the ZnO was deposited this time under a 7 sccm flow of oxygen to test the different film conductivity and transmittance, and the gold layer was doubled in thickness to improve the contact.

The goal of this series is to try and optimize the performance of the preceeding solar cell. A schematic representation of the solar cell is presented in the following **Figure 36**:

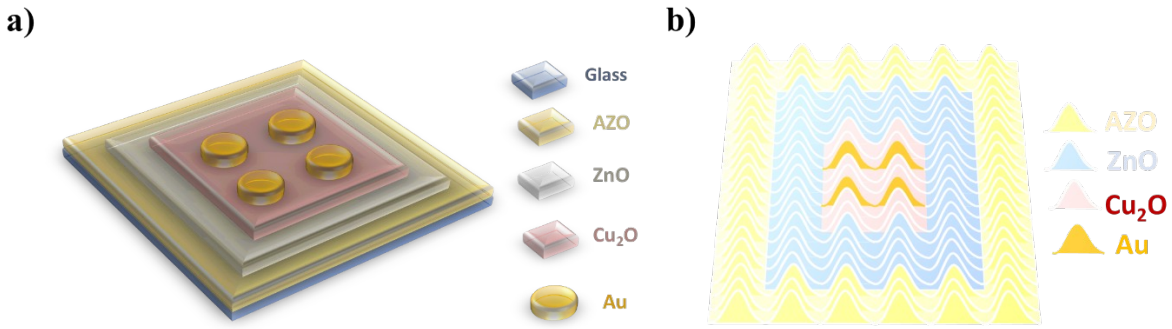

Figure 36: Scheme of the solar cell structure of the fourth solar cells series fabricated on two different substrates: **a)** Flat glass and **b)** Structured glass of p = 1.5 µm periodicity. Each solar cell was made twice with two different applied voltages of AZO, 545 and 550 V.

2.5. Material characterization methods

In this part, we describe the characterization methods used to evaluate the electrical, optical and structural performances of the thin films used in this work, with the AZO films being the main focus. The characterization techniques used for the textured glass substrate as well as the final solar cells series are also reported.

2.5.1. Evaluation of film thickness by profilometry

In order to monitor the deposition rate and to calculate the resistivity of the thin films, measuring their thickness after deposition is needed. For this purpose, a Bruker's DektakXT® Stylus Profiler with a 2 µm diamond tip was used to perform contact thickness measurements among other diverse surface measurements that this profiler is able to do. This profilometer provides reliable and reproductive thickness measurements down to the nanometer scale with a 4 Å repeatability, as well as rapidly-obtained results and ease of use. The profiler is coupled to the Vision64 Operation and Analysis software that efficiently analyses large data and provides an easy manipulation of the profiler. To perform a measurement, the tip is dragged from the glass substrate to the film, and the difference between the two thicknesses is the thickness of the thin film as shown in **Figure 37**.

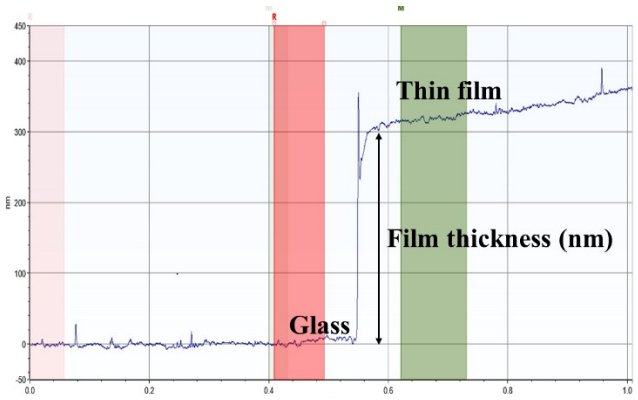

Figure 37: A graphic example of the curve obtained after measuring the thickness of an AZO film with the profiler.

2.5.2. Four point probe and Hall effect methods

One of the most important properties of thin films required for this work is the conductivity of the thin films, and especially the transparent electrode of the final solar cell i.e. the AZO layer. In fact, the compromise between the transmittance and the conductivity of the AZO films can be achieved, on the one hand, by carefully monitoring the resistivity of the films after deposition to try and reach the lowest resistivity possible while, on the other hand, making sure that the film is not too absorbent. In this section, is presented the four point probe method used for the resistivity measurements as well as the Hall effect method applied for the most conductive films. They provide the film resistivity, conductivity, electron mobility and carrier concentration values.

Our 4 point probe setup is used in an equidistant linear configuration as shown in **Figure 38**: A current is applied on the two outer probes using a Keithley 237 High Voltage Source-Measure Unit generator which sources a current from 100 fA to 100 mA; however the measured voltage drop is not considered reliable for a nA applied current, in this case the voltage drop values were not considered and the film was labelled resistive. The resulting voltage drop is measured between the two inner probes and was shown on a Keithley 2700 multimeter/Data acquisition system after 100 acquisitions from the applied current and then the resistivity was calculated as follows (**Equation 17**):

$$\rho = R_S \, t = \frac{U}{I} \, C \, t \qquad \textbf{(Eq. 17)}$$

with ρ the resistivity of the AZO film (Ω.cm), R_S the sheet resistance (Ω/sq), U the measured voltage drop (V), I the applied current (A), C a correction factor of 4.5324 because the film thickness is much larger than the distance between the probes and t the thickness of the film (cm).

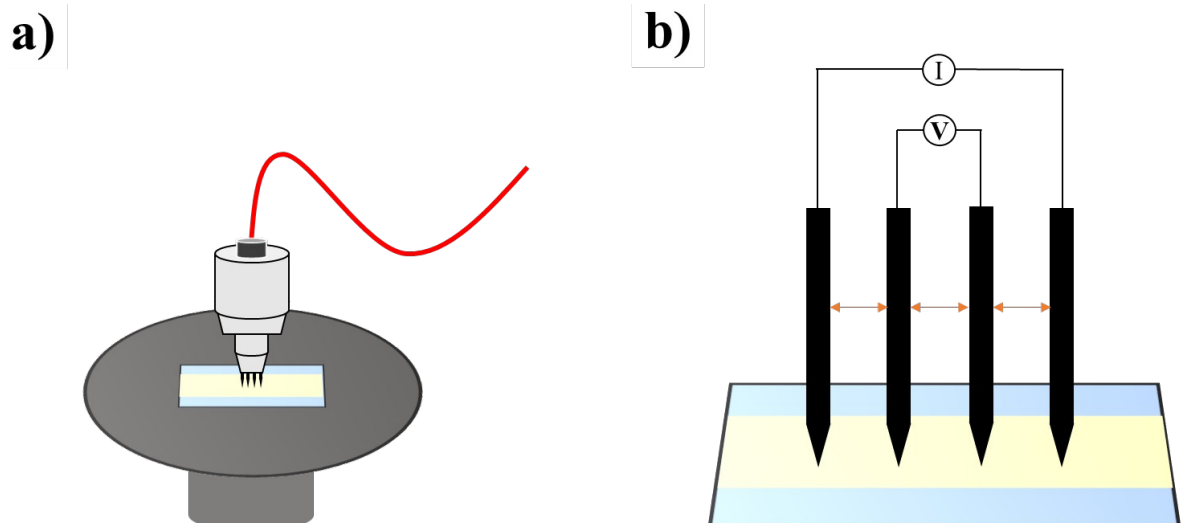

Figure 38: Schematic representation of **a)** the four point probe setup while measuring the resistance of an AZO film (yellow) deposited on glass (blue) and **b)** A close up on the equidistant four probes showing the applied current wiring on the outer probes and the measured voltage drop wiring on the inner probes.

Additionally, in order to study the influence of the temperature on the properties of the AZO films, the four point probe was coupled with a Linkam® HFS600E heating plate. The samples were heated, depending on the at.% of Al and the film's electrical ability to withstand high temperatures, to 100°C, 150°C, 200°C and 225°C while applying a current of 10 μA and, finally, at 225°C while applying a current of 1 mA for the most conductive films; the process is shown in **Figure 39**. It took approximately 2 mins to go from one plateau to another since the Linkam speed was estimated at 30°/ min. From the measured R_S, the resistivity was calculated from the same previous **Equation**.

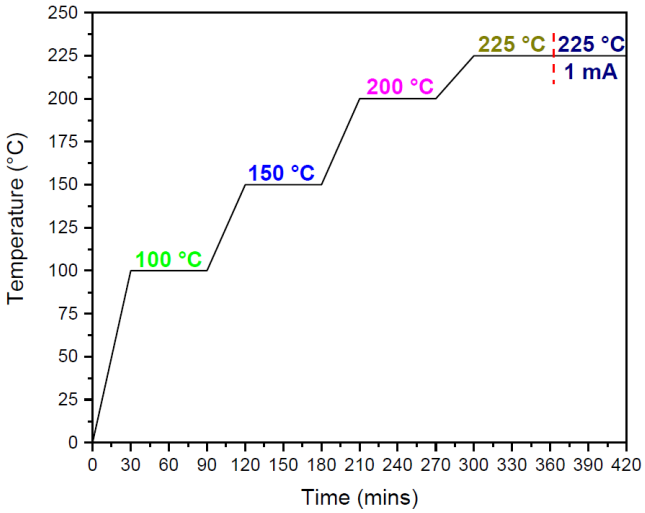

Figure 39: Graphical representation of the temperature (°C) as a function of time (mins) showing the heating process of the AZO films in order to study the influence of temperature on their electrical properties.

The second electrical characterization method employed on most conductive AZO films was the Hall effect. An Escopia HMS-5000 Hall Effect Measurement System applying a DC magnetic field of B = 0,57 T was used to measure the resistivity (ρ), conductivity (σ), Hall mobility ($\mu_H = \frac{t\ V_H}{B\ I\ \rho}$ **(Eq. 18)** with t the film thickness, V_H the Hall voltage and I the applied current) and charge carrier concentration ($n = \frac{1}{\rho\ e\ \mu}$ **(Eq. 19)** with e the electron charge) of the AZO films. The samples, cut down ideally into a square shape, are submitted to the Van der Paw configuration where four contacts are placed on each corner of the film (**Figure 40 a)**). As shown in **Figure 40 b)**, the applied magnetic field B is perpendicular to the film surface while a current I is circulating in the x direction through two opposite corners of the sample. The charge carriers follow the y direction under the influence of the Lorentz force. The Hall voltage V_H is detected on the other two opposite corners of the film due to the charge accumulation **[1314]**.

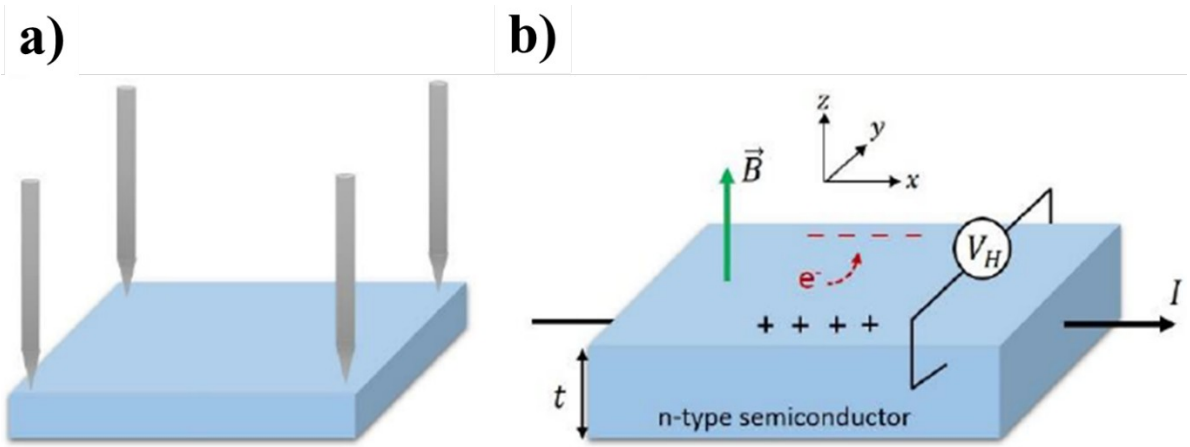

Figure 40: Schematic representation of **a)** The Van der Pauw contact configuration method used in the Hall effect measurement and **b)** the process that occurs during a Hall effect measurement of a thin film **[14]**.

2.5.3. UV Visible Near-Infra-Red spectroscopy

As mentioned above, one consideration while optimizing the AZO films is to ensure that the films are not too absorbent for application as transparent electrodes. The transmittance of the AZO films was monitored using a Varian Cary 5000 UV-Vis-NIR spectrophotometer in the visible range (200-800 nm). In this setup, the light beam is split into two beams with one beam directed towards the reference glass slide and the other is directed towards the sample to measure the film's transmittance. Before starting any measurement, a baseline correction must be performed in order to calibrate the two beams and to compensate the fluctuation of the emission in the chosen range of wavelength. To

calculate the film transmittance T_{Film}, the following equation, while referring to the **Figure 41,** is used **[34]**:

$$\frac{T_{Substrate}}{T_{Measured}} = \frac{I_0 T_1^2}{I_0 T_1 T_2 T_{Film}} = \frac{T_1}{T_2 T_{Film}} \qquad \textbf{(Eq. 20)}$$

With $T_{Substrate}$ the transmittance of a glass slide, $T_{measured}$ the measured transmittance, I_0 the beam intensity, T_1 the transmission coefficient at the air/glass interface, T_2 the transmission coefficient at the glass/film interface and T_{Film} the transmittance throughout the film.

By neglecting the reflection at glass/film interface, we can write:

$$T_2 = I_0 = 1 \text{ and } T_1 = \sqrt{T_{Substrate}}, \qquad \frac{T_{Substrate}}{T_{Measured}} = \frac{\sqrt{T_{Substrate}}}{T_{Film}} \textbf{(Eq. 21)}$$

Therefore a good approximation of the film transmittance is:

$$T_{Film} = \frac{T_{measured}}{\sqrt{T_{Substrate}}} \qquad \textbf{(Eq. 22)}$$

Experimentally, if the substrate is used as reference, the measured transmittance corresponds directly to the film transmittance. However, this way is neglected the effect of the substrate-film interface on the measurement. Only when the air is used as reference, the previous equation may be applied to calculated the film's transmittance **[13]**.

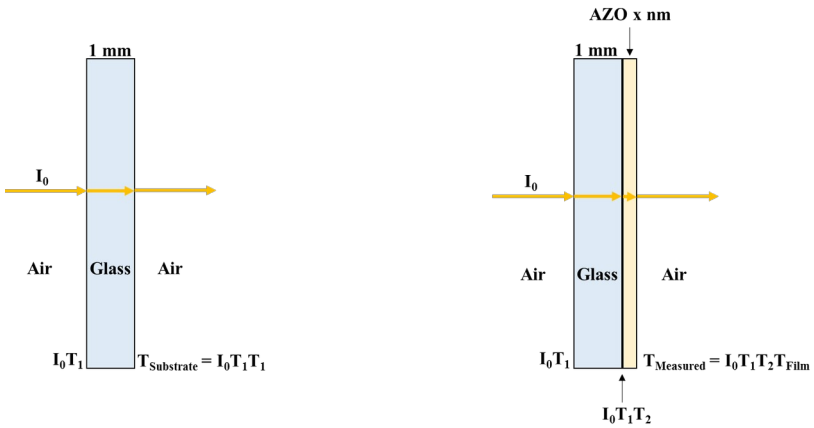

Figure 41: Schematic representation of light passing through **(Left)** a simple glass substrate and **(Right)** an AZO film deposited on a glass substrate. One must note that the beam intensity decreases gradually for each light penetrated layer or material.

To include the influence of the film thickness on the optical properties, the absorption coefficient α is calculated from the Beer-Lambert law (**Equation 23**):

$$\alpha = \frac{1}{t} \mathrm{Ln}\left(\frac{1}{T_{Film}}\right) \qquad \textbf{(Eq. 23)}$$

with α the film absorption (m^{-1}) , t the film thickness (nm) and T_{Film} the film transmittance.

Next, the band gap (E_g) of all the AZO films was calculated using the Tauc plot method for direct band gap materials. This method consists in plotting $(h\alpha v)^2$ as a function of (hv) with h Planck's constant (J.s), α the absorption coefficient (m^{-1}) and v the light frequency (s^{-1}). Once the curve is plotted, the linear part of the curve is extrapolated in order to reach $(h\alpha v)^2 = 0$ as shown in **Figure 42**; the corresponding (hv) value is the AZO film's band gap **[13]**.

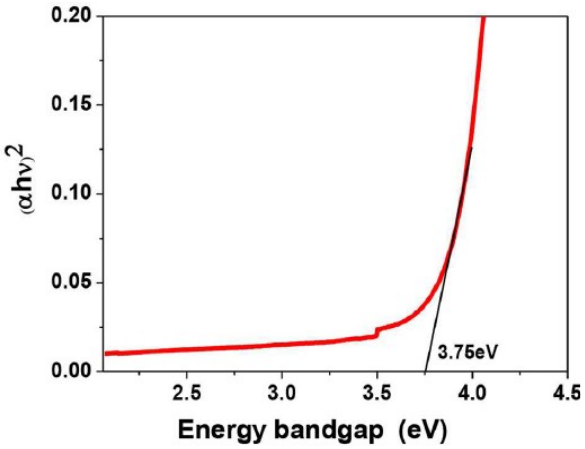

Figure 42: An example of a Tauc plot; the point where the straight line meets the hv axis corresponds to the band gap energy **[161]**.

2.5.4. Scanning Electron Microscopy (SEM)

The Scanning Electron Microscope was used in this study to obtain some information about the microstructure morphology of the AZO films.

An electron beam in the microscope chamber is sent towards a sample as shown in **Figure 43**; the electrons penetrate the sample to meet the sample's atoms and produce a region of primary excitation from which the following signals are produced: Backscattered Electrons (BSE) and Secondary Electrons (SE) that result from elastic and inelastic interactions respectively; as well as X-rays, Auger electrons and cathodoluminescence signals. The size and form of the primary excitation region depends on the electron beam energy and the density of the sample. The "tear drop" shape shown in **Figure 43** belongs to a low atomic number sample whereas a hemisphere is observed for high atomic number samples because they have more particles to hinder electron penetration **[162]**.

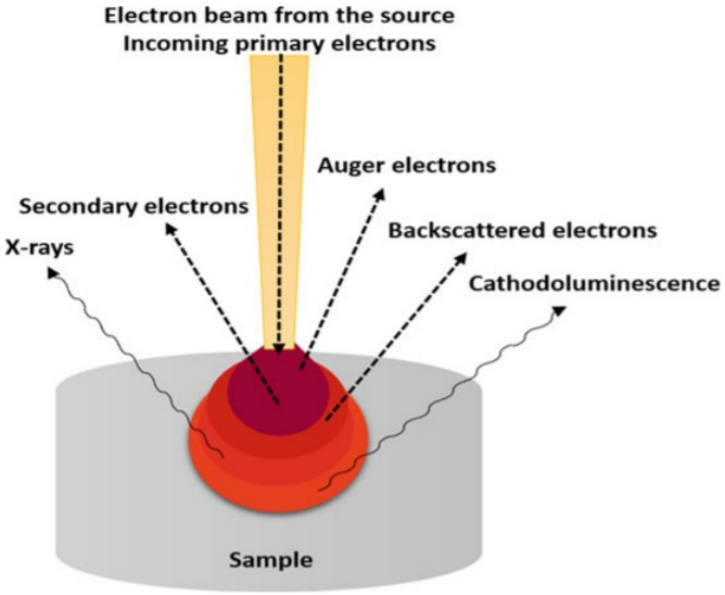

Figure 43: Image showing the interaction of an incident electron beam during a SEM analysis with a sample as well as the resulting different emitted signals **[163]**.

When the sample's atoms deflect the incident electron beam, a negligible energy loss and an elastic electron scattering with an angle greater than 90° occurs; those types of electrons have energies higher than 50 eV and are called BSE. The BSE signal is higher for high atomic number atoms because they have more positive charges to backscatter the electrons; they also come from a bigger region than that of the SE due to their high energy which is why a BSE image's lateral resolution is less clear than that of a SE image. BSE are responsible for the compositional and topographic information of the sample on deep surface levels. When the sample's atoms and electrons interact with the incident electron beam, the latter transfers a considerable amount of energy to the sample atoms which depends on the excitation state of the sample's electrons and the atom-electron binding energy. Once the sample's electrons are excited, SE with low energies (less than 50 eV) are emitted within a few nanometers from the sample surface, which results in surface images of good resolution that provide information on the texture and roughness of the sample surface **[162]**.

In this work, the SEM top-view images were obtained from a FEI™ SEM-QUANTA™ 650 FEG as well as a FIB microscope. The latter was used to perform top view and cross-section images as well as FIB lamellae for Transmission Electron Microscope measurements but this part will be discussed further in the TEM **Section 2.5.6**.

2.5.5. X-ray Diffraction (XRD)

Another very important analysis of the thin films used for the to be fabricated-solar cell is the microstructure analysis. While verifying that the proper and to be expected thin film was successfully deposited was important for the Cu_2O layer deposition by ALD; studying the evolution of the structure and microstructure of the AZO films with the at.% of Al in the Zn/Al target was one of the main goals of the optimization of the AZO film deposited by reactive-HiPIMS.

XRD is a great first step microstructure analysis method at the microscale, allowing the user to obtain the main structural information before coupling their study with TEM measurements for more local analysis. In fact, TEM requires very thin films (less than 100 nm thickness) which can be easily destroyed by-the powerful electron beam. Additionally, samples ready for TEM observation must be prepared very accurately and carefully; hence, TEM is not a routine method.

XRD is a non-destructive surface analysis method that gives information on the structure and crystallinity of the samples, it identifies the present phases, the preferred crystal orientation, the lattice parameters, the atomic positions, the average grain size, as well as the strain and crystal defects **[164]**.

As shown in **Figure 44**, monochromatic X-ray beams are sent towards a sample surface. Only the constructive interference of the X-rays results in scattering at certain angles from each set of lattice planes that do not show extinction; this is how the XRD peaks are obtained. This is interpreted by Bragg's law (**Equation 24**):

$$2d_{hkl}\sin\theta = n\lambda \qquad \textbf{(Eq. 24)}$$

With d_{hkl} the lattice spacing (Å or nm), θ is the angle of the diffracted beam (°), n is the order of diffraction (n = 1 in this work) and λ the wavelength of the incident X-ray beam (Å or nm) .

The positions of atoms in their lattice planes determines the intensity of XRD peaks . The XRD pattern is the fingerprint of the periodic atomic arrangement in a material. Phase identification is realized by comparing the obtained XRD pattern to a reference standard database for X-ray powder diffraction patterns for crystalline samples **[165,166]**. It can also be obtained by modelling the intensity distribution of X-ray diffractograms.

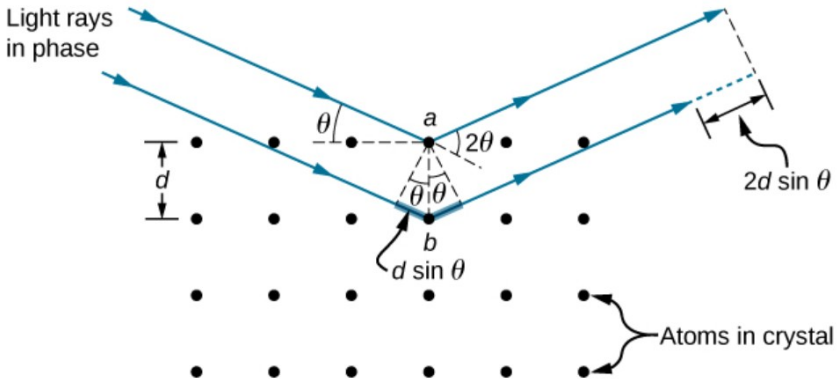

Figure 44: Schematic representation of X-ray diffraction from a crystal sample **[167]**.

The conventional Bragg-Brentano geometry diffraction was the configuration adopted for this work's XRD analysis. It is used for phase identification and to determine the precise lattice parameters, the accurate crystallite mean size and micro strain. **[164]**. The average size of crystallites (L) present inside of the sample particles can be calculated from the widely known Scherrer formula, applicable for polycrystalline samples with size of crystallites smaller than 100 nm (**Equation 25**):

$$L = \frac{K\lambda}{\beta \cos\theta} \qquad \textbf{(Eq. 25)}$$

With K is a constant attributed to the crystallite shape and considered as 0.829, λ the X-ray wavelength (nm), β is the Full Width at Half Maximum (FWHM) (radians) of the diffraction peak profile **[168,169]**.

In this work, we used a Bruker D8 Advance diffractometer in a Bragg-Brentano geometry, with a monochromatic radiation of $CuK\alpha_1$ of a 1.54056Å wavelength from a Cu anode. The detector was a Bruker LynxEye detector and the XRD pattern analysis was done via Bruker's very own DIFFRAC.EVA software. During measurements, the source and detector were moving symmetrically to a plane containing the direction normal to the sample surface in order to cover the 2θ range needed for analysis.

2.5.6. Transmission Electron Microscopy (TEM)

In order to go deeper into the microstructural and chemical analysis, a high resolution Transmission Electron Microscope was adopted in order to perform Transmission Electron Microscopy (TEM) and Scanning Transmission Electron Microscopy (STEM). In TEM, the electron beam is perpendicular to the sample surface while in STEM it is converged into one point, this of course makes this method more destructive to the film **[171]**. From TEM, High Resolution-TEM (HR-TEM) and Selected Area

Electron Diffraction (SAED) analyzes were conducted; while from STEM, Energy Dispersive Spectroscopy (EDS) and Energy Loss Near Edge Structure (ELNES) data were collected.

A Jeol JEM - ARM 200F Cold FEG TEM/STEM operating at 200 kV and equipped with a spherical aberration (Cs) probe and image correctors (point resolution 0.12 nm in TEM mode and 0.078 nm in STEM mode) was used. Since very thin samples are needed for TEM, FIB lamellae were extracted from the AZO films using a FEI Helios Nanolab 600i Focused Ion Beam-Scanning Electron Microscope (FIB-SEM) as shown in **Figure 45**. The FIB uses a focused ion beam to extract the zone of interest to be observed by TEM. It can even extract regions containing interesting defects or grain boundaries that we would want to closely observe in TEM **[170]**.

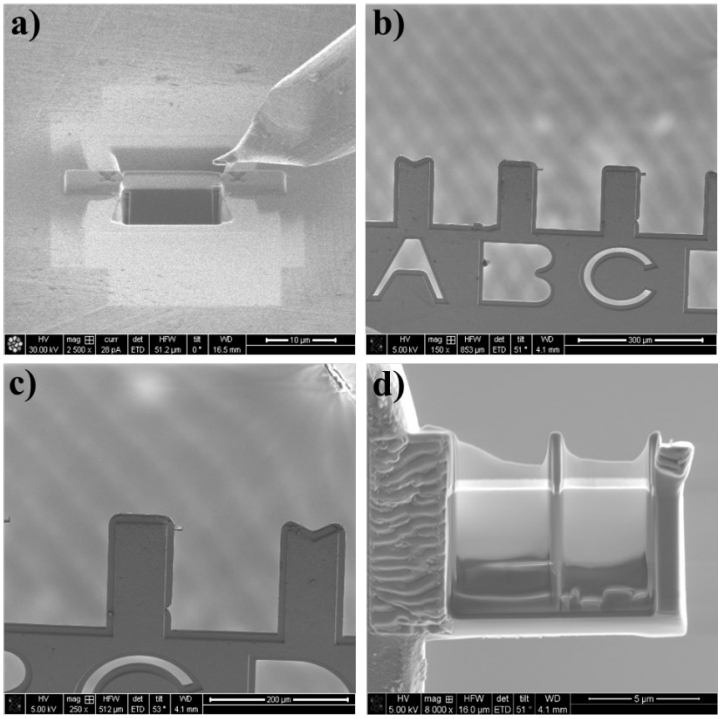

Figure 45: FIB images showing **a)** the transfer probe getting ready to lift the thinned sample lamella, **b)** and **c)** the FIB lamella fixed onto a copper grid and **d)** an example of a FIB lamella taken from an AZO film deposited from a Zn/Al 2 at.% target.

A transmission electron microscope is composed mainly of an electron gun, magnetic lenses, a sample holder, detectors and some other apertures in a vacuum column. The electron gun projects an electron beam towards a thin sample; the electrons are either transmitted through the sample without interaction or they interact with the atoms. Two TEM modes can be distinguished, as shown in **Figure 46 (Left)**, and switched by adjusting the strength of the intermediate lens:

- The imaging mode where the object plane of the intermediate lens is adjusted to the image plane of the objective lens; this allows magnification of the sample image. There are three

image modes shown in **Figure 46 (Right)**: Bright-Field (BF), Dark-Field (DF) and High-Resolution (HR).

- In BF mode, only transmitted beams pass through the sample because the objective aperture is at the back focal point of the objective lens. Image contrast due to thickness, scattering variation and different crystallographic directions appears: Thicker or stronger electron scattering regions, as well as zone axis-parallel-oriented grains are darker.
- In DF mode, only diffracted beams pass through the sample because the object aperture is moved or the beam is tilted to consider only the signal that produce a specific signal in SAD. The spots of the diffraction pattern reveal the size or shape of the corresponding grains in diffraction condition and that appear in bright in a dark background.
- In HR mode, a large objective aperture is used and both the transmitted and diffracted beams interfere on the sample to form an HR image at an atomic scale. The image could even be a single unit cell of the crystal, therefore it is used for detection of point defects, dislocations, precipitates at grains boundaries and stacking faults **[172,173]**.

❖ The diffraction mode where the intermediate lens focuses on the back focal plane of the objective lens, the latter itself focuses parallel beams responsible for the diffraction pattern; the back focal plane becomes the object plane for the intermediate lens. The sample diffracts the electron beam by Bragg's law and diffraction from selected region happens when the Selected Area Diffraction (SAD) is inserted into the image plane of the objective lens **[172]**. A diffraction pattern is thus obtained: Rings with bright spots appear for polycrystalline materials, with some spots brighter than other indicating a preferential orientation in a certain direction. The crystallographic planes of the material in question can be determined by matching the distance from the center of the pattern to the diffraction spots to the reciprocal value of the interplanar distance corresponding (hkl) planes found in the XRD database. Contrary to XRD diffractograms, one can see the orientation of crystals not necessarily parallel to the surface of the films. In the case of fine polycrystalline samples the number of spots is so high that they join to constitute rings whose diameter is the reciprocal value of the interplanar distance of (hkl) planes. For amorphous samples, diffuse rings are observed. A diffraction pattern can also be obtained by performing FFT on HRTEM images.

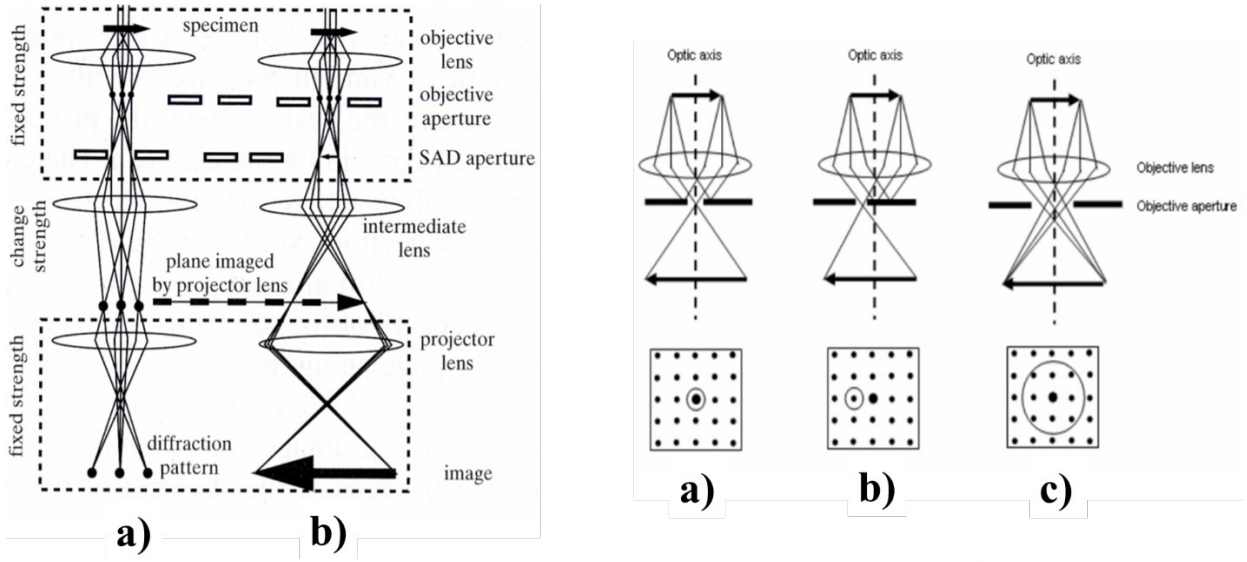

Figure 46: **(Left)** Ray diagram of TEM in **a)** diffraction mode and **b)** image mode **(Right)** Types of image mode: **a)** BF image, **b)** DF image and **c)** HR image **[172]**.

Finally, STEM was adopted to perform Electron Energy Loss Spectroscopy (EELS). EELS collects the electrons that go through the sample. It can be measured at specific elemental edges corresponding to specific electronic transitions in the sample. We limit our study to a short energy range of few tens of eV after the edges of interest. Doing so, the collected Energy Loss Near Edge Structure (ELNES) spectra are the result of energy loss after energy transfer of primary incoming electrons to the material for inducing electronic transitions from valence to conduction band. The spectral intensity represents the density of unoccupied states (DOS) in the probed region of the conduction band. Given the sensitivity of the DOS to any change in the material, ELNES gives information on element coordination, valence, bonding and oxidation state **[174,175]**. ELNES was used in our study to obtain the information at the Al-K, Al-$L_{2,3}$, O-K and Zn-L_3 edges. We used it to study the influence of the Al content on the properties of the AZO films and thus extract the corresponding information regarding the bonding of element, in particular of the Al dopant and its relationship to the electrical behavior.

2.5.7. Confocal Laser Scanning Microscopy (CLSM)

The Confocal laser Scanning Microscope was used during and after laser glass substrate structuring. In fact, in order to find the focus point on the glass with the picosecond laser, as well as to study the influence of modifications in the laser parameters, the sample topography was measured using CLSM.

The CLSM used was an OLYMPUS® LEXT OLS 4100 3D measuring Laser Microscope. The microscope setup holds two parts: a LSM section with a 405 nm short-wavelength semiconductor violet laser as the light source and a photomultiplier as the detector; and a color observation section with a white LED as the light source and a 1/1.8-Inch 2-Megapixel Single-Panel CCD as the detector.

The advantage of a laser scanning microscope, in contrast to conventional contact surface based systems, is the eliminated risk of touching the surface and destroying the structure like shown in Figure 47 especially since the microscope produces low power light **[176]**.

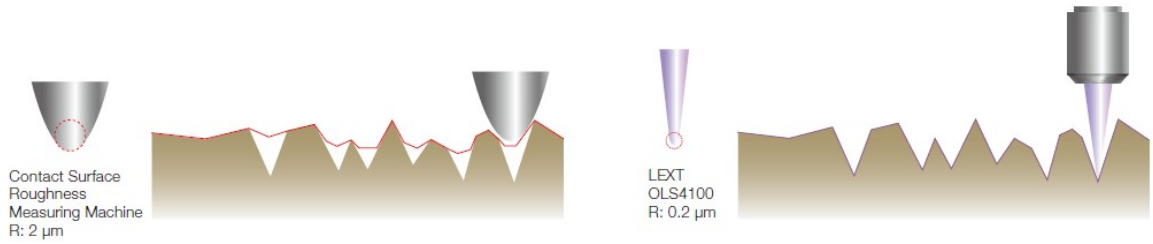

Figure 47: Representation of the difference between the LSM and the contact-type surface roughness gauges **[176]**.

Additionally, no sample preparation is required prior to the measurement. Also, the LSM uses a larger aperture objective lens and a smaller wavelength (405 nm) than a normal optical microscope using visible light (550 nm); this ensures a precise laser movement on the sample yielding a high lateral resolution of 0.12 micron which enables high-definition images, and a 10 nm resolution in the *Z*-axis direction which enables 3D surface measurements of three types: real-colour 3D image, confocal 3D laser image and height information shown in Figure 48 **[176]**.

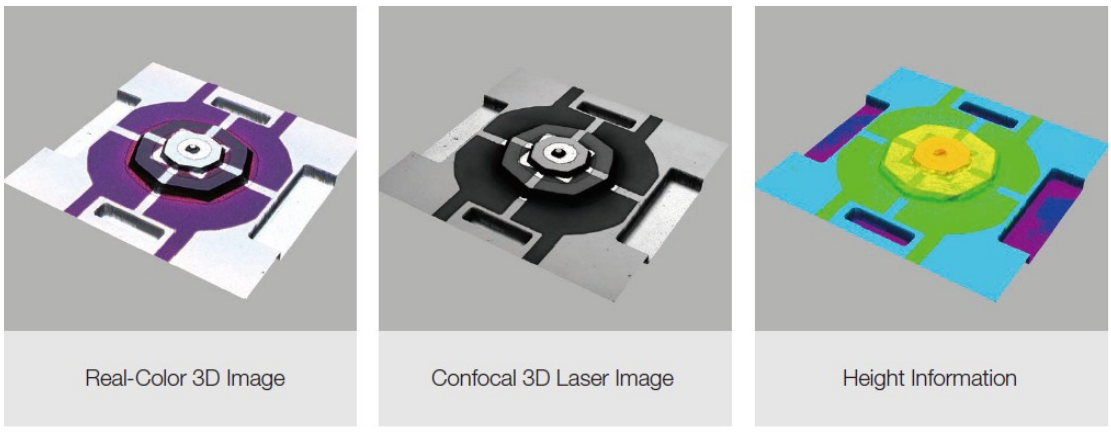

Figure 48: Images showing the three types of 3D surface measurements done by the CLSM **[176]**.

2.5.8. Current-Voltage (I-V) measurements

The final step of this work, after producing a full model solar cell, is measuring the current density by applying the I-V measurements. In our case, the measurements were performed mainly in dark mode, i.e. without a light shining through the sample.

A PV cell can be represented by a circuit model in dark mode (**Figure 49 a)**), where the ideal cell plays the role of the diode, and in light mode (**Figure 49 b)**) where current is generated **[177]**:

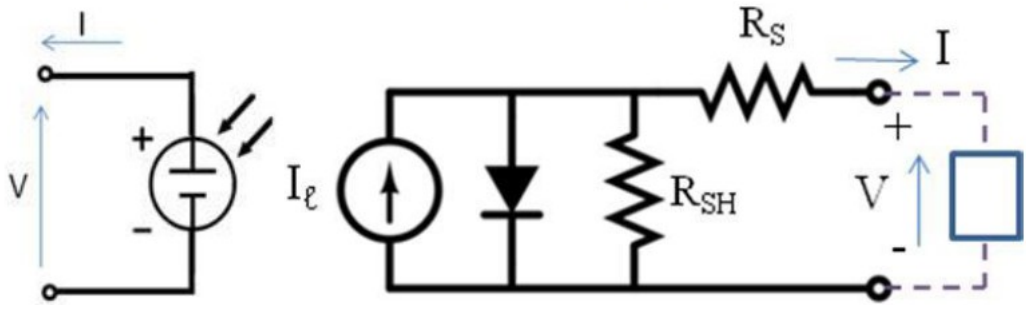

Figure 49: Circuit model for a solar cell in **(Left)** dark mode and **(Right)** light mode **[177]**.

The total current *I* for the PV cell in dark mode and in light mode respectively is presented in these **Equations 26 and 27**:

$$I = I_l - I_D = I_l - I_0\left(e^{\frac{qV}{kT}} - 1\right) \qquad \textbf{(Eq. 26)}$$

$$I = I_l - I_0\left(e^{\frac{q(V+IR_s)}{nkT}} - 1\right) - \frac{V+IR_s}{R_{sh}} \qquad \textbf{(Eq. 27)}$$

With I_l being the current resulting from the photoelectric effect, I_D the diode's current, I_0 the diode's saturation current, q the elementary charge, V the produced or applied measured cell voltage, k a constant of 1.6 x 10^{-23} J/K , T the temperature of the cell (K), R_s the series resistance, n the diode's ideality factor of 1-2 and R_{sh} the series shunt resistance.

R_s and R_{sh} are parasitic resistances because they are responsible for the dissipation of the solar cell's power which reduces its efficiency. For a perfect solar cell, R_{sh} needs to be infinite and must not to be the cause of a short current in the circuit and R_s needs to be null to avoid the voltage drop before the load **[177]**.

The I-V measurements were done in the LMOPS (Laboratoire Matériaux Optiques Photonique et Systèmes) laboratory in Metz. The CAREL platform was used as shown in **Figure 50** consisting of a measurement station with four point probes, a microscope and a CCD camera (Dimension > 10 µm). The Source/Measurement electrical unit consisted of three Keithley models 2602, 2636B and 236

with a current and voltage range of 10 fA-100 mA and 1 µV-40 V respectively. Also, Keysight impedance analyzers are included in the platform and they function with a frequency and voltage range of respectively 5 Hz-2 MHz and -35 to 35 V. Finally, a 230-1200 nm modulated photocurrent stand is also included. The acquisition and analysis software used to perform the measurements were developed by the laboratory. All this equipment is used to study the transport properties of novel semi-conductive materials by applying the following characterizations: I-V as a function of temperature, four point probe, I-V Transmission Line Method (TLM), C-V measurements with *C* being the capacity and finally admittance and photocurrent spectroscopy.

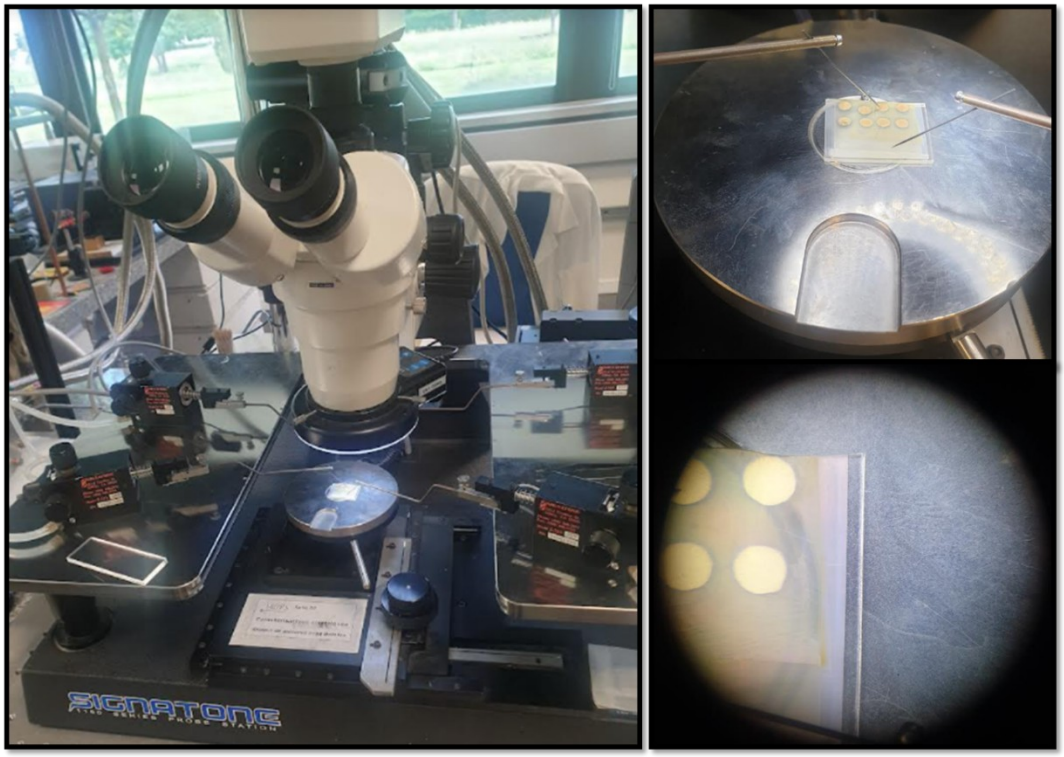

Figure 50: Photos taken at the LMOPS laboratory showing **a)** the equipment used to perform the I-V measurements on a solar cell and **b,c)** a zoom-in on the process where one probe is placed on the AZO back-contact layer (light yellow) and the other on the Au front-contact layer (gold dots).

Chapter 3

Synthesis by reactive HiPIMS and microstructure of AZO films

3.1. Introduction

In recent years, TCOs have been found to be of great interest in many research fields due to their unique optical and electrical properties as well as the possibility of scaling to large industrial surfaces. They find applications as anti-icing layers on aircraft windows, as antistatic coatings, in Light Emitting Diodes (LED)s, in optoelectronic devices, in solar cells etc. **[47,178]**. As mentioned in **Chapter 1**, among the well-known and performant TCOs are the ITO films due to their high transparency and electrical conductivity; however their components are toxic, expensive and rare, which encouraged the search for other TCO materials with similar properties but with more environmentally friendly, abundant and less expensive constituents **[3,45]**. This description fits well the AZO films adopted in the major part of this thesis. However, obtaining an optimal AZO film with simultaneously good optical and electrical properties is a challenge. For instance, aiming for high density of charge carriers (n) in order to increase the film's conductivity has repercussions on the optical transmittance since the defects at the origin of those very same carriers tend to absorb light and thus decrease the film's transparency **[178]**. Many authors have adopted the AZO films in order to improve their optical and electronic properties by various means such as trying different deposition methods (sputtering, PLD, sol-gel etc.) **[21]**. And within these different methods, they found room for more improvement by trying different substrates **[13]**, substrate heating during deposition **[44]**, changing the target-substrate distance in sputtering deposition **[179]**, trying different precursors in ALD **[180]**, and even post-deposition methods such as annealing **[181]**. All these methods were successful in improving the properties of the AZO films to a certain extent, some of them even being able to reach properties close to those ideal ITO properties.

In this work, AZO films were deposited on glass substrates by magnetron sputtering in the HiPIMS mode. Our way of optimizing the properties of the AZO films is through testing different Al at.% content in the Zn/Al alloyed targets used for the depositions; Zn/Al targets with 1, 2, 5, 10 and 15 at. % of Al were tested. For each different Al content, the deposition parameters were modified through the oxygen flow rate and the applied voltage in order to obtain the most conductive and transparent AZO film possible from each target. This detailed study is however not presented in this work, but

we were rather more interested to show the evolution of film properties with the Al content in the target by characterizing only the best AZO film obtained from each target.

In this chapter, we will study the properties related to the deposition process directly through the monitoring of the discharge current or the HiPIMS pulse for each of the Al content, as well as the thickness and deposition rate evolution. From this point on, the characterization of the AZO films will be presented. First off, we present all the results related to the chemical characterization of the AZO films starting with the EDS qualitative and semi-quantitative analysis; the first one consisted on EDS mapping in order to have an idea on the Zn, Al and O species distribution inside the AZO films while the second one consisted on extracting the atomic content of each of the previous species in the film. Next, the structure and microstructure was evaluated through XRD measurements from which we calculate the size of crystallites and the crystallinity index for films with sufficient crystallinity. To extend this further, the samples were investigated by TEM analysis in order to observe the film's structure through TEM images, SAED and FFT patterns extracted from the HR-TEM images. To conclude this chapter, we displayed some XRD measurements done on AZO films deposited from a Zn/Al target with 1 at.% of Al but by DC sputtering, in order to evaluate the difference in crystallinity when using DC sputtering or HiPIMS sputtering.

3.2. Discharge current and deposition rate

To accomplish the AZO films optimization for each Zn/Al target, we need to test different parameters in order to find the optimum pair of applied voltage and oxygen flow rate. By optimum, we mean parameters that allowed us to obtain the best compromise between the transparency and conductivity of the AZO films. Actually, it consisted on trying to reach the highest (lowest) possible conductivity (resistivity) while maintaining good transparency. This strategy was used because an optimum of conductivity is generally obtained for films that are slightly sub-stoichiometric in oxygen, i.e. still well transparent **[52,182]**. The chosen HiPIMS setups, i.e. the 100 µs pulse duration, the 10% duty cycle are based on previous works using a Zn/Al target with 2 at.% of Al in which lowest resistivity values were obtained for a discharge voltage near 475 V and a peak current close to 3A for 80 sccm Ar and 20 sccm O_2 reactive gas mixture leading to a total pressure of 1 Pa **[44,52]**. In **Figure 51**, the discharge current waveforms for all 5 best AZO films deposited from Zn/Al targets with 1, 2, 5, 10 and 15 at.% of Al are presented. To the best of our knowledge, this is the first time a reactive HiPIMS deposition from a Zn/Al 1 at. %Al target is reported. One can see from **Figure 51 a)**, that the peak current slightly increased when the Al content went from 1 to 2 at. % Al targets for the same applied voltage. For this reason, the applied voltage was adjusted to 560 V for the 1 at. %

Al target and to 555 V for the 2 at.% Al target. In **Section 4.3 of Chapter 4**, we will present a detailed study about the effect of the applied voltage on the electrical properties of the AZO films deposited by a Zn/Al target with 1 at.% of Al by measuring the respective resistivity of the films obtained by applying 560 V to 575 V with steps of 5 V. This will help understand the discharge behaviour for low Al content targets and the resulting electrical properties. Moving on to **Figure 51 b)**, we note that the applied voltage and the chosen oxygen flow rate are different for the AZO films deposited from Zn/Al targets with higher Al contents due to the instability of the discharge at higher voltages and oxygen flow rates, yielding very high and unstable peak currents. Those parameters were 450 V of applied voltage and 10 sccm of oxygen flow rate (**Table 1**). One can see that the pulse current gradually increases with the Al content, but also the discharge current waveform changes from a flat pulse to a more peaked pulse.

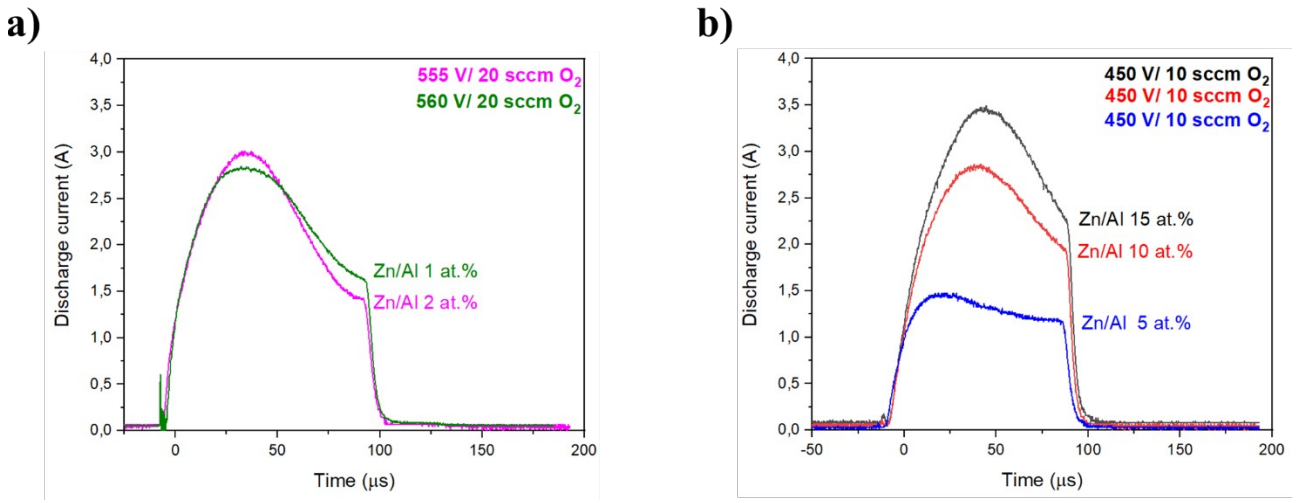

Figure 51: Discharge current waveforms for the AZO films deposited by HiPIMS from five Zn/Al targets: **a)** Zn/Al 1 and 2 at.% Al and **b)** Zn/Al 5, 10 and 15 at.% Al. The applied voltage and the flow of O_2 gas used for each film are mentioned in the top right corner of the graphs.

This change in pulse form has been linked to the greater compression and subsequent gas rarefaction when the peak current increases **[183]**. The gas rarefaction results from gas heating leading to the decrease in gas density, and also from the sputter wind effect where a momentum is transferred from the sputtered atoms to the gas atoms due to the high density of sputtered atoms in HiPIMS **[44,123]**. Yet, the origin of the higher current upon increasing the Al content needs to be interpreted. Several effects can be at the origin of this observation. First of all, one must consider that the Gibbs enthalpies of formation in normal conditions ($\Delta G°$) of Al_2O_3 and ZnO are respectively ≈ - 1050 and ≈ - 600 kJ/mol of O_2, which makes Al much more reactive towards oxygen than Zn. Hence, by increasing the Al content in a target, we are encouraging its surface oxidation. The latter is what can

trigger the transition of film deposition from a metallic mode to compound mode characteristic of target poisoning.

As can be seen from the supplementary material of ref. **[184]**, during reactive HiPIMS of AZO from a zinc target containing 3 at.% Al, the plasma impedance decreases much faster than during DC sputtering. Several mechanisms can explain this behaviour. Aiempanakit et al. **[185]** found that when a target is poisoned when using HiPIMS, O atoms are sputtered from the oxidized target surface and ionized into O^+ then they strongly contribute to the ion current and to the increase in the secondary electron emission yield; A.N. Reed et al. **[186]** not only detected O^+ ions, but also O^{2+} and O_2^{2+} ions in abundance during their ZnO film deposition from a ZnO target in reactive HiPIMS mode with a 50 µs pulse duration and under a similar discharge currents than the ones observed in our study. These species may be present in reactive sputtering from a poisoned metallic target as well and contribute to the discharge current. Interestingly, energetic electrons are usually found at the beginning of HiPIMS pulses **[187]**. Moreover, Corbella et al. **[188]** found that a beam of energetic Auger electrons is emitted from the surface of oxidized aluminium target upon Ar^+ ions sputtering, which is also possibly the case of Zn/Al targets, especially those with high Al at.%. Both these electrons' type are expected to facilitate the dissociation then ionization of O_2 and the ionization of sputtered oxygen. While the electron emission yield is found to either increase or decrease during transition to the oxide mode in reactive DC sputtering, it is always increased in reactive HiPIMS due to the formation of the O^+ ions **[187-189]**. So the observed increase of the peak current with the Al content is primarily attributable to ionized sputtered oxygen atoms and possibly easier dissociation and ionization of the O_2 molecules. The formation of these different ionized oxygen species can be eased by increased electron emission from the target surface upon oxidation of the target surface.

To further understand the influence of the target Al content on the sputtering process, we plotted the thickness (**Figure 52 a)**), the deposition rate (**Figure 52 b)**) and the deposition rate normalized by the average discharge power (**Figure 52 c)**) as a function of the position to the substrate holder axis. The average discharge power was calculated from the pulse shape, applied discharge voltage and duty cycle. The lateral inhomogeneity of the curves finds its origins in the dynamics of the substrate-holder, the spatial distribution of sputtered particles and their transport towards the substrate. Similarly to the pulse shape, one can see that all three graphs show two groups of curves: a first one for the films deposited from targets with higher Al contents (5, 10 and 15 at. %), and a second one with much higher deposition rates for the films deposited using targets of lower Al contents (1 and 2 at.%). This is interesting because when referring back to the pulse shapes in **Figure 51**, one can see that the AZO films deposited from Zn/Al targets with 1, 2, 10 and 15 at. % Al have close peak

currents, but the deposition rate is found to be doubled for films deposited using targets of 1 and 2 at. % Al compared to 10 and 15 at.% Al. Nevertheless, in order to limit the influence of a change in applied voltage and discharge power in the interpretation of the data, we also plotted the deposition rate normalized by the average discharge power for all five AZO films in **Figure 52 c)** to enhance this analysis and comparison. Still, the AZO films deposited from lower Al contents targets present a much higher normalized deposition rate and the deposition rate is found all the more higher than the Al content in the target is lower.

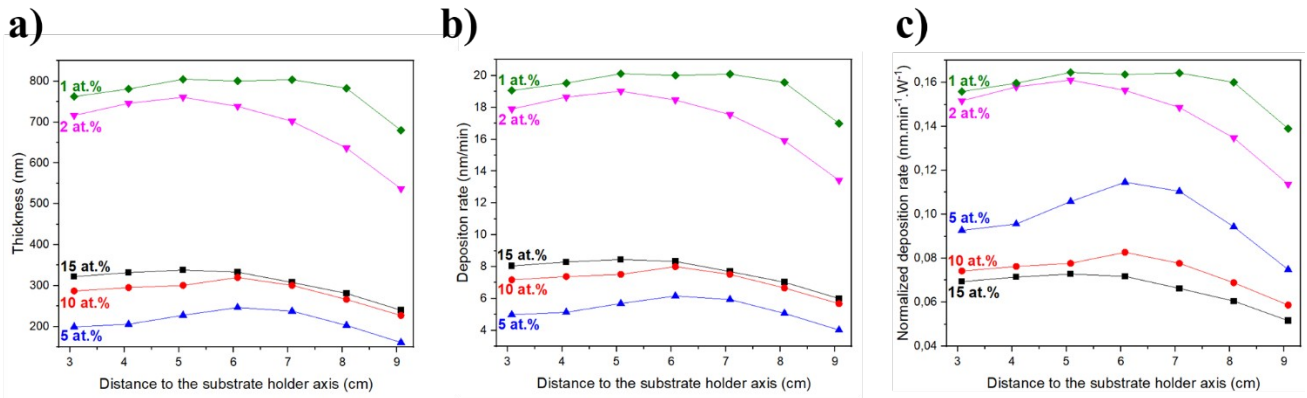

Figure 52: a) Thickness (nm), **b)** Deposition rate (nm/min) and **c)** Normalized deposition rate ($nm.min^{-1}.W^{-1}$) as a function of the distance to the substrate holder axis (cm) for the AZO films obtained from the Zn/Al targets with 1, 2, 5, 10 and 15 at.% of Al respectively.

We can try to explain this by referring to the work of O. Kappertz **[190]** who studied via TRIM simulations the evolution of the sputter yield with the discharge voltage when the Zn target was in a metallic or compound mode while considering different projectiles. In the range of applied voltages employed in his study, he found after the metallic mode to the compound mode transition a major drop of nearly 3 fold of the sputter yield. This reinforces the established hypothesis from the pulse shape evolution, that increasing the Al content in Zn/Al targets can further and help maintain the target surface oxidation. This explains why the normalized deposition rate decreased gradually with the decrease of the Al content used in the target since, as already hypothesized, the increase in Al content may favour target oxidation. From these observations, we can already expect a major impact on the structural properties studied in the following section, as well as on the electrical and optical properties considered in **Chapter 4**, all known to be sensitive to the oxygen content.

3.3. Chemical composition analysis

From this point forward, a measurement done at the position corresponding to 3 cm from the substrate-holder axis will be labelled "*off-axis*" or "*low ρ*". This means that this position is far from the circumference on the substrate-holder that faces the target axis and, as will be shown in **Section 4.3.1 of Chapter 4**, produces films of low electrical resistivity. In contrast, the position at 7 or 8 cm from the substrate-holder axis will be labelled "*in-axis*" or "*high ρ*" as it is on, or close to, the circumference on the substrate-holder that faces the target axis and leads to films of highest electrical resistivity.

To start the chemical composition analysis, we present in **Figure 53** a STEM image for each of the AZO films deposited from a Zn/Al target with 1, 2, 5, 10 and 15 at.% Al in both the *in-axis* (**Figure 53 (Top)**) and *off-axis* (**Figure 53 (Bottom)**) positions, with their corresponding EDS mapping performed with TEM. The STEM images evidence a columnar growth for films grown from 1, 2 and 5 at.% Al targets but the films deposited from 10 and 15 at.% Al targets do not exhibit evidence of columnar growth. The distribution of Zn, O and Al is colored in green, purple and yellow, respectively. We note that for the AZO film deposited from the 2 at.% Al target, there is a second layer of ZnO that was deposited for future analysis. One can see a rather even distribution of all three species accross the entire section of the AZO films and, occasionally, in the glass substrate as well as in the platinum layer used for the extraction of the FIB lamellae for the TEM analysis; the EDS mapping of the Si-K and Pt-M are shown in the **Figure A1** of the **Appendices**. The fact is that the platinum metal used for this extraction is not pure but mixed with some metals such as Al, and the borosilicate glass other than obviously containing lots of oxygen atoms, presents some metal impurities such as Al. When looking at the intensity of the Al distribution in the films, it is clear that it gradually increases with the Al content present in the Zn/Al target used for the corresponding deposition of the AZO film. These observations are the same for both the *in-axis* and *off-axis* positions. In order to gain more quantitative information on the films composition, semi-quantitative EDS analysis was conducted on the AZO films and is presented below.

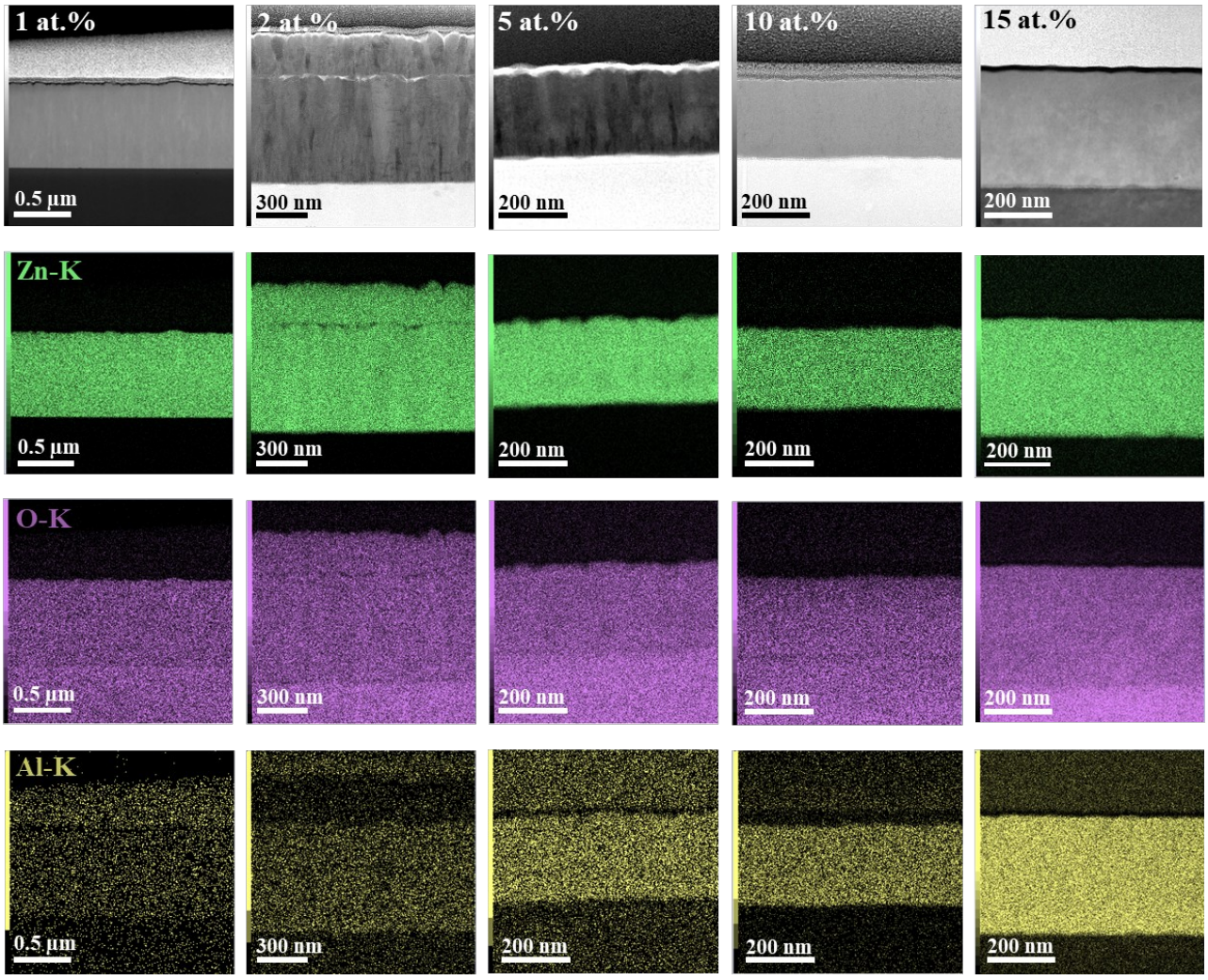
1 at.%
2 at.%
5 at.%
10 at.%
15 at.%
0.5 µm
300 nm
200 nm
200 nm
200 nm
Zn-K
0.5 µm
300 nm
200 nm
200 nm
200 nm
O-K
0.5 µm
300 nm
200 nm
200 nm
200 nm
Al-K
0.5 µm
300 nm
200 nm
200 nm
200 nm

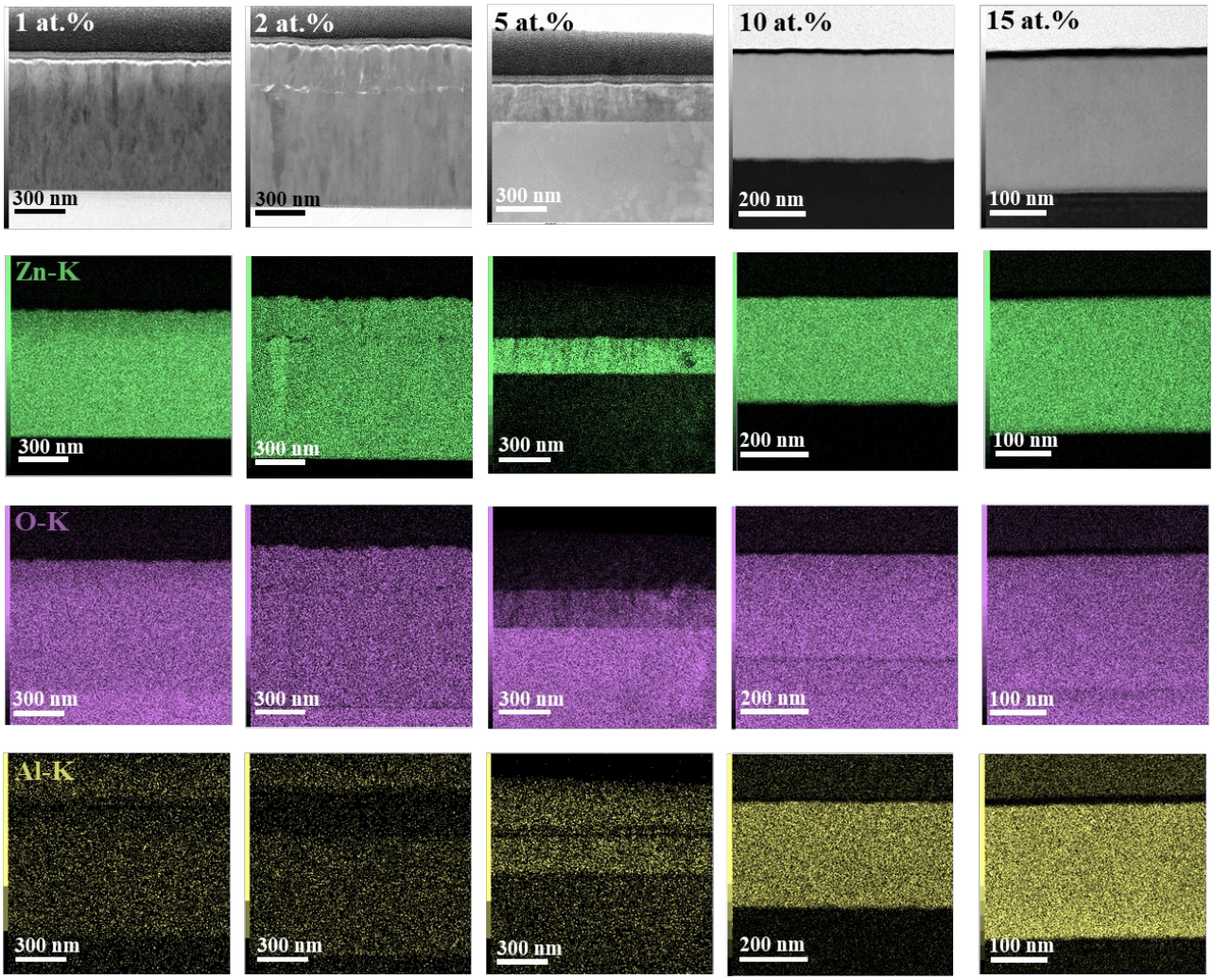

Figure 53: STEM images in the *in-axis* **(Top)** and *off-axis* **(Bottom)** positions of the AZO films deposited from a Zn/Al target with 1, 2, 5, 10 and 15 at.% of Al respectively and their corresponding EDS mapping of the Zn (green), O (purple) and Al (yellow) compositions.

In **Table 3**, the atomic concentrations of the Zn, O and Al species for each of the five AZO films deposited from a Zn/Al target with 1, 2, 5, 10 and 15 at.% Al in both the *in-axis* and *off-axis* positions are summarized. It is verified that the Al content inside the film increases with that of the target used for the deposition. Looking at the Al/(Al+Zn) ratio, we can note that, for both positions, the Al content actually incorporated in the AZO films is rather close to the Al content in the target for targets containing 1, 2 and 5 at.% Al but is significantly higher than that of the target in the films deposited from targets containing 10 and 15 at.% Al. This can be the sign of a preferential resputtering of Zn from films containing higher amounts of aluminum and possible strengthening of the bonding involving Al atoms (e.g. Al-O bonds). In **Chapter 5** will be presented results verifying the change in the atomic bonding of Al.

Due to the lack of precision and reproducibility on the oxygen content measured by EDS and the fact that studying the sensitivity of electrical and optical properties to the oxygen content would require a precision in the order of 0.1 at.% Al, we do not consider the oxygen content measured by EDS as a relevant way to detect eventual oxygen sub- or over-stoichiometry.

Table 3: EDS composition analysis of the Zn, O and Al contents in the AZO films deposited from a Zn/Al target with 1, 2, 5, 10 and 15 at.% of Al in the *in-axis* and *off-axis* positions. The "P" and "E" abbreviations stand for position and element concentration (at.%) respectively.

Film	AZO 1 at.%		AZO 2 at.%		AZO 5 at.%		AZO 10 at.%		AZO 15 at.%	
P / E	In-axis	Off-axis	In-axis	Off-axis	In-axis	Off-axis	In-axis	Off-axis	In-axis	Off-axis
Zn	51.91	46.46	51.79	45.79	46.35	52.55	38.71	39.18	37.42	38.85
O	47.54	52.86	47.29	53.24	50.74	45.51	55.05	53.78	47.87	47.84
Al	0.56	0.68	0.93	0.97	2.91	1.95	6.24	7.04	14.71	12.09
$\frac{Al}{(Al+Zn)}$	1.07	1.44	1.76	2.07	5.91	3.58	13.88	15.23	28.22	23.73

In **Figure 54** are presented the results of the concentration profiles of the Zn, O and Al species for all AZO films by showing a STEM image with the points on which the analysis was done and the evolutions of the Zn, O and Al species at the positions chosen. From a general look on the EDS mapping results for the columnar grown AZO films both in the *in-axis* and *off-axis* positions, one can detect an evident change of composition between columns. It is interesting to note that even for the non-columnar films, i.e. the AZO films deposited from a 10 and 15 at.% Al target, the evolution of all three species varies.

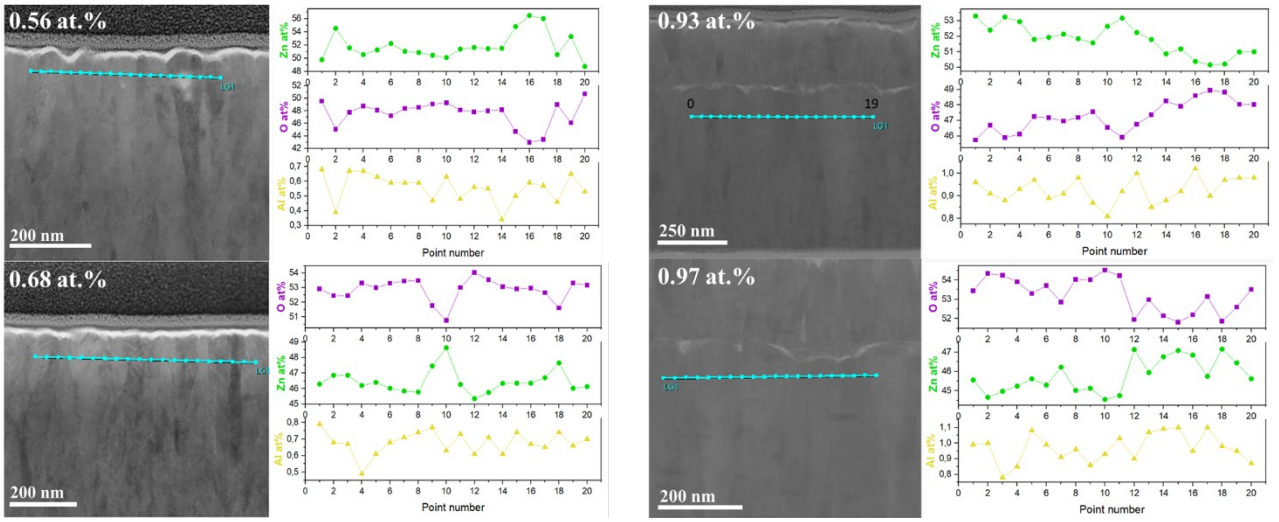

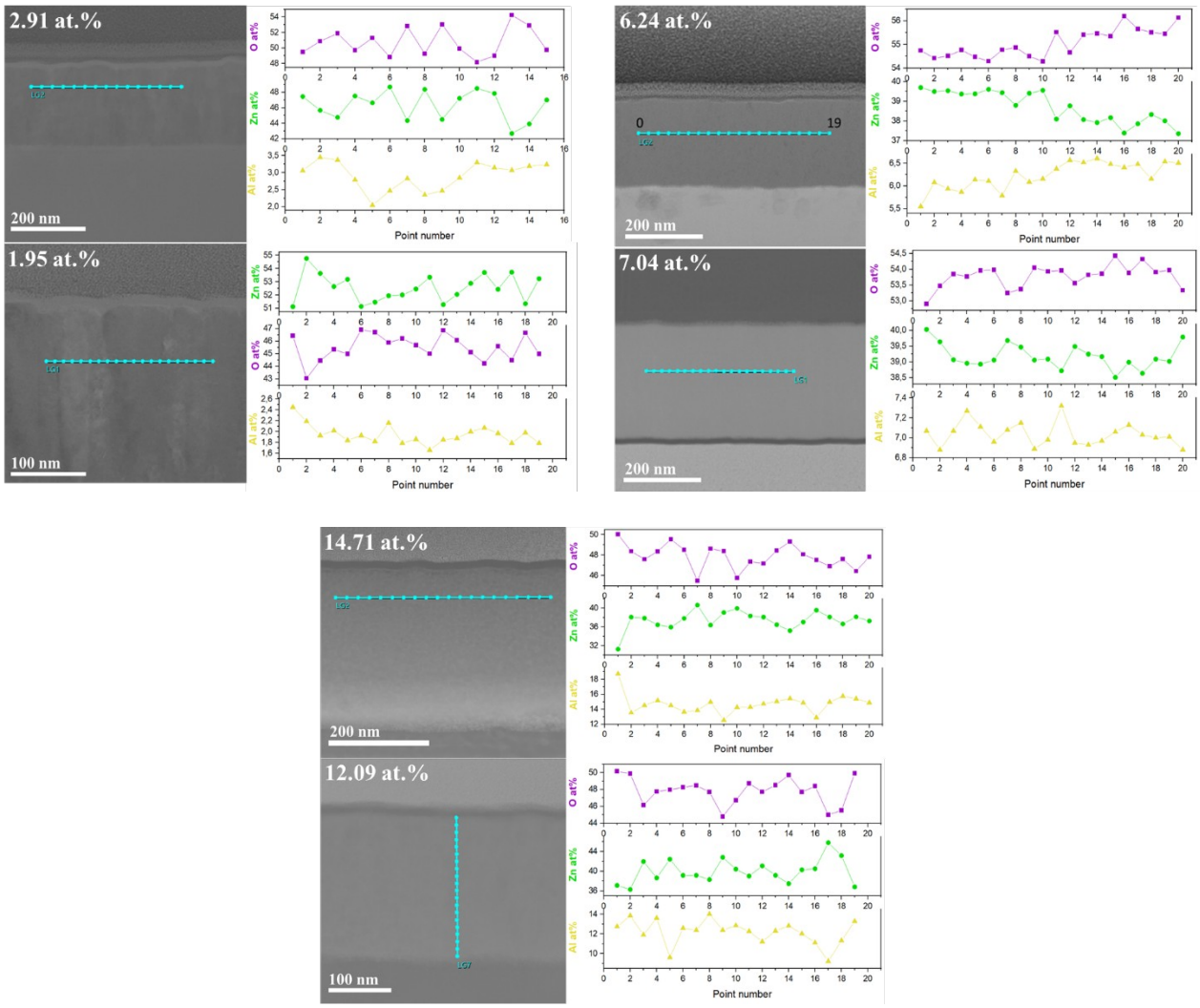

Figure 54: STEM image and the corresponding Zn, O and Al atomic concentration profiles measured by EDS for the AZO film containing 0.56/0.68 at.% of Al deposited from a Zn/Al 1 at.% target, 0.93/0.97 at.% of Al deposited from a Zn/Al 2 at.% target, 2.91/1.95 at.% of Al deposited from a Zn/Al 5 at.% target, 6.24/7.04 at. % of Al deposited from a Zn/Al 10 at.% target and 14.71/12.09 at.% of Al deposited from a Zn/Al 15 at.% target with the at.% values representing the real Al at.% in the AZO films *in-axis*/*off-axis* positions.

M. Mickan et al. **[52]** measured with a smaller step size by EDS the oxygen concentration profile of an AZO film deposited by HiPIMS at a position of 8 cm from the substrate holder axis, the result is shown in **Figure 55**. One can see an obvious oxygen fluctuation, as in our case, but with an easily-determined higher localization at the interface of the crystalline domains. They attributed this to the incorporation of molecular oxygen at the grain boundary. Despite the fact that the overall composition measured by Rutherford backscattering was equivalent to overall over-stoichiometric films, inside all the grains, the oxygen concentration was approximately 48 at.%, which corresponds to a sub-stoichiometric ZnO. This is an important fact because oxygen sub-stoichiometry plays a

major role in the intrinsic doping of ZnO. This also highlights that overall EDS measurements are not sufficient in order to draw a conclusion on the actual O/Zn ratio in ZnO grains in ZnO or AZO polycrystalline films.

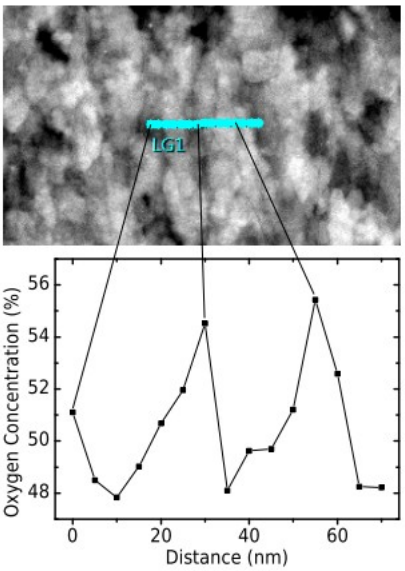

Figure 55: Image extracted from **[52]** representing a TEM image and its corresponding oxygen concentration profile measured by EDS for an AZO film deposited by HiPIMS at 8 cm from the substrate holder axis.

3.4. Structural and microstructural analysis

In this part, we show the results obtained from the XRD and the TEM measurements and analysis in order to study the influence of Al content in the target and substrate position on the structure and microstructure of the AZO films.

AZO films employed as transparent electrodes in solar cells tend to contain 0.5-3 at.% of Al, this is why most works on the evolution of properties of the AZO films deposited by reactive sputtering with the Al content did not go beyond 3 at.% of Al **[4,44]**. In general, the AZO films deposited by magnetron sputtering present the hexagonal wurtzite structure of ZnO with a strong preferential growth, or occasionally a fibre texture, with the *c*-axis direction aligned with the film growth direction **[4,52]**. Additionally, other orientations of the ZnO wurtzite structure have been detected in the case of sub-stoichiometric films **[52,118]**. However, only some researchers **[191,192]** deposited AZO films from Zn/Al targets with larger Al contents in order to study the evolution of the films properties with the Al content and even none of those studies employed reactive HiPIMS as a deposition technique. Even though M. Vinnichenko et al. **[4]** studied the structural and electronic structure modification of the AZO films for Al contents of up to 19 at.%, a substrate temperature change was used to adjust the film composition. They did not observe in their XRD diffractograms

any signals assigned to Al_2O_3 or $ZnAl_2O_4$, which supports the hypothesis that the supersaturation of Al in ZnO is encouraged when out of stable equilibrium deposition techniques such as magnetron sputtering are used. Nonetheless, analysis of their electronic structure data for AZO films using XANES at the O-K, Al-K and Zn-L_3 edges detected local structure modifications that were assigned to the presence of the $(ZnO)_3Al_2O_3$ homologous metastable phase in their AZO films. Also previous investigations done in our research group on AZO films deposited by DC sputtering with Al contents as low as 2-3 at.% indicated the possible formation of a homologous phase responsible for the deactivation of the Al dopant and for the inhomogeneity of the films resistivity as a function of their position **[7,193]**. However such sign of phase transformation was not observed, at least for low Al content AZO films, when reactive HiPIMS is adopted as the deposition method **[3]**. J.G. Lu et al. **[192]** stated from XRD data that the solubility limit of the Al dopant in the ZnO structure is 20-30 at. % when magnetron sputtering is used. Already at 10 at.% of Al, their XRD diffractograms exhibited crystallinity degradation and the diffraction signal of Al_2O_3 appeared upon reaching 30 at.% Al. Still and all, we extended our structure analysis to an electronic structure one by means of ELNES in **Chapter 5** because the XRD method is not reliable on detecting changes in the local structure of the AZO films; that and an observed homologous peak is in reality very similar to that of the wurtzite ZnO and it is not possible to confirm the presence of a homologous phase with results solely based on XRD measurements.

In **Figure 56**, we present the XRD diffractograms of the AZO films deposited from the Zn/Al targets with different Al contents in the *in-axis* and *off-axis* positions with the diffracted intensity being normalized by the films thickness. For each position, the crystallinity gradually degrades when the Al content increases and the AZO films produced using the 15 at.% Al target are amorphous or ultrafine-grained nanocrystalline. While the AZO deposited from 1 and 2 at.% Al targets exhibit a fine intense (002) peak, the crystallinity degradation is presented by the less intense and broader becoming of the (002) peak when moving gradually to the AZO films deposited from 5 at.% then 10 at.% Al targets. Other than the AZO films deposited from the 15 at.% Al target, the XRD diffractogram corresponds to the hexagonal wurtzite structure of ZnO with the (002) peak being the distinctive peak or the main orientation of this type of film. This peak is intense and fine for the low Al content films (from 1 and 2 at.% Al targets) then tends to become less intense and broader for the higher Al content films (from 5 and 10 at.% Al targets). Additionally, multiple orientations appear in the lower Al content films (from 1, 2 and 5 at.% Al targets) and they have been linked by previous authors to oxygen sub-stoichiometry **[52,193]**. One must also note the better crystallinity of the AZO films in the *off-axis* position majorly noticeable for the AZO films deposited from 5 and 10 at.% Al

targets due to the more intense (002) peak; as well as the appearance of more multiple orientations in the *in-axis* position for the AZO films deposited from the 5 at.% Al target. Finally, we mention that despite the wide range of Al contents explored in this study, no characteristic peak of the $ZnAl_2O_4$ was detected, which is a positive sign of the successful incorporation of the Al dopant into the wurtzite lattice of ZnO.

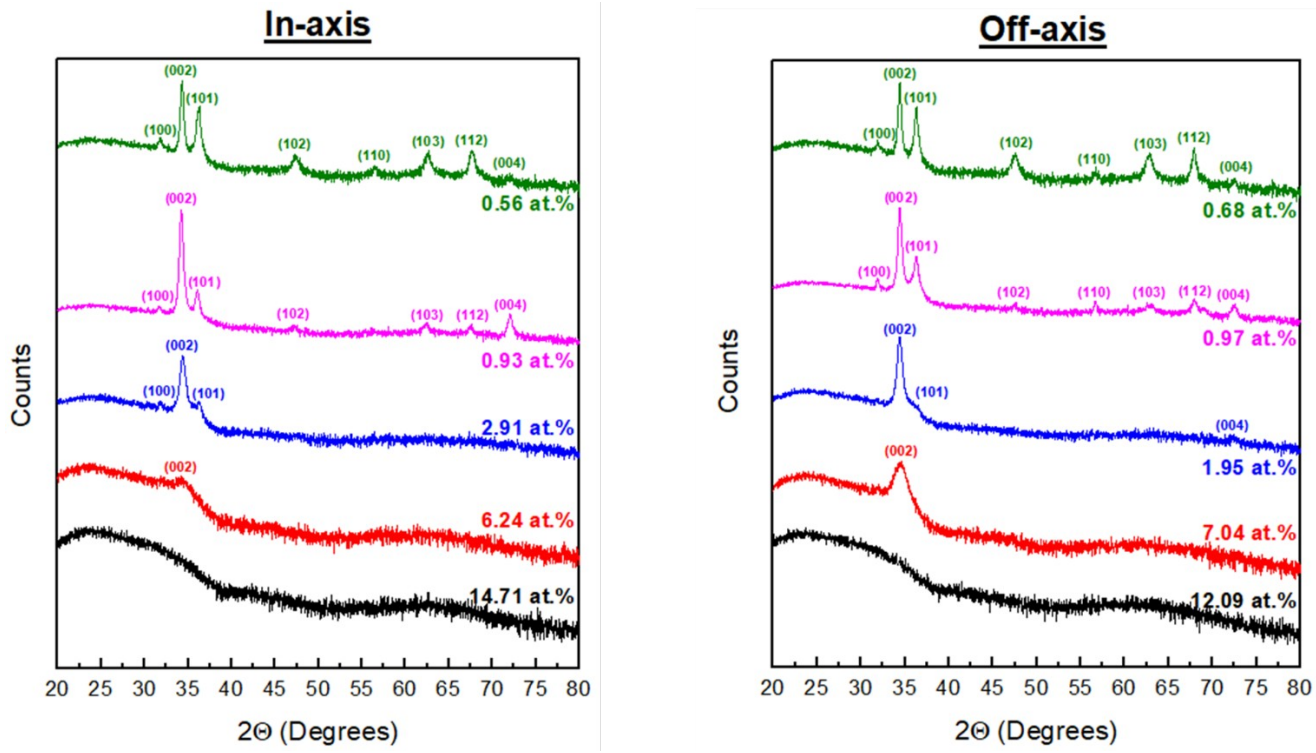

Figure 56: XRD measurements normalized by the thickness of the AZO films containing 0.56/0.68 at.% of Al deposited from a Zn/Al 1 at.% Al target, 0.93/0.97 at.% of Al deposited from a Zn/Al 2 at.% Al target, 2.91/1.95 at.% of Al deposited from a Zn/Al 5 at.% Al target, 6.24/7.04 at.% of Al deposited from a Zn/Al 10 at.% Al target and 14.71/12.09 at.% of Al deposited from a Zn/Al 15 at.% Al target with the at.% values representing the real Al at.% in the AZO films *in-axis*/*off-axis* positions. The indicated contents represent the actual Al content in the AZO films as measured by EDS.

From the XRD data, we extracted the average size of crystallites for the AZO films with Al contents up to 10 at.% and plotted them in **Figure 57** as a function of the distance from the substrate-holder axis. The crystallite size of the AZO film deposited from the 10 at.% Al target is presented in a dashed line to represent the uncertainty of the values due to the low intensity of the (002) peak from which the calculation was done. One can see that the crystallite size decreases when the Al content increases, which means that the increased introduction of Al dopants into the ZnO structure inhibits the crystalline growth. Some authors consider that for high dopant concentrations, the atoms tend to locate in or next to the grain boundaries, which is responsible for the films' crystalline quality

deterioration **[194]**. Additionally, mechanical stress also plays a role in the crystallite size decrease due to the difference of the ion sizes of Zn and Al ($r_{Zn^{2+}}$ = 0.074 nm and $r_{Al^{2+}}$ = 0.054 nm) **[195]**. This is consistent with our XRD data since the crystalline quality of the films is deteriorated when the Al content is increased. Yet, the crystallite sizes of the AZO films deposited from the 1 at.% Al target are lower than those measured for the films deposited from the 2 at.% Al target. .

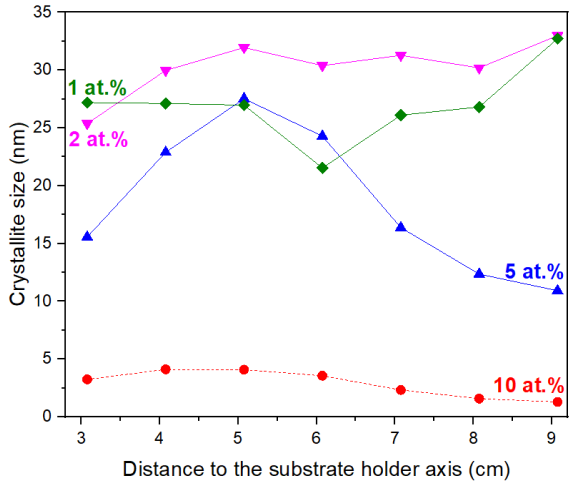

Figure 57: Average size of crystallites (nm) as a function of the distance to the substrate-holder axis (cm) for the AZO films deposited from a Zn/Al target with 1, 2, 5 and 10 at.% of Al.

Also from the XRD data and specifically from the (100), (002) and (101) peaks, we calculated the crystallinity index presented in **Table 4** for only the AZO films deposited from1, 2 and 5 at.% of Al since they are the most crystallized films. The results for the film deposited from 10 at.% Al target were not reliable, so they were not included in this table. One can see a global decrease of the crystallinity index when the Al content increased, which is consistent with the XRD data and the average size of crystallies analysis. The inconsistency between the values in the *in-axis* and *off-axis* positions is simply due to the presence/absence and intensity of all three peaks.

Table 4: Crystallinity index (%) for the AZO films deposited from a Zn/Al target with 1, 2 and 5 at.% in the *in-axis* and *off-axis* positions.

Target composition (at.%)	Film composition (at.%)	Crystallinity index (%)
	In-axis/Off-axis	
Zn/Al 1 at.%	0.56/0.68	93.44/92.13
Zn/Al 2 at.%	0.93/0.97	86.07/91.08
Zn/Al 5 at.%	2.91/1.95	88.77/80.09
Zn/Al 10 at.%	6.24/7.04	≈ 7.8/24.4

To further study the microstructure, all AZO films were subjected to TEM analysis. **Figures 58 to 62** shows a panel of four images for each film and position with the panel comprised of a TEM image, an indexed SAED pattern, an HR-TEM image and its corresponding indexed FFT pattern. Additionally to the *in-axis* position data and for space reason, we provide the *off-axis* data only for the AZO films deposited from the 1, 2 and 5 at.% Al targets because for the rest of the AZO films the results at both positions are not much different and are available in the **Appendices** (**Figures A2 and A3**). Looking at the Selected Area Electron Diffraction (SAED) images, one can see that it is consistent with the XRD data:

- For the AZO films deposited from 2 and 10 at.% of Al at both the *in-axis* and *off-axis* positions, the diffraction spots assigned to the (002) plane are most intense indicating a strong preferential orientation along the *c*-axis. The same is observed for the AZO film deposited from the 5 at.% Al target only in the *off-axis* position.
- For the AZO film deposited from the 1 at.% Al target at both the *in-axis* and *off-axis* positions, the SAED pattern shows a group of diffraction spots associated to the (002) plane but distributed around the growth direction. This indicates the absence of the aforementioned strong preferential orientation in these films. The same is observed for the AZO film deposited from the 5 at.% Al target but only in the *in-axis* position.
- From the panels of the films deposited from the 10 and 15 at.% Al targets, we can conclude that the films are nanocrystalline with a crystallite size of ≈ 5 nm despite the very weak or amorphous signal seen in **Figure 56**. Not only that, but the FFT patterns show some planes attributed to the wurtzite structure of ZnO. We can then conclude that in our study, even for the high Al contents, the incorporated Al in ZnO can still maintain the crystalline wurtzite structure of ZnO.
- For all AZO films at both positions, only the diffraction signal of wurtzite ZnO was observed.
- We can also see that the growth mode evolves with the Al content. Up to 5 at.% Al in the target, the AZO films have a typical columnar growth of ZnO or AZO deposited by sputtering with a larger

column width in the *in-axis* position. This could be explained by the difference in bombardment intensity by fast particles that more or less stimulate the surface mobility of the adatoms. We will elaborate more on this in **Section 4.3.1 of Chapter 4** when presenting the influence of substrate position on the electrical properties. For the AZO films deposited from 10 and 15 at.% Al target, no columnar growth is observed.

This evolution of structure and microstructure can be explained by different mechanisms. First off, it was concluded from DFT calculations **[196,197]** and later experimentally confirmed **[198,199]** that when the ZnO thickness is of a few atomic layers, the material will grow in a graphite-like layer structure where the O and Zn atoms are present in the same plane. This structure is the precursor of the *c*-axis oriented wurtzite ZnO because such transition requires less energy to occur than transitions to other orientations **[196]**. Therefore, we propose that the common ZnO growth in a wurtzite structure with a preferred *c*-axis orientation could be initiated by this graphite-like structure. However, as previously discussed, oxygen sub-stoichiometry was related in the literature to more randomly-oriented films. This could be explained by the fact that the formation of the graphitic ZnO may be hindered by the presence of a dopant, non-stoichiometry or even mechanical stress **[200,201]**. This tends to indicate that our films presenting multiple orientation in the XRD signal are sub-stoichiometric.

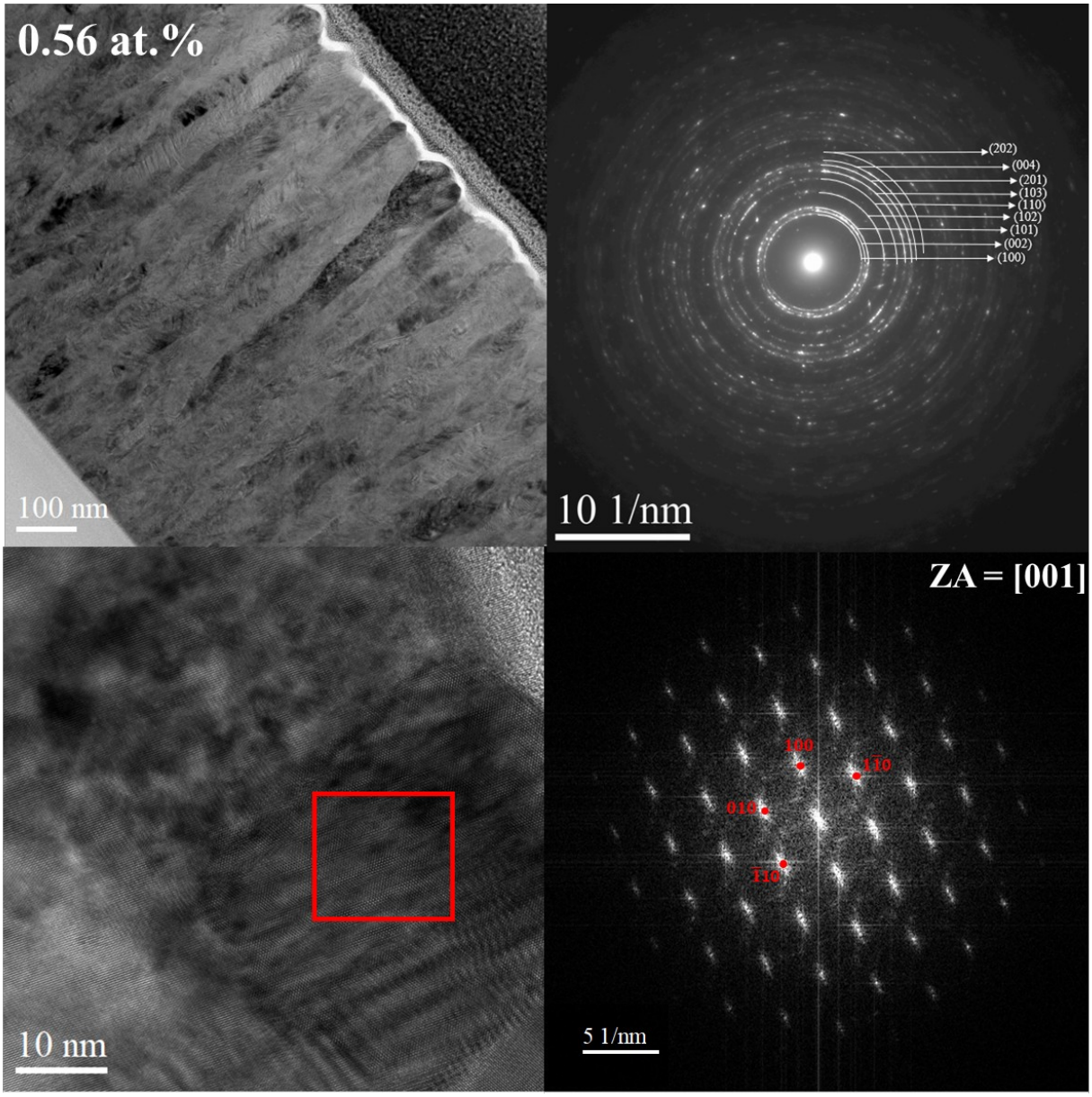
0.56 at.%
100 nm
(202)
(004)
(201)
(103)
(110)
(102)
(101)
(002)
(100)
10 1/nm
10 nm
ZA = [001]
100
1$\bar{1}$0
01$\bar{1}$
$\bar{1}$1$\bar{0}$
5 1/nm

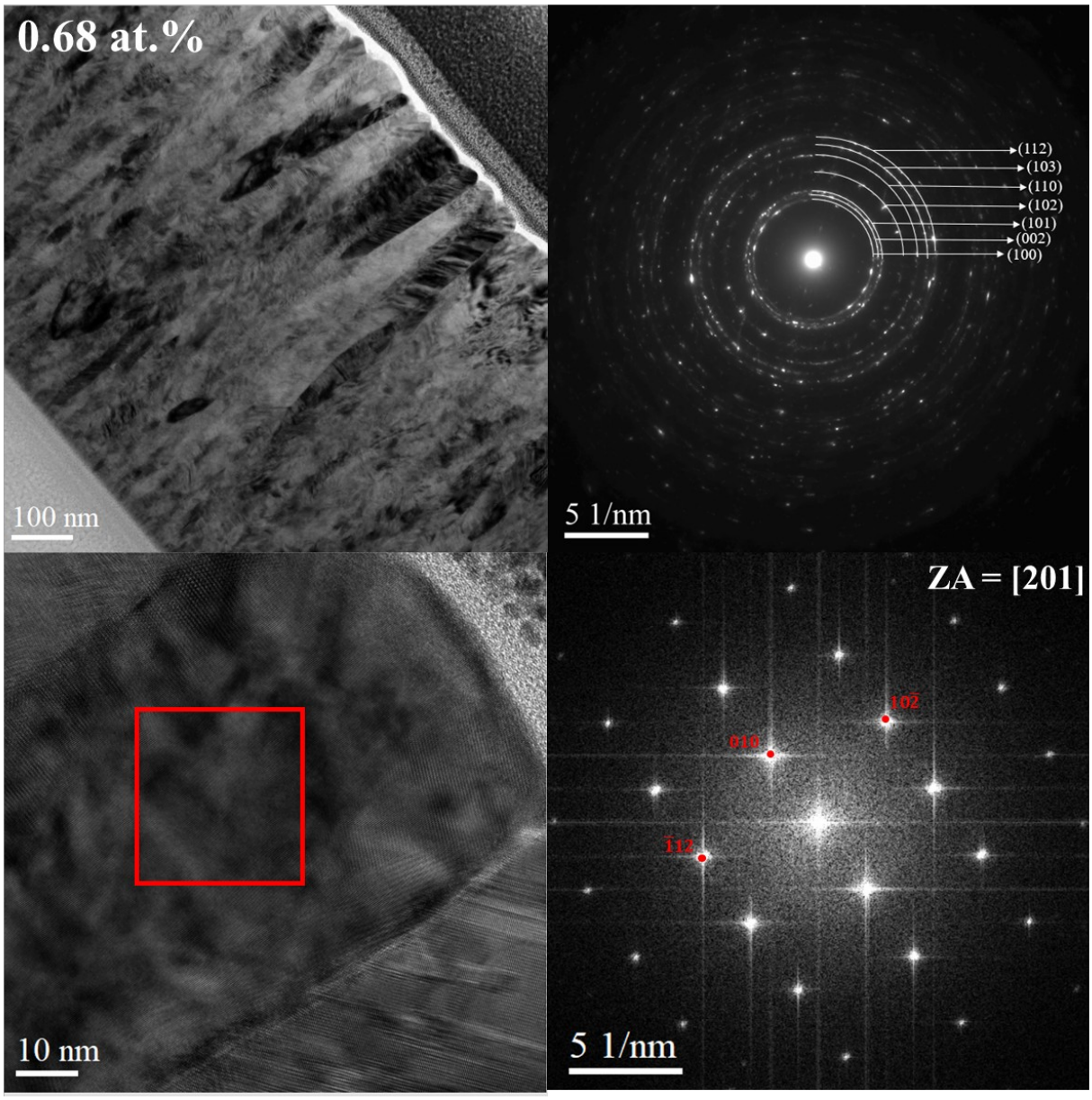

Figure 58: Panels of the main results obtained by TEM measurements including a TEM image, a SAED, a HR-TEM image and its indexed FFT for the AZO film containing 0.56/0.68 at.% of Al deposited from a Zn/Al 1 at.% Al target with the indicated concentration representing the measured Al content (at.%) in the AZO films *in-axis*/*off-axis* positions. ZA stands for Zone Axis.

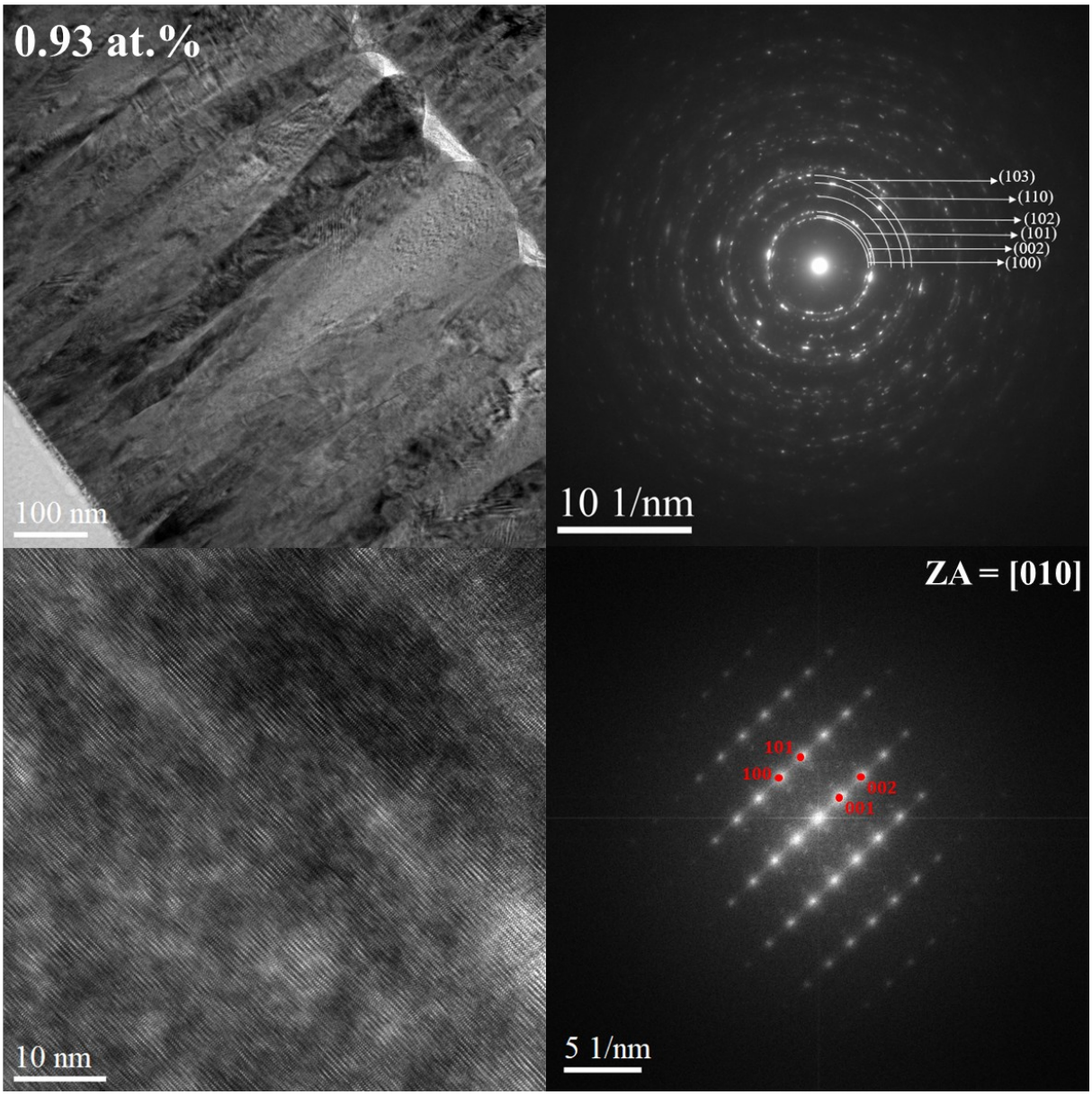
0.93 at.%
100 nm
(103)
(110)
(102)
(101)
(002)
(100)
10 1/nm
10 nm
ZA = [010]
101
100
002
001
5 1/nm

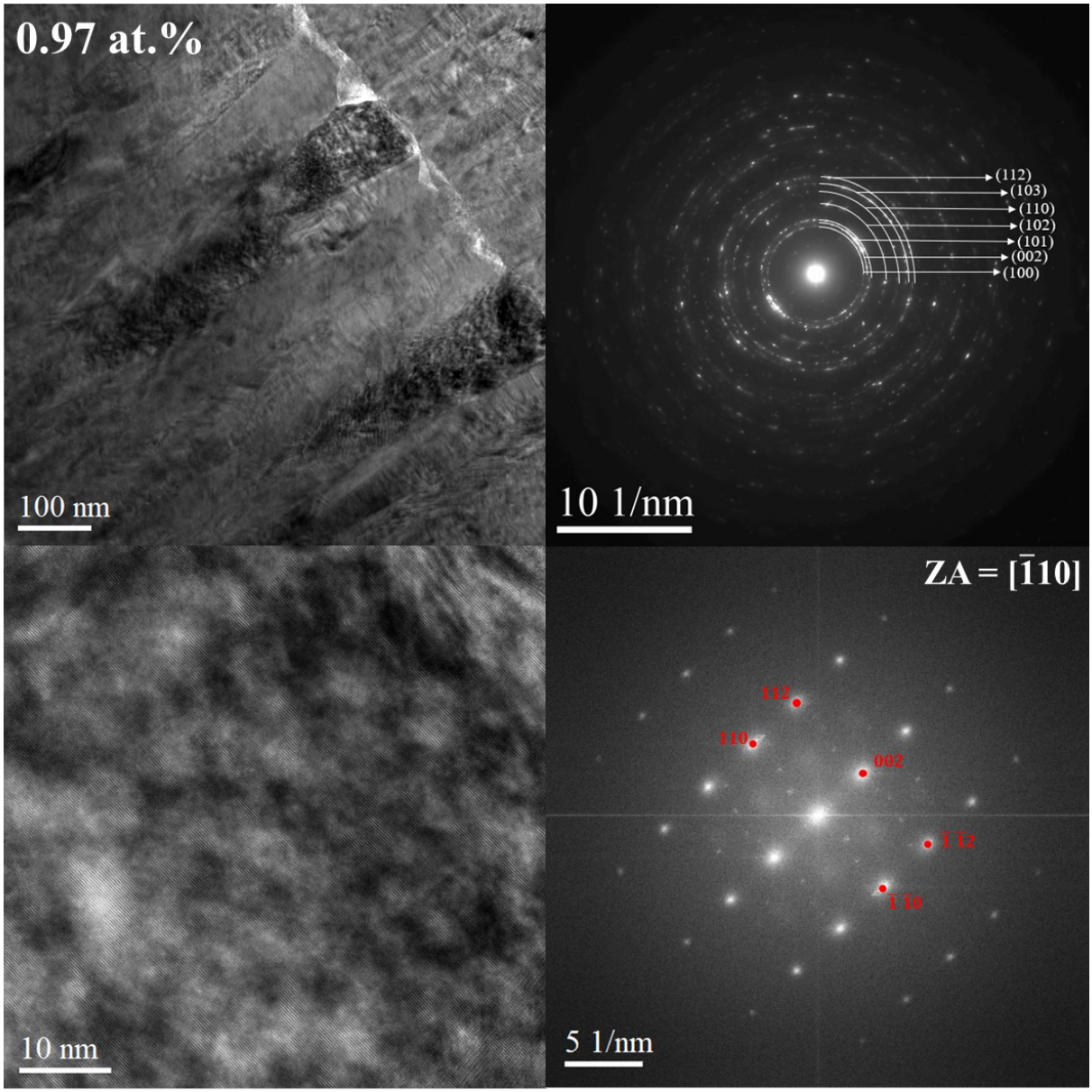

Figure 59: Panels of the main results obtained by TEM measurements including a TEM image, a SAED, a HR-TEM image and its indexed FFT for the AZO film containing 0.93/0.97 at.% of Al deposited from a Zn/Al 2 at.% target with the indicated content representing the measured Al concentration (at.%) in the AZO films *in-axis*/*off-axis* positions. ZA stands for Zone Axis.

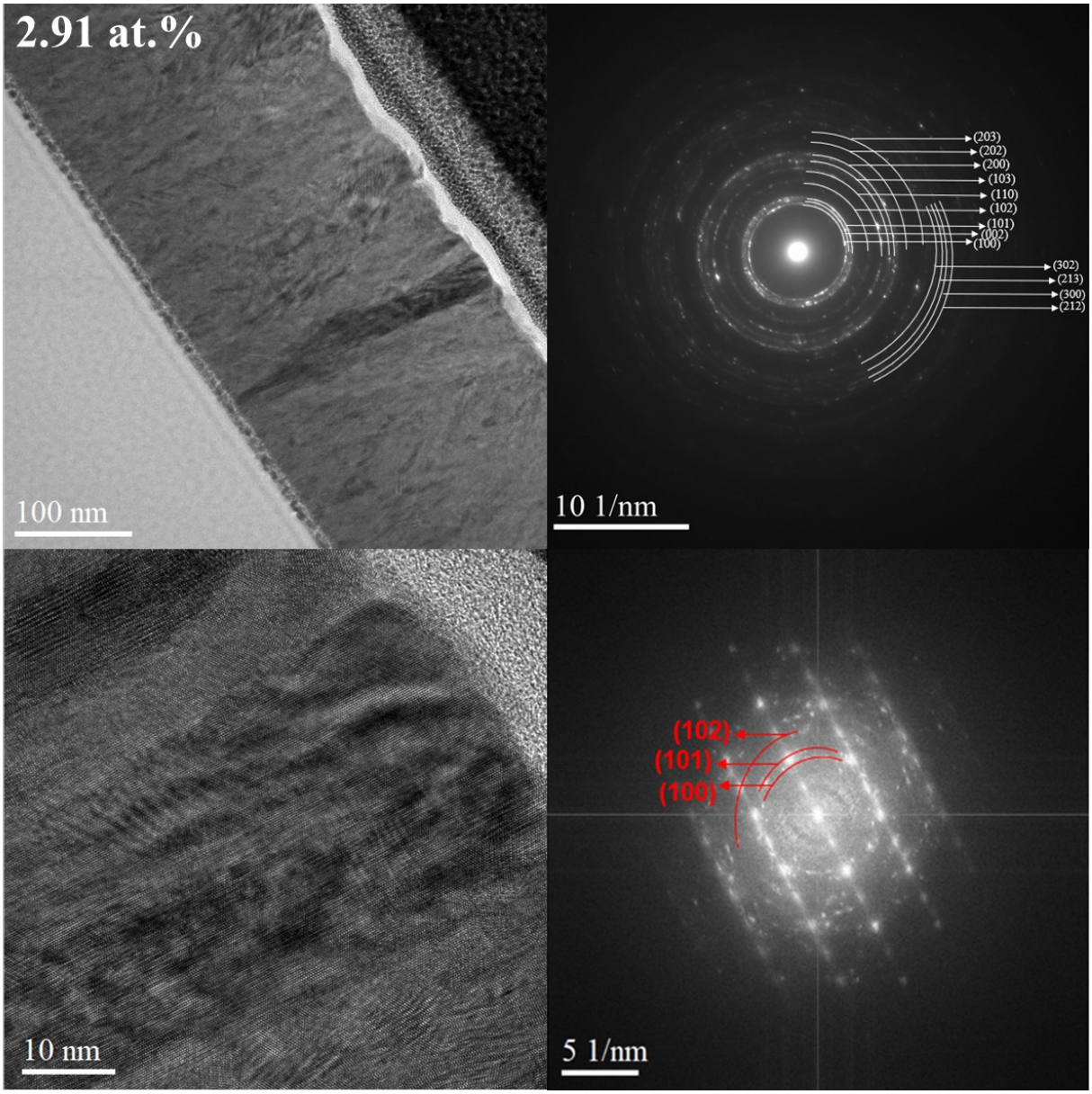
2.91 at.%
100 nm
(203)
(202)
(200)
(103)
(110)
(102)
(101)
(002)
(100)
(302)
(213)
(300)
(212)
10 1/nm
10 nm
(102)
(101)
(100)
5 1/nm

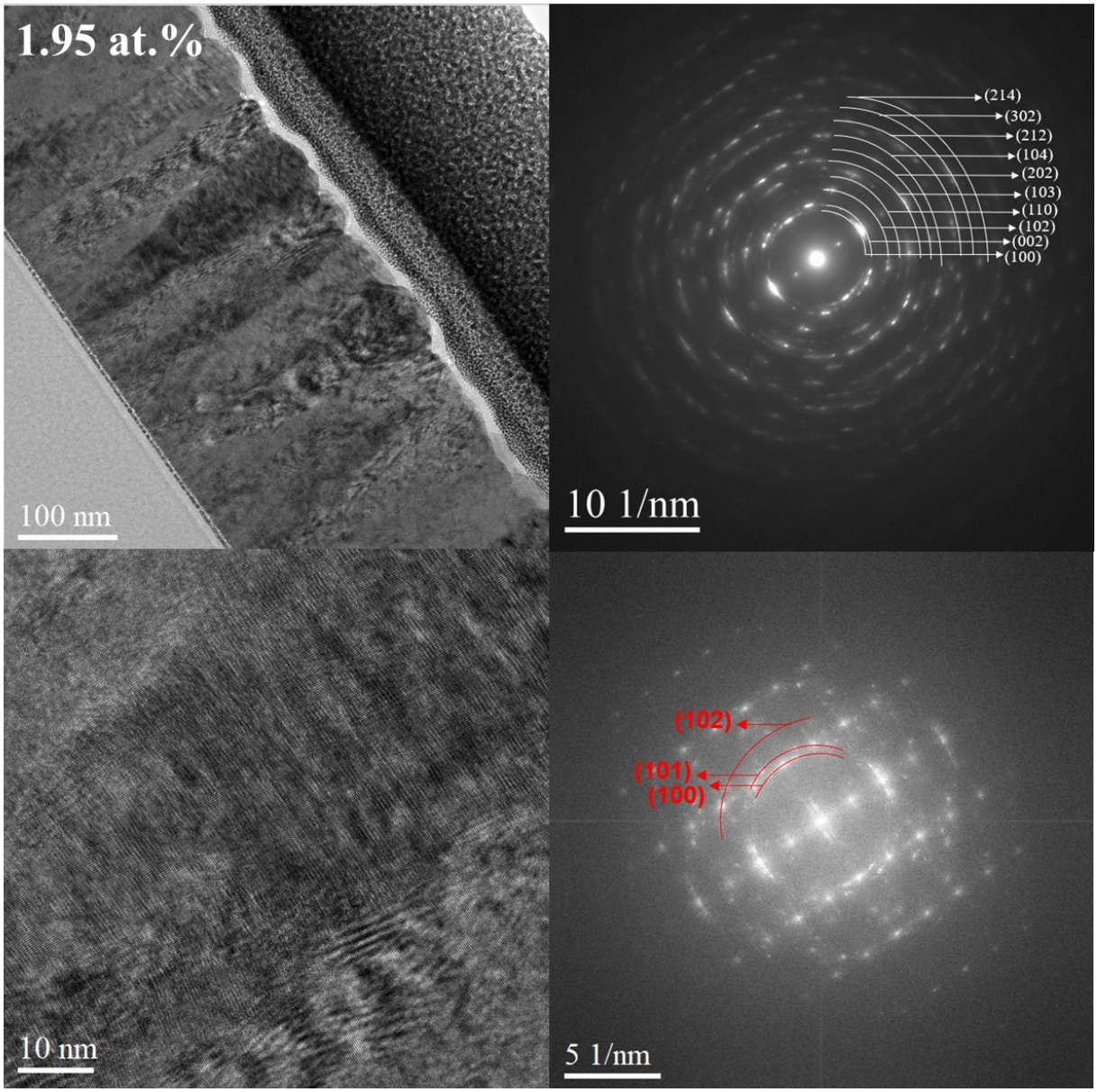

Figure 60: Panels of the main results obtained by TEM measurements including a TEM image, a SAED, a HR-TEM image and its indexed FFT for the AZO film containing 2.91/1.95 at.% of Al deposited from a Zn/Al 5 at.% target with the indicated content representing the measured Al concentration (at.%) in the AZO films *in-axis*/*off-axis* positions. ZA stands for Zone Axis.

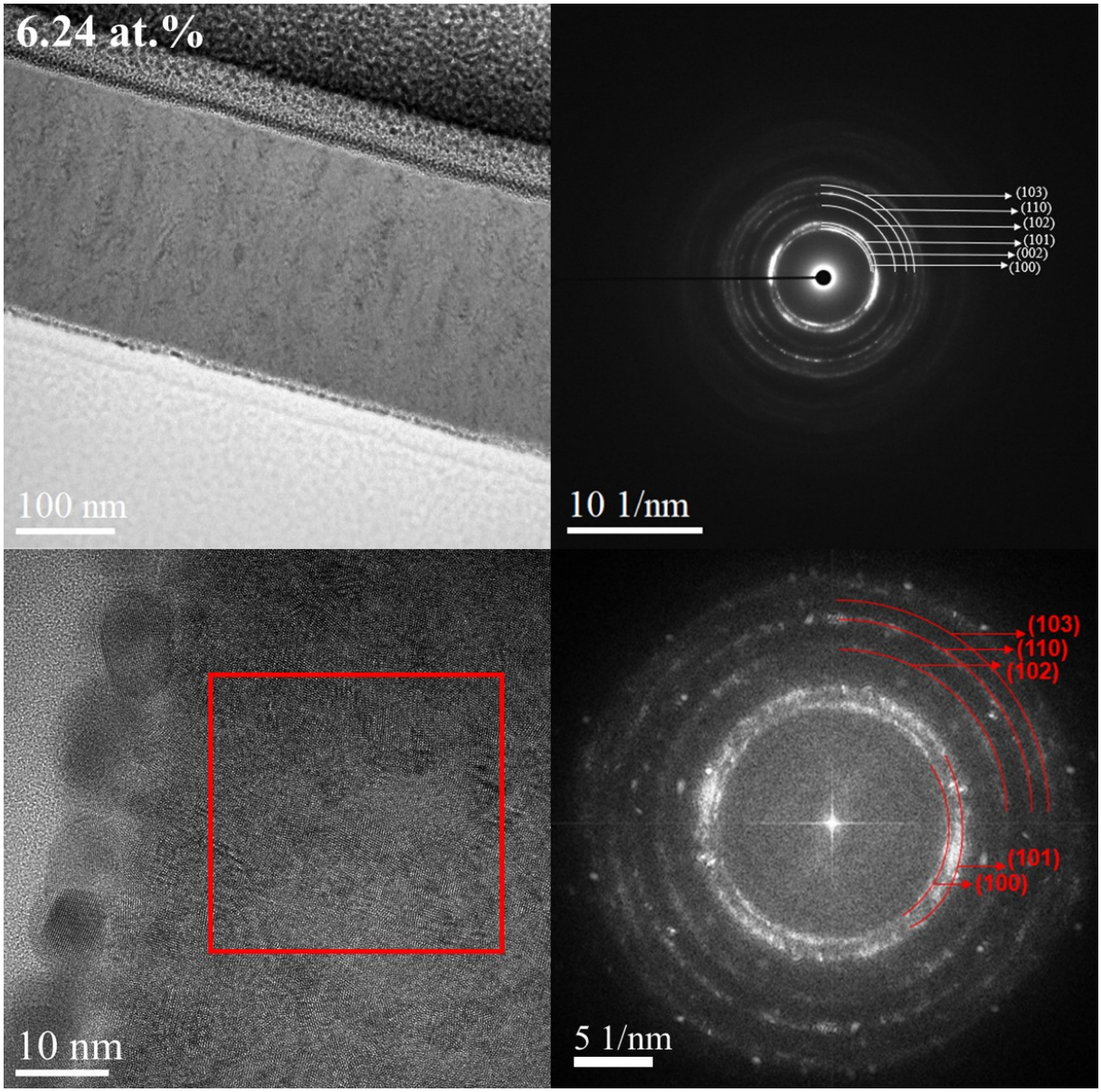

Figure 61: Panels of the main results obtained by TEM measurements including a TEM image, a SAED, a HR-TEM image and its indexed FFT for the AZO film containing 6.24 of Al deposited from a Zn/Al 10 at.% target with the indicated content representing the measured Al concentration (at.%) in the AZO films *in-axis*. ZA stands for Zone Axis.

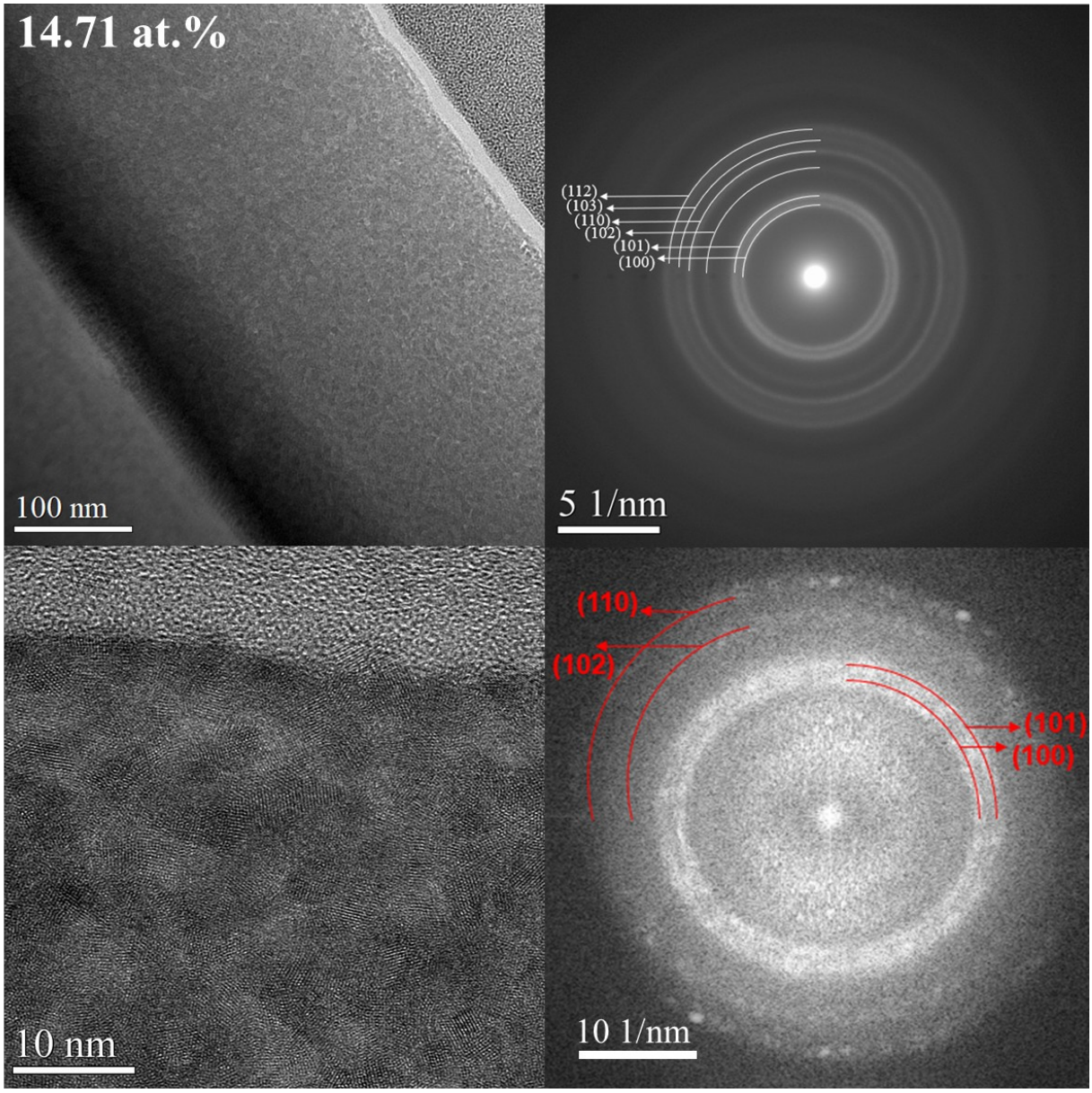

Figure 62: Panels of the main results obtained by TEM measurements including a TEM image, a SAED, a HR-TEM image and its indexed FFT for the AZO film containing 14.71 at.% of Al deposited from a Zn/Al 15 at.% target with the indicated content representing the measured Al concentration (at.%) in the AZO films *in-axis*. ZA stands for Zone Axis.

In order to further illustrate the influence of the oxygen sub-stoichiometry on the XRD signal of AZO films, we present the XRD diffractogram in **Figure 63** collected from AZO films deposited by DC sputtering using a Zn/Al target with 1 at.% Al at the *in-axis* position. It also enables us to compare the structure of the films to those obtained by HiPIMS deposition. First off, we tested the DC deposition of the AZO film under an applied voltage of 0.3 A (i.e. close to the average discharge current used during HiPIMS deposition) and a 20 sccm flow of oxygen (**Figure 63 a)**). The obtained films were of good transparency and had the wurtzite structure of ZnO with a preferential orientation

along the *c*-axis. By trying another set of parameters, that being 0.35 A of applied current and 15 sccm of oxygen (**Figure 63 b)**), the film became very absorbent, indicating strong sub-stoichiometry. This appears logical since we encouraged the sputtering of the Zn and Al species, while also decreasing the oxygen flow. Indeed, the XRD diffractogram of the film exhibits the wurtzite structure of ZnO with almost all orientations present, indicating a more random orientation in the *c*-axis. Increasing the oxygen flow rate to 18 sccm (**Figure 63 c)**), some transparency is regained and preferential orientation along the *c*-axis is observed again. For all films, the same results are observed in the *off-axis* position which is shown in the **Figure A4** of the **Appendices**. In conclusion, transparent and crystalline AZO films can be deposited from a Zn/Al 1 at.% target by using DC sputtering just as well as HiPIMS. Much like the latter, a compromise must always be found between the parameters in order to obtain the sought out properties of the AZO films. Yet, in the case of DC sputtering it is much more difficult to obtain films of simultaneous high conductivity and high optical transparency on large surface areas.

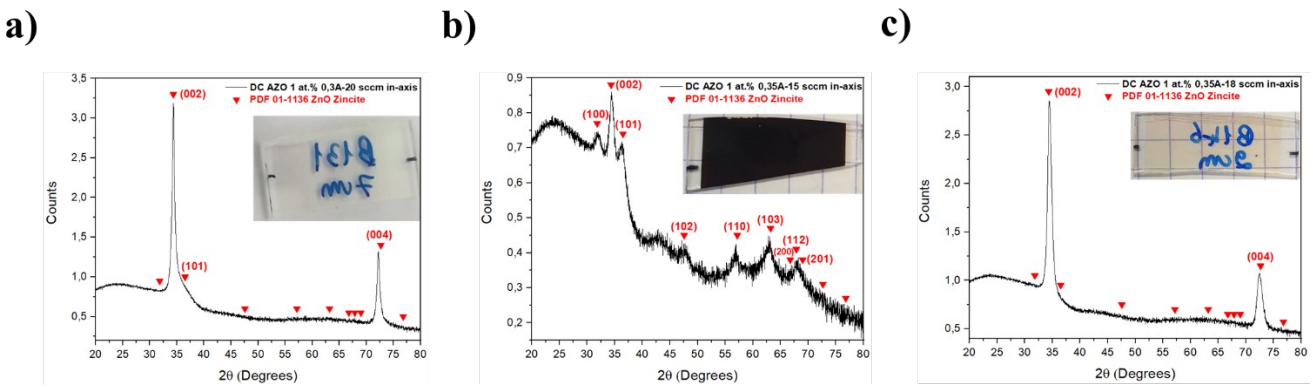

Figure 63: XRD diffractogram of AZO films deposited from a Zn/Al target with 1 at.% of Al at the *in-axis* position by DC sputtering at different applied currents and oxygen flow rates. The inset represents the photograph of the corresponding film.

3.5. Chapter conclusions

In this chapter, we debuted the characterization of the AZO films to be used as transparent electrodes by an evaluation of their deposition process through the study of the pulse waveforms and deposition rate of the AZO films as a function of the Al content present in the Zn/Al targets used for the deposition. From these results we concluded that the Al content has a great impact on the deposition mode of the HiPIMS process; in fact, we inferred that high Al contents encourage the formation of the undesired oxide layer on the surface of the target transitioning the deposition process from a metallic mode towards a compound mode characterized by a drop in the deposition.

We started off the films characterization by the chemical analysis via EDS measurements done by TEM. The results proved an even distribution of the Zn, O and Al species in the films with an increasing Al content when the Al content in the used Zn/Al target increased. To quantify this, we measured the content of each of the species for all AZO films both in the *in-axis* and *off-axis* positions. Other than confirming the previous observation, we also saw from the Al/(Al+Zn) ratio at both positions that the Al content incorporated in the film is close to that of the target for the films deposited from targets containing 1, 2 and 5 at.% of Al. But for the 10 and 15 at.% Al containing targets, the amount of Al in the film was much higher. We attributed this to a re-sputtering of Zn from the AZO films with higher Al contents along with stronger established bonds with Al, such as Al-O. Also with EDS, we observed the evolution of the Zn, O and Al contents through consecutive grains.

Next, we studied the effect of the Al content in the *in-axis* and *off-axis* positions on the structure and microstructure of the AZO films. From the XRD measurements, we concluded that the wurtzite structure crystallinity of the film degrades when the Al content increased to the point where the films became almost amorphous for 15 at.% Al target. The AZO films produced from the 1 and 2 at.% targets crystallized in the wurtzite structure but without strong preferential orientation along the *c*-axis. They were probably sub-stoichiometric due to the presence of the (101) peak. The AZO films deposited from 5 and 10 at.% Al targets were less crystalline but still exhibited the wurtzite structure of ZnO preferentially oriented along the *c*-axis. From the XRD data, we calculated the average size of crystallite and the crystallinity index from the most crystallized AZO films. We observed a decrease of crystallite size with the increase of Al content. To extend the structure and microstructure analysis, we performed TEM analysis on all the AZO films in both positions. The results confirmed the crystallinity degradation with the increase of the Al content in the targets or in the AZO films. However, even the films with the highest Al content was not found to be amorphous but nanocrystalline, indicating the possibility to maintain the structure even for high Al contents without thermal assistance. Films deposited from targets containing up to 5 at.% Al were found to grow in a columnar growth mode while those deposited with 10 and 15 at.% Al targets do not show evidence of this behavior.

In the next chapter, we will continue the AZO films characterization on another level by studying the optical and electrical properties of the AZO films.

Chapter 4

Dependence of the optical and electrical properties on the Al content

4.1. Introduction

While AZO films are of great interest in many fields, with application in solar cells being the topic of interest in this work, the main challenge that researchers are facing is trying to produce AZO films with electrical and optical properties almost as good as those of the ITO films, considered as the ideal transparent electrode to be used in a solar module. But, since the ITO films production cost is very high due to the rare and pricy components of the film, not to mention their toxicity, a replacement must be found. Almost all industries require compromise between the electrical and optical properties of TCOs in general, but in the solar cells field it is crucial for their efficiency.

The difficulty in optical and electrical properties optimization of AZO films lies in the difficulty of improving a parameter that affects positively one of the properties, but unfortunately reduces the other since they are interconnected in several ways. For instance, high thicknesses lowers the radial electrical resistance, but also reduces optical transmittance through the film. In another example, the electrical conductivity is known to increase with the free carrier concentration; however, this also shifts the boundary in the near-UV region, but mostly in the near-IR region, to shorter wavelengths, which decreases the transmission window. One solution to this problem is decreasing the carrier concentration to avoid the free carrier absorption in the IR region, and increasing the carrier mobility to improve the film's conductivity since the latter is equally proportional to the carrier's concentration and mobility. Additionally, it was found that the optical and electrical properties of materials depend on their surface morphology, the presence of intrinsic or extrinsic defects, as well as the nature, number and atomic arrangements of metal cations in the amorphous or crystalline oxide structures **[202,203]**. In fact, the presence of defects at grain boundaries and inter-grain voids places energy trap levels in the band gap which decreases progressively the carrier lifetime, the electron mobility and thus the film's electrical conductivity. Post-deposition annealing could solve this problem by improving the films crystallinity and reducing the strain energy **[203]**. T. Dhakal et al. **[204]** deposited AZO films by ALD with 80-90% of transmittance in the visible region and good transmittance in the infra-red region, however the film's conductivity was quite low. For this reason, they resorted to post-annealing treatment at 400 °C in Ar after which a sheet resistance of 25 Ω/sq and a carrier density of 2.4 x 10^{20} cm^{-3} for a 575 nm thickness were obtained while still maintaining a

high film transmittance in the visible region. This improvement in electrical properties was due to the increase of oxygen deficiencies in the films. Yet, degradation of the electrical properties could also occur after post-deposition annealing due to aluminum oxidation and ionization of oxygen vacancies. Proposing another solution, Q. Nian et al. **[203]** applied UV Laser Crystallization (UVLC) to AZO films deposited by PLD at room temperature to ensure a compromise between their optical and electrical properties. They were able to obtain high quality AZO films with high Hall mobility (79 cm^2/Vs), low carrier concentration (7.9 x 10^{19} cm^{-3}) and 36% improved transmittance in the 900-5000 nm range. Our approach contrasts the above-cited ones. Effectively, without thermal assistance during reactive HiPIMS deposition, obtained AZO films deposited by Mickan et al. **[52]** from a 3 at. % Al target exhibit resistivity values in the order of 10^{-4} Ω.cm, among the highest carrier density values (1.1 x 10^{21} cm^{-3}) found in the literature and carrier mobility values generally between 4 and 10 cm^2/Vs. The large conductivity was obtained despite the films consisting on small grains. This can be achieved due to lowered contribution of grain boundary scattering at large carrier concentrations **[205]**. In this work, we explore the influence of the Al content by following the elaboration procedure developed by Mickan et al. in order to evaluate the possibility to further manipulate the electrical and optical properties.

In this chapter, we continue the evaluation of the effect of the Al content on the properties of the AZO films. Once the deposition process, the chemical analysis, the structure and microstructure study were done and discussed in **Chapter 3**, we move on to the study of the optical and electrical properties of the AZO films as a function of the Al content. In the optical properties section, we will take on the transmittance measurements from which the band gap will be extracted and analyzed. The electrical properties section is divided into two parts; in the first one we will study the influence of the Al content on the resistivity of the AZO films via the four point probe method, and Hall effect measurement setup. Then, to show the compromise between the electrical and optical properties, the figure of merit that takes into consideration both properties will be presented. Next, we will study the evolution of the films resistivity and structure upon sequential annealing in air. Finally, since the AZO film deposition from a Zn/Al 1 at.% Al target displays a peculiar behavior, we will dedicate a section to the study of the resistivity and discharge waveforms in the case of low content AZO films deposition in order to gain more insights onto the Al content-dependent deposition mechanisms.

4.2. Optical properties

In **Figure 64**, we present the optical transmittance in the UV and visible range for AZO films deposited from the different Zn/Al targets. Looking at each of the *in-axis* (**Figure 64 a)**) and *off-axis*

(**Figure 64 b)**) positions, one can see that the transmittance increases with the increase in Al content. This increase can partially be explained by the higher thickness for lower Al contents already reported in **Figure 52 a)** of **Section 3.2 of Chapter 3**. Some "ripple oscillation" in the transmittance spectrum of all the AZO films but especially for the thickest one, i.e. the AZO films deposited from a Zn/Al target with 1 and 2 at.% of Al, could also be noticed. In fact, an interference effect occurs when the light is reflected on the front and back of the AZO films or in other words on the film/air and film/substrate interfaces; this leads to the so-called "ripple oscillations" with a larger number of oscillations for high film thicknesses **[204,206,207]**.

Finally, we can also notice the shift of the absorption edge to the left when the Al content in the AZO films increases; this is an indication that the band gap of the AZO films increases.

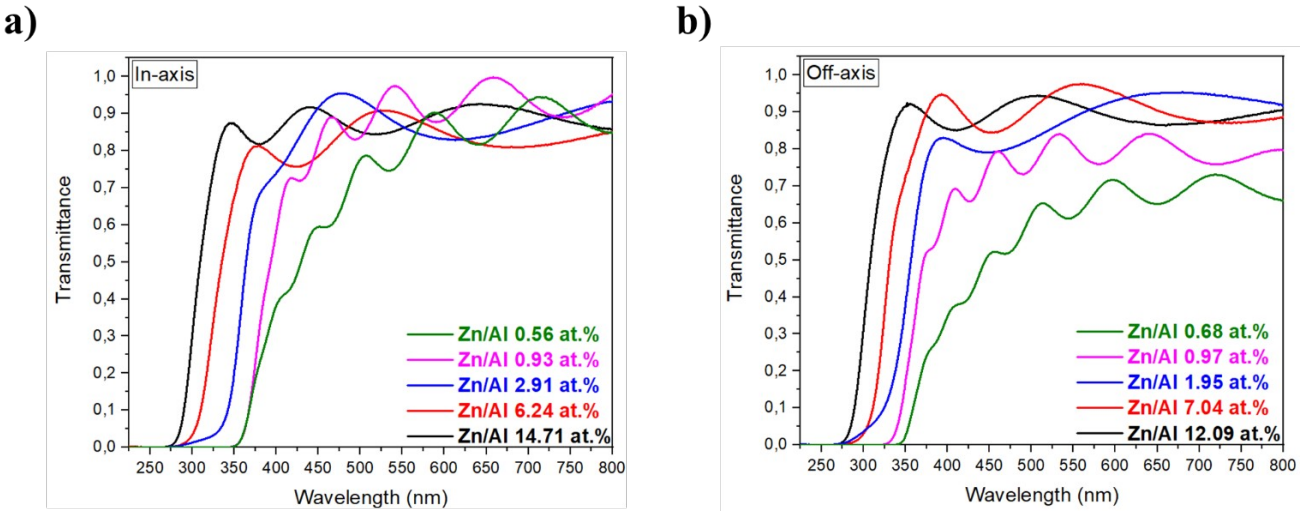

Figure 64: Transmittance as a function of the wavelength in the UV and visible region for the AZO films deposited from a 0.56/0.68 at.% of Al deposited from a Zn/Al 1 at.% target, 0.93/0.97 at.% of Al deposited from a Zn/Al 2 at.% target, 2.91/1.95 at.% of Al deposited from a Zn/Al 5 at.% target, 6.24/7.04 at.% of Al deposited from a Zn/Al 10 at.% target and 14.71/12.09 at.% of Al deposited from a Zn/Al 15 at.% target with the at.% values representing the real Al at.% in the AZO films in the *in-axis*/*off-axis* positions.

In order to avoid misinterpretation due the influence of the film thickness, the absorption coefficient (α) was calculated for each wavelength and is plotted in **Figure 65** for the different films and for both positions. It is observed that the films with lower contents of aluminium exhibit higher values of α, especially above 300 nm where there is no influence of the contribution of the glass substrate in the absorption. In zinc oxide, the increase in α in the visible range is generally ascribed to the formation of oxygen vacancies induced by oxygen sub-stoichiometry **[193,208]**. Therefore, it is a good way to detect the presence of oxygen sub-stoichiometry in AZO films. The presented results support the hypothesis proposed in **Section 3.2 of Chapter 3** that the films deposited from targets with the lower amounts of aluminum are more prone to exhibit oxygen sub-stoichiometry.

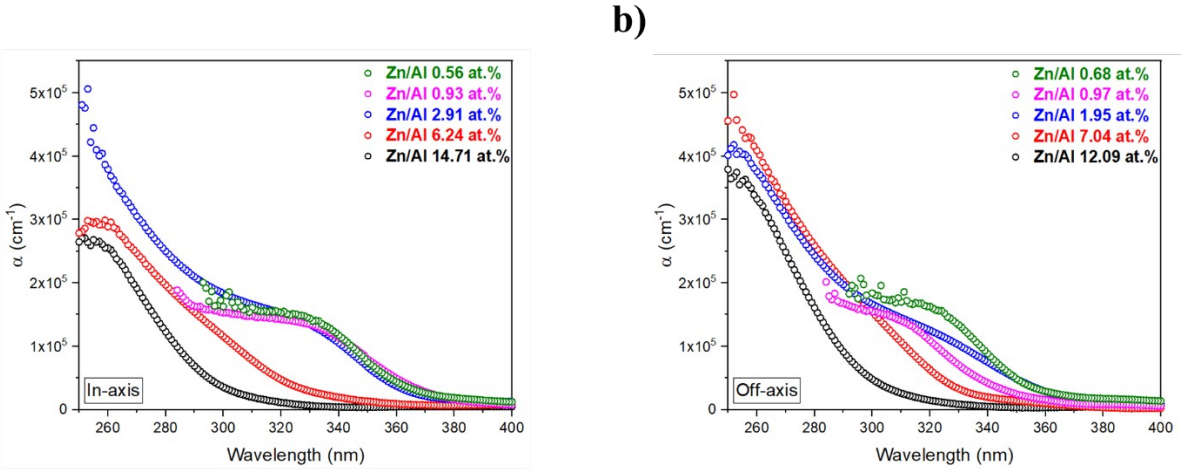

Figure 65: Absorption coefficient as a function of the wavelength in the UV and visible region for the AZO films from a 0.56/0.68 at.% of Al deposited from a Zn/Al 1 at.% target, 0.93/0.97 at.% of Al deposited from a Zn/Al 2 at.% target, 2.91/1.95 at.% of Al deposited from a Zn/Al 5 at.% target, 6.24/7.04 at.% of Al deposited from a Zn/Al 10 at.% target and 14.71/12.09 at.% of Al deposited from a Zn/Al 15 at.% target with the at.% values representing the real Al at.% in the AZO films in the *in-axis*/*off-axis* positions.

In **Figure 66**, we present the calculated band gap of each AZO film studied from the transmittance results using the Tauc method already explained and detailed **in Section 2.5.3. of Chapter 2**. First of all, we can confirm the conclusion drawn from the transmittance results in **Figure 64** since the band gap does indeed increase when the Al content in the AZO films increases. Undoped ZnO has a direct band gap of approximately 3.37 eV, and we can see that the absorption edge of all the deposited AZO films is shifted towards higher energy values and tends to be more shifted as the Al content is increased. Yet, some fluctuations are observed for contents below 3 at.% Al. The latter might indicate some fluctuations in the density of free electrons. In a classic AZO structure, the Al atoms substitute the Zn atoms in the ZnO structure and get singly ionized, then they act as donor levels giving one extra electron. As the electron density exceeds the Mott density of typically 10^{18} cm^{-3} for ZnO, a shift of the Fermi level into the conduction band is observed, which is known as the Burstein-Moss effect **[13,209]**. The band gap (ΔE_g) increases with the electron concentration n_e through the following **Equation 28**:

$$\Delta E_g = \frac{h^2}{8m^*}\left(\frac{3}{\pi}\right)^{2/3} n_e^{2/3} \qquad \textbf{(Eq. 28)}$$

With m^* is the effective mass of the electron.

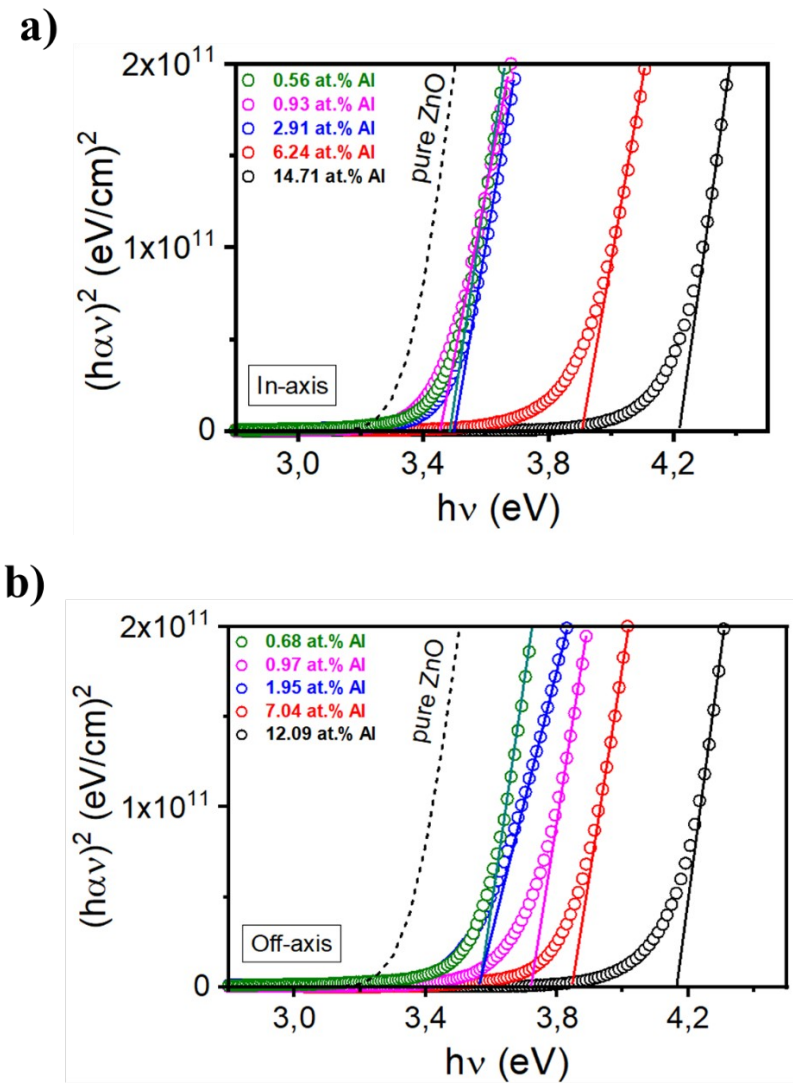

Figure 66: Energy band gap graphs of the AZO films deposited from a 0.56/0.68 at.% of Al deposited from a Zn/Al 1 at.% target, 0.93/0.97 at.% of Al deposited from a Zn/Al 2 at.% target, 2.91/1.95 at.% of Al deposited from a Zn/Al 5 at.% target, 6.24/7.04 at.% of Al deposited from a Zn/Al 10 at.% target and 14.71/12.09 at.% of Al deposited from a Zn/Al 15 at.% target with the at.% values representing the real Al at.% in the AZO films in the **a)** *in-axis* and **b)** *off-axis* positions.

We plot in **Figure 67** the bandgap values as a function of the Al content in the AZO films in the *in-axis* and *off-axis* positions in order to understand how the Al composition of the films affects the band gap.

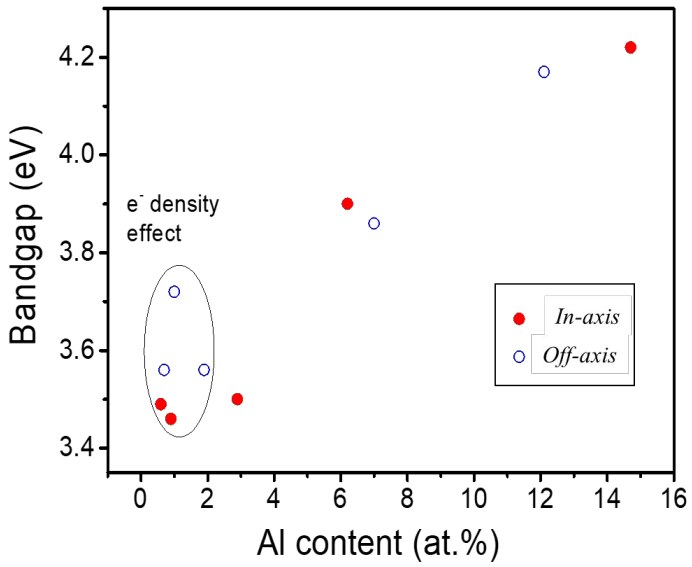

Figure 67: Evolution of the optical bandgap as a function of the Al content in the AZO films corresponding to 0.56/0.68 at.% of Al deposited from a Zn/Al 1 at.% target, 0.93/0.97 at.% of Al deposited from a Zn/Al 2 at.% target, 2.91/1.95 at.% of Al deposited from a Zn/Al 5 at.% target, 6.24/7.04 at.% of Al deposited from a Zn/Al 10 at.% target and 14.71/12.09 at.% of Al deposited from a Zn/Al 15 at.% target with the at.% values representing the real Al at.% in the AZO films in the *in-axis*/*off-axis* positions.

For Al contents above 3 at.% Al, the bandgap energy rises progressively with the Al content. The very high values obtained for the aluminum richer films are way beyond the usual reported magnitude for Burstein Moss effect in doped ZnO. Therefore, this may rather be an indication of a change in the local bonding; **Chapter 5** is dedicated to study this fact by the electronic structure measurements.

The presented results suggest that our AZO films deposited from 1 and 2 and eventually 3 at. % Al targets have higher density of electrons and so a higher conductivity. However, as can be seen in **Figure 64**, this is also the composition range in which the optical transmittance starts to drop, highlighting again the need to achieve a compromise between optical and electrical properties.

Finally, it's worth noting that the band gap values for the *off-axis* positions were slightly higher than those of the *in-axis* position, especially for the AZO films deposited from Zn/Al targets with 1, 2 and 5 at.% of Al. Going back to **Equation 28** showing that the band gap energy is related to the electron concentration n_e, suggests that the AZO films in *off-axis* positions have higher carrier concentrations. In fact, several authors have reported that *off-axis* position AZO films are submitted to less bombardment of highly energetic negative ions compared to the *in-axis* position **[52,210-212]**. The bombardment of the film surface by these energetic particles has been correlated to degradation of

the electrical conductivity for the *in-axis* position. This will be discussed in more details in the next section (**Section 4.3**) dedicated to the electrical characterization of the AZO films.

4.3. Electrical properties

4.3.1. General approach

In **Figure 68 a)**, we present the electrical resistivity of the AZO films deposited from Zn/Al targets with different Al contents as a function of the distance of the film to the substrate-holder axis. One can see that the resistivity increases with the Al content in the target going from 1 to 10 at.%, except at 3 and 4 cm from the substrate-holder axis for 1 to 2 at.% Al targets. This increase applies also to the 15 at.% film since it was so resistive that the resistivity could not be measured with our 4-point probe setup. This was already observed by various works for low Al contents films **[213,214]**. Additionally, the highest value of resistivity is observed for all films at 7-8 cm from the substrate-holder axis which happens to be the position on the substrate-holder circumference that faces the target axis. This *in-axis* position will also be referred to as *high ρ*, and the *off-axis* position corresponding to the lowest resistivity (3 cm) will be referred to as *low ρ*.

a)

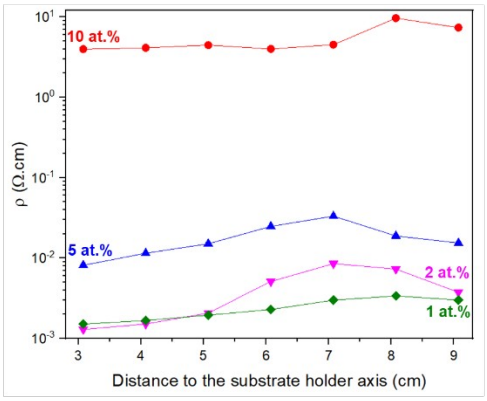

b)

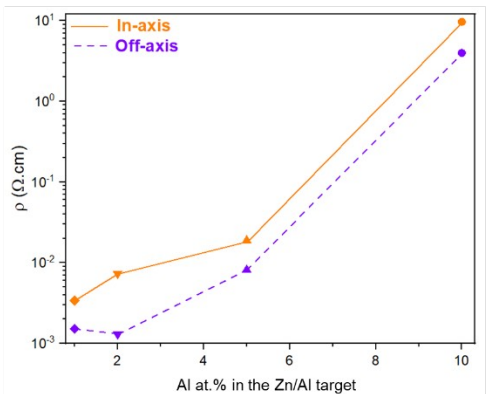

c)

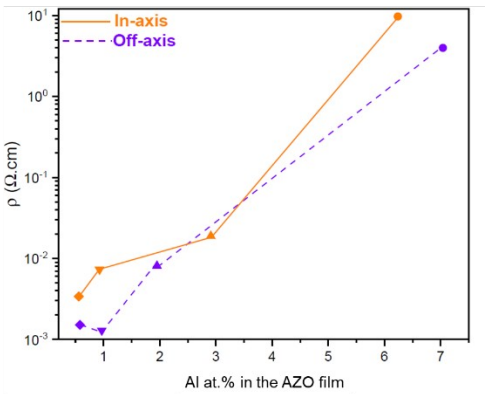

Figure 68: Graph of **a)** the resistivity ρ (Ω.cm) as a function of the distance to the substrate holder axis (cm) for the AZO films deposited from Zn/Al targets with 1, 2, 5 and 10 at.% of Al. The AZO film deposited from a Zn/Al target with 15 at.% of Al was not presented because the resistivity was too high to be measured; and graphs of the resistivity ρ (Ω.cm) as a function of the Al at.% in **b)** the Zn/Al targets and **c)** the AZO films at the *in-axis* and *off-axis* positions.

The causes of degradation of the electrical properties are numerous such as possible formation of secondary phases, scattering of charge carriers by grain boundaries, dislocations, phonons and ionized impurities. To start with the interpretation, we reconsider the following **Equation 1** to understand the relation between the resistivity (ρ), the carrier concentration (n) and the electron mobility (μ):

$$\rho = \frac{1}{ne\mu} \qquad \textbf{(Eq. 1)}$$

This equation means that a high carrier concentration and electron mobility is needed to achieve low resistivity films. S. Cornelius et al. **[191]** observed a decrease of the carrier concentration n and the electron mobility μ_e when the concentration of Al in the target increased up to 8.7 at.%; Ka Eun Lee et al. **[195]** found a minimum resistivity of 4,2 x 10^{-3} Ω.cm for their AZO film with 1 at.% of Al, the resistivity started increasing from the film doped with 2 at.% of Al and up to the one doped with 4 at. % of Al. They explained this by the fact that incorporating Al above the solubility limit leads to the formation of Al_2O_3 at the grain boundaries which traps free electrons and forms a potential barrier, or it might lead to the formation of Al-Al and Al-O clusters like AlO_x that are electrically inactive even trapping electrons leading to a decrease in their concentration **[192]**. Additionally, when the growing film is doped, which is the case of the AZO films, a lateral inhomogeneity of the properties of the films is detected. As was already assumed from the optical characterization, AZO films *in-axis* may have low carrier concentration due to the high bombardment by the energetic particles. K. Tominaga et al. **[215]** have already reported in 1985 that bombardment of a ZnO film surface by energetic oxygen atoms emitted from the target impairs the film conductivity by lowering the carrier density and mobility. This topic is still of importance today **[52,211,212]**. In fact, when performing reactive sputtering in the presence of a reactive gas such as oxygen, progressive oxidation of the target surface occurs upon increasing the oxygen flow rate. Oxygen atoms sputtered from the oxidized target surface can combine with a secondary electron also emitted from the target surface. T. Welzel and K. Ellmer **[128]** have shown that the formed energetic O^- oxygen ions are accelerated perpendicularly from the target surface, where they go through the cathode sheath and gain a kinetic energy equivalent to the discharge voltage before reaching the substrate. As these species reach the

growing film, they introduce acceptor defects like O_i into the film and may induce the formation of secondary phases such as the homologous $Al_2O_3(ZnO)_m$ phase **[193]**. In contrast, AZO films *off-axis* are far less subjected to the fast oxygen ions bombardment and thus have high carrier concentrations coming from the donor defects in the film, such as the oxygen vacancies and the interstitial Al atoms, which may explain the lower resistivity in this position seen from **Figures 68 a) and b)** **[52,184,210-212]**. M. Mickan et al. **[52]** deposited using HiPIMS AZO films with a transmittance comparable to that seen in films deposited by DC sputtering but with lower and more homogeneous resistivity when using proper discharge voltage. They also proposed that the HiPIMS process enables the successful removal of the oxide monolayer formed between pulses because the surface density of sputtered atoms during one pulse almost equals the surface atom density of the oxide layer formed at the racetrack as shown in **Figure 69**. Here, it is found that films deposited from 1 and 2 at.% Al targets leads to films of low resistivities independently of the substrate position, but that the resistivity tends to increase in front of the target axis and as the Al content is increased. It does not seem possible to improve the conductivity beyond what has been achieved by Mickan et al. who used a 3 at.% Al target and similar sputtering conditions to ours.

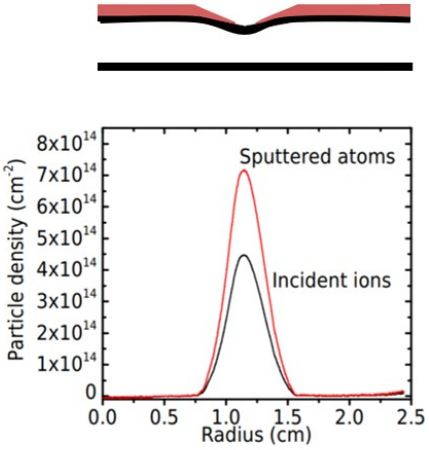

Figure 69: Graph showing the particle density on the target of the incident ions (black curve) and the sputtered atoms (red curve) as a function of the position from the target center for Y = 1.6 atoms/ion. The top illustration shows schematically the racetrack position on the target as well as the oxide layer in red. The surface atom density is 10.9, 6.8, 5.9, 5.2 for (001), (110), (100) and (101) ZnO planes, respectively **[52]**.

Hall effect measurements were performed on the AZO films to further understand their electrical behavior; these results are presented in **Figure 70**. Unfortunately, this method very sensitive to conductivity was only applicable for the AZO films deposited from 1 and 2 at.% Al targets, and from the 5 at.% Al target in the *off-axis* position since they were the only AZO films conductive enough to be measured. The results for the AZO film deposited from the 5 at.% Al target will be presented later on in **Table 5**. The resistivity results for the AZO films deposited from the 1 and 2 at.% Al targets

are presented in **Figure 70**. The resistivity values are very close to those obtained with the four point probe setup (**Figure 68**), which confirms these measurements. As was explained above, we can confirm the decrease of the resistivity when the carrier concentration and mobility increase. The carrier density values are found between 4.28 x 10^{20} and 11.61 x 10^{20} cm^{-3} for films deposited from the 1 at. % Al target and from 3.53 x 10^{20} and 18.98 x 10^{20} cm^{-3} for the film deposited from the 2 at. % Al target. It is maximized at the position the farthest away from the target axis. It should be noted that the carrier concentration is usually above 10^{20} cm^{-3} for films containing 1-7 at.% Al deposited at 400°C, i.e. for films deposited with high crystallinity and reduced density of point defects **[192]**. Maximal values of electron mobility between 20 and 40 cm^2/Vs could be expected depending on the carrier concentration but could not be achieved due to the absence of thermal assistance during deposition **[191]**. Finally, we notice that the lower values of carrier concertation and mobility are observed for the *in-axis* position. We interpret it, once again, as due to the higher bombardment by oxygen ions introducing defects into the films **[191,216]**.

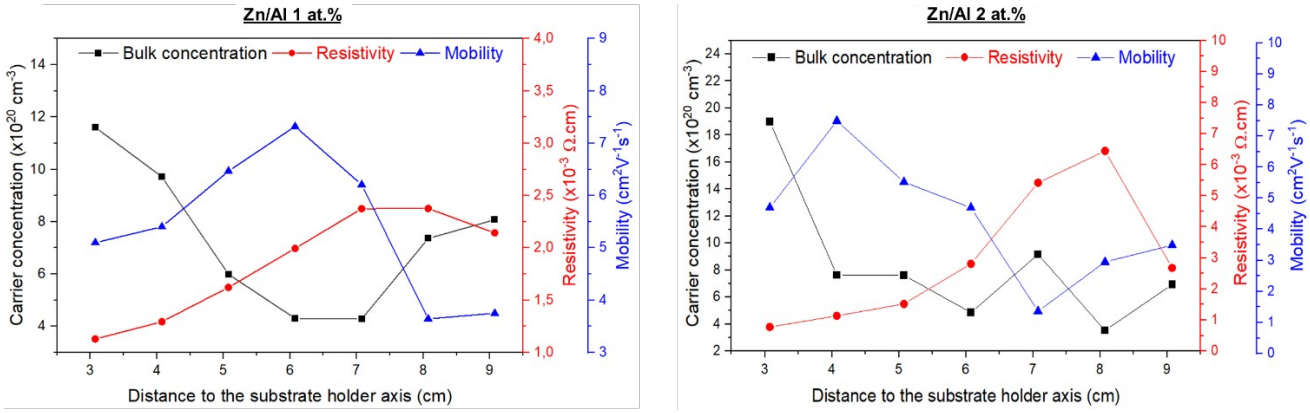

Figure 70: Hall effect measurements of the AZO films deposited from a Zn/Al target with 1 and 2 at.% of Al. They represent the variation of the carrier concentration (cm^{-3}), the resistivity (Ω.cm) and mobility ($cm^2V^{-1}s^{-1}$) as a function of the distance to the substrate holder axis (cm).

To summarize some of the main results obtained so far, we assembled in **Table 5** for all five target compositions, in the *high ρ* (*in-axis*) and *low ρ* (*off-axis*) positions, the film composition, the average size of crystallites and the electrical properties consisting of the resistivity, the electron density and the electron mobility. As seen in **Figure 68**, the resistivity is higher in the *in-axis* position whatever the target composition. From the Hall effect measurements resumed in this table, we correlated it to the decrease of both the electron density and electron mobility which were only possible to measure for the low target compositions (1, 2 and 5 at.% Al). No clear relationship between the electrical resistivity and the size of crystallites could be found. This indicates that grain boundary scattering is not the main parameter that degrades the film conductivity in this case **[205]**.

Table 5: Summary of some chemical, structural and electrical properties obtained thus far for the AZO films deposited from Zn/Al targets with 1, 2, 5, 10 and 15 at.% of Al at the *high ρ* and *low ρ* positions.

[a]Average size of crystallites for 15 at.% Al was deduced from TEM analysis while XRD was used to evaluate the size of crystallites for other conditions; NM : non-measurable.

Target composition	Film composition (at.% Al)	Resistivity (Ω.cm)	Electron density (cm^{-3})	Electron mobility ($cm^2V^{-1}s^{-1}$)	Average size of crystallites (nm)
High ρ/Low ρ					
1 at.% Al	0.56/0.68	$3.4\ 10^{-3}/1.5\ 10^{-3}$	$7.3\ 10^{20}/1.2\ 10^{21}$	3.7/5/1	27/27
2 at.% Al	0.93/0.97	$8.5\ 10^{-3}/1.3\ 10^{-3}$	$3.5\ 10^{20}/1.9\ 10^{21}$	3.0/4.7	30/25
5 at.% Al	2.91/1.95	$3.3\ 10^{-2}/8.1\ 10^{-3}$	NM/$5.0\ 10^{19}$	NM/0.4	12/16
10 at.% Al	6.24/7.04	9.68/3.98	NM/NM	NM/NM	≈ 5 nm[a]
15 at.% Al	14.71/12.09	NM	NM/NM	NM/NM	≈ 4 nm[a]

While the study of the evolution of the optical and electrical properties of the AZO films as a function of the Al content is interesting, what is even more important is correlating these two properties together in order to identify a good enough AZO film to be used as a transparent electrode. For this reason, we used the Figure Of Merit (FOM) calculated from a formula taking in consideration both the resistivity, to represent the electrical properties, and the absorption parameter, to represent the optical properties: $\frac{1}{\rho\alpha}$ **(Eq. 29)**. This means that for high film resistivity and absorption, both undesired for transparent electrodes, the value of the FOM is low. We calculated and plotted in **Figure 71 a)** the FOM as a function of the Al content present in the Zn/Al targets used for the deposition of the AZO films both in the *in-axis* and *off-axis* positions and also as a function of the Al content in the AZO films shown in in **Figure 71 b)**. Since no value of resistivity could be obtained for the film deposited from the 15 at.% Al target, the FOM could not be calculated. As expected, the FOM decreased with the increase of the Al content which is only normal since both the resistivity and absorption coefficient increased. Additionally, the FOM values for the all the AZO films in the *off-axis* position were higher than the *in-axis* one due to the lower resistivity. In order to determine which of the AZO films are good enough to be used as a transparent electrode based on their FOM values, one must refer to the literature. M. Zubkins et al. **[5]** deposited AZO films on glass substrates by reactive HiPIMS under 500 µs long pulses from Zn/Al targets with an Al content of 2 wt.% and at room temperature; they obtained a FOM value of 0.0008 Ω^{-1}. Comparing their results with other works, the highest FOM value of 0.0281 Ω^{-1} was obtained for an AZO film deposited by reactive DC sputtering from a Zn/Al 1 wt.% target at a substrate temperature of 290 °C. B. K. Sarma et al. **[217]** deposited AZO films by DC sputtering from a ZnO/Al_2O_3 target with an Al_2O_3 content varying from 0.5 to 5 wt.% on glass and polyethylene terephthalate (PET) substrates. For one, the FOM value was always higher when the AZO film was deposited on glass rather than on

PET since the latter tends to absorb light on a higher level than glass. Second, the highest values of FOM were obtained for the 1, 2 and 3 wt.% Al_2O_3 content targets (0.0502 – 0.0633 Ω^{-1}). Finally, they were able to deposit an AZO film by pulsed DC sputtering on glass with a FOM value (0.0759 Ω^{-1}) almost four times higher than their ITO films (0.0119-0.0197 Ω^{-1}) deposited by different methods. In our work, the FOM of the AZO films deposited from a Zn/Al target with 5, 10 and 15 at.% were lower than those of ITO; however it can be seen that only the films deposited from a Zn/Al target with 1 and 2 at.% yielded FOM values more than twice higher than the FOM values of ITO films, even reaching 0.2 Ω^{-1} for the film deposited from a Zn/Al 2 at.% target in the *off-axis* position. It can be deduced that Zn/Al targets with 1 and 2 at.% of Al, especially in the *off-axis* position, are suitable for the fabrication of AZO films to be used as transparent electrodes. Yet, there may still be room for improvement since the highest FOM value for AZO films reported in the literature is close to 5 Ω^{-1} **[218]** and Mickan et al. **[44]** obtained a FOM of 0.9 Ω^{-1} by using reactive HiPIMS at a substrate temperature of 500°C using a 2 at.% Al target and similar electrical parameters as the ones used in this work.

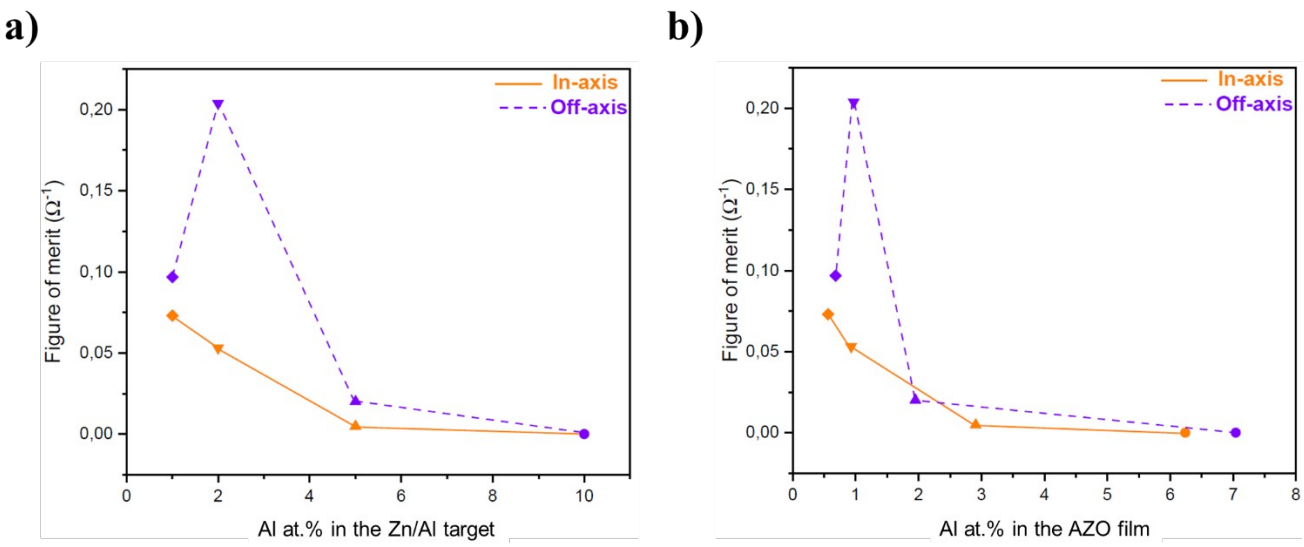

Figure 71: Graph of the figure of merit (Ω^{-1}), in the *in-axis* and *off-axis* positions, as a function of **a)** the Al content (at.%) present in the Zn/Al targets used for the deposition of the AZO films and **b)** the actual Al content present in the AZO films.

To conclude this section, we present the resistivity measurements using the four point probe setup for the AZO films deposited from 1, 2, 5 and 10 at.% Al targets, in both the *high ρ* and *low ρ* positions but this time under sequential annealing in air at 100, 150, 200 and 225 °C for one hour at each temperature with 10 µA of applied current. For the AZO films deposited from a Zn/Al target with 1 and 2 at.% of Al, one extra treatment at 225 °C for 1 hour was done under 1 mA of applied current. Many authors state that post-deposition thermal annealing leads to better electrical properties due to

the increase in crystallite size and film density; the latter reduces the carrier scattering at grain boundaries and increases carrier mobility due to the enhancement of oxygen release which favors the presence of V_O **[219-223]**. S. Singh et al. **[181]** observed a resistivity decrease in the AZO films when the post-annealing temperature was increased from room temperature to 450 °C. This was accompanied by an increase in the free carrier concentration that they attributed it to the donated electrons by the Al dopant. The carrier density also increases when the Al^{3+} ions substitute the Zn^{2+} ions in the ZnO structure or when Al_i is formed. D. Meljanac et al. **220]** post-heated their AZO films for one hour in a hydrogen atmosphere at 200, 300 and 400 °C. To the previous observation, they added the decrease of the activation energy of the recombination of close proximity interstitial-vacancy pairs and of free migration of interstitial atoms and vacancies, which activates the donor Al dopant that contributes as well to the increase of the free carrier concentration. In fact, the typical energy barriers for the migration of those defects in monocrystalline ZnO are approximately 1.4 eV for V_{Zn}, 2.4 eV for V_O, 0.5 eV for Zn_i and 1 eV for O_i. Since those energy values are so low, one can understand the positive effect of thermal treatment on the reduction of the activation energy. Also, while being valid for equilibrium processes and not entirely certain for magnetron sputtering, the elimination of the Al_{Zn}-V_{Zn} complex is very important since it is one of the dominant defects in AZO films and contributes greatly to the reduction of the n-type doping efficiency by removing the Al donor level; this results in reduction of carrier concentration and mobility. The formation of such a complex is due to the fact that, on the one hand, the Al donor tends to energetically favor substituting Zn in the ZnO structure forming a donor Al_{Zn} rather than being an interstitial (Al_i). On the other hand, V_{Zn} formation in AZO films is very probable due do its low formation energy. Those two facts explain the high possibility of establishment of a Al_{Zn}-V_{Zn} complex. The thermal treatment is able to dissociate this complex due do its very low formation energy and re-establish the donor role of the Al_{Zn} **[223]**. Mickan et al. **[53]** also explained that AZO films tend to absorb water and form $Zn(OH)_2$ which degrades the electrical properties of the films; they explained this by the formation of hydroxyl groups acting as trap states at grain boundaries decreasing the charge carrier concentration as well as their mobility due to the potential barrier increase. However, the electrical properties can be partially restored by performing a heat treatment in argon or nitrogen. In fact, the $Zn(OH)_2$ formed after exposure to air for a long time decomposes and the absorbed water diffuses out of the film due to the reconstruction of the grain boundaries that can act as diffusion paths for the water. Their SIMS spectra showed that the H atom no longer existed in the film and O 1s core level spectra showed that the amount of hydroxyl groups decreased. This confirms the decomposition of the hydroxyl groups and the water diffusion out of the film. Nonetheless, in some studies the resistivity is observed to increase after a certain annealing temperature due to the possible oxidation of the material **[221]**. In

fact, when the AZO films are heat treated in air, the oxygen absorption on the film's surface at the grain boundaries is encouraged and an electron trap is placed, which results in dopant oxidation and is manifested by the increase of resistivity. This effect is the more detrimental with the increase of heat treatment time **[224]**. In our case, the annealing was performed in air in order to serve as a complementary way to detect the presence of oxygen sub-stoichiometry and, eventually, to improve the electrical properties. From **Figure 72**, one can see that the resistivity of the AZO films decreases at first, bettering the electrical properties, followed by an increase due to film oxidation when the heat treatment is long enough or is done at high temperatures. For the AZO film deposited from the 10 at.% Al target, the resistivity decreased during the 100 °C heating to start increasing thereafter. For both the *in-axis* and *off-axis* positions, the electrical properties degraded respectively at the beginning and middle of the 150 °C treatment. For the film deposited from the 5 at.% Al target, the same behavior was observed only that the resistivity increase or film oxidation lasted to roughly the end of the 225 °C treatment, for both positions. For the films deposited from the 1 and 2 at.% Al targets, the resistivity decrease continued roughly till the end of the 150 °C (or even 225 °C for 1 at. % Al *off-axis*) treatment for all films and positions. After this point, the resistivity started to increase until the very end of the treatment at 225 °C with 1 mA of current applied and during 1 hour. From these observations we can conclude that when the Al content in the AZO films increase, the heat treatment must be done et relatively low temperatures (100 °C) to improve the electrical properties while for lower Al content films, it may be done at higher temperatures (150 °C or more, depending on the case). This is in line with the initial electrical properties of the films, meaning that the more the AZO films are resistive, the less room for electrical properties improvement by heat treatment there is. Moreover, these results also tend to confirm that the films are all the more oxygen sub-stoichiometric as the Al content in the target used for their preparation is low.

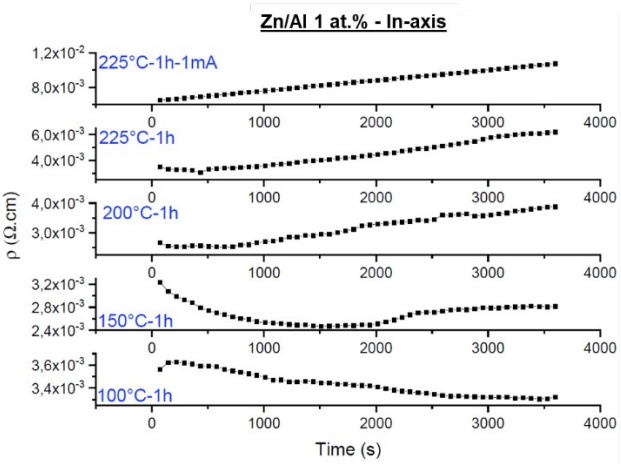

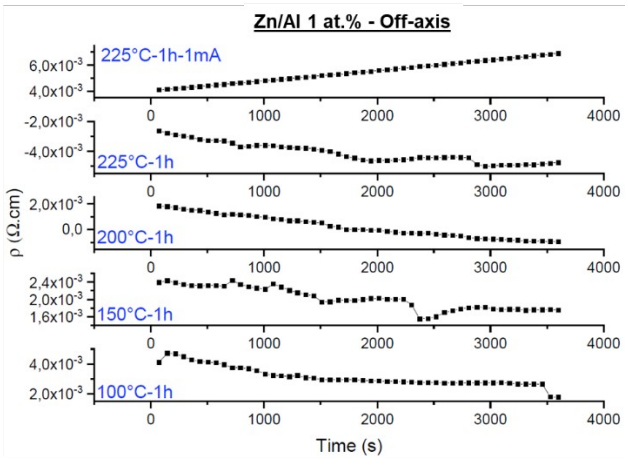

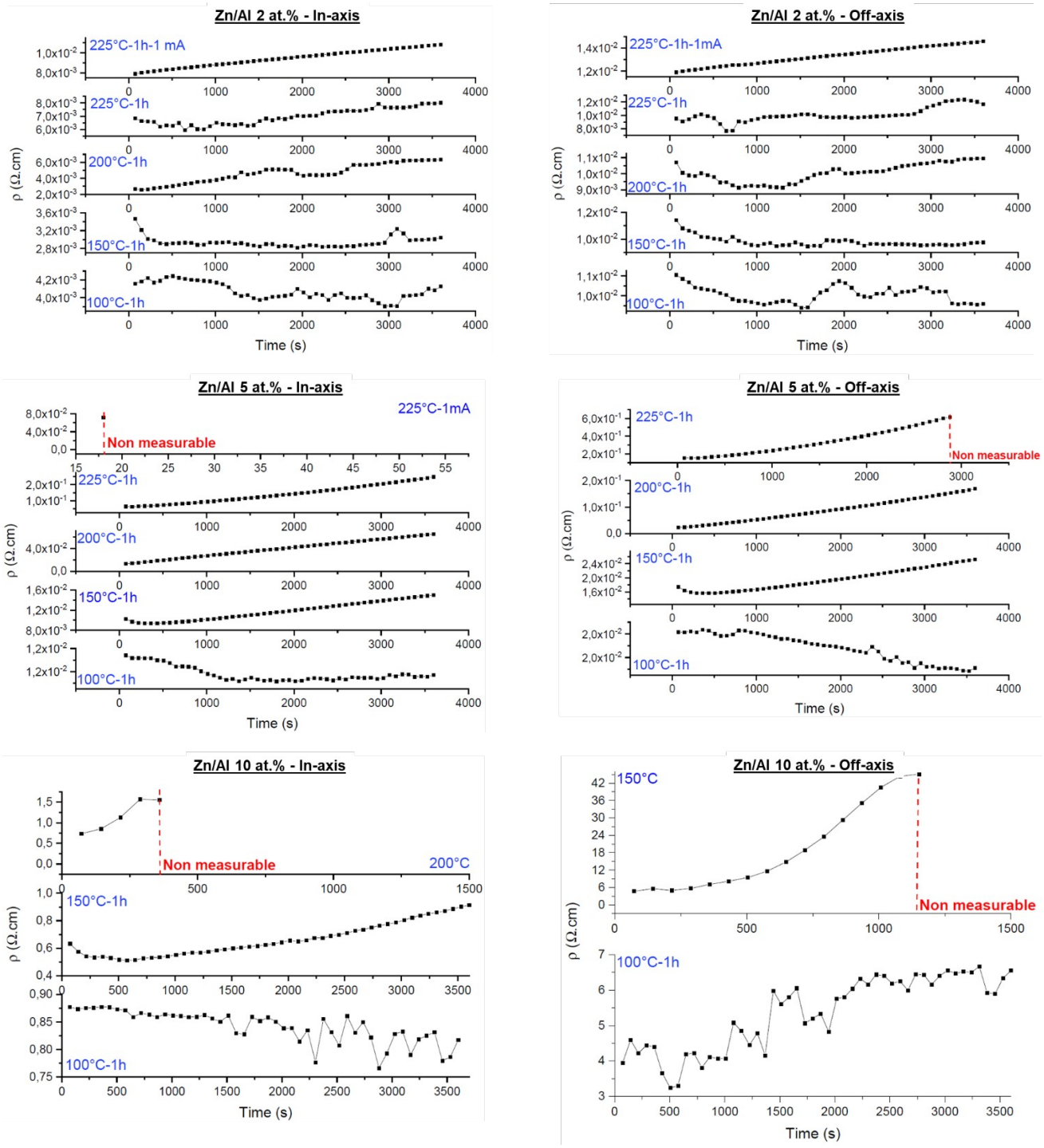

Figure 72: Resistivity evolution as a function of time of the AZO films deposited from Zn/Al targets with 1, 2, 5, 10 and 15 at.% of Al, at the *in-axis* and *off-axis* positions, during heat treatment in air at 100, 150, 200 and 225 °C for 1 hour at each temperature under 1 µA of applied current. For the AZO films deposited from 1 and 2 at.% Al targets, one extra treatment at 225 °C for 1 hour was done under 1 mA of applied current.

In **Figure 73**, we present the XRD diffractograms of the AZO films before and after heat treatment at both the *in-axis* and *off-axis* positions. The diffractograms collected after the sequential annealing

treatments for each film are presented in black. As mentioned above, if the heat treatment is long and strong enough, it could be detrimental to the structure of the films. However from **Figure 73**, we see almost no change in the wurtzite structure of the films up to 3 at.% of Al in the films. It is only for the AZO films deposited from 10 at.% Al target that the films became amorphous *in-axis* and the intensity of the (002) peak decreased *off-axis*. This is not surprising since the film was already little crystalline and the heat treatment almost immediately degraded its electrical properties, so the destruction or degradation of the film's structure is expected.

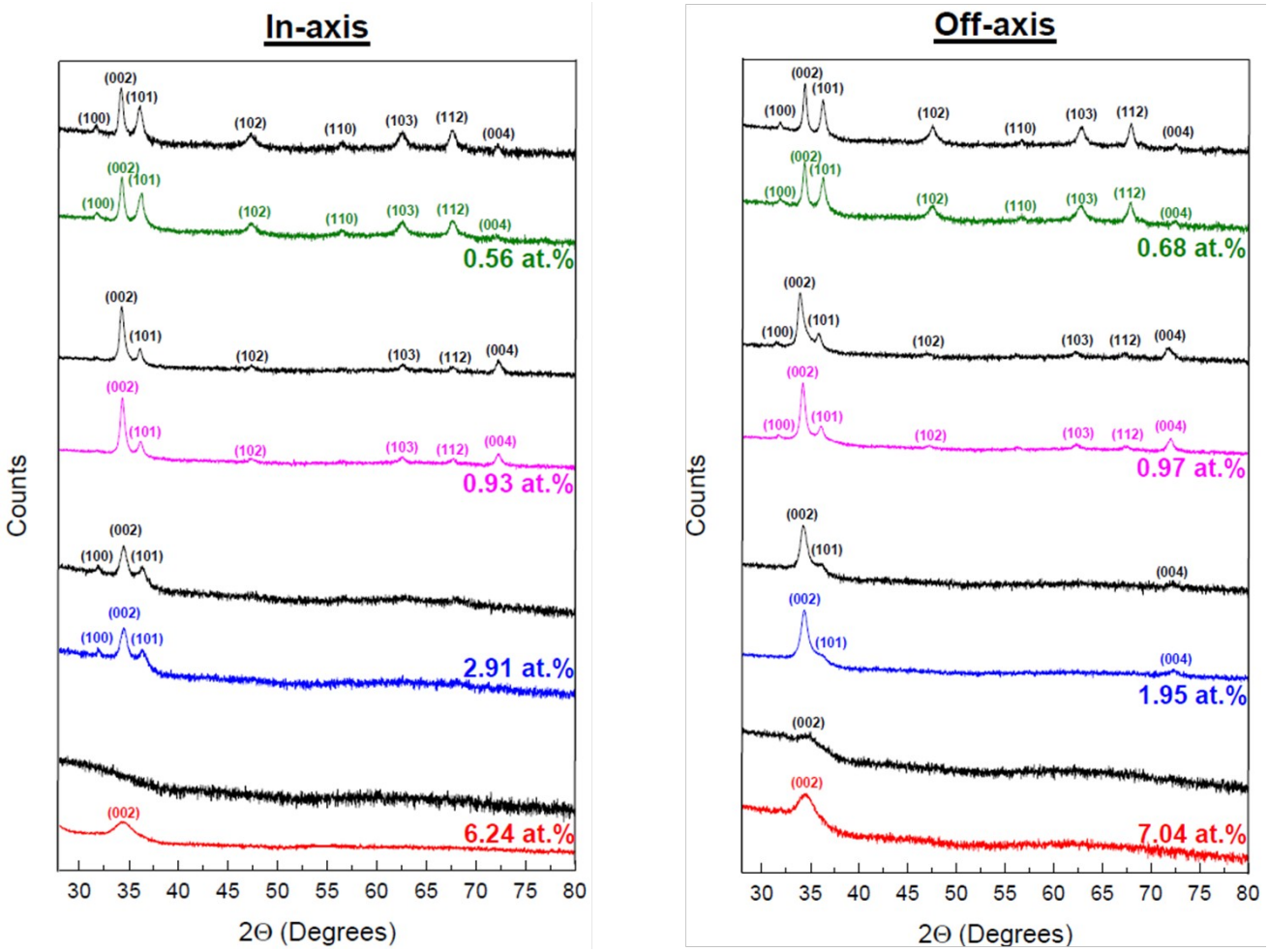

Figure 73: XRD diffractograms normalized by the thickness of the AZO film containing 0.56/0.68 at.% of Al deposited from a Zn/Al 1 at.% target, 0.93/0.97 at.% of Al deposited from a Zn/Al 2 at.% target, 2.91/1.95 at. % of Al deposited from a Zn/Al 5 at.% target and 6.24/7.04 at.% of Al deposited from a Zn/Al 10 at.% target with the at.% values representing the real Al at.% in the AZO films *in-axis*/*off-axis* positions. The colored curves correspond to the XRD measurement of the AZO film after deposition and the black curve above each Al composition corresponds to the XRD measurement after heat-treatment.

4.3.2. Specific approach on the low Al content films

While the effect of the Al content on the AZO films electrical properties seemed quite simple, meaning that the increase of the Al content in the Zn/Al target used for the deposition of the AZO films degrades their electrical properties; the experiments done on the low Al content target, namely Zn/Al with 1 at.% of Al, proved a more complex mechanism. This section is dedicated to the treatment of such case.

The data for the resistivity for the 1 at.% and 3 at.% Al targets are presented in **Figure 74** as a function of the distance to the substrate-holder axis for the different conditions. For the 3 at.% Al target, the evolution of the resistivity is opposite to that of the discharge voltage. It has been interpreted by Mickan et al. **[52]** that operating closer to the metallic mode due to a more complete removal of the surface oxide formed between pulses leads to a discharge voltage and, consequently, a peak current increase. From the film perspective, this results in a better-controlled oxygen sub-stoichiometry and lower degradation of electrical conductivity resulting from the bombardment by fast oxygen particles. A similar study was performed on a new and a used Zn/Al 1 at.% target. The resulting resistivity measurements as a function of the position to the substrate-holder axis are plotted in **Figure 74 b)**. What is interesting and completely opposite from what was observed in M. Mickan et al.'s work, and also in our work for the higher Al content targets, is the fact that the resistivity decreased when the voltage applied to the target was decreased. One can see that all films follow the same pattern of a maximum resistivity *in-axis* at 8 cm from the substrate holder axis followed by a decrease of the resistivity when getting closer to the *off-axis* position (3cm).

a) **b)**

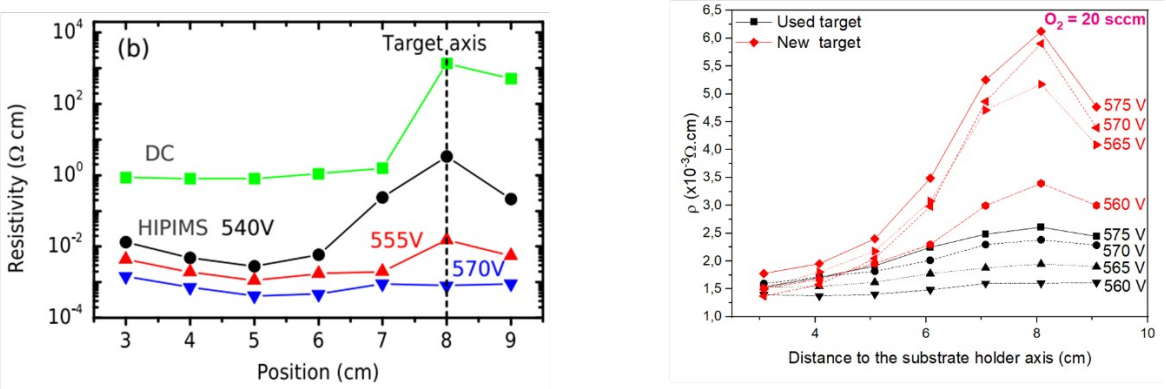

Figure 74: Graph of the resistivity as a function of the position of the substrate to the substrate-holder axis for **a)** AZO films deposited from a new Zn/Al target with 3 at.% of Al deposited by DC, and by HiPIMS under 540, 555 and 570 V of applied voltage. The oxygen flow rate was kept constant at 20 sccm **[52]**; and for **b)** AZO films deposited by HiPIMS from a Zn/Al used (black) or new (red) target with 1 at.% of Al under an applied voltage of respectively 575, 570, 565 and 560 V. The oxygen flow rate was kept constant at 20 sccm.

To further show the difference of electrical properties behavior between a low Al content target and higher ones, the resistivity was plotted in **Figure 75** as a function of the applied voltage for both the AZO films deposited from a Zn/Al target with 1 and 3 at.% of Al; the latter extracted from **Figure 74 a)**. The results at *high ρ* (**Figure 75 a)**) and *low ρ* (**Figure 75 b)**) positions are shown. It is clear that for a higher Al content target, the resistivity decreases continuously with the increase of the applied voltage; whereas for a low Al content target, the same behavior is observed until a minimum applied voltage, after which the resistivity starts to increase with the applied voltage proving a unique behavior for low content AZO films.

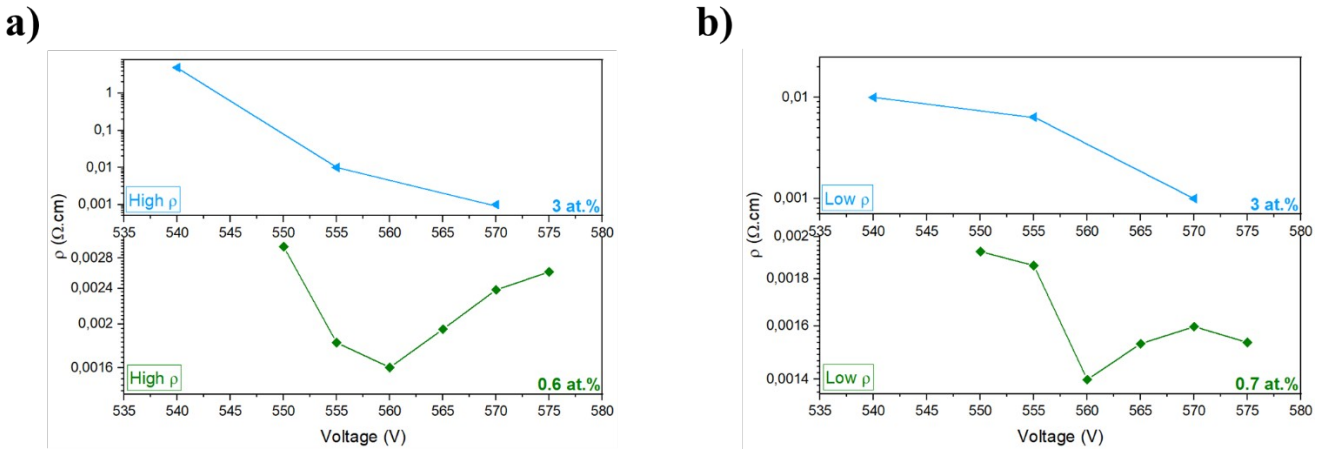

Figure 75: Graphs of the resistivity as a function of the applied voltage for AZO films deposited from a new Zn/Al target with 3 at.% of Al **[52]** and a used Zn/Al target with 1 at.% of Al in the **a)** *high ρ* and **b)** *low ρ* positions. **Changer % 1% ?**

To try and explain these results, we can suppose that for a given discharge voltage, a given oxygen flow rate and a given target utilization, the target surface is overall more oxidized for the higher Al content. In order to illustrate this hypothesis, we refer to the study realized using reactive DC sputtering of undoped ZnO by Uthanna et al. depicted in **Figure 76 a)**. One can see that for $P_{O_2} < 10^{-3}$ mbar, the resistivity decreases with the oxidation of the ZnO film. At $P_{O_2} = 10^{-3}$ mbar, an optimum in oxygen sub-stoichiometry is supposed to be obtained and, when $P_{O_2} > 10^{-3}$ mbar, the increase in resistivity is due to lower density of donor defects and higher density of acceptor defects **[182]**. Moreover, the introduction of acceptor defects from the bombardment of the forming film by the negative oxygen ions can also be a source of donor defects. Hence, a reverse bell shape is obtained for the resistivity vs P_{O_2}curve. By analogy, in order to explain our results with the AZO film deposited from a Zn/Al target with 1 at.% of Al, we adapted Uthanna's results to ours in **Figure 76 b)**. We could consider that for low Al contents, the sub-stoichiometry of the AZO film decreases and

leads to a decrease of the resistivity when the applied target voltage is decreased and oxygen sub-stoichiometry is progressively lowered. Our results for the “old” target indicate that the target utlization also plays a strong role in the sputtering behavior and, therefore, the film oxygen sub-stoichiometry. For higher Al contents, the opposite behavior is observed and the films are in this case evolving towards the right part of the reverse bell shape curve. A complementary study is needed to carefully measure the evolution of the electrical parameters for various Al contents and target utilizations in order to clearly identify the mechanisms in action.

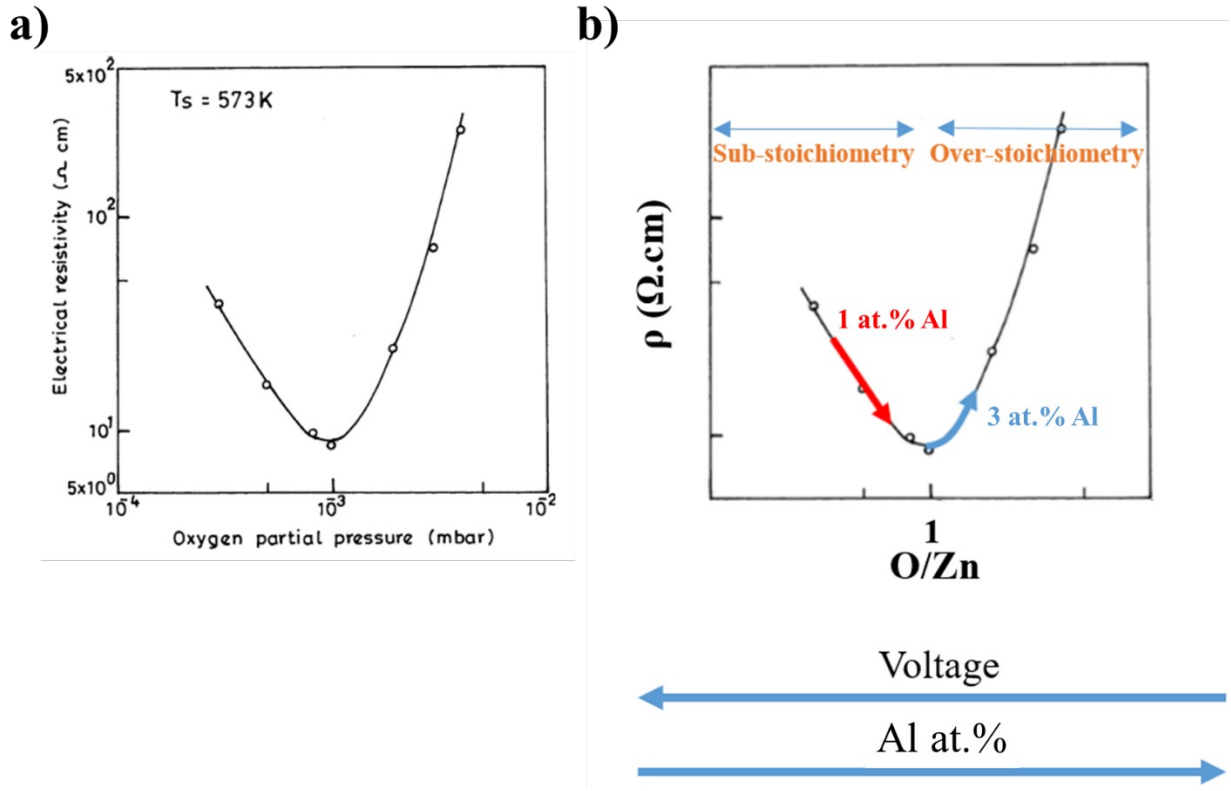

Figure 76: a) Graph representing the electrical resistivity as a function of the oxygen partial pressure P_{O_2} at a substrate temperature of 573 K of a ZnO film deposited by DC magnetron sputtering extracted from **[182]** and **b)** An adaptation of the previous graph to correspond to our results with the *x* axis replaced by the O/Zn value to represent the film’s stoichiometry.

4.4. Chapter conclusions

In this chapter, we pursued the AZO films properties evolution as a function of the Al content present in the Zn/Al targets used for their deposition. This chapter was dedicated to the optical properties study, as well as that of the electrical properties both from a general approach on all the Al contents and from a specific approach on low content AZO films.

From the optical properties study, and starting off with the transmittance measurements, an increase of transmittance along with the Al content of the AZO films was observed. We attributed this to the evolution of the oxygen sub-stoichiometry. Band gap extraction using the Tauc method enabled us to see that the optical bandgap is increased upon increasing the Al content in the films as measured by EDS embedded in a TEM. It was observed that the AZO films deposited from 1 and 2 at.% Al targets have slightly higher band gaps than intrinsic ZnO; this was attributed to the donor level provided by the Al dopant leading to the Burstein-Moss effect, as confirmed by the high electron concentration measured by the Hall effect setup. This higher electron concentration could also explain why the band gap values *off-axis* were higher. The bandgap values for films deposited from 5, 10 and 15 at.% Al targets were high and increasing with the Al content. This increase is not compatible with the Burstein-Moss effct as the electron density drops with the Al content in this range. Rather, we speculated it is due to the establishment of Al-O bonds such as in an insulating phase like alumina. This hypothesis will be further tested by the analysis of ELNES measurements in **Chapter 5**.

From the electrical properties study, we observed the increase of resistivity with the Al content with a higher value always in the *in-axis* position, i.e. the position facing the magnetron axis, for all films. The increase with the Al content was attributed to the possible formation of parasite phases that trap electrons decreasing their carrier concentration; since the latter and the electron mobility are inversely proportional to the resistivity, they lead to its decrease. This was confirmed by the Hall effect measurements done on films deposited from the 1 and 2 at.% Al targets. Additionally, no relation between the electrical resistivity and the size of crystallites was found which meant that electrons might be mostly affected by the ionized impurity scattering when their density is high rather than by the grain boundary scattering. As for the higher resistivity value *in-axis*, it is thought to be due to the bombardment of the AZO films by the fast oxygen ions than introduce acceptor defects into the films or induce the formation of a secondary phase such as the homologous $Al_2O_3(ZnO)_m$ phase. Yet, HiPIMS remains a better deposition mode than DC because the oxide layer formed, and responsible for the formation of the energetic oxygen ions, is more effectively removed between HiPIMS pulses. In order to show the effect of both the optical and electrical properties on the AZO films, the FOM was calculated. The results showed that it decreases with the increase of Al content, especially *in-axis*, due to the higher resistivity and light absorption. Comparing the FOM values with other works from the literature, we were able to determine that depositing AZO films from a Zn/Al target with 1 and 2 at.% of Al, mainly in the *off-axis* position, is suitable for their application as transparent electrodes. Next, the study of the electrical properties was extended by studying the evolution of the resistivity when the films were subjected to sequential heating in air.

The results showed that the resistivity at first decreases due to the probable destruction of the Al_{Zn}-V_{Zn} complex. Also, $Zn(OH)_2$ is known to exist in AZO films at grain boundaries, playing the role of trap states and causing the decrease in the carrier concentration and mobility which degrades the AZO films electrical properties. Annealing can reestablish the grain boundaries and decompose the $Zn(OH)_2$, letting the water diffuse out of the films. The resistivity was then seen to increase after a certain temperature plateau, because those very same reconstructed grain boundaries are also trap states for oxygen facilitating the oxidation of the AZO film. What was also important to note was that the first positive effect of heat-treatment, meaning its contribution to the drop in resistivity, was observed for longer time and at higher temperature for the low content AZO films. Also, the high content films were quick to become very resistive. Post-heat treatment XRD even showed a drop or even disappearance of the (002) peak for the AZO films deposited from the 10 at.% Al target. This meant that high resistivity AZO films might not be too easy to redeem at least via heat treatment. Measurement of the electrical resistivity during annealing in air can also be an interesting indirect way to track the presence of oxygen sub-stoichiometry because oxidation could take longer in films that are more sub-stoichiometric.

From the extended study on the discharge voltage behavior during deposition of low Al content AZO films, we found an anomalous sputtering behavior: the resistivity decreased with the decrease in discharge voltage all the more the target utilization was high. This seems to appear in a given window of target voltages and to be dependent on the Al content too. The electrical behavior of the films produced with the 1 at.% Al target appears to be ruled by the need to have an optimized oxygen sub-stoichiometry to lower the electrical resistivity. The oxygen sub-stoichiometry in itself is affected by the sputtering deposition process controlled by the target state (new or used); this effect however cannot be validated without further experiments.

From the optical and electrical properties of the AZO films studied in this chapter, we speculated the formation of alumina or other dopant-deactivating phases explaining the degradation of the electrical properties for high Al content films. To try and uncover this, we present in the next chapter the ELNES analysis results conducted on the AZO films at the Al-K, Al-$L_{2,3}$, Zn-L_3 and O-K edges.

Chapter 5

Activation/inactivation of dopants detected by electronic structure measurements

5.1. Introduction

Over the years, the optical and electrical properties of AZO films were studied as a function of various deposition parameter changes such as the substrate temperature, the distance to the magnetron axis, the gas flow rate in the case of reactive deposition, the applied voltage, etc. All these parameters influence the properties of the AZO films. Some authors, much like us, attributed those effects to an electronic level changes in the structure of the AZO films. M. Chaves et al. **[225]** deposited AZO films on glass substrates from a Zn/Al 5 at.% Al target by RFMS at room temperature, and studied the effect of the deposition pressure variation on the structural, electrical and optical properties of the films. They observed that at a high pressure induced by high oxygen flow rate, the AZO films presented low carrier density values which they related to the oxidation of the Al dopant, in a $Al_2O_3(ZnO)_m$ homologous phase for example, deactivating the dopant. In fact, the high oxygen pressure increases the lifetime of the O species making them more prone to react with Zn and Al. This decreases the efficient ionization of Al doping and thus may favor the formation of a homologous phase. In another way, R.B.H. Tahar **[226]** studied the effect of Al dopant increase in AZO films prepared by a sol-gel process. Similarly to our study, he observed the drop in carrier concentration and mobility at high doping levels exceeding the solubility limit of Al in ZnO. He attributed this to the formation of electrically inactive impurities. For this reason, it was necessary to try and uncover the direct effect of the Al dopant variation on the resulting electronic structure of the AZO films. For instance, T-Thienprasert et al. **[129]** applied the XANES technique to relate the local atomic structure of the AZO films, deposited by RFMS at different growth conditions and Al contents, to their optical and electrical properties. They observed for high Al content films, and for films grown under O-rich conditions, a non-donor Al_{Zn}-V_{Zn} and $2Al_{Zn}$-V_{Zn} complex formations consistent with the drop in carrier concentration and mobility. They even witnessed the presence of α-Al_2O_3 and nAl_{Zn}-O_i in some samples. Other works have also tried to understand the dopant

deactivation by studying the AZO films electronic structure, but to date the results are still under discussion **[3,4,7,227-230]**.

In the previous chapter, we have presented and discussed the electrical and optical performances of the AZO films depending on the Al concentration present in the films. From the various results and similarly to many authors, we speculated the degradation of the properties as being due to changes in the AZO films occurring with the increase of the Al content on an electronic structure level. Especially some aspects such as dopant compensation, contributions to free electron scattering and intrinsic-extrinsic doping interplay are valuable parameters that have a major effect on the optical and electrical properties of the films. For these reasons, we dedicated this chapter to the study of the influence of the Al content on the electronic structure and local bonding of the AZO films, both at the *in-axis* and *off-axis* positions, by means of electron Energy Loss Near Edge Structure (ELNES) at the Zn-L_3, O-K, Al-K and Al-$L_{2,3}$ edges. This method probes the density of empty states in the conduction band for different orbitals.

5.2. Zn-L_3 and O-K edge analysis

Since the solubility limit of Al in Zn is typically about 0.3 at.%, and in our study we have tested the deposition of AZO films from targets with an Al content going up to 15 at.%, some speculations on Al dopant deactivation by aluminum segregation or the formation of other phases are justified. In fact, J.G. Lu et al. **[192]** in their study of AZO films with Al contents higher than 30 at.% deposited while using thermal assistance of 400 °C, discovered segregation of Al in ZnO which could lead to the formation of alumina (Al_2O_3). The latter has an optical band gap of 7-8.8 eV in bulk crystalline form, 5.1-7.1 eV in amorphous form and 3.2-6.2 eV when deposited as a thin film **[231,232]**. A second possibility is the formation of a stable secondary phase such as the spinel $ZnAl_2O_4$ where the Al is in a octahedral conformation with oxygen, and its optical band gap is of 3.9-6 eV when it is in a nanocrystalline form **[233-235]**. However, Bikowski et al. **[229]** performed XANES analysis in the Al-K, O-K and Zn-L edges on AZO films with 2 at.% Al deposited at temperatures as high as 500 °C, and still couldn't find a trace of the spinel phase formation. Another possible phase formation is the homologous $Al_2O_3(ZnO)_m$ phases **[228]** where nanolaminates of poorly-doped ZnO blocks with Al in tetrahedral and pentahedral conformations are alternated in the *c*-axis direction by monolayers of Al_2O_3. Several authors have proposed the formation of this homologous phase in their AZO films in their interpretation of XANES analysis in the Al-K edge **[3,4,7,227,228]**. Similar to the nano-laminated homologous phase, Rjipstra et al. **[230]** used an evolution algorithm to suggest the

formation of a more energetically-favorable phase resembling to the homologous phase but consisting in separate Al_2O_3-threads woven into a ZnO medium. Additionally, instead of secondary phase formation, the generation of Al_{Zn}-O_i complexes was proposed by Bikowski et al. **[229]** as interpretation of small changes at their Al-K edge XANES. Nevertheless, no direct evidence of the formation of such phases or complexes is available to date since in XRD and electronic structure analysis their signature peaks is difficult to distinguish from that of wurtzite ZnO, and there is no complementary TEM analysis to prove it either. All in all, the exact mechanism(s) of Al dopant deactivation in AZO films is (are) yet to be solved. For this reason we performed ELNES analysis on our AZO films in order to detect the active Al dopant, and to understand the transition from an active dopant to an inactive one. In contrast with previous studies we have considered the Al-L_3 edge as a possible interesting tool to detect such changes because this edge is known to be highly sensitive to small changes in the bonding of Al.

We start off by presenting the ELNES analysis at the Zn-L_3 edge for all the AZO films in the *in-axis* (**Figure 77 a)**) and *off-axis* (**Figure 77 b)**) positions. The Zn-L_3 edge is the result of the electronic transition from the Zn-$^{2p_{\frac{3}{2}}}$ state to the Zn-s and Zn-d derived empty states. It probes the density of the empty Zn-4s and Zn-4d states with an overlap of other orbitals because the Zn-3d is fully occupied. In **Figure 77** are shown the four distinct features observed for this Zn-L_3 edge: $A_{Zn\text{-}L}$ ascribed to the density of Zn-4s corresponding to the bottom of the CB, $B_{Zn\text{-}L}$ to the density of Zn-4s and Zn-4d combined, $C_{Zn\text{-}L}$ and $D_{Zn\text{-}L}$ to the density of Zn 4d **[236,237]**. Despite the small variations in the intensity of feature $A_{Zn\text{-}L}$, one can still tell that the spectral shape of the ELNES of all the AZO films with Al contents of up to 2.91 at.% is ascribed to the wurtzite structure of ZnO. In fact, B. Gilbert et al. **[238]** presented in their study the Zn-$L_{2,3}$ edge of the Zinc Blend and wurtzite structure of ZnO and by comparing their spectra to ours, one can confirm the formation of the AZO films in a wurtzite structure because in a Zinc Blend ZnO a rather intense pre-threshold peak is present, which is not observed in our spectra. For higher Al contents, the rest of the features, $B_{Zn\text{-}L}$, $C_{Zn\text{-}L}$ and $D_{Zn\text{-}L}$, weaken and smear out probably due to the crystallinity degradation of the films and local crystal distortions that induce changes in the Zn-4s and Zn-4d overlap with oxygen **[237]**. What is interesting though, is that even at a high Al content, the 7.04 at.% Al film (*low ρ* position) still shows detectable ELNES features of the Zn-L_3 edge which reminds the presence of the (002) peak with rather high intensity in its XRD diffractogram from **Figure 56**. However, the film deposited from the same target but at a *high ρ* position (6.24 at.% Al film), shows less detectable and defined features of the Zn-L_3 edge which also reminds of a weaker (002) diffraction peak in its XRD diffractogram

(Figure 56). Finally, since the $A_{Zn\text{-}L}$ increases for the films from 1.95 at.% of Al and beyond, this means that the Zn-4s states are progressively emptied.

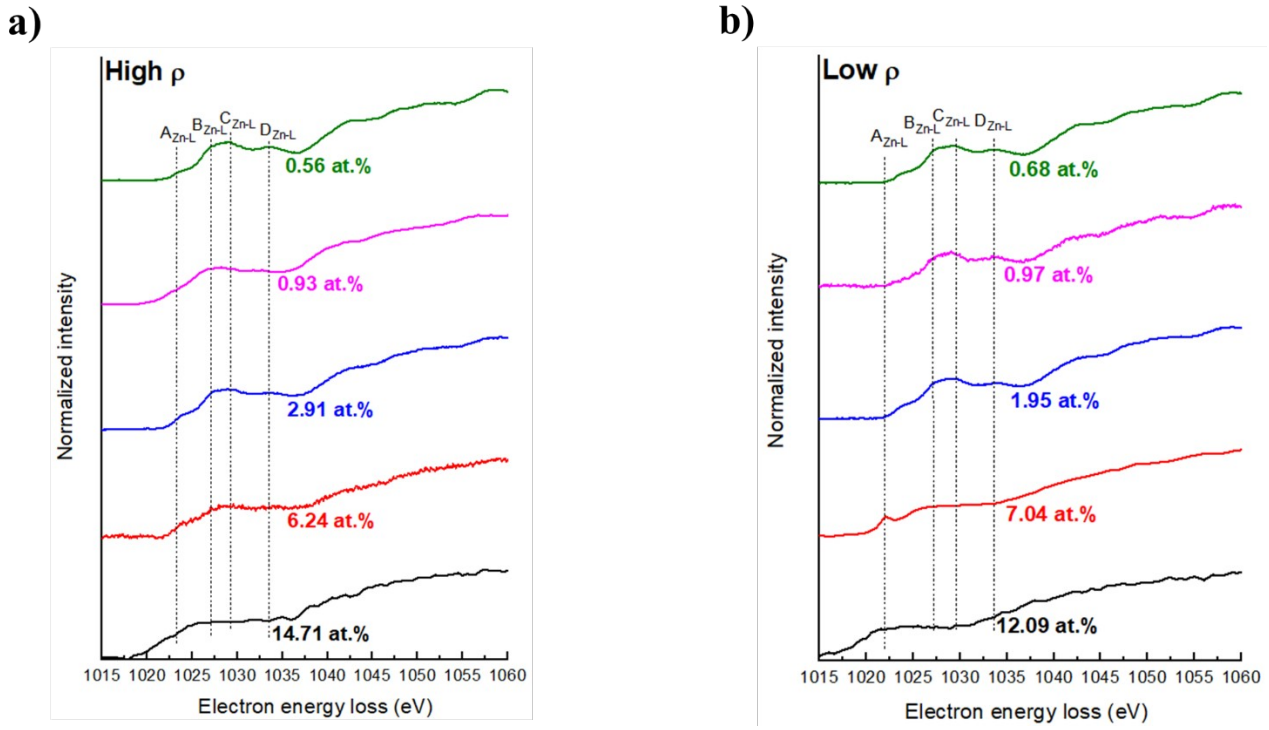

Figure 77: Zn-L_3 electron energy loss near edge structure at the **a)** *high ρ* and **b)** *low ρ* positions of the AZO films with 0.56/0.68 at.% of Al deposited from a Zn/Al 1 at.% Al target, 0.93/0.97 at.% of Al deposited from a Zn/Al 2 at.% Al target, 2.91/1.95 at.% of Al deposited from a Zn/Al 5 at.% target, 6.24/7.04 at.% of Al deposited from a Zn/Al 10 at.% target and 14.71/12.09 at.% of Al deposited from a Zn/Al 15 at.% target with the at.% values representing the real Al at.% in the AZO films *high ρ*/*low ρ* positions.

Next, we move on to the O-K edge to continue the electronic structure analysis of the AZO film. The O-K edge presented in Figure 78 is associated to the transition from O 1s to O $2p_\pi$ and O $2p_\sigma$ states, and is a typical wurtzite ZnO O-K edge, which confirms once again that the AZO films grew in a wurtzite structure of ZnO. In the O-K edge, 7 contributions labelled $A_{O\text{-}K}$, $B_{O\text{-}K}$, $C_{O\text{-}K}$, $D_{O\text{-}K}$, $E_{O\text{-}K}$, $F_{O\text{-}K}$ and $G_{O\text{-}K}$ can be identified. Doping ZnO with Al enhances the p-d coupling leading to higher localization of those different features and, therefore, more pronounced peaks **[239]**. As for the evolution of the different contributions in Figure 78, it occurs as follows: The peaks $A_{O\text{-}K}$ to $F_{O\text{-}K}$ present in the AZO film deposited from a 1 at.% Al target decrease in intensity when the Al content increases, and completely disappear in the AZO film deposited from a 10 at.% Al target where the $A_{O\text{-}K}$ to $F_{O\text{-}K}$ contributions are merged together. However, it is difficult to determine the reason behind this; it could be either due to the poor activated Al doping or the lower crystallinity that is displayed through smeared out contributions. Also, the $D_{O\text{-}K}$ feature becomes broader when the Al content in the AZO films increased; this was ascribed to the formation of Al-O bonds as well as the

deterioration of the crystallinity of the films, which was clearly verified from our XRD and TEM data **[4]**. The absence of a pre-edge peak at around 530 eV in our samples indicates that molecular oxygen has not been introduced in contrast to the study from Yuste et al. **[240]** who detected it in films deposited by reactive DC sputtering in O_2-rich atmospheres.

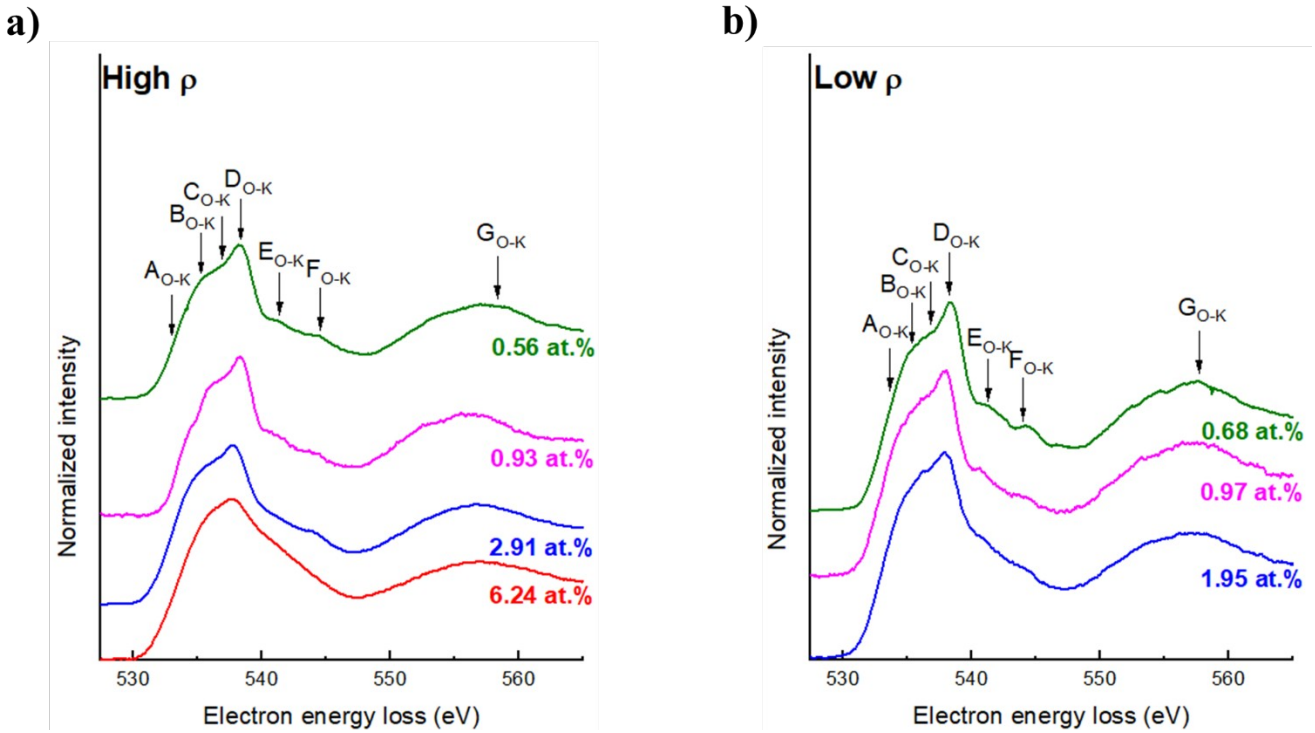

Figure 78: O-K electron energy loss near edge structure at the **a)** *high ρ* and **b)** *low ρ* positions of the AZO films with 0.56/0.68 at.% of Al deposited from a Zn/Al 1 at.% target, 0.93/0.97 at.% of Al deposited from a Zn/Al 2 at.% target and 2.91/1.95 at.% of Al deposited from a Zn/Al 5 at.% target, with the at.% values representing the real Al at.% in the AZO films *high ρ*/*low ρ* positions. Only the AZO film with 6.24 at.% of Al deposited from a Zn/Al 10 at.% target is shown.

While the Zn-L_3 and O-K edges did provide valuable general information for this analysis, the following sections dedicated to the Al-K and Al-$L_{2,3}$ edges of the aluminum might be able to give us information on the Al dopant activation/deactivation.

5.3. Al-K and Al-$L_{2,3}$ edge analysis

In **Figure 79**, the Al-K edge spectra of the AZO films both in the *in-axis* (**Figure 79 a)**) and *off-axis* (**Figure 79 b)**) positions is presented. Three main contributions can be distinguished: $A_{Al\text{-}K}$, $B_{Al\text{-}K}$, and $C_{Al\text{-}K}$. $A_{Al\text{-}K}$ is a non-bonding contribution and $C_{Al\text{-}K}$ an anti-bonding orbital σ^* both resulting from the p-d hybridization splitting of the T_2 orbital in Al_{tet} where the Al dopant substitutes Zn in the wurtzite

structure of ZnO in a tetrahedral conformation. $B_{Al\text{-}K}$ is mainly ascribed to the T_{1u} orbital in Al_{oct} when an Al_2O_3-like configuration or a homologous $Al_2O_3(ZnO)_m$ phase exists in the AZO film with the Al place din a octahedral conformation **[3,7,193]**. Yet, Y. Etinger-Geller et al. **[241]** assigned both the contributions $A_{Al\text{-}K}$ and $B_{Al\text{-}K}$ to Al_{oct}. This can be explained by the fact that the peak $A_{Al\text{-}K}$ can be observed in both Al_{oct} and Al_{tet} which was also observed by Vinnichenko et al **[4]**. Because the normal electron energy range of the Al-K edge is close to the upper detection limit of the detector used in this study, our Al-K edge spectra have a weak signal/noise ratio compared to the Al-$L_{2,3}$ edge **[242]**. We were not able to obtain the Al-K edge for the AZO films with the lower Al contents (0.56, 0.68, 0.93 and 0.97 at.%) because of the low sensitivity. Of the most important conclusions that can be drawn from the Al-K edge is the activation or non-activation of the Al dopant in the AZO films. In fact, when the Al atom is able to substitute the Zn atom in the wurtzite structure in the tetrahedral position, the activation is complete. However, when the Al atom is in an octahedral coordination with Al, there is an excess of oxygen that prevents the Al from producing free electrons, the dopant is then deactivated. The increase or decrease of the $B_{Al\text{-}K}$ peak may be indicative of such changes i.e. the more the peak $B_{Al\text{-}K}$ is prominent the more deactivated Al might be present in the film **[3]**. Despite the fact that some fluctuations seem to manifest in the intensities of the different contributions, unfortunately, since our Al-K spectra are not very clear, we could not draw much information on the activation/deactivation of the Al dopant. For this reason, we resorted to the Al-$L_{2,3}$ edge discussed in the following part of this section.

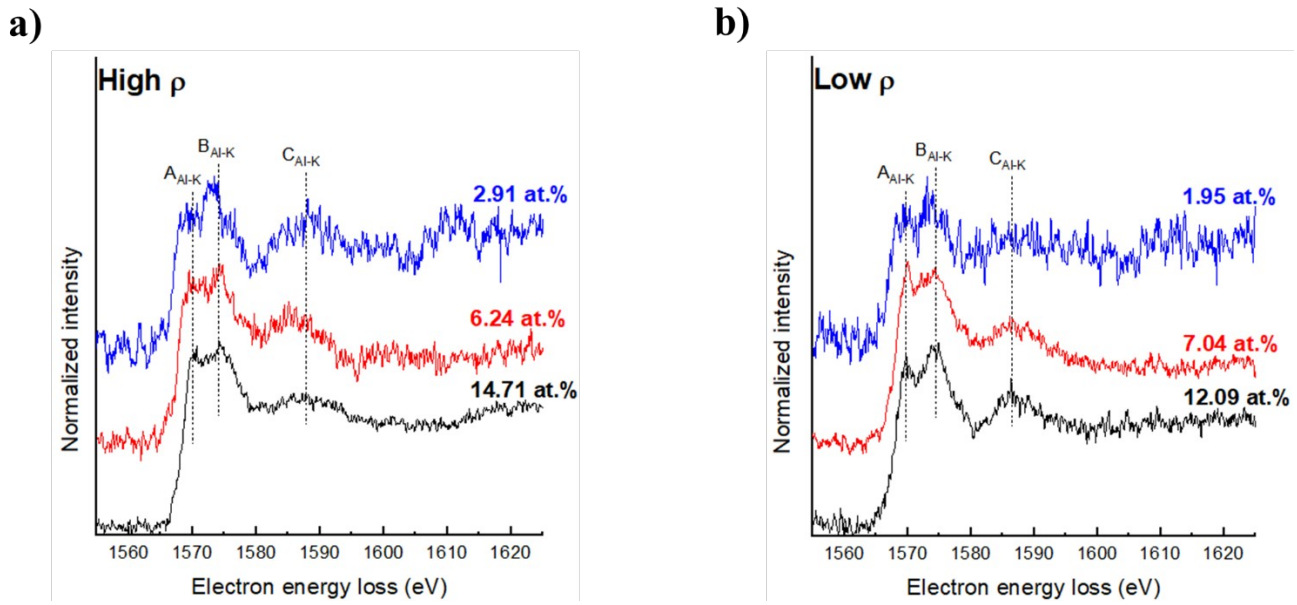

Figure 79: Al-K electron energy loss near edge structure at the **a)** *high ρ* and **b)** *low ρ* positions of the AZO films with 2.91/1.95 at.% of Al deposited from a Zn/Al 5 at.% target, 6.24/7.04 at.% of Al deposited from a Zn/Al 10 at.% target and 14.71/12.09 at.% of Al deposited from a Zn/Al 15 at.% target with the at.% values representing the real Al at.% in the AZO films *high ρ*/*low ρ* positions.

In **Figure 80**, the Al-$L_{2,3}$ edge of all the AZO films is presented. The Al-$L_{2,3}$ edges is the result of the electronic transition from the Al-$2p_{\frac{3}{2}}$ (L_3 edge) and the Al-$2p_{\frac{1}{2}}$ (L_2 edge) states to the Al-s and Al-d derived states where the L_2 and L_3 edges correspond to the signal below and above ≈105 eV, respectively. In a general view, one can see that the features at the L_2 edge are broader and weaker replica of those at the L_3 edge. At the bottom of both edges, and for AZO films with ≤ 2.91 at.% Al, the ELNES spectra presents a wide signal that, to the best of our knowledge, has not been found or attributed to either Al in a tetrahedral or octahedral conformation in the ELNES or XANES analyses of minerals. We believe that this is the first time that the Al-L_3 edge ELNES is collected on AZO. Therefore, this contribution that appears specific to AZO films with low Al contents might be a specific feature of electrically active Al. Interestingly, Imai et al. **[243]** and Wang et al. **[244]** have found that the electronic conductivity in AZO films comes from the highly delocalized Al 3s state that appears near the Fermi level next to the CB's minimum. Imai et al. **[243]** have calculated the partial density of Al 3s state in AZO containing 0.93 at.% Al and found that it contains a broad contribution near the bottom of the CB, close to the Fermi level. We believe that this is seen in our ELNES spectra at the Al-$L_{2,3}$ edges as broad features for the AZO films with less than 2.91 at.% of Al. If we are right, this feature in the Al-$L_{2,3}$ ELNES is very specific to active Al in ZnO and these broad Al-3s contributions would thus be very useful for determining the activation/inactivation of the Al dopant. Next, J.A. Van Bokhoven et al. **[245]** ascribed the feature named $B_{Al\text{-}L}$ in our work to Al in a tetrahedral conformation which means the successful substitution of Zn by Al in the original wurtzite structure of ZnO and so the confirmation of an active Al doping. Yet, this feature is relatively close in shape to that of octahedral Al. Moving on to the AZO films with Al contents higher than 6.24 at.%, one can already tell that their spectral shape is quite different. First, they do not show the evident presence of the broad features detected in the films with lowest Al contents. In contrast they all exhibit the $A_{Al\text{-}L}$ feature naturally present for Al in minerals. This feature seems more localized in the *high ρ* position. Yet, it is not easy to ascribe to octahedral or tetrahedral aluminum since it exists in both conformations **[245]**. Nevertheless, the broadening of feature $B_{Al\text{-}L}$ compared with that in the films of lower Al contents is in line with the presence of Al_{oct} and, therefore, with the dopant deactivation and our electrical analysis (**Section 4.3.1 of Chapter 4**). Despite that we do not see clear evidence at first sight of the presence of the broad signals we attributed above to dopant activation in the spectra corresponding to films containing 6.24 at.% Al or more, some slight changes may be indicative of their contribution to the spectral shape. Indeed, in the AZO films containing 6.24 and 7.04 at.% of Al, one can see that the $A_{Al\text{-}L}$ contribution is broader than for the higher films containing 12.09 and 14.71 at.% Al and small humps are present at the left

side of feature $A_{Al\text{-}L}$ and at the right side of feature $B_{Al\text{-}L}$. This means that the ELNES spectra for the AZO films with 6.24 at.% of Al and up are possibly constituted by a convolution of active and inactive Al signals.

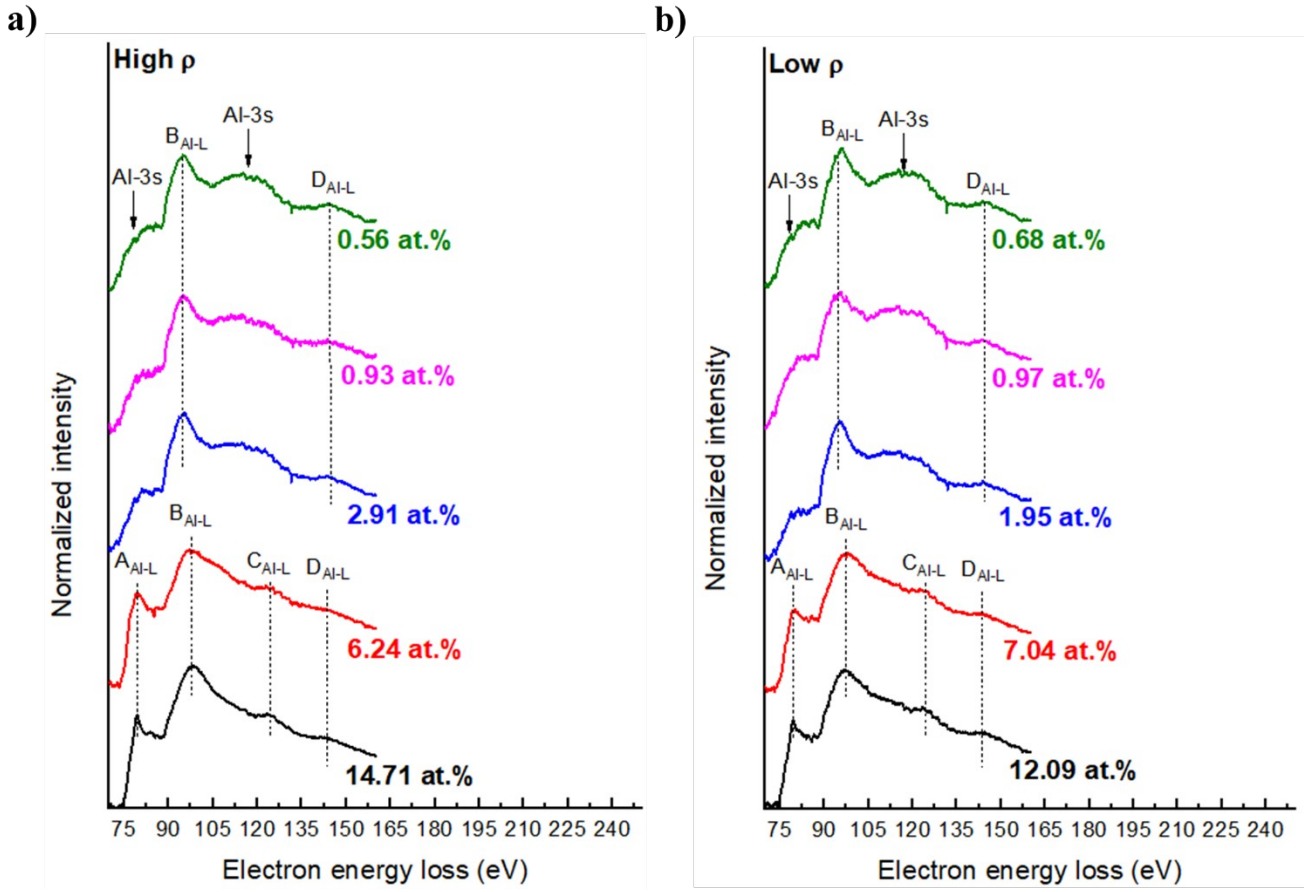

Figure 80: Al-$L_{2,3}$ electron energy loss near edge structure at the **a)** *high ρ* and **b)** *low ρ* positions of the AZO films with 0.56/0.68 at.% of Al deposited from a Zn/Al 1 at.% target, 0.93/0.97 at.% of Al deposited from a Zn/Al 2 at.% target, 2.91/1.95 at.% of Al deposited from a Zn/Al 5 at.% target, 6.24/7.04 at.% of Al deposited from a Zn/Al 10 at.% target and 14.71/12.09 at.% of Al deposited from a Zn/Al 15 at.% target with the at.% values representing the real Al at.% in the AZO films *high ρ*/*low ρ* positions.

To try to prove this assumption, we mixed the reference ELNES spectra of inactive Al with that of active Al (0.56 at.% Al) in order to model the ELNES spectra of the AZO film with 7.04 at.% of Al. The inactive Al was the result of a possible overlap of the signal of inactive Al (supposedly octahedral) with that of active Al in the ELNES spectra of the 14.71 at.% Al sample, by trying to maximize the intensity of the $A_{Al\text{-}L}$ feature and the bump at the right side of $B_{Al\text{-}L}$. The results are shown in **Figure 81**, with the ELNES spectra of the 14.71 at.% Al sample being composed of 70 mol. % of inactive Al and 30 mol. % of active tetrahedral Al, and that of the 7.04 at.% sample is composed by a mixture of 55 mol. % of inactive Al and 45 mol. % of active tetrahedral Al. Even though the reproduction of the $A_{Al\text{-}L}$ feature broadening is not perfect, the model still reproduces the

inactivation of the Al dopant when the Al content, and also the resistivity, increases. This model might be useful for future studies that need to determine the solubility of the Al dopant in the wurtzite structure of ZnO as well as the activation/deactivation of the Al dopant in far out of stable equilibrium conditions. For example, using reactive HiPIMS in our work to deposit the AZO films led to a possible solubilization of ≈ 3 at.% of Al into ZnO. Nonetheless, some of the Al atoms in the 0.56 at.% Al film that served as reference for tetrahedral Al may already be in deactivated conformation. Hence, future works might be needed to refine this model.

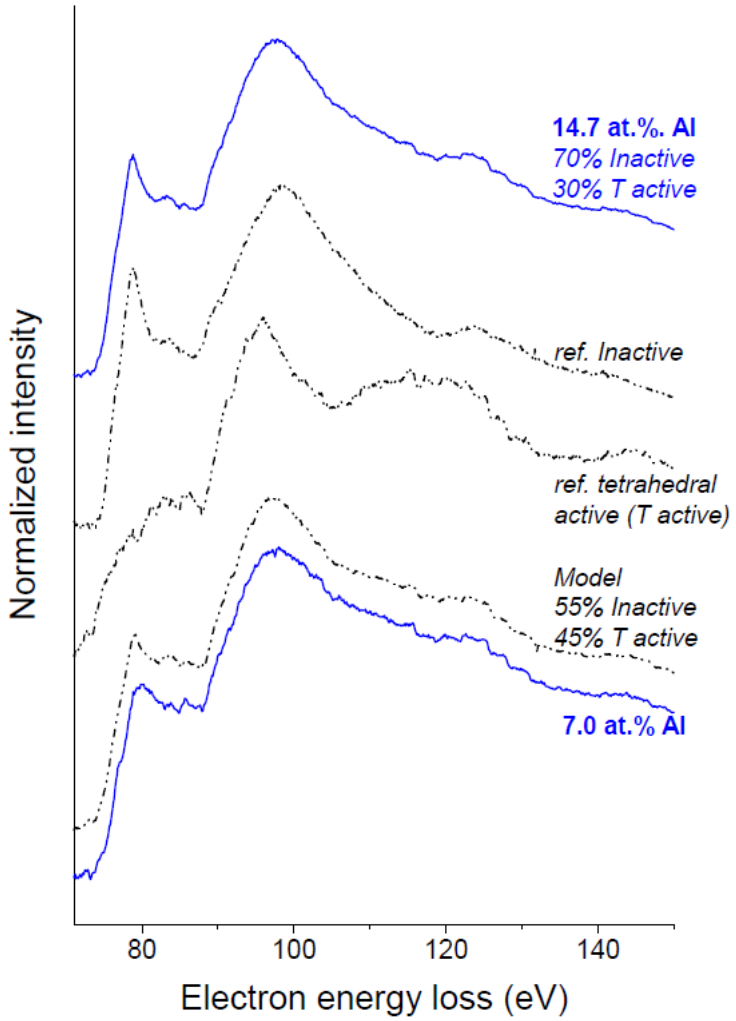

Figure 81: Al-$L_{2,3}$ edges reference spectra for electrically inactive and active Al serving as a basis to extract the proportions of inactive and active Al.

5.4. Chapter conclusions

In this chapter, we studied the activation/inactivation of the Al dopant in AZO films by analyzing the ELNES spectra obtained from the electronic structure measurements performed on the AZO films deposited from Zn/Al targets with 1, 2, 5, 10 and 15 at.% of Al on glass substrates by reactive

HiPIMS in both the *high ρ* and the *low ρ* positions. The AZO films structure and microstructure studied in **Section 3.4 of Chapter 3** by XRD and TEM showed that the films go from a nanocrystalline columnar morphology to ultrafine nanocrystalline films, all of wurtzite structure of ZnO, when the Al content is increased. Also, the studied electrical properties in **Section 4.3.1. of Chapter 4** by the four-point probe setup and the Hall effect conveyed that Al doping is successful for an Al content of up to 3 at.% when employing HiPIMS as a deposition technique without thermal assistance. But from the optical properties studied in **Section 4.2 of Chapter 4** and the Al-$L_{2,3}$ edge of ELNES studied in this chapter, we were able to find signs of dopant activation/deactivation and segregation which is very useful to understand the electrical properties degradation of the AZO films and how to avoid them.

From the Zn-L_3 edge, at least up to 2.91 at.% of Al, we confirmed the wurtzite structure of the AZO films due to the absence of a pre-threshold peak as observed from previous studies. The weaker and smeared out $B_{Zn\text{-}L}$, $C_{Zn\text{-}L}$ and $D_{Zn\text{-}L}$ features when the Al content increased were probably due to the crystallinity degradation and the local crystal distortion increase. For example, due to the presence of the (002) peak in the XRD diffractogram of the 7.04 at.% Al film, the Zn-L_3 edge features were still well detectable. They were less defined for the 6.24 at.% Al film because the (002) peak was less intense *in-axis*. From the O-K edge typical of a wurtzite ZnO structure, the features $A_{O\text{-}K}$ to $F_{O\text{-}K}$ were seen to decrease with the Al content increase to finally merge in the 6.24 at.% film. Crystallinity degradation, or the poor Al dopant donor effect might have caused this evolution. Also, the broadening of the $D_{O\text{-}K}$ feature was assigned to the formation of Al-O bonds and crystallinity degradation. No molecular oxygen is present in the film due to the absence of a pre-edge peak. To gain more information on the activation/deactivation of the Al dopant, we resorted to the Al-K and Al-$L_{2,3}$ edges. Unfortunately, the Al-K edge was not very clear due to the poor sensitivity of our equipment to large electron energy losses and, therefore, no clear conclusion could be drawn from this edge. However, the Al-$L_{2,3}$ ELNES edge is especially sensitive to the change in the Al conformation of the AZO films, can be easily measured with the EELS detector used and can more precisely explain the activation/inactivation of the dopant. From the Al-$L_{2,3}$ edge analysis, we were able to conclude that the degradation of the electrical properties at the *in-axis* position, or for high Al content films, is probably due to the segregation of Al in an inactive octahedral conformation with oxygen deduced from broadening of a spectral feature attributable to octahedral Al and the apparent disappearance of a “new” spectral feature likely attributable to active tetrahedral Al and manifesting as a broad feature near the conduction band minimum. Finally, we proposed a model to extract the relative contributions of active and inactive Al in AZO and that could be efficiently used by future

works to understand the degradation of the electrical properties of the AZO bulk and thin films, as well as to optimize them. In the next and final chapter, we will use the results obtained from **Chapters 3 to 5** to deposit an AZO transparent electrode, and fabricate then characterize flat and structured solar cells devices based on a ZnO/Cu_2O heterojunction.

Chapter 6

Towards ZnO/Cu_2O patterned solar cells

6.1. Introduction

As has been mentioned several times in this work, AZO films are very interesting TCO materials used as replacement for ITO layers in various applications. Among these applications, the fabrication of a solar cell device with the extensively optimized AZO transparent electrode was the ultimategoal in this work. Additionally, we aimed for a patterned solar cell and a n-ZnO/p-Cu_2O heterojunction-based solar cell structure. In fact, photovoltaics is among the most interesting renewable energy sources with a sustainable energy supply. It responds to the need to protect the environment, climate and resources while still maintaining a high quality electrical power. However a cost reduction of the power generation by solar cells, from the economic, energetic and environmental point of views, is necessary to maintain their popularity in the industry and market. For this reason, light trapping by solar cell structuring was adopted to increase the optical path in the cells. This ensures a higher photon absorption within the cell increasing its photocurrent generation and thus efficiency **[246,247]**. Additionally, substrate structuring makes room for active layers thinning which can reduce material consumption, enhance production rates and decrease the carrier collection length and bulk recombination. One should mention that thin active layers are very bad light absorbers; which is why to benefit from their aforementioned positive effects on the efficiency of the solar cell, substrate texturing is considered a good solution. Structures would be of different forms depending on the sought application such as pyramidal texture, periodical nanodomes or nanocones, sinusoidal patterns, etc. **[247]**. The latter was the structure of choice in this work due to its very efficient light trapping mechanism displayed in **Figure 29**. Our solar cell model also adopted the n-ZnO/p-Cu_2O heterojunction widely used in photovoltaics and photocatalysis due to its interesting properties **[96,248]**. For one, such heterojunction was a solution adopted to try producing good efficiency of Cu_2O-based solar cells by inserting an appropriate n-type semiconductor material. n-ZnO was a good

choice due to the favorable alignment of the conduction band edges of ZnO and Cu_2O **[92-96]**. However, it is important to eliminate the lattice-mismatch defects between the two layers as not to compromise the performance of the solar cell shown by the rectifying behavior of the I-V curve **[95]**. In fact, the growth sequence of the two layers affects the valence band-offset of the heterojunction, and it is more delicate in n-ZnO/p-Cu_2O heterojunctions due to the large difference in lattice parameters between the two layers; the ZnO being a wurtzite structure type (a = 3.25 Å and c = 5.21 Å) while Cu_2O grows in a cubic structure (a = 4.27 Å) **[96]**.

This main goal of this study was the optimization of the AZO films as a function of their Al content to enable them to be used as transparent electrodes in solar cells, which is the application envisaged in this work. From the previous chapters, we were able to understand that the increase in Al content led to the degradation of the films properties on many levels; optical, electrical, structural and electronic structural levels. While the previous chapters were dedicated to the interpretation of these observations and analyzing their origin, this chapter considers the AZO films deposited from 1 and 2 at.% Al targets as the films with properties conform with transparent electrode demands. These low Al content films proved to be highly conductive (≈ 1.5 x 10^{-3} Ω.cm) with a suitable transmittance (≈ 70%) which is the compromise required for their use in solar cells. In order to fabricate a complete solar cell device, we will consider a structured glass substrate with different periodicities patterned by USP-DLIP with a picosecond laser, the aforementioned AZO films as the transparent electrode, a ZnO film deposited by DC sputtering with a Cu_2O film grown on top by ALD in order to form the n-ZnO/p-Cu_2O heterojunction of this solar cell, and finally the gold contact layer. We should mention that the following results are done either on a complete solar cell device, or a sample with different layers in preparation to be turned into a complete solar cell but was fabricated for various characterizations. We named such samples “towards solar cells” samples. Gradually, we will present the results related to the glass substrate patterning via the modelling done by Dr. Marcos Soldera from the Institut für Fertigungstechnik of the Technische Universität Dresden **[1]** and the actual patterning performed at the chair of Functional Materials of Saarland University. Next, the morphological and structural properties will be studied to verify the correct growth of the Cu_2O film on top of ZnO by ALD and not the CuO film. The results from top view and cross-section SEM images collected by a FIB microscope, especially for structured samples will be shown. The structural and microstructural analysis will be extended to TEM analysis including TEM images, micro-diffractions, HR-TEM images and their FFT. From the STEM technique, we will also perform chemical analysis on the samples mainly by EDS and ELNES in order to probe the distribution of the Zn, Al, O and Cu species in the different layers, and especially confirm through ELNES at the O-K

and Cu-L edges the formation of the Cu_2O phase. Finally, two solar cells series will be tested by I-V measurements in the last section of this chapter.

6.2. Glass substrate structuring

In this section, the solar cell modelling done by Dr. Marcos Soldera **[1]** is divided into two simulation runs. The first one was mainly needed to determine what structure periodicity or range of periodicity is needed for successful photocurrent production by the solar cells. The second one was performed after a first set of testing.

From the first simulation run, we start by presenting the graph in **Figure 82** where the photocurrent is plotted as a function of the Cu_2O film thickness for two modelling methods; the Transfer Matrix Method (TMM) only suitable for flat or 1D solar cells and the Finite Element Method (FEM) that will be used for the simulation of the structured solar cells. One can see that the FEM method agrees with the well-established TMM method, which makes it convenient for the simulation of structured solar cells. For the Cu_2O semiconductor with a band gap of approximately 1.95 eV, the ideal and maximum attainable photocurrent is 16.36 mA/cm^2.

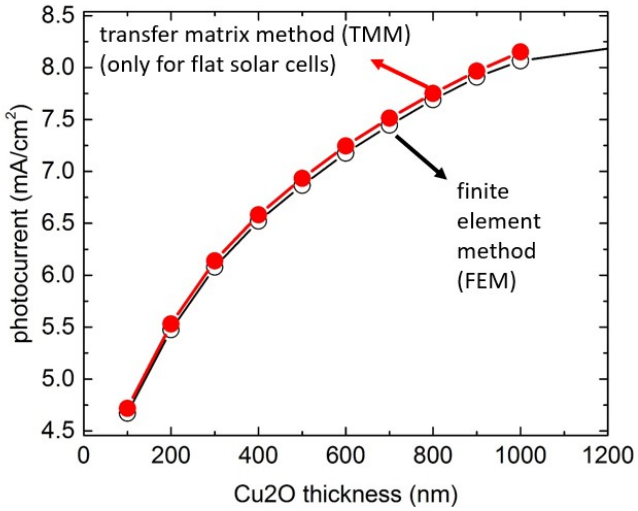

Figure 82: Photocurrent (mA/cm^2) as a function of the Cu_2O layer thickness (nm) for the Transfer Matrix Method (TMM) and the Finite Element Method (FEM).

In **Figure 83**, the evolution of the photocurrent as a function of the structure period for three Cu_2O film thicknesses of 100 (**Figure 83 a)**), 300 (**Figure 83 b)**) and 500 (**Figure 83 c)**) nm is presented. For each of the thicknesses, the case of a flat cell and structured cells with 100, 200 and 300 nm

structure height or depth are studied as well. The arrows represent the maximum relative photocurrent increase. One can see that when the Cu_2O film thickness increased, the photocurrent reached higher values due to the reduced carrier collection length and bulk recombination. And for each graph at a constant thickness, other than the fact that the photocurrent is higher for a structured cell than for a flat one, the photocurrent increased with structure depth or height since light trapping is more efficient. Additionally, the photocurrent decreased with the increase in structure period. The exact reason or mechanism behind these evolutions was extensively explained in **Section 2.3 of Chapter 2**. One must mention that larger heights could be numerically tested but they would be more difficult to fabricate. Thicker Cu_2O films could also be simulated but this reduces the experimental efficiency, due to the typically short carrier diffusion lengths in this material. From these results, one can conclude that high Cu_2O thicknesses and structure heights but low periods are needed. Ideally, we need to produce structures on the glass substrate with a periodicity as low as 1 µm and a structure height as high as 300 nm. As for the Cu_2O film thickness, it was not possible in a first approach to produce high thicknesses because ALD is employed as the deposition method for this layer in the solar cells; in fact it could take almost two days to produce a maximum thickness of 70 nm. Future fabrications may combine ALD and sputtering. The optical losses were calculated and shown in the **Appendices** (**Figure A5**).

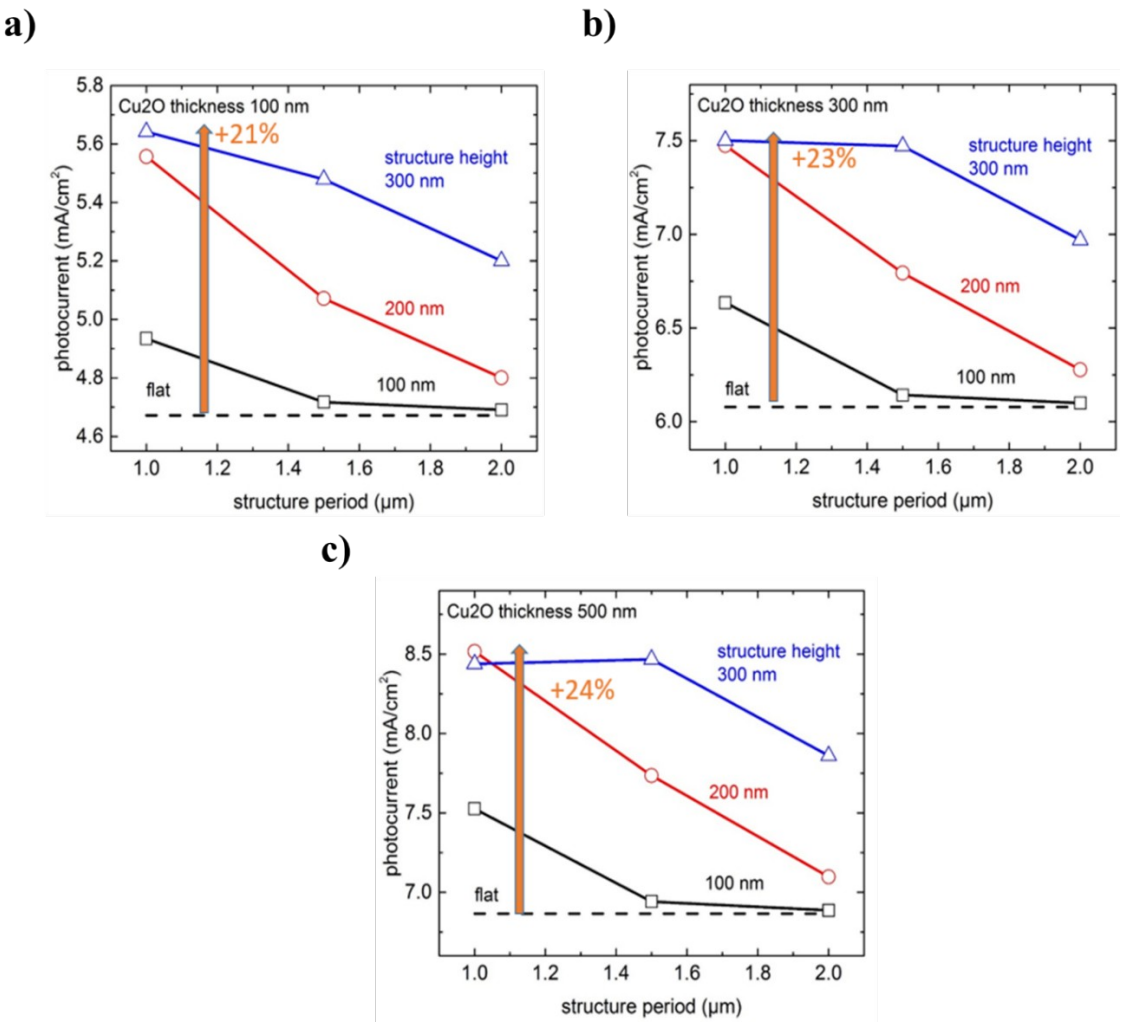

Figure 83: Photocurrent (mA/cm^2) as a function of structure period (µm) for Cu_2O layer thicknesses of **a)** 100, **b)** 300 and **c)** 500 nm. In each graph, the case of a flat cell and a structured cell with 100, 200 and 200 nm structure height are considered. The arrows represent the maximum relative photocurrent increase.

Based on the previous simulation run, the glass substrates were structured by USP-DLIP with a picosecond laser aiming to produce a low structure periodicity of 1 µm and the deepest possible structure height. Structure periodicities of 1, 1.5 and 2 µm were tested and observed by the CLSM; the images are shown in **Figure 84**. One can see that the patterning was quite successful for the 1.5 and 2 µm structure period; both the period structures had a maximum structure depth of 0.6 µm which is quite good for a glass substrate. However, the 1 µm structure period was not successful, at least on a glass substrate and/or by means of a picosecond laser, since no patterning was observed from the microscope image. Consequently, glass substrates patterned with a 1.5 and 2 µm periodicity could be tested in the to be fabricated solar cell devices.

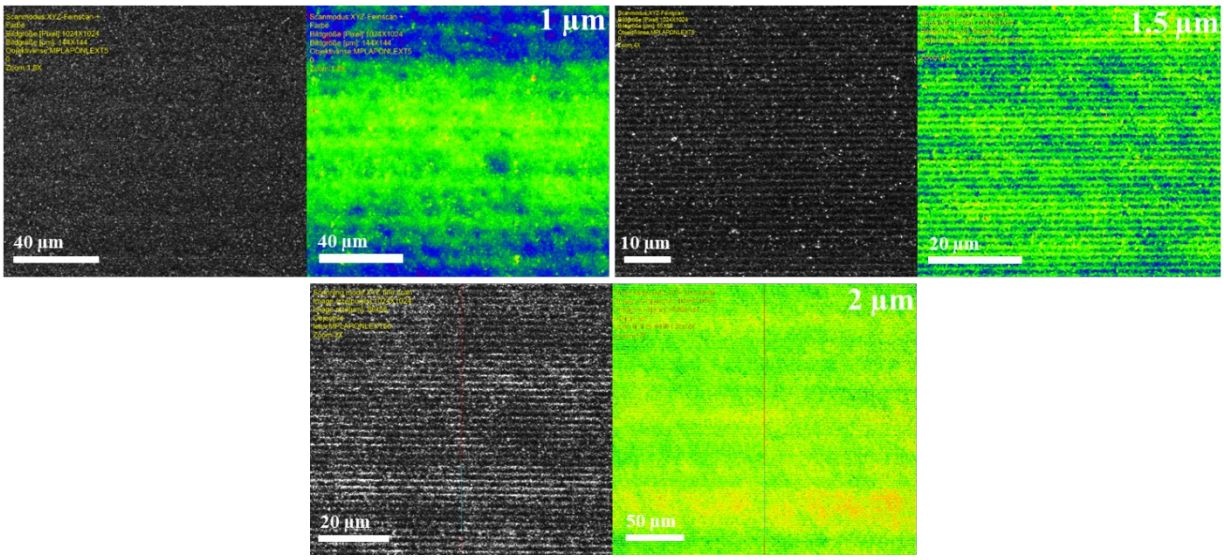

Figure 84: CLSM images taken on the glass substrate structured by a picosecond laser with structure periodicities of 1, 1.5 and 2 µm.

Based on the previous results, Dr. Marcos Soldera **[1]** conducted a second simulation run presented in **Figure 85**. The photocurrent graph was this time presented as a function of structure depths going from 0 nm (flat cell) to 600 nm, which was the maximum obtained depth with our patterning tests. Also, the three thicknesses of Cu_2O were again considered. The arrows represent the maximum relative photocurrent increase. Same as was seen from the graph of the first simulation run (**Figure 83**), the photocurrent increased with the Cu_2O film thickness. What is interesting though, is that the photocurrent already reaches a maximum around 300 to 450 nm of structure height and continues to saturate up to 600 nm. This saturation could be due to the limited light trapping effect by the designed structure; this means that 300 nm structure depth is already sufficient for significantly improved photocurrent generation. The optical losses were again calculated and shown in the **Appendices** (**Figure A6**).

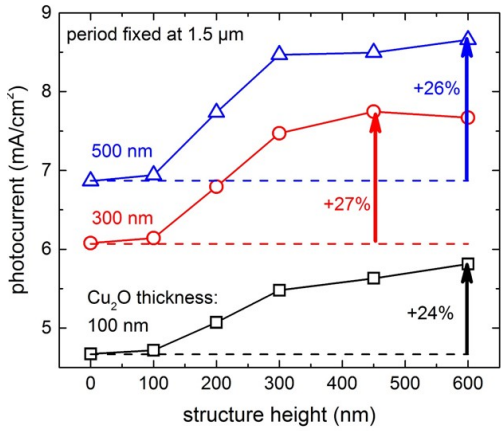

Figure 85: Photocurrent (mA/cm^2) as a function of structure height (nm) for Cu_2O layer thicknesses of 100, 300 and 500 nm. The structure period was fixed at 1.5 µm and the arrows represent the maximum relative photocurrent increase.

In conclusion, the patterned glass substrate adopted for the elaboration of the solar cells in this study are of 1.5 µm and 2 µm periodicities and of 0.6 µm depth.

6.3. Morphology, structure and microstructure

This section is dedicated to the study of the morphology, structure and microstructure of the "towards solar cells" devices, as well as the realized solar cell devices.

A Cu_2O layer was grown by ALD on top of the ZnO deposited by DC sputtering under 8 sccm of oxygen flow rate, to study the structure of the ZnO/Cu_2O heterojunction. In **Figure 86** we show the X-ray diffractograms of the heterojunction deposited on a glass substrate, and on a Si substrate placed at 2 and 8 cm from the substrate-holder axis for comparison. We note that the untextured XRD diffractogram of the Glass/ZnO/Cu_2O sample (**Figure 86 b)**) was treated this way by **[Pascal Boulet, Head of the XGamma competence center (CNRS)-Institut Jean Lamour Nancy]** in order to see the peaks assigned to the Cu_2O layer; the logarithmic scale was also necessary to be able to see the smaller peaks. The ZnO clearly grew in a wurtzite structure but this time not necessarily preferentially oriented in the *c*-axis direction, as suggested by the presence of the (100) and possibly the (101) peaks. The Cu_2O was successfully obtained due to the clear presence of the (311) and (220) peaks of the cuprite phase. The (111) peak however is very closely positioned to the (101) peak of ZnO and is hardly distinguished by XRD. The same goes for the peak at approximately 93° assigned to the (222) peak of Cu_2O and (202) of ZnO. Next, in the XRD diffractograms of the Si/ZnO/Cu_2O heterojunction with the ZnO deposited at 2 or 8 cm from the substrate holder axis in **Figure 86 c) and d)**, one can see that the ZnO is again in a wurtzite structure of ZnO verified by the (002) and (004) peaks. This time, the Cu_2O is even more clearly identified from the (110) and the (220) peaks. At 8 cm however, an extra peak at 37° can be either attributed to the ZnO layer or the Cu_2O one. One can notice that this peak does not exist in the X-ray diffractogram of the DC Si/ZnO (**Figure 86 a)**) and the Si-2cm/ZnO/Cu_2O sample. This means that this peak is most probably assigned to the ZnO film deposited at a different position relative to the substrate-holder axis. Nonetheless, one might wonder about the effect of the Zn orientation on the growth orientation of the Cu_2O film by ALD not visible from the XRD analysis. For this reason, an extensive study of the structure and microstructure will be presented later on in this section.

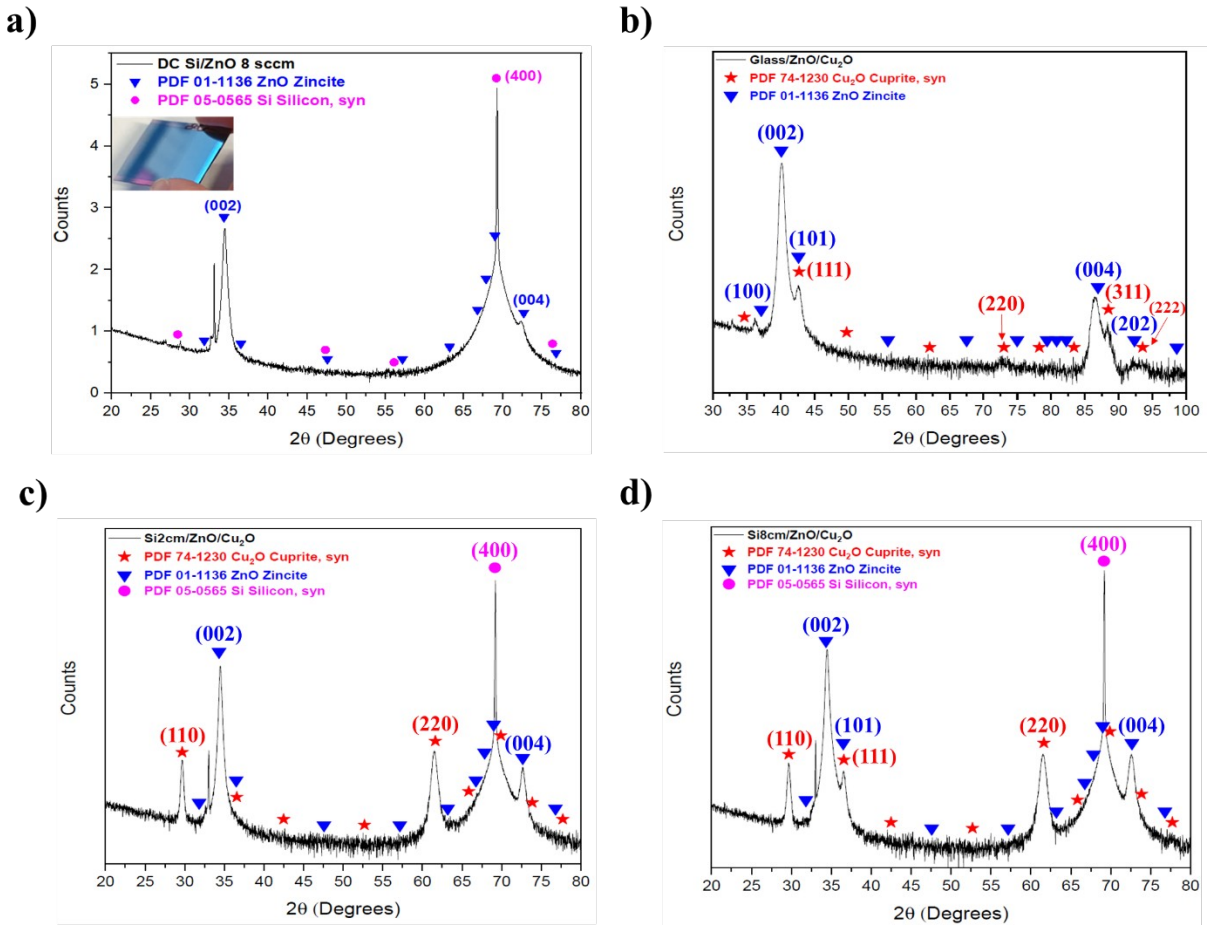

Figure 86: **a)** X-ray diffractogram of a ZnO film deposited on a Si substrate by DC at 2 cm from the substrate-holder axis at 8 sccm oxygen flow rate. In the inset is shown the photo of the corresponding film; **b)** Untextured X-ray diffractogram of a Glass/ZnO/Cu_2O sample **[Pascal Boulet, Head of the XGamma competence center (CNRS) -Institut Jean Lamour Nancy]**; X-ray diffractogram of **c)** a Si-2cm/ZnO/Cu_2O sample and **d)** a Si-8cm/ZnO/Cu_2O sample. The peaks assigned to ZnO, Cu_2O and Si are indexed respectively in blue triangles, red stars and pink dots; their reference is indicated in the legend on the far left of each graph.

In **Figures 87 and 88**, cross-sections of the Glass/ZnO/Cu_2O (1-A), Glass/AZO1at.%/ZnO/Cu_2O (1-B) and Structuredglass1.5µm/AZO1%/ZnO/Cu_2O (1-C) samples, are shown respectively. For the abbreviations of each sample, the reader can refer back to **Table 2** in **Section 2.4 of Chapter 2**. The images for the (1-A) and (1-B) samples were mainly shown for comparison with that of the (1-C) sample; they will also be observed by TEM later in this section. The top view of the (1-C) sample shows columns closely positioned towards one another with no gaps or deformations visible. While the (1-A) and (1-B) samples consisted of very well adhered films on the substrate and between each other, the (1-C) cross-section shows cavities between the AZO and ZnO films as well as at the bottom curve of the structure. The detachment of the ZnO film from the AZO film might be due to a

non-sufficient RF cleaning prior to the DC sputtering of the ZnO on the underlying AZO film. Further observations are needed and will be presented later on to better observe these cavities.

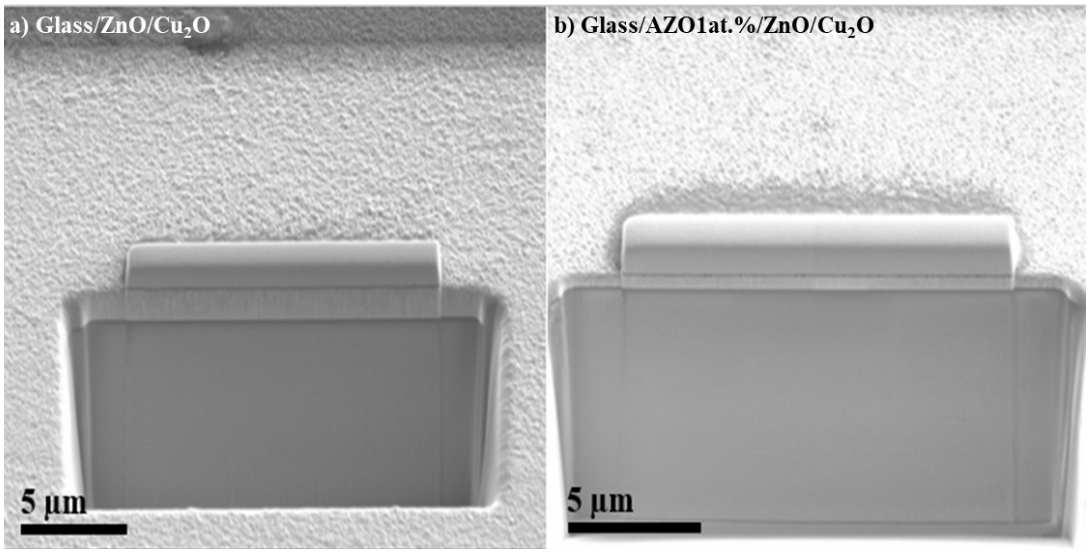

Figure 87: Top and cross-section SEM images taken with a FIB microscope of **a)** Glass/ZnO/Cu_2O (1-A) and **b)** Glass/AZO 1 at.%/ZnO/Cu_2O (1-B).

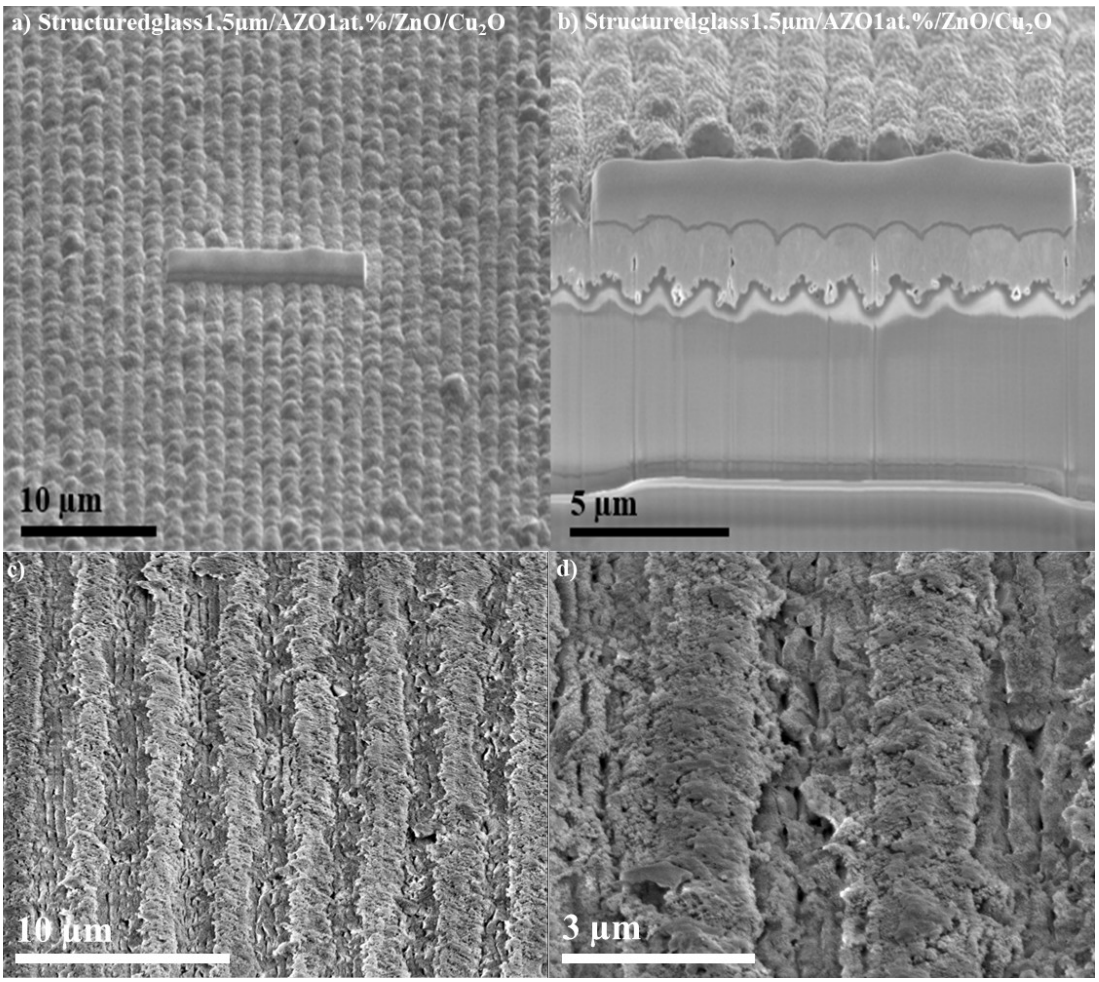

Figure 88: SEM images taken with a FIB microscope of a Structured glass1.5µm/AZO1at.%/ZnO/Cu_2O (1-C) samples from **a)** a top view and **b)** a cross-section view. The images in **c)** and **d)** are shown for reference; they are of a femtosecond laser structured glass substrate with 3 µm periodicity provided by **[Daniel Müller, Group Leader-Surface Engineering at the Chair of Functional Materials, Saarland University]**. The samples were coated with a thin layer of $Au_{80}Pd_{20}$ for observation with the SEM microscope.

In the following, the images resulting from the TEM measurements for the (1-A), (1-B) and (1-C) samples as well as for the Si-2cm/ZnO/Cu_2O and Si-8cm/ZnO/Cu_2O samples are presented.

In **Figure 89**, the TEM image of the Glass/ZnO/Cu_2O sample (**Figure 89 a)**) is displayed as well as the SAED image of the ZnO layer (**Figure 89 b)**). One can see that the ZnO film presents a columnar structure typical of wurtzite ZnO thin films. On top of the ZnO film, one can see the presence of a very thin layer of Cu_2O not yet distinguished very well. The SAED of the ZnO film shows that the film grew in a preferential orientation in the *c*-axis direction since the spots corresponding to (002) planes are very bright and oriented along the normal of the substrate.

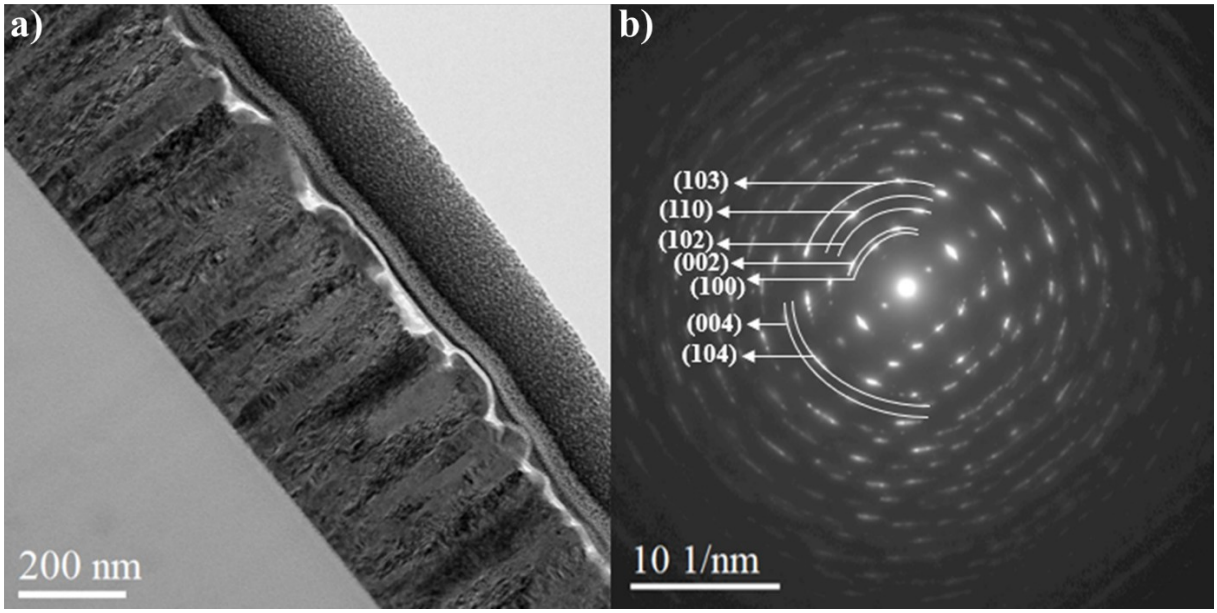

Figure 89: **a)** TEM image of the Glass/ZnO/Cu_2O sample and **b)** SAED image of the ZnO layer of the sample.

Next, we show the TEM results for the Glass/AZO1at.%/ZnO/Cu_2O sample in **Figure 90** consisting of a TEM image, a microdiffraction of the ZnO film (**Figure 90 a)**), an HR-TEM images with its corresponding FFT (**Figure 90 b)**). As was already speculated from the FIB imaging, we do see some gaps between the AZO and ZnO films confirming the need to further increase the RF cleaning time of the AZO film's surface prior to the ZnO film deposition. Both the AZO and the ZnO films present a columnar growth from the glass substrate. The microdiffraction of the ZnO with a $[1\bar{1}0]$

zone axis is shown and it confirms the growth of the ZnO films with (002) planes parallel to the substrate surface. Additionally, a HR-TEM image of the ZnO/Cu_2O heterojunction is shown and the FFT imageds issued from the orange zone on the ZnO films confirms once again its growth with (002) planes parallel to the substrate surface under the same [$1\bar{1}0$] zone axis. So far, the SAED or the FFT of the Cu_2O layer were not shown but they will however be studied further on.

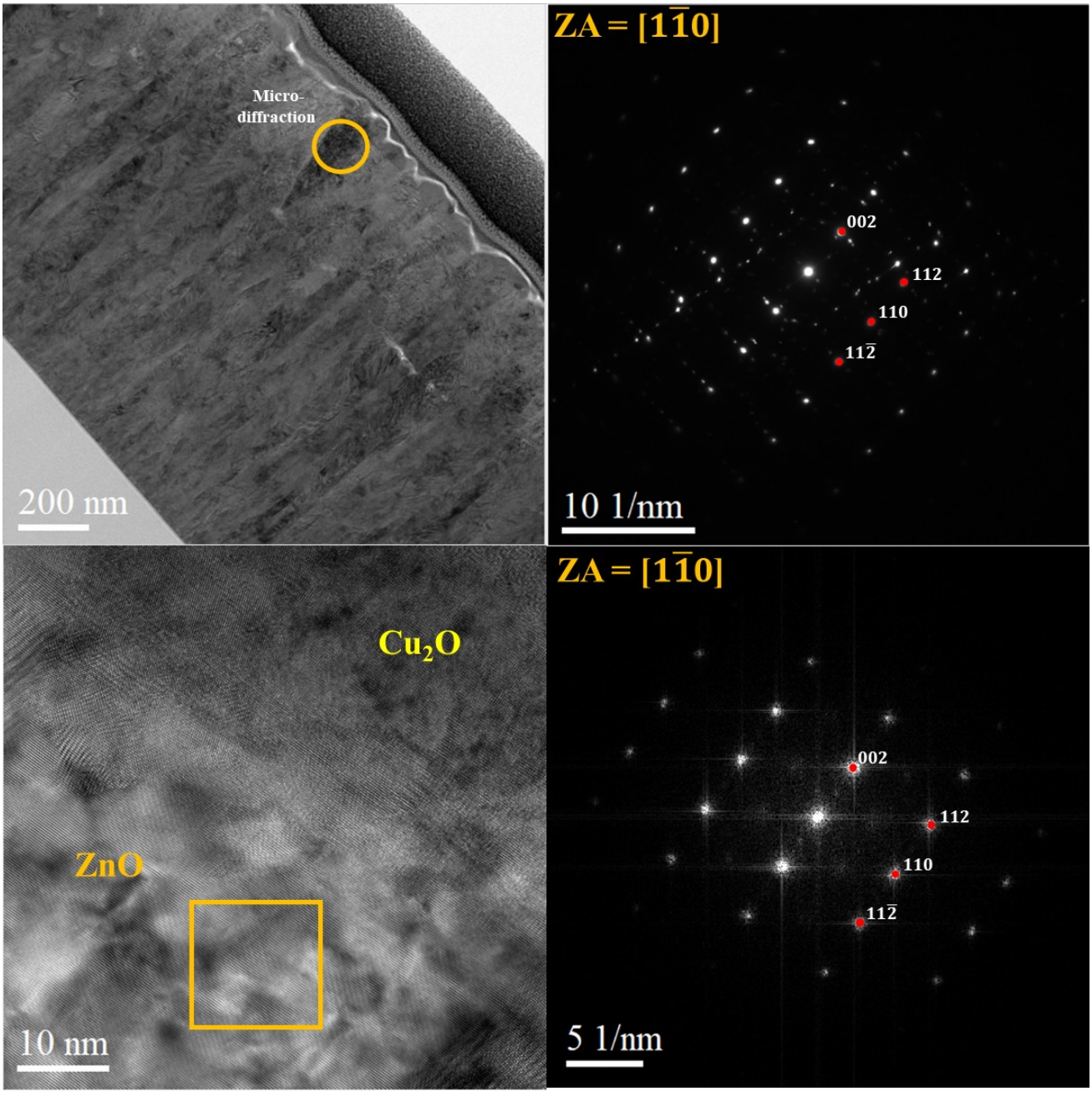

Figure 90: a) (Left) TEM image of the Glass/AZO1at.%/ZnO/Cu_2O sample and (Right) the micro-diffraction image of the orange area shown on the ZnO layer; **b)** (Left) HR-TEM image at the ZnO/Cu_2O heterojunction and (Right) the corresponding FFT image of the orange area shown on the ZnO layer.

Moving on to **Figure 91**, we simply displayed the TEM images of the Structured glass1.5µm/AZO 1at.%/ZnO/Cu_2O sample because the rest of the TEM analysis is the same as for the two previous cases since the films were deposited at the same time, in the same conditions. We confirm from these images, once again, the presence of cavities at the bottom of the structure as well as between the AZO and ZnO films especially in the structure crease. Nonetheless, the AZO and ZnO films grew in a very densely- packed columnar structure with (002) planes parallel to the substrate surface.

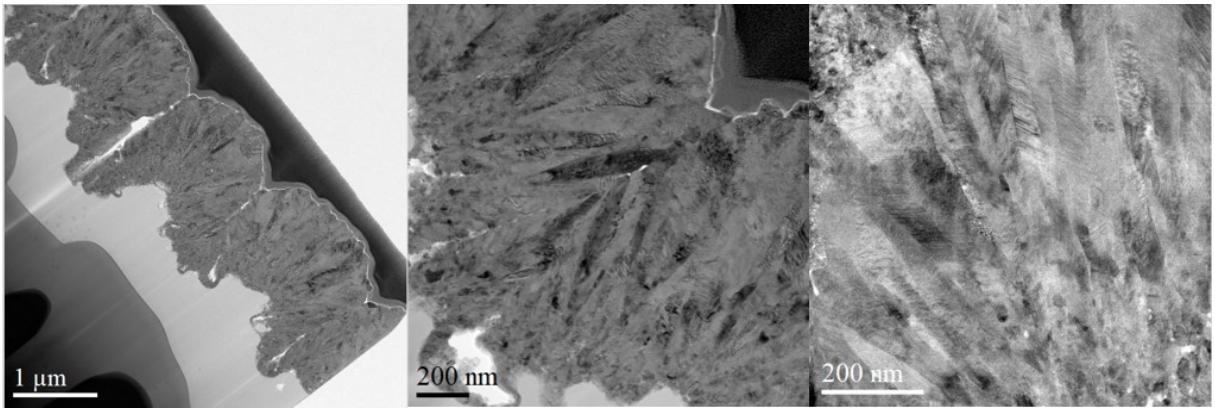

Figure 91: TEM images of the Structured glass1.5µm/AZO1at.%/ZnO/Cu_2O sample.

In another set of samples, the results of the TEM measurements performed on the Si-2cm/ZnO/Cu_2O and Si-8cm/ZnO/Cu_2O samples are displayed. From **Figure 92 a)**, we confirm once again the columnar growth of the ZnO film with the *c*-axis aligned with the growth direction for both samples. Also this time, the Cu_2O layer can be more easily distinguished. What is interesting about this study though, is the HR-TEM images of the sample with their corresponding FFT; micro-diffraction images were also done and available in the **Appendices** (**Figures A7 and A8**). For both the 2 and 8 cm distances, the ZnO film always grew with the (002) planes parallel to the film surface under a [100] zone axis. However, the Cu_2O layer does not grow in the same direction for all samples. In fact, in the Si-2cm/ZnO/Cu_2O sample, the Cu_2O grows in two different directions; [111] and $[11\bar{1}]$ under the respective [110] and $[1\bar{1}0]$zone axis. What is more surprising though, is that in the Si-8cm/ZnO/Cu_2O sample, Cu_2O also grows in two different directions only they are different from the prior ones ($[10\bar{1}]$ and $[1\bar{1}0]$ under the respective [111] and [001] zone axis). This confirms the XRD observations that the growth of the Cu_2O film on ZnO by ALD depends on the position of the substrate relative to the distance to the substrate-holder axis, but not due to the ZnO orientation since the ZnO was always preferentially grown with (002) planes parallel to the substrate surface. And yet, the Cu_2O films grew in different orientations which might be due to the growth conditions and/or possibly due to the termination of the ZnO layer. In fact, a 2 cm deposited ZnO film is far from the target axis while the 8 cm one is directly in front of it. As explained in **Section 4.3.1. of Chapter 4**,

the *in-axis* position may be subjected to bombardment by negative oxygen ions, this introduces acceptor defects among other types of defects which decreases the donor effect of the dopant, and thus the ZnO film in this position is more resistive than the one at 2 cm from the substrate-holder axis. Since ALD is a very sensitive deposition method, the slightest change can induce variations in the film's growth. In our case, this variation of the electrical property is most probably behind this difference of orientation growth of the Cu_2O films.

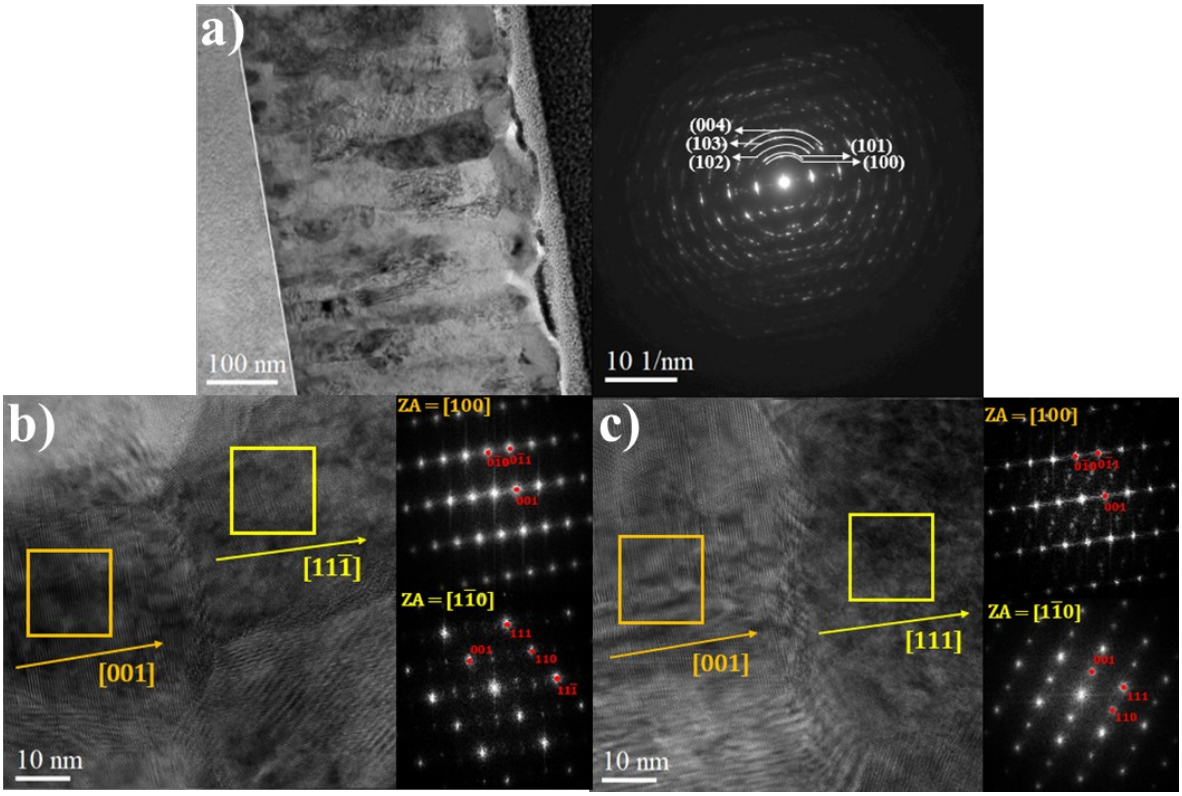

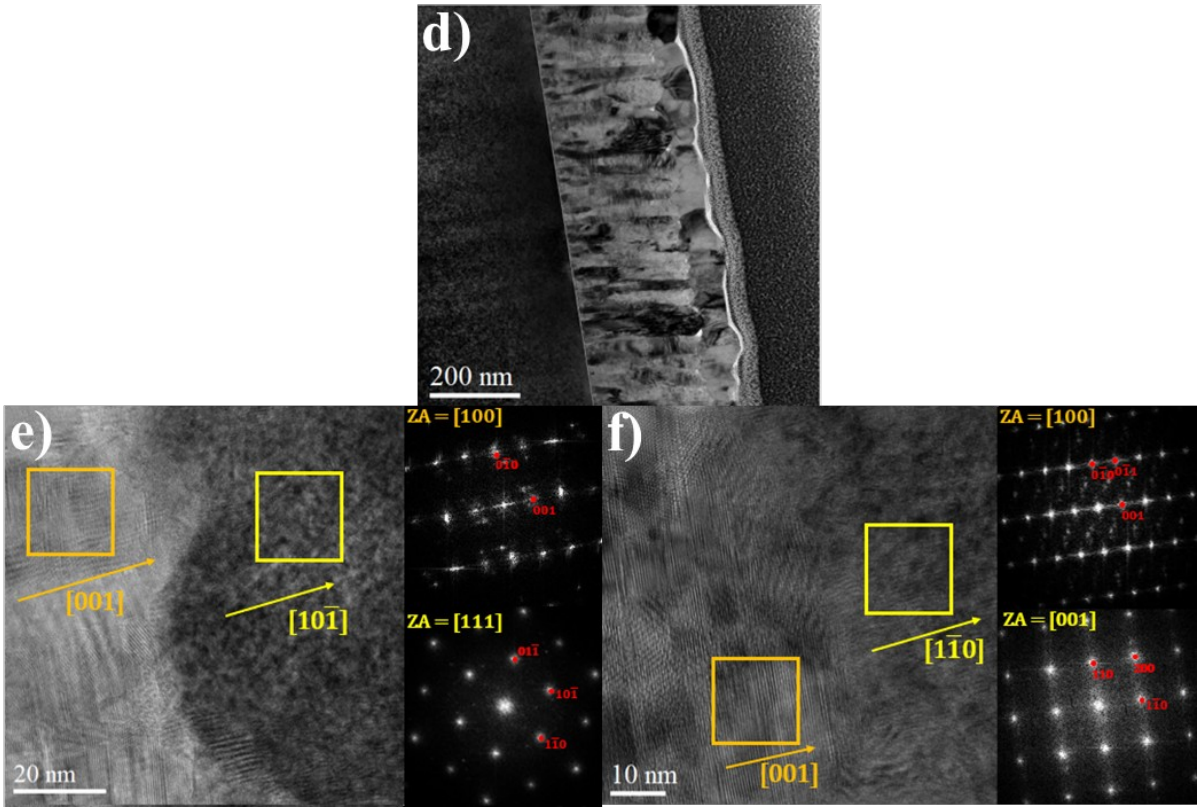

Figure 92: a) (Left) TEM image of the Si-2cm/ZnO/Cu_2O sample and (Right) the SAED image of the ZnO layer of the sample; **b) and c)** (Left) HR-TEM image of the Si-2cm/ZnO/Cu_2O sample and (Right) the indexed FFT image corresponding to the ZnO (orange) and Cu_2O (yellow) films; **d)** TEM image of the Si-8cm/ZnO/Cu_2O sample; and **e) and f)** (Left) HR-TEM image of the Si-8cm/ZnO/Cu_2O sample and (Right) the indexed FFT image corresponding to the ZnO (orange) and Cu_2O (yellow) films.

Figure 93 shows the schematic representation of the orientation relationships between Cu_2O and ZnO for the Cu_2O film deposited on the sample positioned at 2 cm from the substrate-holder axis. The orientation relationships deduced from the FFT patterns of **Figures 92 b) and c)** are (001)ZnO// $(11\bar{1})$ or (111) Cu_2O; [100]ZnO//$[1\bar{1}0]Cu_2O$. The (001) planes of ZnO and the copper atoms at the planes belonging to the {111} family in the cuprite Cu_2O structure both present an hexagonal arrangement. The O-O distance in ZnO to the lattice parameter of ZnO is 3.250 Å while the Cu-Cu distance in Cu_2O is close to 3.019 Å. The resulting lattice mismatch induces a relative deformation of ~7.7 % to enable continuity of the ZnO and Cu_2O lattices in the context of epitaxial growth of Cu_2O on ZnO

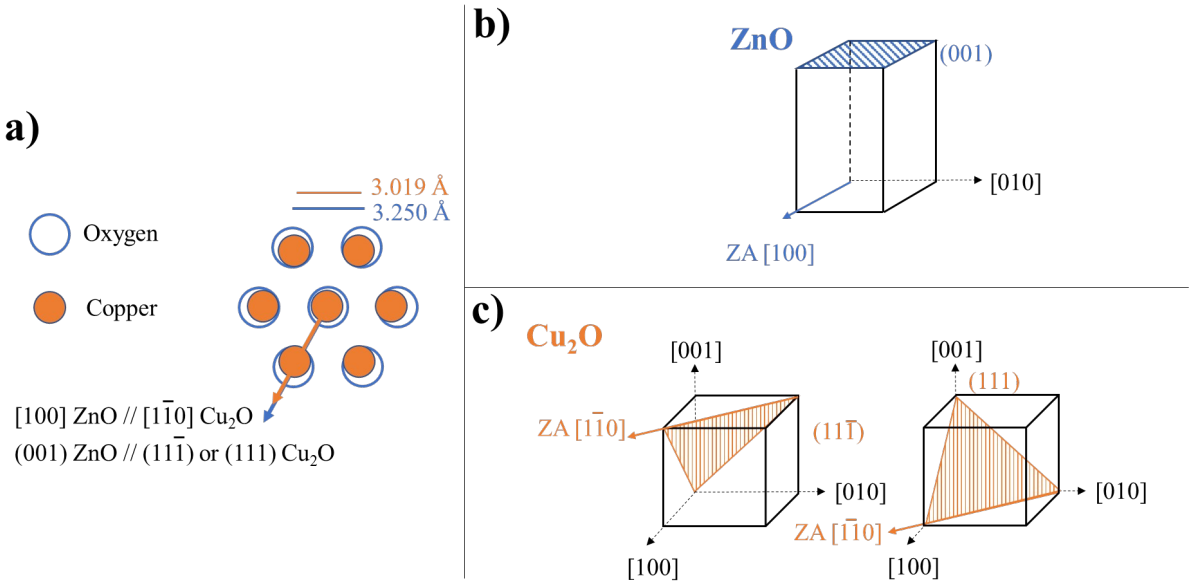

Figure 93: Schematic representation of **a)** the top view schematic of a plane of copper atoms belonging to the {111} family of the Cu_2O cuprite structure on a (001) plane of O-terminated ZnO. The orientation relationships between Cu_2O and ZnO deduced from **Figures 92 b) and c)** are indicated; **b)** a hexagonal unit cell showing the (001) plane and the [100] zone axis; and **c)** cubic unit cells showing the $(11\bar{1})$ and (111) planes under the same $[1\bar{1}0]$ zone axis.

Figure 94 shows the schematic representation of the orientation relationships between Cu_2O and ZnO for the Cu_2O film deposited on the sample positioned at 8 cm from the substrate-holder axis. The orientation relationships deduced from the FFT patterns of **Figures 92 e) and f)** are (001)ZnO// $(10\bar{1})$ or $(1\bar{1}0)$ Cu_2O; [100]ZnO//[111] or [001]Cu_2O. It is observed that both the (001) plane of wurtzite ZnO and the {110} family of planes in cuprite exhibit a diamond-shaped 2D lattice. The larger angle of the diamonds are very similar, i.e ~110° for the 2 structures. The edges of the 2D lattices are 3.250 Å and 3.698 Å for ZnO and Cu_2O, respectively. Hence, epitaxial growth considering the orientation relationships obtained from **Figures 92 e) and f)** lead to a relative deformation of ~11.1 %. Note that we have considered the Zn-terminated ZnO surface to bind with the oxygen atoms at the {110} Cu_2O surface because the O-terminated surface would repel the oxygen atoms of the O atoms of {110}. Therefore, it is likely that, in these deposition conditions, the ZnO film underneath the Cu_2O layer is Zn-terminated. It has been reported that changes in oxygen stoichiometry could change the ZnO termination **[249]**. This could explain why a change in orientation relationships is observed as the sample position during ZnO film growth was modified.

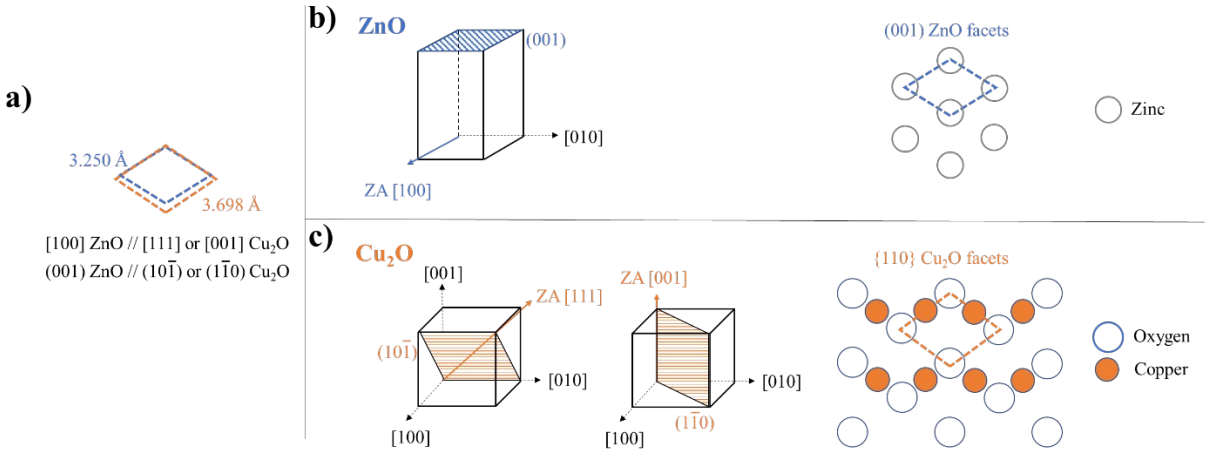

Figure 94: Schematic representation of **a)** 2D lattices exhibiting diamond-shaped in the (001) planes of ZnO and {110} family of planes in Cu_2O with indication of edge lengths for both. Orientation relationships deduced from **Figures 92 e) and f)** are indicated; **b)** (Left) a hexagonal unit cell showing the (001) plane and the [001] zone axis and (Right) a top view schematic of the zinc atoms in the (001) Zn terminated ZnO facets with indication of the diamond-shaped 2D cell; and **c)** (Left) cubic unit cells showing the $(10\bar{1})$ and $(1\bar{1}0)$ planes and the [111] and [001] zone axis, respectively, and (Right) a top view schematic of the oxygen and copper atoms at the {110} Cu_2O facets with indication of the diamond-shaped 2D cell.

In the final part of this section, we show SEM images taken with the FIB microscope of the third and fourth solar cells sample series, corresponding to solar cells devices: Glass/AZO2at.%/ZnO/Cu_2O/Au (3-A), Structuredglass1.5µm/AZO2at.%/ZnO/Cu_2O/Au (3-B) and the same samples labelled (4-A) and (4-B) except the deposition conditions for the AZO and ZnO films were different and detailed in **Section 2.4 of Chapter 2**. From the **Figures 95 a), d) and e)** of the (3-A) and (4-A) samples, one can see the perfect adherence of all films, especially the AZO and ZnO films to the point where they are not distinguishable; the Cu_2O layer also seems quite homogeneous. Additionally, the film deposition propagates the topography of the underlying patterned glass substrate with some smoothening. Next, in **Figures 95 f) to i)** the top-view image of each of the layers are shown; all films are granular but the Au and Cu_2O layers have larger grain sizes than the AZO and ZnO films. What is more interesting is the SEM images of the (3-B) sample. Effectively, the top view image shows a rather successful deposition on the structured glass even if the cross-section displays many defects. Various cavities are observed in **Figures 95 d) and e)** at the bottom of the device and specifically at the bottom of the curve of the structure; their presence is detrimental for photon conversion and must be avoided. The same observation is obtained from the **Figures 95 n) and o)** for the (4-B) sample. Many hypothesis could be established one of them being linked to the surface features of the laser-processed glass (undercuts). However, one can clearly see the deposition of a thin AZO layer at the bottom of the structure before the cavity is formed and closed off by the rest of

the deposition. One can assume that the AZO films are deposited with interfering growth orientations; this is backed up by the fact that small ranged roughness features of glass trigger this leading to high cavity density in the structure. Since the structure period of choice is small for light trapping reasons, one solution to this problem might be reducing the thickness of the films, mainly the bottom AZO film but without affecting its electrical properties. This way, it will be easier to avoid the eradication of the topographic effect provided by the patterning. Nevertheless, it is surprising that the AZO film could reach the lateral walls of some of the cavities because magnetron sputtering is known to be rather directive and to suffer from the atomic shadowing effect making it difficult to coat cavities, trenches, etc. This rather successful covering of some of the cavity walls may indicate that substrate-holder rotation helps. Other than controlling the deposition rate, another deposition method could be adopted such as ALD since it is known that the chemical reactions that occur are self-limiting and so the film will grow completely and evenly at the entrance of the structure curve before covering the bottom part; this ensures a full coverage of the glass substrate and might be a solution for the cavity formation. Finally, working on the laser interference patterning process in order to try to generate smoother patterns is another option to be considered.

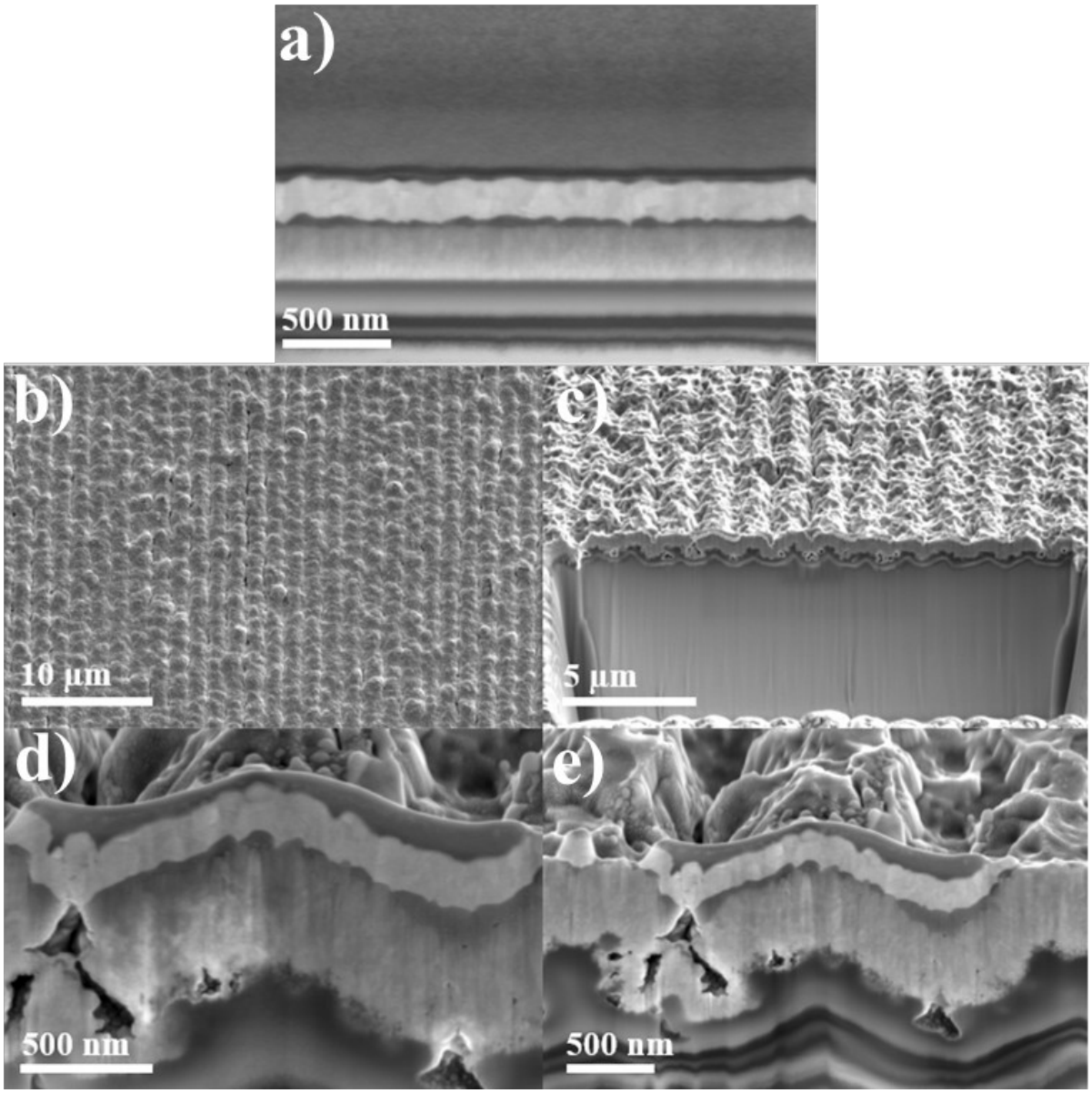
a)
500 nm
b)
10 µm
c)
5 µm
d)
500 nm
e)
500 nm

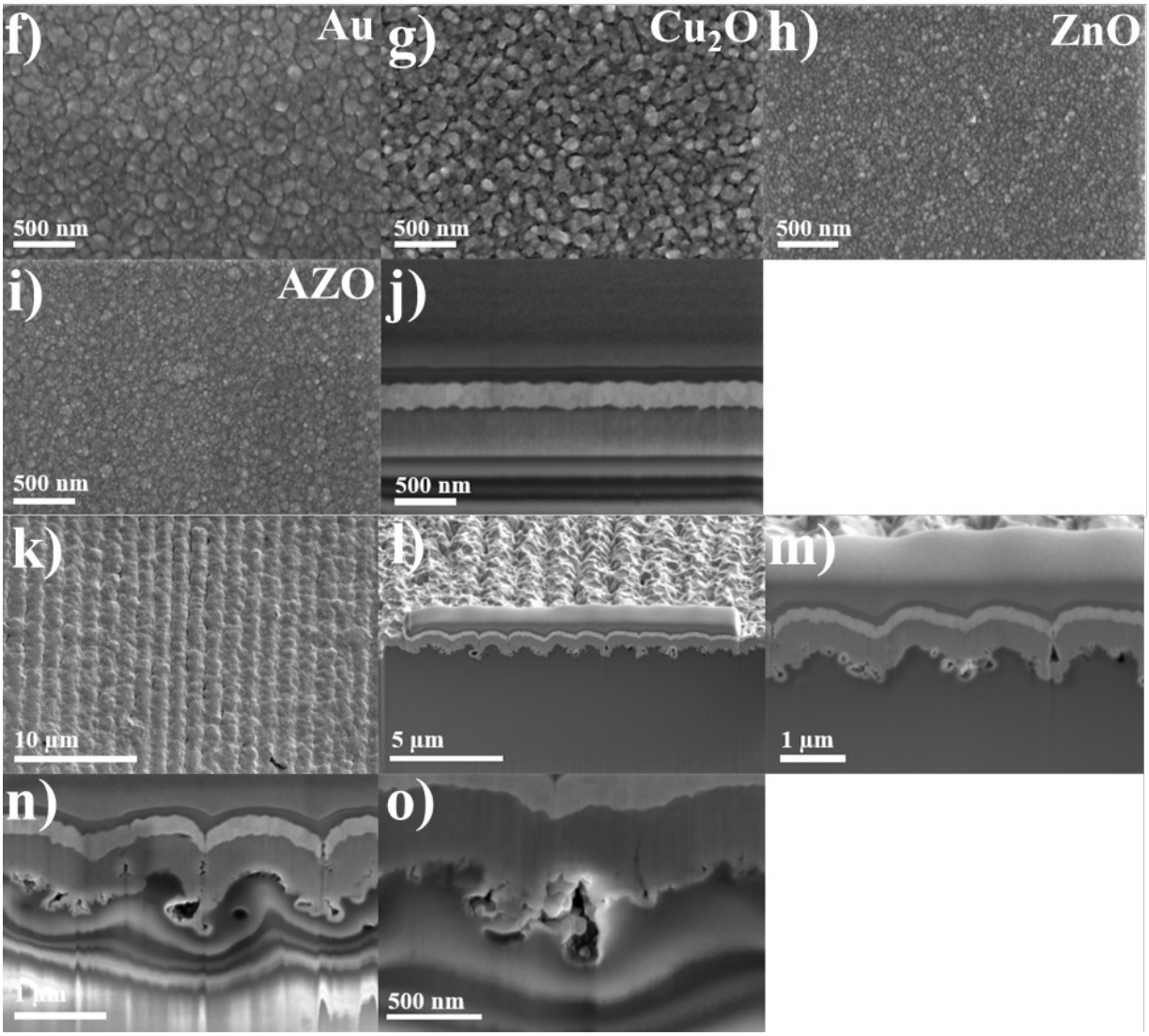

Figure 95: Top view SEM images and cross-sections of the **a)** Glass/AZO2at.%/ZnO/Cu_2O/Au (3-A); **b) to e)** Structuredglass1.5µm/AZO2at.%/ZnO/Cu_2O/Au (3-B); **f) to j)** Glass/AZO2at.%/ZnO/Cu_2O/Au (4-A) and **k) to o)** Structuredglass1.5µm/AZO2at.%/ZnO/Cu_2O/Au (4-B).

6.4. Chemical analysis

In this section, the chemical analysis results for the towards the solar cells and the solar cells devices consisting of the EDS and the ELNES analysis are presented.

First of all, the EDS mapping of the (1-A), (1-B) and (1-C) samples are presented in **Figure 96**. The Zn and O species distribution is homogeneous throughout the surface of all films. However for the (1-B) sample they accentuate the gap between the AZO and ZnO films further insisting on the importance of RF cleaning prior to ZnO deposition on top of the AZO film. Interestingly, this was not a problem for the (1-C) sample probably due to the densely packed columnar structure with (002) planes parallel to the substrate surface as observed from the TEM images in **Figure 91**. The Al

mapping for the (1-B) and (1-C) samples is important to distinguish the AZO layer from the ZnO layer; obviously, more Al species will be present in the AZO films. The Cu mapping is also very important firstly to determine the location of the film since it is very thin compared to the AZO and ZnO films, and to evaluate the homogeneity of the deposition. In this case, the film seems to agglomerate on the surface of the ZnO and is not evenly distributed. This observation is what encouraged us to alter the deposition parameters of the Cu_2O film by ALD for the next series. We note the presence of some Cu in the AZO and ZnO layers, and some Al in the ZnO and Cu_2O layers. This could be due to the FIB lamellae extraction where the cut might have let some of the material escape from one layer to another. Finally, other than the presence of oxygen and Al in the borosilicate glass being normal, the presence of Cu is due to some impurities. Also, as mentioned before, the platinum layer deposited to extract FIB lamellae contains some metals and impurities such as O, Cu and Al.

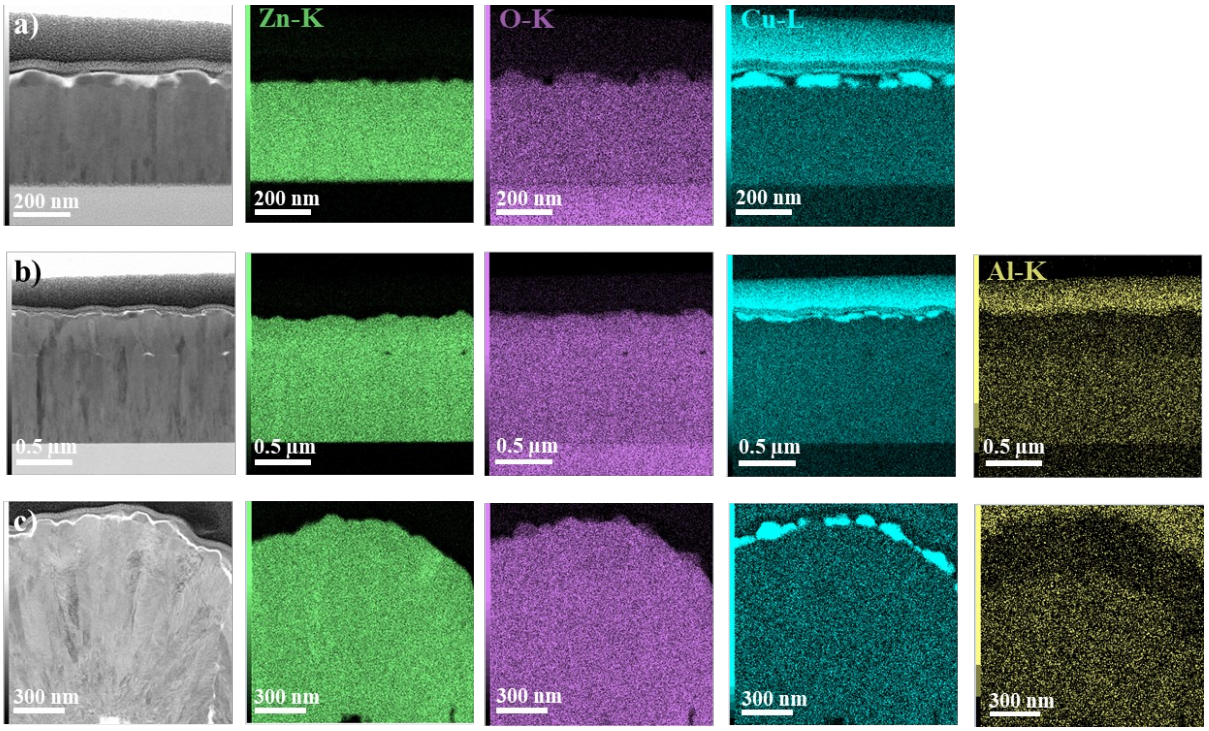

Figure 96: STEM images of the **a)** (1-A), **b)** (1-B) and **c)** (1-C) samples and their corresponding EDS mapping of the Zn (green), O (purple), Cu (blue) and Al (yellow) compositions.

Next, we tabulate in **Table 6** the atomic concentration of the Zn, O, Cu and Al species in each of the AZO, ZnO and Cu_2O layers for all three (1-A), (1-B) and (1-C) samples. Starting with the AZO layer present only in the (1-B) and (1-C) samples, one can note first the presence of 0.66 and 0.68 at.% of Al, respectively. This is in agreement with the results obtained for the AZO films deposited from the 1 at.% Al target in **Section 3.3 of Chapter 3** in the *off-axis* position since this one was chosen for

this deposition due to the lowest resistivity observed at this position for any deposited AZO films. Next, the oxygen content (48.72 at.%) is a bit higher than the Zn at.% (46.46 %) in the ZnO layer of sample (1-C) and even higher in sample (1-B) (55.51 O at.% and 43.83 Zn at.%). Moving on to the ZnO layer, one can note a possible over-stoichiometry in the (1-B) and (1-C) samples while a sub-stoichiometry is seen in sample (1-A). As for the Cu_2O layer, a possible oxygen sub-stoichiometry is noted for the (1-A) and (1-B) samples while an over-stoichiometry is seen for the (1-C) sample. Surprisingly it seems to correspond to a CuO film rather than a Cu_2O film, however EDS is not reliable for the determination of the nature of the film especially when oxygen is involved. Besides, we already performed XRD analysis on these samples and the diffractogram corresponded to the cuprite structure of Cu_2O film. Nonetheless, we performed ELNES measurements on the samples to further extend the chemical analysis.

Table 6: EDS analysis results on the (1-A), (1-B) and (1-C) samples consisting of the at.% concentration of the Zn, O, Cu and Al species for the different AZO, ZnO and Cu_2O layers. "E" stands for element and "L" stands for layer.

Sample	Glass/ZnO/Cu_2O (1-A)			Glass/AZO1at.%/ZnO/Cu_2O (1-B)				Structured glass 1.5 µm/AZO1at.%/ZnO/Cu_2O (1-C)			
E / L	Zn	O	Cu	Zn	O	Cu	Al	Zn	O	Cu	Al
AZO				43.83	55.51		0.66	46.45	48.72	4.15	0.68
ZnO	52.06	47.94		44.96	55.04			40.87	59.13		
Cu_2O		45.51	54.49		47.72	52.28			53.98	46.02	

To extend further the chemical analysis of the towards solar cells samples, we performed ELNES measurements on the (1-A), (1-C), (2-A) and (2-B) samples at the Zn-L, O-K and Cu-L edges. However, for similarity and space reasons, we only show in **Figure 97** the ELNES spectrum of the Zn-K edge of the AZO and ZnO films as well as the O-K edge of the AZO, ZnO and Cu_2O films in the (1-C) sample. The rest of the spectra are displayed in the **Appendices** in **Figures A9, A10 and A11**. For comparison, we also added reference spectra from previous works in order to compare it to our ELNES spectra and draw the appropriate conclusions. We will not discuss the Zn-L and O-K edges of the AZO and ZnO films since they were already extensively treated in **Section 5.2 of Chapter 5**.

From the work of L. Laffont et al. **[250]**, we display the ELNES spectra (**Figure 97 b)**) of a Cu (Cu^0) metal, CuO (Cu^{2+}) and Cu_2O (Cu^+) films from reference oxides. The Cu-$L_{2,3}$ edge is obtained from

the 2p core shell transition to the empty 3d states of the Cu. The spin orbit splitting of the 2p core hole generated the strong L_3 and L_2 white lines separated by 20 eV; the L_3 edge results from the $2p_{\frac{3}{2}}$ transition and the L_2 edge from the $2p_{\frac{1}{2}}$ level by spin-orbit splitting. The Cu-$L_{2,3}$ edge of the Cu metal shows a strong peak at 935.5 eV followed by two small ones. This edge however displays a strong and asymmetric threshold peak at 936.1 eV followed by three small peaks marked by arrows in **Figure 97 b)**. The Cu-L_2 edge is quite similar. However, the L_3 (933.6 eV) and L_2 edges of the CuO ELNES spectra are symmetric. Based on these difference, we are able to determine the copper oxidation state **[250,251]**. In G. Yang's **[251]** study presented in **Figure 97 c)**, the Cu-$L_{2,3}$ edge of metallic Cu nanoparticles is flat and broad due to the fully occupied 3d states. The Cu-$L_{2,3}$ edge of the Cu_2O film presents a peak between the two L_3 and L_2 white lines at 947.5 eV indicated by an arrow and probably due to the transition into the 4s state of Cu above the Fermi level. Due to the 4s band states of the Cu and CuO compounds, this peak is very weak in their ELNES spectra. As for the O-K edge, reference spectra are presented in **Figure 97 e)**. One can also see that the O-K edge for the Cu, CuO and Cu_2O films is different. Y. Wang et al. **[252]** observed an intense peak at 532.5 eV followed by smaller peaks in the O-K edge of the Cu_2O film, whereas four peaks are seen in the O-K edge of CuO at 528.4, 532.9, 537.4 and 541 eV. A similar observation is seen in **[14]** and **[253]**. From this analysis, and comparing those reference spectra with our Cu-$L_{2,3}$ and O-K edges, we can be sure of the deposition of a Cu_2O film and not a CuO film.

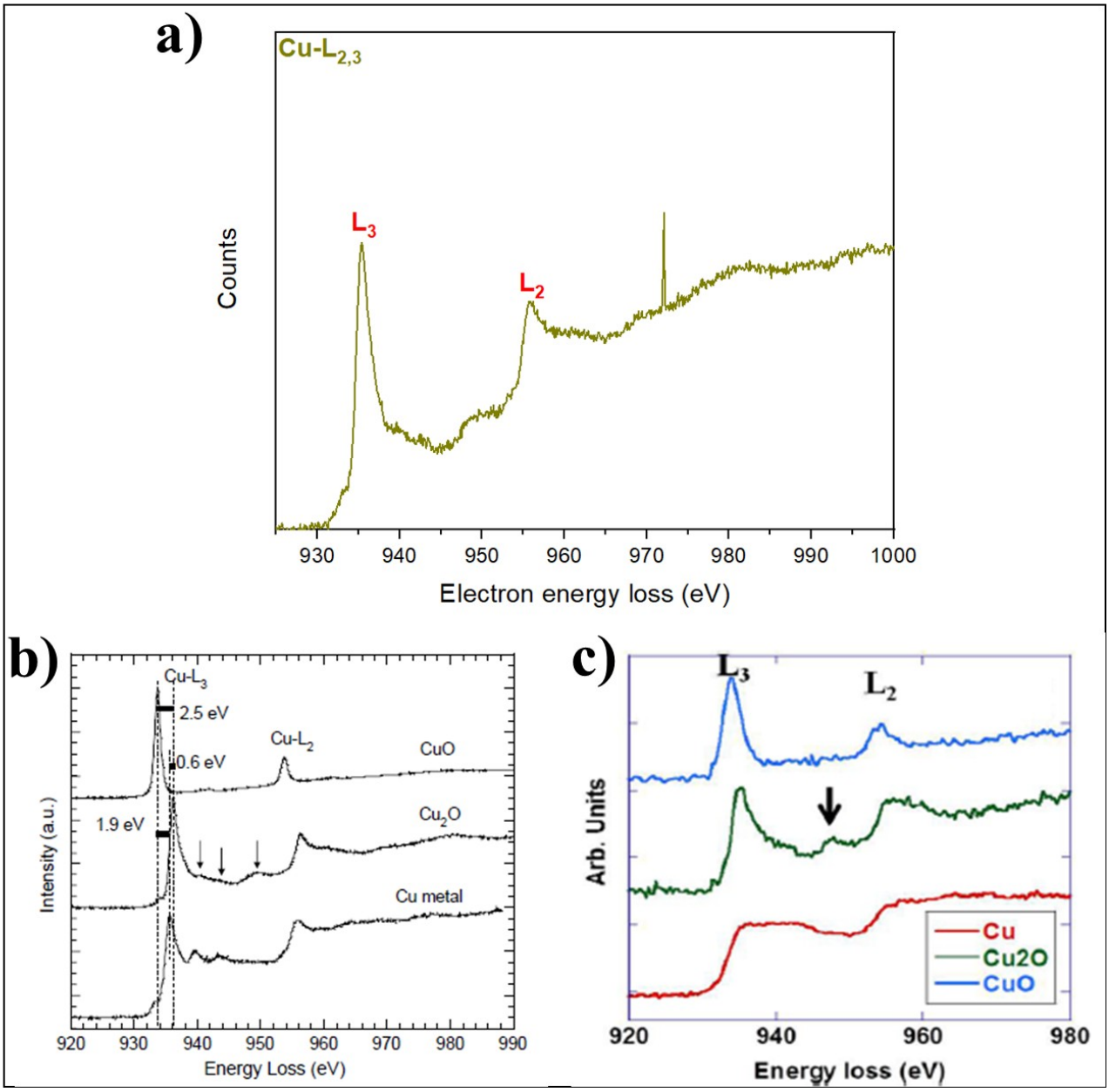
a)
Cu-L2,3
L3
L2
Counts
930
940
950
960
970
980
990
1000
Electron energy loss (eV)
b)
Cu-L3
2.5 eV
Cu-L2
CuO
0.6 eV
1.9 eV
Cu2O
Cu metal
Intensity (a.u.)
920
930
940
950
960
970
980
990
Energy Loss (eV)
c)
L3
L2
Arb. Units
Cu
Cu2O
CuO
920
940
960
980
Energy loss (eV)

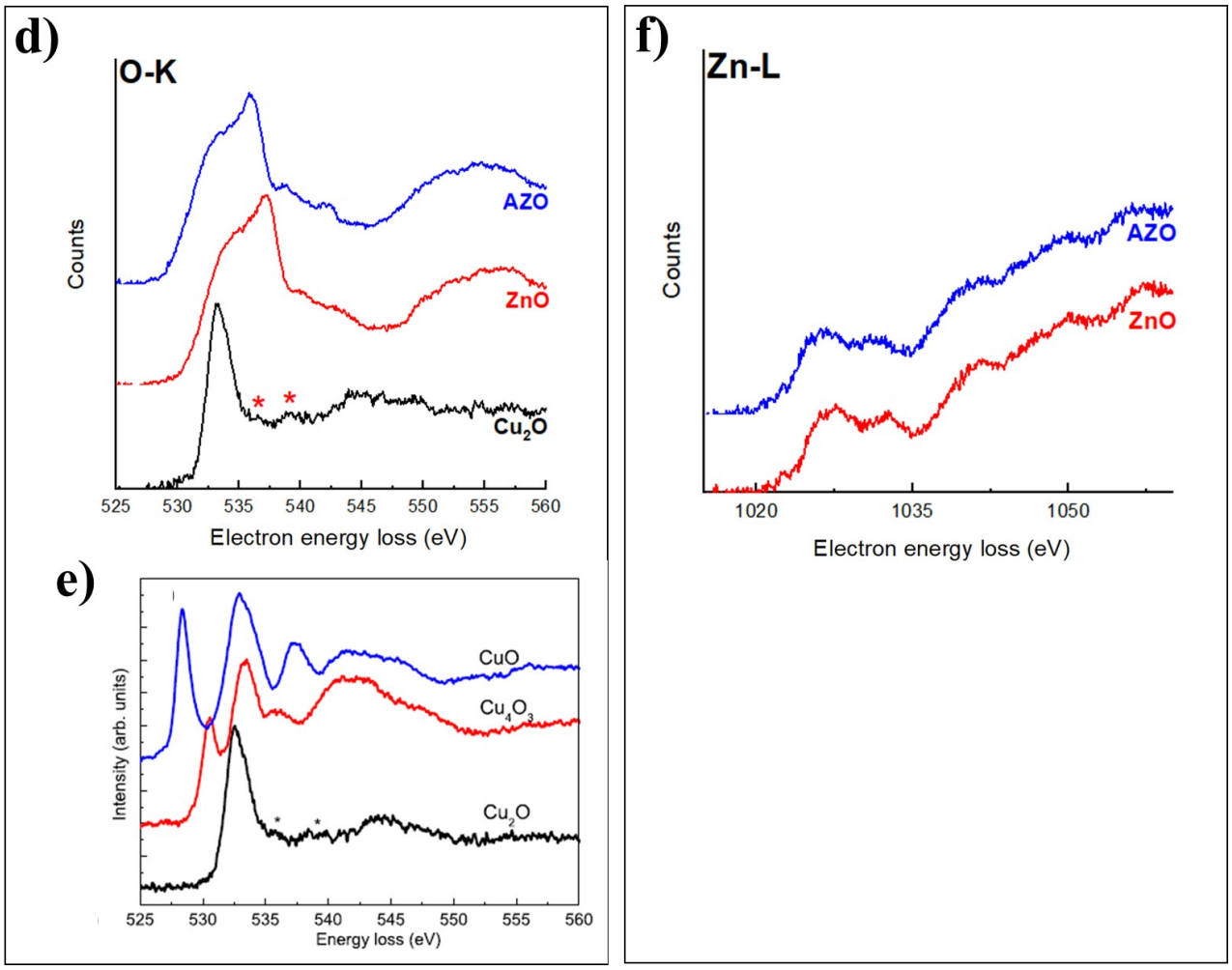

Figure 97: ELNES spectra from the structuredglass1.5µm/AZO1at.%//ZnO/Cu_2O sample of the **a)** Cu-$L_{2,3}$ edge, and **d)** O-K edge of the Cu_2O film; and **f)** the Zn-L edge of the ZnO and AZO layers. References of the Cu-$L_{2,3}$ edge are presented in **b)** from **[250]** and in **c)** from **[251]**; reference of the O-K edge is shown in **e)** from **[252]**.

6.5. I-V measurements of the flat and patterned solar cells

In the final part of this section, we present the I-V measurements performed on the solar cells series 3 and 4.

From **Figure 98**, we present the photocurrent density as a function of the applied voltage for the third solar cells series realized on a flat and a structured glass substrate with 1.5, 2 and 3 µm of structure periodicity shown in **Figure 84** in **Section 2.3.1 of Chapter 2**. We note that the 3 µm sample was produced by our partners in Saarbrucken in order to expand the solar cell testing on 3 structure periods. Despite the overall photocurrent being extremely low and unsuitable for a good solar cells production, we can however draw some conclusions. First off, one must note the very good electrical behavior of the AZO films which is considered successful for a solar cell. Next, it seems that the

photocurrent for all structured cells is higher than the one for the flat cell. Additionally, even though the photocurrent is very low, the curve still shows a nonlinear rectifying behavior standard for p-n junctions. This at least confirms the establishment of a heterojunction between the ZnO and Cu_2O films. However problems within the different layers of the solar cell hinder its good performance. To try to solve these problems, another solar cells series (Series 4) was realized where the layer on layer deposition mechanism was modified. From **Figure 36** in **Section 2.4 of Chapter 2**, one can see that the glass was completely covered with the AZO films and then the respective films on top were deposited in smaller squares each time. This was done to be sure to eliminate the possibility of short-circuit effect obtained when the Cu_2O layer is in contact with the AZO layer. Despite the difficulty of covering the rest of the sample prior to the ALD growth of the Cu_2O layer, the separation of the Cu_2O film from the AZO layer was quite successful. We also doubled the deposition time of the Au contact layer by DC sputtering in order to try to improve the contact. Finally, we tried to optimize the electrical property of the ZnO film since the latter was very transparent but also quite resistive. Unfortunately due to limited time we were not able to improve this property in this work. The I-V measurements of this solar cells series showed a still good electrical behavior of the AZO layer but the nonlinear rectifying behavior of the p-n junction was not obtained, which means that further optimization of the ZnO and maybe even of the Cu_2O layer is necessary.

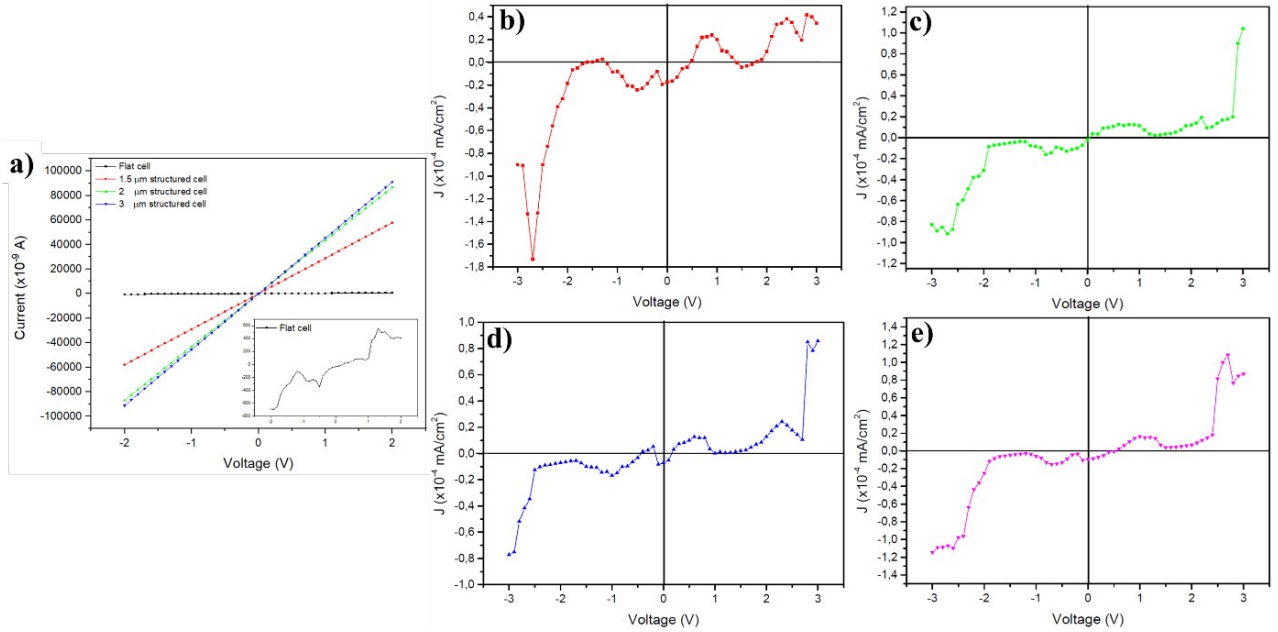

Figure 98: a) Current as a function of voltage for the AZO layer in all the samples of the third series solar cells; I-V measurements of the solar cells on **b)** flat glass, **c)** 1.5 µm, **d)** 2 µm and **e)** 3 µm structured glass.

6.6. Chapter conclusions

In this last chapter, we used the optimized AZO films studied throughout this work in the fabrication of towards solar cells and solar cells samples. The samples consisted of a structured glass substrate, an AZO film deposited from 1 or 2 at.% Al target as the transparent electrode, a ZnO/Cu_2O heterojunction and a gold contact. Glass structuring, morphological, structural and chemical analyses and I-V measurements were the main studied aspects and properties of the samples in this chapter.

For glass structuring, different parameters were simulated in order to determine the proper ones for our solar cells. The FEM method was applied in the framework of a collaboration with Dr. Marcos Soldera **[1]** to perform those simulations. From the first run, we deduced that the photocurrent is increased when the thickness of the Cu_2O layer is increased due to lower bulk recombination and carrier collection length. Unfortunately not more than 70 nm could be deposited for this work since we are using ALD to deposit the Cu_2O layer, which is a very slow deposition technique. Additionally due to more efficient light scattering, the photocurrent increased for structured substrates compared to flat ones with values augmenting with deeper structures and smaller periodicities (down to 1 µm). Based on these results, we performed glass substrate structuring by USP-DLIP using a picosecond laser and we discovered that the smallest periodicity possible on glass by this method is 1.5 µm with 600 nm depth. The second simulation run proved that with these conditions the maximum photocurrent is already reached for 300-450 nm structure depth.

Next, the morphology and structure of the towards solar cells and solar cells samples was studied. From the XRD measurements, it was deduced that ZnO deposited on Si by DC sputtering at 2 cm from the substrate holder axis, and under 6 or 8 sccm of oxygen flow, is in a wurtzite structure preferentially oriented with (002) planes parallel to the substrate surface. However on glass and under 8 sccm of oxygen flow rate, the (100) and maybe even the (101) and (202) peaks appeared. For the latter ones, confirmation is required due to the similar position of the (111) and (222) peaks of Cu_2O, respectively. Cu_2O was grown on ZnO and the formation of cuprite structure was confirmed from the presence of (311) and (220) peaks. For ZnO/Cu_2O stacks using ZnO deposited on Si at 2 or 8 cm from the substrate-holder axis, it was deduced that ZnO grows preferentially with (002) planes parallel to the substrate surface at 2 cm but is more oriented in other directions at 8 cm. To further the structure analysis, we performed SEM and TEM measurements on the samples. We witnessed from the observations of the samples of the first series (**Table 2** in **Section 2.4 of Chapter 2**), the presence of cavities and voids at the bottom of the structured samples, i.e. between the glass and the AZO layer. The adherence of the AZO and ZnO layers was not good due to poor RF etching prior to the ZnO deposition, however this problem was solved in the next series. In the first series samples,

the AZO and ZnO grew in columnar structures oriented in different directions in the case of the AZO 1 at.% layer already witnessed in **Section 3.4 of Chapter 3** while the ZnO grew in the [002] direction. On the structured sample however the columns were in a densely packed columnar structure with (002) planes parallel to the substrate surface. In the second series samples, i.e. Si-2cm/ZnO/Cu_2O and Si-8cm/ZnO/Cu_2O, while the ZnO always grew in the [002] direction, the Cu_2O was oriented in two different directions for each sample; [111] and $[11\bar{1}]$ at 2 cm, and $[10\bar{1}]$ and $[1\bar{1}0]$ at 8 cm. This was interpreted as a consequence of the change in growth conditions and/or possibly the termination of the underlying ZnO layer. From the third and fourth series SEM observations, we saw that all layers were granular from a top view with different grain sizes. Sadly the cavities at the bottom of the structured solar cells appeared once again and we attributed this to the laser processing of glass, and to the shadowing effect that prevents homogeneous covering by the AZO film deposited from a 2 at.% Al target.

From the chemical analysis, we saw that the Cu_2O layer was not homogeneous in the first series, but became so in the following series due to changes in the ALD deposition process. ELNES analysis on the O-K and Cu-$L_{2,3}$ edges was conducted to confirm the Cu_2O structure; comparing our results with spectra from the literature, we were able to confirm the formation of Cu_2O and not CuO.

Finally, we performed I-V measurements on the third and fourth solar cell series, and we concluded that the AZO layer was very performant, the photocurrent for the structured cells seemed higher than that of the flat ones, and the I-V curve shape was that of a non-linear rectifying behavior standard of a p-n junction which confirmed the establishment of a ZnO/Cu_2O heterojunction. But unfortunately, the photocurrent values were way too small to declare the solar cell as efficient. Another final series, the fourth one, was done by trying to optimize some layers and modifying the layer on layer deposition shape; but the I-V measurements evidenced the need to further work on the film characteristics.

All in all, while this chapter showed some very interesting and promising results via the fabrication of a structuredglass/AZO1or2 at.%/ZnO/Cu_2O/Au solar cell, some further work need to be done mainly on the ZnO and Cu_2O layers for it to be successful.

Conclusions and Outlook

In this thesis, AZO films have been deposited without thermal assistance by reactive High Power Impulse Magnetron Sputtering (HiPIMS) from alloyed Zn/Al targets with an Al content of 1, 2, 5, 10 and 15 at.%. They have been studied for their optical, electrical, structural, chemical and electronic structure properties. It led to the production of an AZO film deposited from Zn/Al targets containing 1 or 2 at.% of Al that are suitable as transparent electrodes. Along with the glass substrate successfully structured by UltraShort Pulsed-Direct Laser Interference Patterning (USP-DLIP) via a picosecond laser, flat and textured solar cells based on a ZnO/Cu_2O heterojunction were fabricated. The chemical and structural properties of samples containing some of the layer stacks of the cell were studied and the I-V electrical measurements were performed on the complete solar cells setups. The results were promising on different levels of the stacks and the complete solar cells device.

In **Chapter 3**, the AZO films study revealed that the Al content greatly affects the HiPIMS deposition process which is mirrored in the films properties studied after deposition. In fact, the formation of the target poisoning oxide layer was encouraged for high Al contents which transitioned the process from a metallic mode to a compound mode observed from a drop in the peak current and deposition rate. When the films were analyzed after deposition, it was found that the Zn, O and Al species were homogeneously distributed in the films with an obvious increase of the Al content in the film along with its increase in the Zn/Al target. However, the Al content in the film was close to that of the target with low Al content (1, 2 and 5 at.%) and much higher than that of the target with high Al content (10 and 15 at.%). We attributed the latter to the probable formation of strong Al-O bonds and possible preferential re-sputtering of Zn from the film. From the structural analysis performed from X-ray diffraction, the AZO films wurtzite structure crystallinity and size of crystallites proved to degrade with the increase of the Al content to the point where the films became X-ray amorphous when deposited from a 15 at.% Al target. Transmission Electron Microscopy (TEM) analysis however proved the films deposited from a 15 at.% Al target are nanocrystalline and maintain the wurtzite structure of ZnO. While the films deposited from a 5 and 10 at.% target were oriented along the *c*-axis of the wurtzite structure observed from the (002) peak, the lower content films grew in a columnar growth mode, were oriented in different directions, and were probably sub-stoichiometric due to the detection of the (101) peak from their X-ray diffractograms.

In **Chapter 4**, the study of the AZO films properties as a function of the Al content was pursued with the optical and electrical properties, the latter being studied on a general approach on al Al contents and on a specific approach on low Al content films. From the optical properties study, the transmittance of the films was seen to increase with the Al content probably due to a decrease of the oxygen sub-stoichiometry; the extracted band gap values were also seen to increase in the same direction. For the low Al content films (1 and 2 at.%), the band gap was slightly higher than that of an undoped ZnO film, which was ascribed to the Burstein-Moss effect coming from the increase in density of free electrons provided by the Al dopant and oxygen sub-stoichiometry. For the high Al content films (5, 10 and 15 at.%), the band gap values were high and gradually increasing with the Al content. The proposed origin of such evolution was the change of Al-O bonding state, which needed to be confirmed from an electronic structure point of view performed by electron Energy Loss Near Edge Structure (ELNES) in **Chapter 5**. From the electrical properties study, an increase of the resistivity above 2-3 at.% Al in the films was observed. The aforementioned change in local bonding could possibly play a role in this by preventing free electrons from being generated or by trapping the electrons, thus decreasing their concentration and mobility values in the films. Also, a maximum resistivity was observed at 7-8 cm from the substrate-holder axis, which is the position facing the magnetron axis. It was attributed to the introduction of acceptor defects in the films or the formation of secondary phases due to the bombardment by the fast energetic oxygen particles. To recapitulate, the Figure Of Merit (FOM) was calculated and it proved higher for the films deposited far from the target axis due to the lower resistivity and light absorption at this position. The AZO films deposited from a Zn/Al target with 1 and 2 at.% of Al, preferably in the *off-axis* position, showed worthy to be used as transparent electrodes in solar cells. The resistivity was also measured when the films were sequentially heated in air. For a longer time and a higher temperature in the case of low Al contents than higher Al contents films, the resistivity decreased. It was interpreted by the possible destruction of the Al_{Zn}-V_{Zn} complex, and the decomposition of the $Zn(OH)_2$ present at grain boundaries. However at longer annealing times, the resistivity increased because grain boundaries act as trap states for oxygen and so facilitate oxidation. Such increase was observed very quickly for high Al content films and it even impacted their structure. Finally in the section dedicated to the low content films, and in contrast to what was observed in a previous study on films with 3 at.% Al, the resistivity was seen to decrease with the discharge voltage decrease all the more than the target was used. This seemed to be related to the films sub-stoichiometry that is affected by the sputtering process controlled by the target state; however more work must be done on this subject for further confirmation.

In **Chapter 5**, the electronic structure of the AZO films in both the *high ρ* (close to the target axis) and *low ρ* (far from the target axis) positions was studied by ELNES method. From the Zn-L_3 edge, and due to the absence of a pre-threshold peak, we were able to confirm the formation of the hexagonal wurtzite structure of the AZO films; the O-K edge shape further confirmed this with the added confirmation of the absence of molecular oxygen incorporated into the films. The weakening of the Zn-L_3 edge's features with the increase in the Al content was ascribed to crystal degradation and local crystal distortion increase. In fact, the more the (002) peak was intense in the XRD diffractogram, the more the corresponding features at the Zn-L_3 edge were distinguishable. Similarly, the features of the O-K edge decreased with the increase in the Al content of the AZO films which was ascribed to the degradation of the doping effect of Al but also to the crystallinity degradation. The latter was especially observed from the broadening of the $D_{O\text{-}K}$ feature, which was also assigned from the literature to the formation of Al-O bonds. From the Al-$L_{2,3}$ edge of ELNES and the optical properties treated in **Chapter 4**, we were able to find signatures of Al dopant activation/deactivation and segregation which helped us understand the degradation of the electrical properties for high Al content films. The broadening of a feature ascribed to octahedral Al, and the disappearance or broadening near the conduction band minimum of a feature ascribed to tetrahedral Al was observed with increasing the Al content. This indicated that a large fraction of Al is most probably segregated in an inactive octahedral conformation with oxygen for high Al content films. From these results we fabricated a model using active/inactive Al features as reference and enabling to extract the relative proportions of Al active and Al inactive states in a film from the modelling of ELNES spectra at the Al-$L_{2,3}$ edge. We believe this model could be used in future works in order to understand the degradation of the AZO bulk and thin films, and eventually optimize them.

In **Chapter 6**, based on all the previous results, AZO film deposited from Zn/Al targets with 1 or 2 at.% of Al were selected as transparent electrodes for integration in solar cell devices. Our fabricated towards solar cells and complete solar cells devices were based on flat or structured glass substrates, an AZO film deposited from a 1 or 2 at.% target, a ZnO/Cu_2O heterojunction, and a gold contact that were analyzed, before or after assembly, on different levels. The modeling of glass structuring indicated that the photocurrent is higher for structured cells compared to flat ones, and it increases further with deeper structures and smaller periodicities (down to 1 µm). They also showed that higher thickness of the Cu_2O layer are favored but using ALD, we are only able to deposit a maximum of 70 nm thickness in a decent time. Applying USP-DLIP via a picosecond laser on the glass substrates, we were able to obtain deep structures (600 nm) with a minimum of 1.5 µm periodicity. However, a second simulation run comparing our results to a flat solar cell, proved that

there is a maximum photocurrent already reached for 300-450 nm structure depth, in our samples. From the XRD measurements, we saw that ZnO grows in the wurtzite structure with preferential orientation with the (002) planes parallel with the film surface. The cuprite phase Cu_2O was detected from the presence of the (311) and (220) peaks. Further structural analysis was performed by TEM along with EDS chemical analysis and ELNES electronic structure analysis. The TEM images showed that in all cases, both the AZO film deposited from a 1 at.% Al target and the ZnO film grew in a wurtzite columnar structure with the AZO and ZnO films oriented preferentially with the (002) planes parallel to the films surface. However that was not the case for the Cu_2O layer orientation which was dependent on the growth conditions. In fact, when it was grown by ALD on a ZnO film deposited by DC sputtering on a Si substrate placed at 2 cm from the substrate-holder axis, the films were oriented in the [111] and $[11\bar{1}]$ direction and showed the following orientation relationships with ZnO: (001)ZnO//$(11\bar{1})$ or (111) Cu_2O; [100]ZnO//$[1\bar{1}0]Cu_2O$. But when the Si substrate was placed at 8 cm from the substrate-holder axis, these orientations became $[10\bar{1}]$ and $\left[1\bar{1}0\right]$ and showed the following orientation relationships with ZnO: (001)ZnO//$(10\bar{1})$ or $(1\bar{1}0)$ Cu_2O; [100]ZnO//[111] or $[001]Cu_2O$. This difference was attributed to the change in growth conditions and possibly the difference in surface termination of the ZnO film. Next, the EDS analysis was used mainly to determine the homogeneity of the Cu_2O layer, and the ELNES analysis on the Cu-$L_{2,3}$ and O-K edges confirmed the formation of the Cu_2O film and not the CuO one. The SEM and TEM images of almost all structured samples showed cavities and voids at the bottom of the sinusoidal structure, between the glass and AZO layer. This was attributed to the laser processing of the glass in combination with the atomic shadowing effect that occurs during the deposition of the AZO layer. From the I-V measurements of the third solar cells series, we were able to confirm the seemingly higher photocurrent of the structured cells compared to the flat ones, the establishment of the ZnO/Cu_2O heterojunction, and the good performance of the AZO layer. The latter was also seen in the fourth series with the additional optimization of the layer on layer deposition shape. Nonetheless, the photocurrent values were way too small to consider the solar cells as efficient. Hence, further improvements are needed.

Perspectives

In the previous, we have reported the main results of this thesis that introduced new aspects to the photovoltaic applications, especially on the transparent electrode level. In the following and to extend this research, we propose some of the experiments that could be of interest for future studies:

- AZO films deposited from high Al content targets (10 and 15 at.%) displayed plasma instability during deposition. Placing an iron sheet between the target and magnetron might contribute to plasma stabilization by weakening the magnetization and electron confinement; so it would be interesting to try and apply that for high content targets.
- We observed from the EDS concentration profiles taken horizontally across the AZO films that there are Zn, O and Al species concentration fluctuations. This was especially detected in the low Al content columnar AZO films, when going from one column to another. It might be interesting to extend this measurement on a smaller scale, possibly across the grain boundaries, to determine where the different species are mostly concentrated.
- We have shown XRD diffractograms of some AZO films deposited from a Zn/Al 1 at.% target using sputtering deposition in a DC mode, to compare their transmittance and structure to those deposited in the HiPIMS mode. We were able to see some interesting differences, but it would be nice to extend this to the other Al target compositions with a more thorough optical, electrical and especially electronic structure analysis.
- We have been able to obtain the values of the carrier concentration and mobility from the Hall effect method only for the low content AZO films (1 and 2 at.%, and only the values at the *off-axis* position for the 5 at.%). It was limited to those films due to the high resistivity of the higher content AZO films, as well as the limitation of our device. It will be interesting, if possible, to find those values for the AZO films deposited from Zn/Al targets with higher Al contents using a more sensitive setup.
- The distinctive electrical properties evolution of AZO films deposited from low Al content targets were studied and analyzed. Some interesting conclusions were drawn but further experiments are needed. For example, a deposition series from a novel and a used target with 1 and 2 at.% of Al (or lower) with applied voltages extended to lower or higher values than the ones used in this study could help validate our observations. Some changes with the oxygen flow rate might also be an interesting variable to test. But, most importantly we need to understand the influence of these parameters on the electrical characteristics of the discharge in order to assess the mechanisms in action.
- We were able to conduct the ELNES analysis on the most possible conditions of the AZO films, but due to the abundance of users on the TEM it was not possible to perform all the measurements. For instance, it would be nice to apply the ELNES analysis on the O-K edge for the AZO films deposited from targets with 10 and 15 at.% of Al. Also, like most studies, the Al-K is not an easy edge to probe with ELNES and especially for low content AZO films but it would be interesting to see the evolution of this edge with the Al content. For this, it is

needed to resort to X-ray absorption near edge structure measurement at a synchrotron facility.

- We only grew Cu_2O films on ZnO by ALD in order to fabricate the solar cells heterojunction. However we are curious to know the effect of the AZO films that we produced from 1, 2, 5, 10 and 15 at.% Al targets, with different electrical properties, on the growth of Cu_2O by ALD. We think it may be interesting to study their electrical and structural properties afterwards.
- The solar cells application in this work was mostly limited to structured glass with 1.5 µm periodicity. It would be interesting to perform morphological, structural, chemical, electrical and electronic structure measurements on patterned solar cells with the glass substrate patterned with 2 and 3 µm periodicity.
- In this work, we were not able to fabricate solar cell devices exhibiting high efficiencies, but we have narrowed down the aspects that need to be improved. The origin of the low photocurrent is most probably present in the ZnO/Cu_2O heterojunction; the junction was successfully established but not yet functioning efficiently. We suggest optimizing the ZnO film by DC sputtering, in a way to maintain the already present transmittance but increase the film's conductivity. As for the Cu_2O film, we propose working on increasing the carrier density for a proper function of the heterojunction. Only when a successful heterojunction is established, one can compare the evolution of the photocurrent from a flat to a structured cell, with different values of periodicity involved.

Appendices

Chapter 3

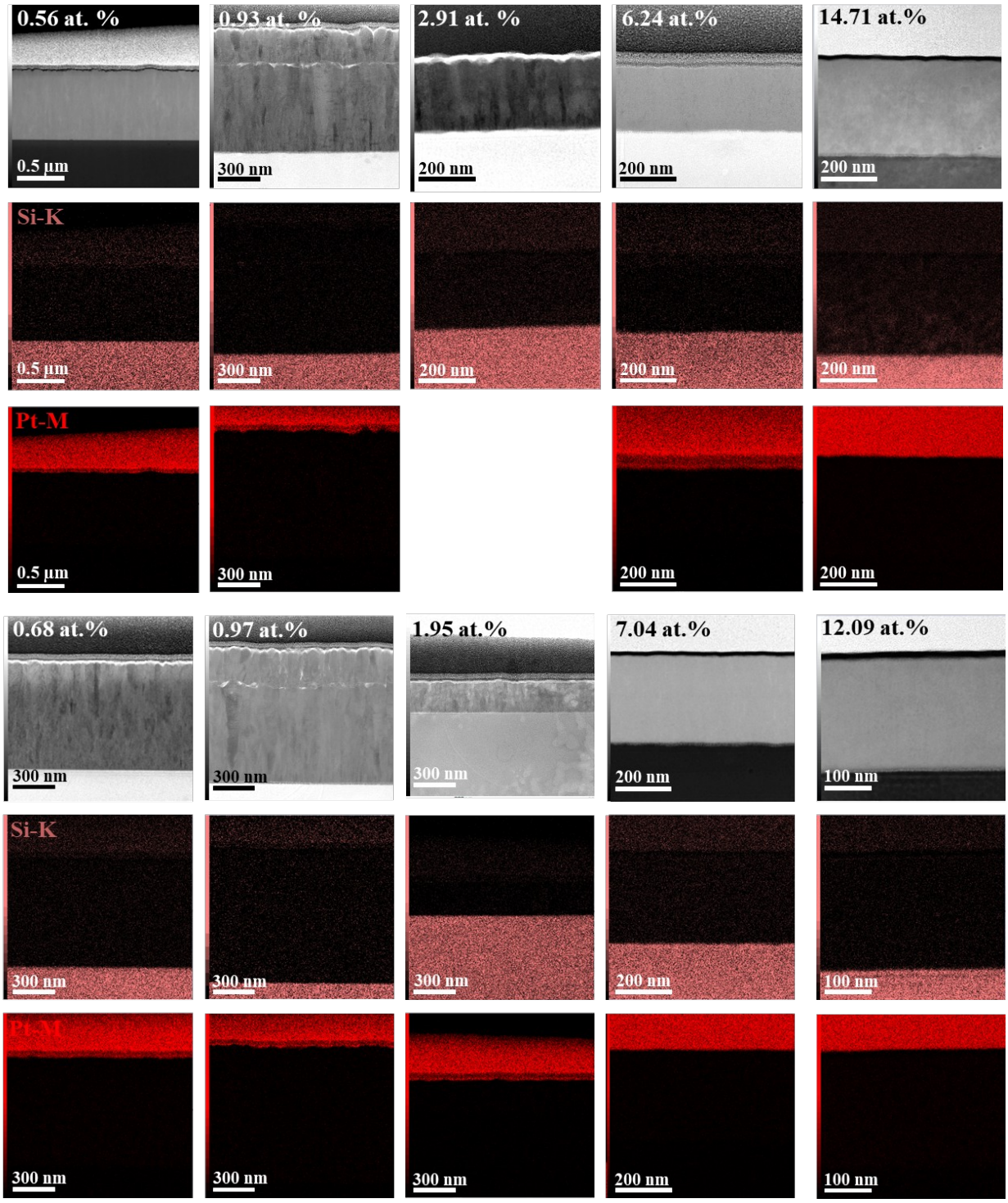

Figure A1: STEM images in the *in-axis* (**Top image**) and *off-axis* (**Bottom image**) positions of the AZO films deposited from a Zn/Al target with 1, 2, 5, 10 and 15 at.% of Al respectively and their corresponding EDS mapping of the Si (Gold rose) and Pt (red) compositions.

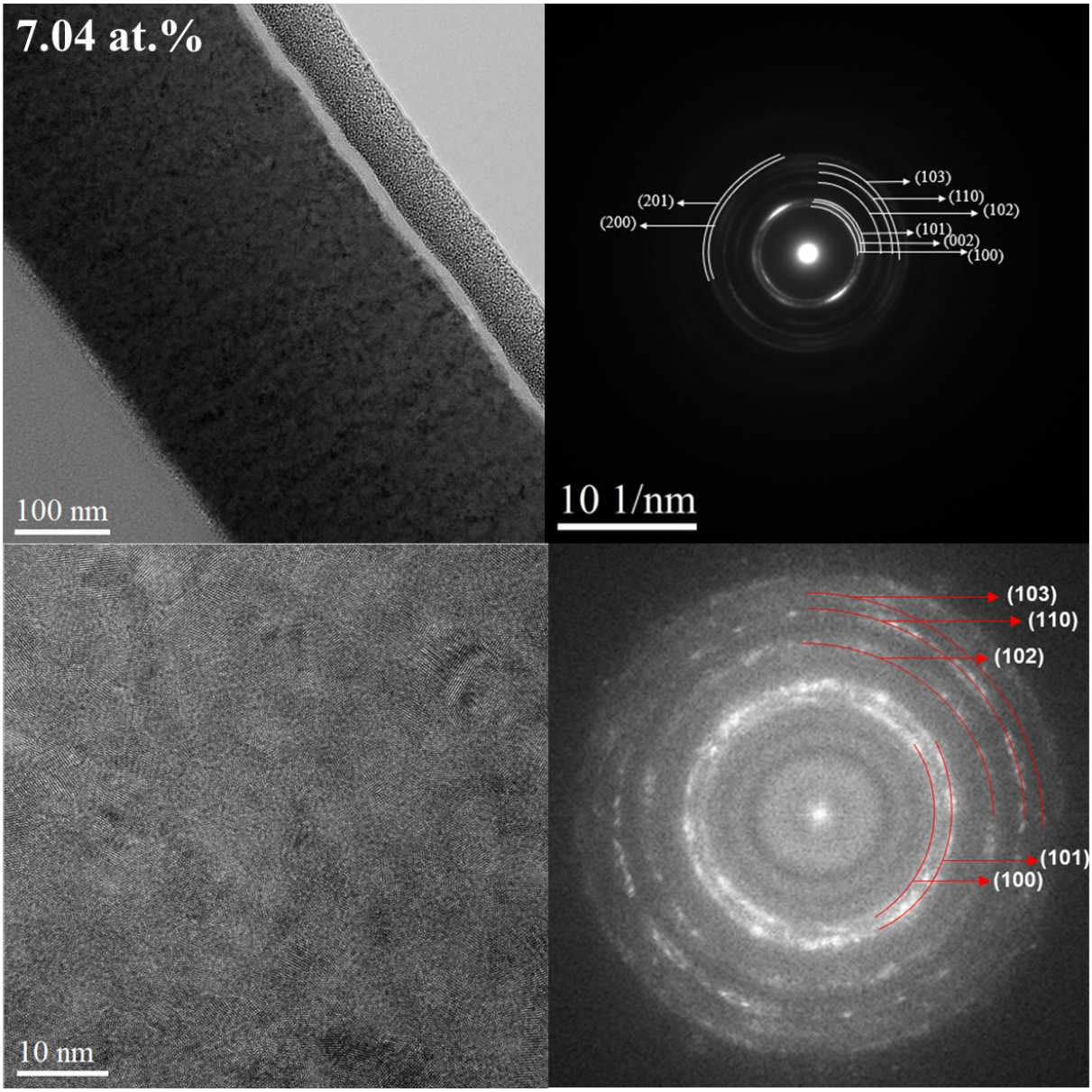

Figure A2: Panels of the main results obtained by TEM measurements including a TEM image, a SAED, a HR-TEM image and its indexed FFT for the AZO film containing 7.04 at.% of Al deposited from a Zn/Al 10 at.% target with the at.% values representing the real Al at.% in the AZO films *off-axis* position.

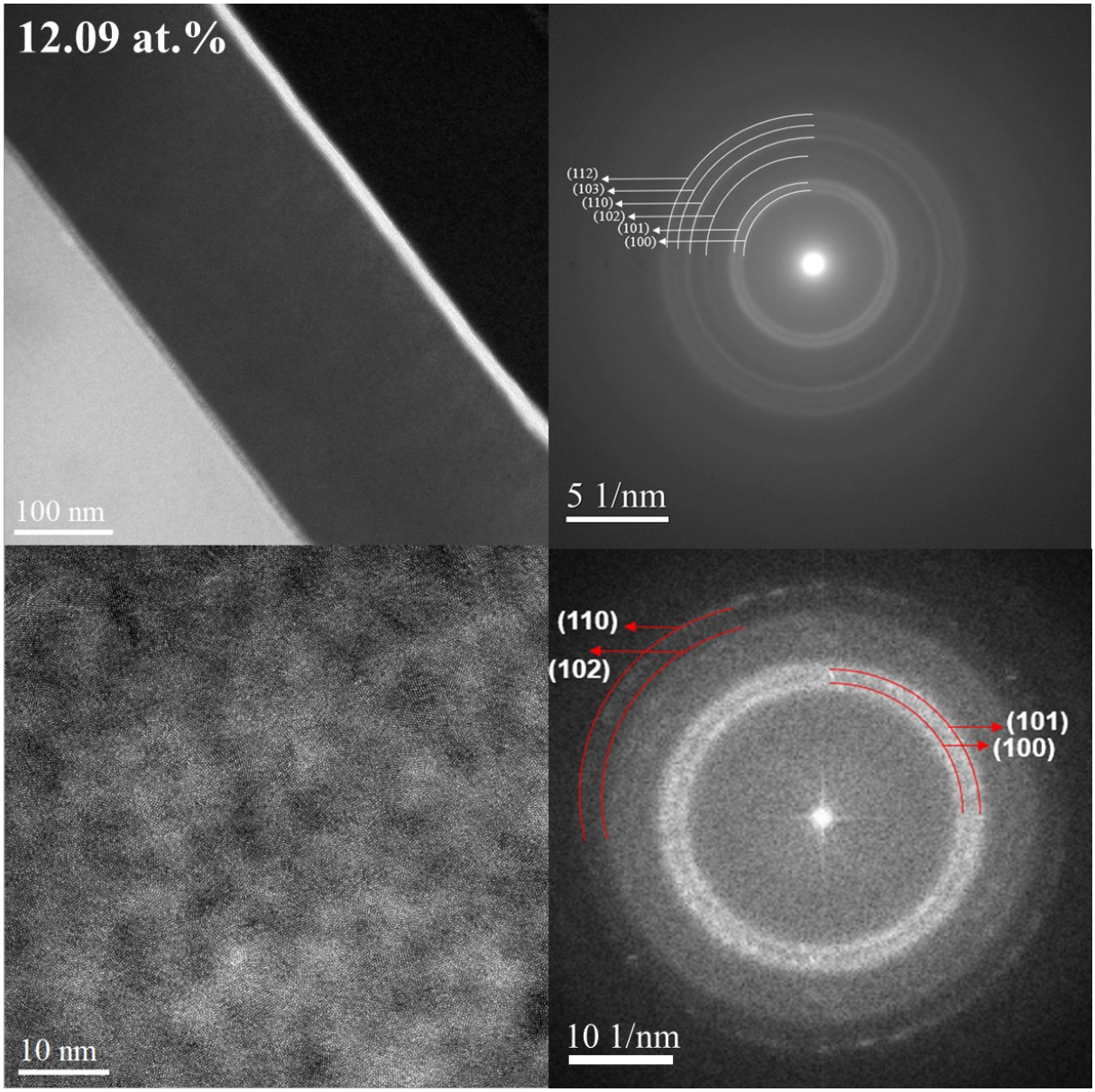

Figure A3: Panels of the main results obtained by TEM measurements including a TEM image, a SAED, a HR-TEM image and its indexed FFT for the AZO film containing 12.09 at.% of Al deposited from a Zn/Al 15 at.% target with the at.% values representing the real Al at.% in the AZO films *off-axis* position.

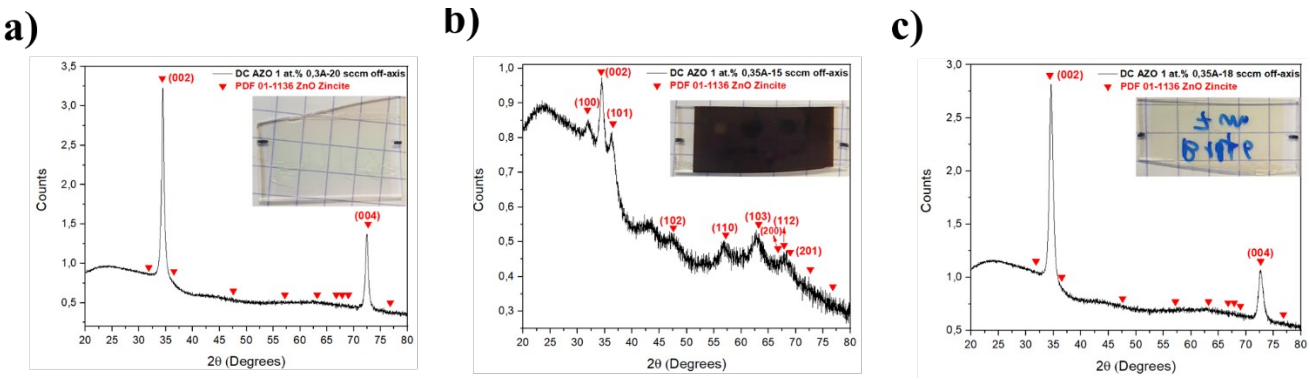

Figure A4: XRD diffractogram of AZO films deposited from a Zn/Al target with 1 at.% of Al at the *off-axis* position by DC sputtering at different applied currents and oxygen flow rates. The inset represents the photograph of the corresponding film.

Chapter 6

In **Figure A5**, we present the absorbance, reflectance graphs as a function of the wavelength for a flat cell with a 500 nm thick Cu_2O versus a structured cell with a 500 nm thick Cu_2O, a 1 µm period and a 300 nm structure height. The optical losses are written between brackets for the reflectance and each of the layers, except for the Cu_2O layer. The increase of the photocurrent due to patterning is explained by the reflectance reduction observed around 450 nm and near the band gap of Cu_2O at 550-600 nm. At this stage, the photocurrent can be even more improved by further reducing the reflectance around 550-600 nm. The optical losses are difficult to decrease for the contact layers. The increased losses observed for the gold layer are probably due to the plasmonic effect and they may be reduced by inserting a layer between the Cu_2O and Au films.

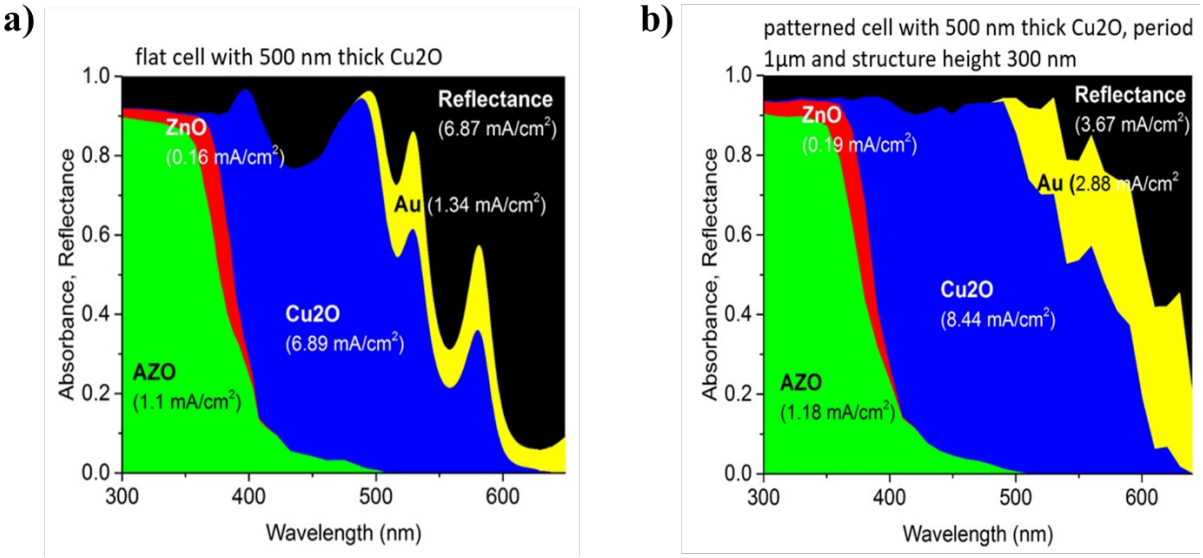

Figure A5: Absorbance, Reflectance as a function of the wavelength (nm) for **a)** a flat cell with a 500 nm thick Cu_2O layer and **b)** a structured cell with a 500 nm thick Cu_2O layer, a 1 µm structure periodicity and a 300 nm structure height. The reflectance is colored in black and the absorbance of each layer is colored respectively for the AZO, ZnO, Cu_2O and Au layers in green, red, blue and yellow. The optical losses are written between brackets for the reflectance and each of the layers, except for the Cu_2O layer.

In **Figure A6**, the optical losses are once again presented this time for a structure period of 1.5 µm and a structure height of 600 nm. Comparing with **Figure A5** of the first simulation run, done at a lower structure period and height (1 µm and 300 nm respectively), one can tell that optical loss for the AZO and the Au layer was a little bit decreased. But most importantly, the reflectance reduction was also observed at 450 nm and 550-600 nm with an even bigger reduction (3.51 vs 3.67 mA/cm^2).

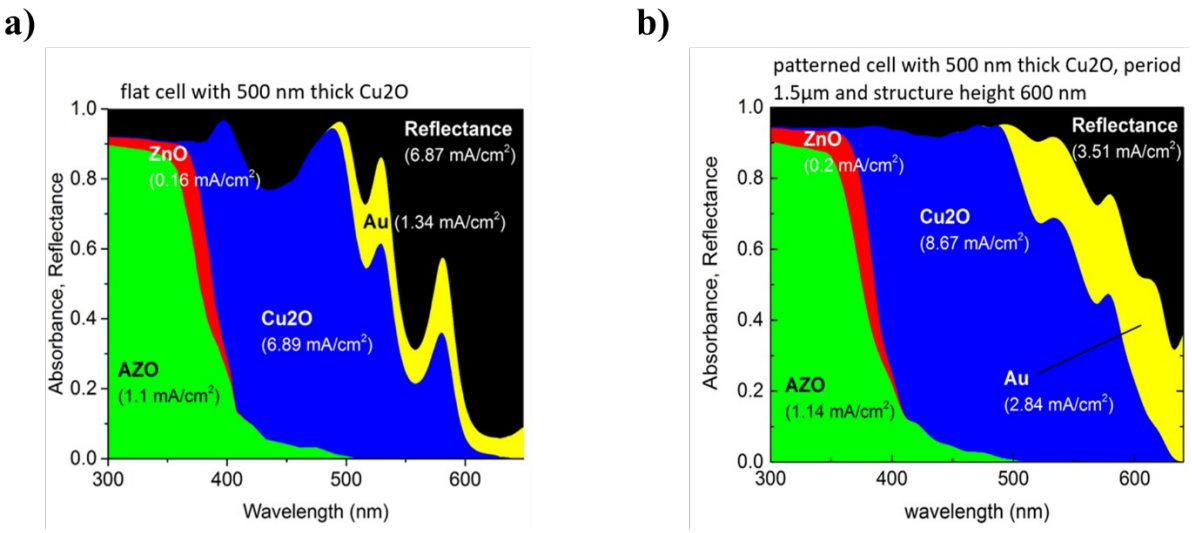

Figure A6: Absorbance, Reflectance as a function of the wavelength (nm) for **a)** a flat cell with a 500 nm thick Cu_2O layer and **b)** a structured cell with a 500 nm thick Cu_2O layer, a 1.5 µm structure periodicity and a 600 nm structure height. The reflectance is colored in black and the absorbance of each layer is colored in respectively for the AZO, ZnO, Cu_2O and Au layers in green, red, blue and yellow. The optical losses are written between brackets for the reflectance and each of the layers, except for the Cu_2O layer.

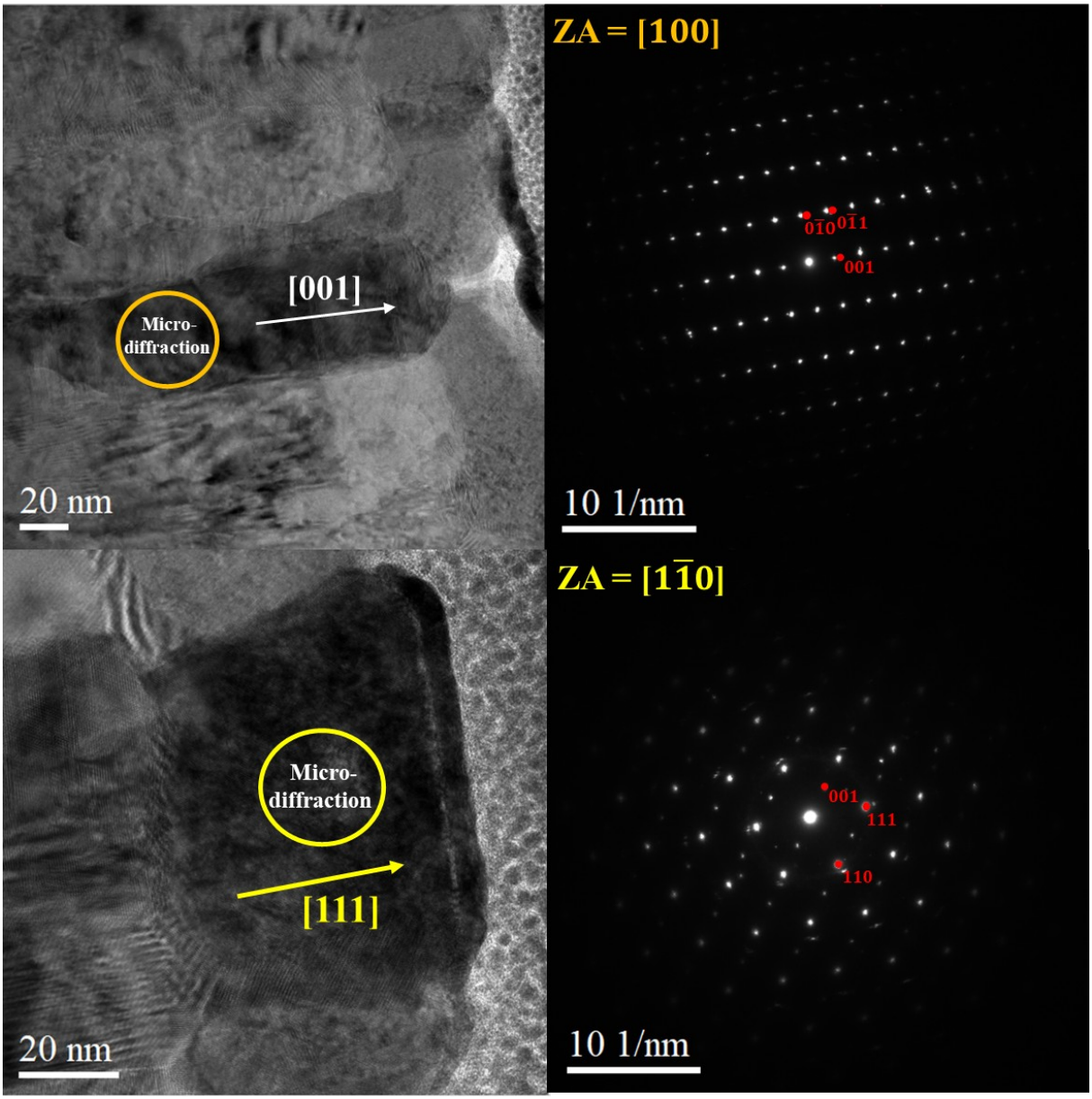

Figure A7: **(Left)** HR-TEM image of the Si-2cm/ZnO/Cu_2O sample and **(Right)** the associated micro-diffraction of the ZnO film (orange) and Cu_2O film (yellow).

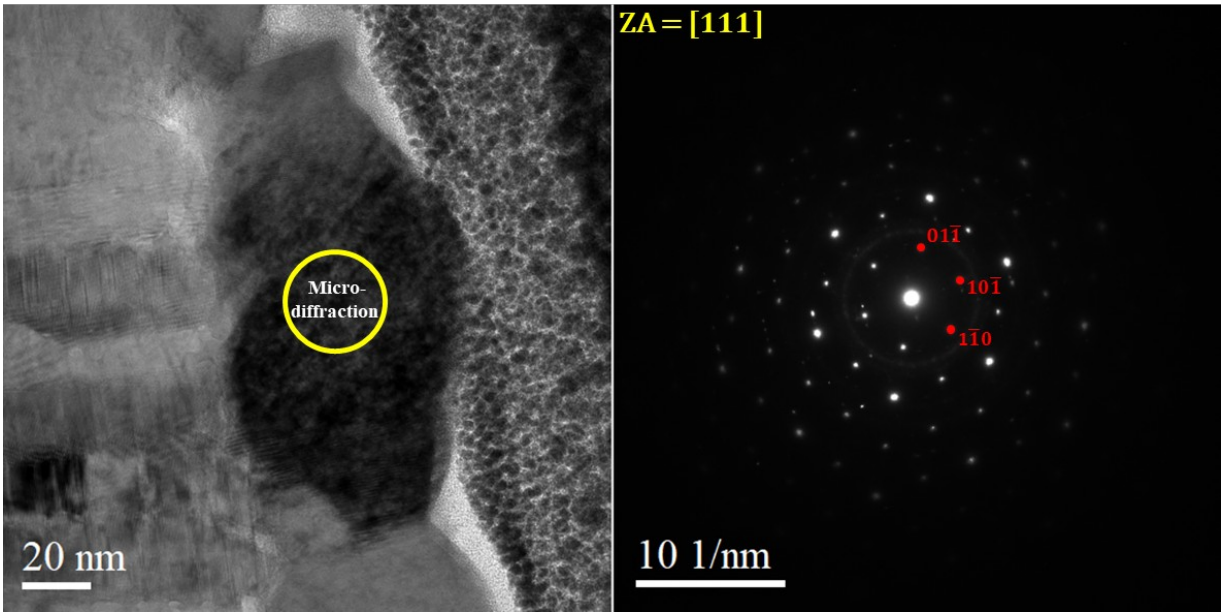

Figure A8: **(Left)** HR-TEM image of the Si-8cm/ZnO/Cu_2O sample and **(Right)** the associated micro-diffraction of the Cu_2O film (yellow).

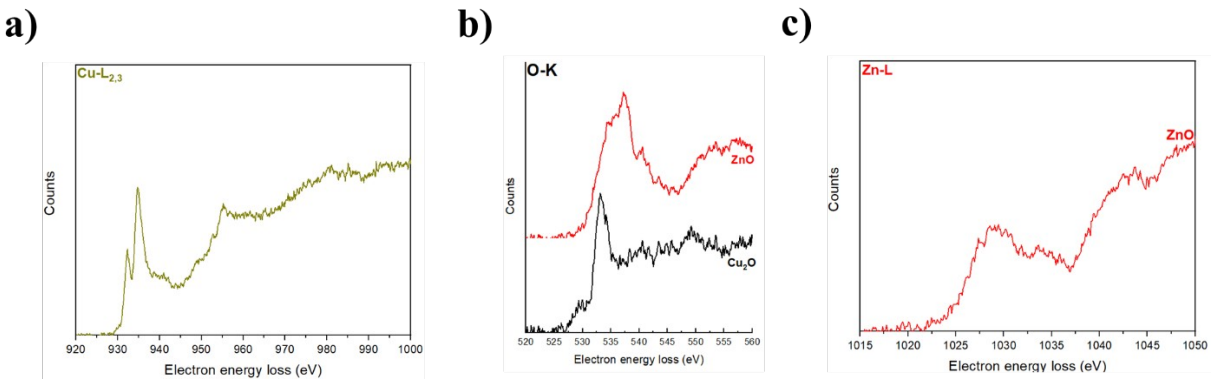

Figure A9: ELNES spectra from the glass/ZnO/Cu_2O sample of the **a)** Cu-$L_{2,3}$ edge of the Cu_2O layer, **b)** O-K edge of the Cu_2O and ZnO layers and **c)** Zn-L edge of the ZnO layer.

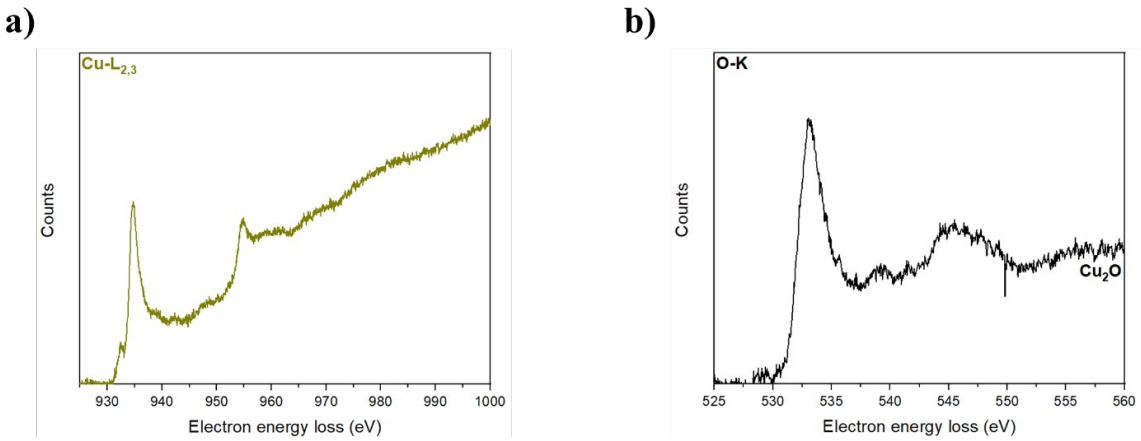

Figure A10: ELNES spectra from the Si-2cm/ZnO/Cu_2O sample of the **a)** Cu-$L_{2,3}$ edge and **b)** O-K edge of the Cu_2O layer.

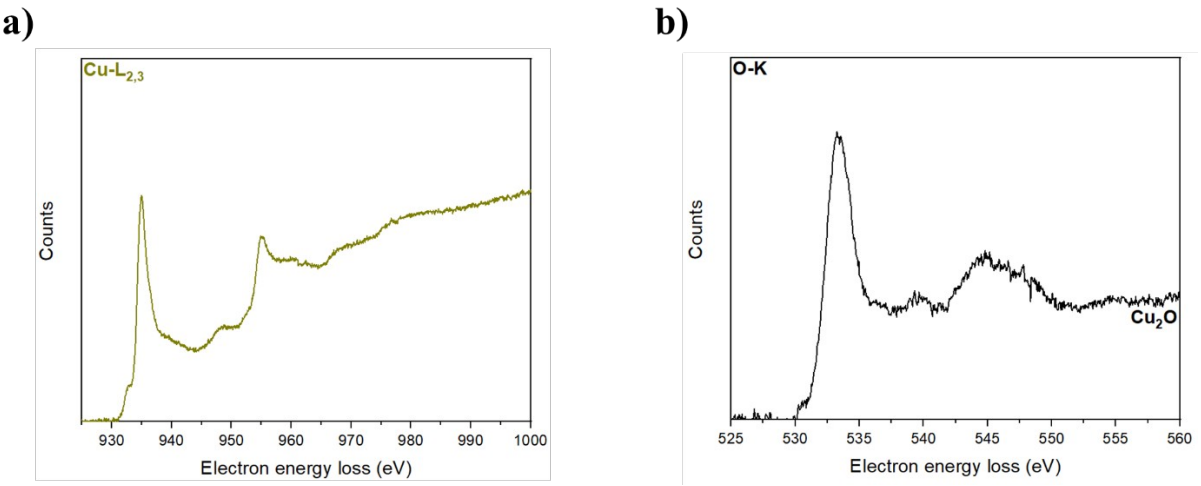

Figure A11: ELNES spectra from the Si-8cm/ZnO/Cu_2O sample of the **a)** Cu-$L_{2,3}$ edge and **b)** O-K edge of the Cu_2O layer.

Bibliography

1. Soldera M., and K. Taretto. "Combining Thickness reduction and light trapping for potential efficiency improvements in perovskite solar cells." physica status solidi (a) 215, no. 6 (2018): 1700906.

2. Mallick A., and D. Basak. "Revisiting the electrical and optical transmission properties of co-doped ZnO thin films as n-type TCOs." Progress in Materials Science 96 (2018): 86-110.

3. Horwat D., M. Mickan, and W. Chamorro. "New strategies for the synthesis of ZnO and Al-doped ZnO films by reactive magnetron sputtering at room temperature." physica status solidi (c) 13, no. 10-12 (2016): 951-957.

4. Vinnichenko M., R. Gago, S. Cornelius, N. Shevchenko, A. Rogozin, A. Kolitsch, F. Munnik, and W. Möller. "Establishing the mechanism of thermally induced degradation of ZnO: Al electrical properties using synchrotron radiation." Applied Physics Letters 96, no. 14 (2010): 141907.

5. Zubkins M., H. Arslan, L. Bikse, and J. Purans. "High power impulse magnetron sputtering of Zn/Al target in an Ar and Ar/O_2 atmosphere: The study of sputtering process and AZO films." Surface and coatings technology 369 (2019): 156-164.

6. Rahmane S., M. A. Djouadi, M. S. Aida, N. Barreau, B. Abdallah, and N. H. Zoubir. "Power and pressure effects upon magnetron sputtered aluminum doped ZnO films properties." Thin Solid Films 519, no. 1 (2010): 5-10.

7. Horwat D., M. Jullien, F. Capon, J.-F. Pierson, J. Andersson, and J. L. Endrino. "On the deactivation of the dopant and electronic structure in reactively sputtered transparent Al-doped ZnO thin films." Journal of Physics D: Applied Physics 43, no. 13 (2010):132003.

8. Masudy-Panah S., S. Zhuk, H. R. Tan, X. Gong, and G. K. Dalapati. "Palladium nanostructure incorporated cupric oxide thin film with strong optical absorption, compatible charge collection and low recombination loss for low cost solar cell applications." Nano Energy 46 (2018): 158-167.

9. Sari, N. B. K. NE Chabane. "Optical properties of ZnO thin film." Advances in Materials Science 13, no. 1 (2013): 35.

10. Nandy S., A. Banerjee, E. Fortunato, and R. Martins. "A review on Cu_2O and CuI-based p-type semiconducting transparent oxide materials: promising candidates for new generation oxide based electronics." Reviews in Advanced Sciences and Engineering 2, no. 4 (2013): 273-304.

11. Kathalingam A., D. Vikraman, H.-S. Kim, and H. J. Park. "Facile fabrication of n-ZnO nanorods/p-Cu_2O heterojunction and its photodiode property." Optical Materials 66 (2017): 122-130.

12. Soldera M., E. Estrada, and K. Taretto. "Simulations of photocurrent improvement through combined geometric/diffracting light trapping in organic small molecule solar cells." physica status solidi (a) 210, no. 7 (2013): 1345-1352.

13. Mickan M. "Deposition of Al-doped ZnO films by high power impulse magnetron sputtering." PhD diss., Université de Lorraine; Université de Linköping (Suède), (2017).

14. de Melo Sanchez C. "Selective growth of Cu_2O and metallic Cu by atomic layer deposition on ZnO and their application in optoelectronics." PhD diss., Université de Lorraine; Saarland University, (2017).

15. Homma S., A. Miyamoto, S. Sakamoto, K. Kishi, N. Motoi, and K. Yoshimura. "Pulmonary fibrosis in an individual occupationally exposed to inhaled indium-tin oxide." European respiratory journal 25, no. 1 (2005): 200-204.

16. Homma T., T. Ueno, K. Sekizawa, A. Tanaka, and M. Hirata. "Interstitial pneumonia developed in a worker dealing with particles containing indium-tin oxide." Journal of occupational health 45, no. 3 (2003): 137-139.

17. Ellmer K. "Past achievements and future challenges in the development of optically transparent electrodes." Nature Photonics 6, no. 12 (2012): 809-817.

18. Coutts T. J., J. D. Perkins, D. S. Ginley, and T. O. Mason. “Transparent conducting oxides: status and opportunities in basic research”. National Renewable Energy Lab (NREL), (1999).

19. Xu R., L. Min, Z. Qi, X. Zhang, J. Jian, Y. Ji, F. Qian et al. "Perovskite transparent conducting oxide for the design of a transparent, flexible, and self-powered perovskite photodetector." American Chemical Society (ACS) Applied Materials & Interfaces 12, no. 14 (2020):16462-16468.

20. Hosono H., and K. Ueda. "Transparent conductive oxides." Springer Handbook of Electronic and Photonic Materials, Springer, Cham, (2017): 1.

21. Stadler A. "Transparent conducting oxides—an up-to-date overview." Materials 5, no.4 (2012): 661-683.

22. Ellmer K., and T. Welzel. "Reactive magnetron sputtering of transparent conductive oxide thin films: Role of energetic particle (ion) bombardment." Journal of Materials Research 27, no. 5 (2012): 765-779.

23. Daichakomphu N., R. Sakdanuphab, A. Harnwunggmoung, Y. Puarporn, N. Chanlek, and A. Sakulkalavek. "Enhanced carrier concentration of Fe doped delafossite $CuAlO_2$ by double-effect: Divalent metal ions doping and excess oxygen." Solid State Ionics 328 (2018): 17-24.

24. Ohta H., M. Orita, M. Hirano, I. Yagi, K. Ueda, and H. Hosono. "Electronic structure and optical properties of $SrCu_2O_2$." Journal of applied physics 91, no. 5 (2002): 3074-3078.

25. James L. “Understanding the difference between n- and p-type semiconductors”. Power & Beyond, (November 19, 2021). https://www.power-and-beyond.com/understanding-the-difference-between-n-and-p-type-semiconductors-a-905805/.

26. Minami T., H. Nanto, and S. Takata. "Highly conductive and transparent zinc oxide films

prepared by rf magnetron sputtering under an applied external magnetic field." Applied Physics Letters 41, no. 10 (1982): 958-960.

27. Eshaghi A., and M. Hajkarimi. "Optical and electrical properties of aluminum zinc oxide (AZO) nanostructured thin film deposited on polycarbonate substrate." Optik 125, no. 19 (2014): 5746-5749.

28. Voon C. H., and S. T. Sam. "Physical surface modification on the biosensing surface." Nanobiosensors for Biomolecular Targeting, Elsevier, (2019): 23-50.

29. Morkoç H., and Ü. Özgür. “Zinc oxide: fundamentals, materials and device technology”. John Wiley & Sons, (2008): 1-76.

30. Sharma D. K., S. Shukla, K. K. Sharma, and V. Kumar. "A review on ZnO: Fundamental properties and applications." Materials Today: Proceedings (2020).

31. Espitia, P. J. Perez, N. de F. F. Soares, J. S. dos R. Coimbra, N. J. de Andrade, R. S. Cruz, and E. A. A. Medeiros. "Zinc oxide nanoparticles: synthesis, antimicrobial activity and food packaging applications." Food and bioprocess technology 5, no. 5 (2012): 1447-1464.

32. Jalil Z. "Structural and optical properties of zinc oxide (ZnO) based thin films deposited by sol-gel spin coating method." Journal of Physics: Conference Series 1116, no. 3, IOP Publishing, (2018): 032020.

33. Idris A. A. M., R. Arsat, M. K. Ahmad, and F. Sidek. "Comparison of deposition methods of ZnO thin film on flexible substrate." Indonesian Journal of Electrical Engineering and Computer Science 5, no. 3 (2017): 536-541.

34. Coral W. C. "Microstructure, chimie et propriétés optiques de films minces ZnO et nanocomposites ZnO-Au synthétisés par pulvérisation cathodique magnétron réactive." PhD diss., Université de Lorraine, (2014).

35. Janotti A., and C. G. Van de Walle. "Fundamentals of zinc oxide as a semiconductor." Reports on progress in physics 72, no. 12 (2009): 126501.

36. Brook R. J., ed. “Concise encyclopedia of advanced ceramic materials.” Elsevier, (2012): 523-525.

37. Rezek J., P. Novák, J. Houška, A. D. Pajdarová, and T. Kozák. "High-rate reactive high-power impulse magnetron sputtering of transparent conductive Al-doped ZnO thin films prepared at ambient temperature." Thin Solid Films 679 (2019): 35-41.

38. Oba F., M. Choi, A. Togo, and I. Tanaka. "Point defects in ZnO: an approach from first principles." Science and Technology of Advanced Materials (2011).

39. Sokol A. A., S. A. French, S. T. Bromley, C. . A. Catlow, H. JJ van Dam, and P. Sherwood. "Point defects in ZnO." Faraday discussions 134 (2007): 267-282.

40. Minami T. "Present status of transparent conducting oxide thin-film development for Indium-Tin-Oxide (ITO) substitutes." Thin Solid Films 516, no. 17 (2008): 5822-5828.

41. Norton D. P., Y. W. Heo, M. P. Ivill, K. Ip, S. J. Pearton, M. F. Chisholm, and T. Steiner. "ZnO: growth, doping & processing." Materials today 7, no. 6 (2004): 34-40.

42. Hagiwara Y., T. Nakada, and A. Kunioka. "Improved Jsc in CIGS thin film solar cells using a transparent conducting ZnO: B window layer." Solar Energy Materials and Solar Cells 67, no. 1-4 (2001): 267-271.

43. Minami T., T. Yamamoto, and T. Miyata. "Highly transparent and conductive rare earth-doped ZnO thin films prepared by magnetron sputtering." Thin Solid Films 366, no. 1-2 (2000): 63-68.

44. Mickan M., U. Helmersson, and D. Horwat. "Effect of substrate temperature on the deposition of Al-doped ZnO thin films using high power impulse magnetron sputtering." Surface and Coatings Technology 347 (2018): 245-251.

45. Liu Y., and Jianshe L. "Optical and electrical properties of aluminum-doped ZnO thin films grown by pulsed laser deposition." Applied Surface Science 253, no. 7 (2007): 3727-3730.

46. Kuroyanagi A. "Properties of aluminum-doped ZnO thin films grown by electron beam evaporation." Japanese journal of applied physics 28, no. 2R (1989): 219.

47. Mallika A. N., A. RamachandraReddy, K. SowriBabu, and K. Venugopal Reddy. "Synthesis and optical characterization of aluminum doped ZnO nanoparticles." Ceramics International 40, no. 8 (2014): 12171-12177.

48. Li L. M., Z. F. Du, and T. H. Wang. "Enhanced sensing properties of defect-controlled ZnO nanotetrapods arising from aluminum doping." Sensors and Actuators B: Chemical 147, no. 1 (2010): 165-169.

49. Yin S., M. M. Shirolkar, J. Li, M. Li, X. Song, X. Dong, and H. Wang. "Influences of defects evolvement on the properties of sputtering deposited ZnO: Al films upon hydrogen annealing." AIP Advances 6, no. 6 (2016): 065020.

50. Ding M., Z. Guo, L. Zhou, X. Fang, L. Zhang, L. Zeng, L. Xie, and H. Zhao. "One-dimensional zinc oxide nanomaterials for application in high-performance advanced optoelectronic devices." Crystals 8, no. 5 (2018): 223.

51. Mendelsberg R. J., S. H. N. Lim, Y. K. Zhu, J. Wallig, D. J. Milliron, and A. Anders. "Achieving high mobility ZnO: Al at very high growth rates by dc filtered cathodic arc deposition." Journal of Physics D: Applied Physics 44, no. 23 (2011): 232003.

52. Mickan M., U. Helmersson, H. Rinnert, J. Ghanbaja, D. Muller, and D. Horwat. "Room temperature deposition of homogeneous, highly transparent and conductive Al doped ZnO films by reactive high power impulse magnetron sputtering." Solar Energy Materials and Solar Cells 157 (2016): 742-749.

53. Mickan M., M. Stoffel, H. Rinnert, U. Helmersson, and D. Horwat. "Restoring the properties of transparent Al-doped ZnO thin film electrodes exposed to ambient air." The Journal of Physical Chemistry C 121, no. 27 (2017): 14426-14433.

54. Anh D., Duc, K. N. Hui, K. S. Hui, J. Singh, P. Kumar, and W. Zhou. "Parameters Affecting the Electrical and Optical Properties of p-Type Aluminum-Doped ZnO: A Review." Reviews in Advanced Sciences and Engineering 2, no. 4 (2013): 259272.

55. Krawczak E., Z. Agata, S. Gulkowski, A. Fave, and E. Fourmond. "Influence of sputtering deposition parameters on electrical and optical properties of aluminium-doped zinc oxide thin films for photovoltaic applications." E3S Web of Conferences 22, EDP Sciences, (2017): 00090.

56. CHIȚANU E. "The influence of deposition parameters on structural, optical and electrical properties of AZO thin film." Journal of Optoelectronics and Advanced Materials 23, no. 5-6 (2021): 270-274.

57. Swatowska B., W. Powroźnik, H. Czternastek, G. Lewińska, T. Stapiński, R. Pietruszka, B. S. Witkowski, and M. Godlewski. "Application properties of ZnO and AZO thin films obtained by the ALD method." Energies 14, no. 19 (2021): 6271.

58. Özdal T., and H. Kavak. "Fabrication and characterization of ZnO/Cu_2O heterostructures for solar cells applications." Superlattices and Microstructures 146 (2020): 106679.

59. Soon A., M. Todorova, B. Delley, and C. Stampfl. "Thermodynamic stability and structure of copper oxide surfaces: A first-principles investigation." Physical Review *B* 75, no. 12 (2007): 125420.

60. Yin M., C.-K. Wu, Y. Lou, C. Burda, J. T. Koberstein, Y. Zhu, and S. O'Brien. "Copper oxide nanocrystals." Journal of the American Chemical Society 127, no. 26 (2005): 9506-9511.

61. Johan M. R., M. S. M. Suan, N. L. Hawari, and H. A. Ching. "Annealing effects on the properties of copper oxide thin films prepared by chemical deposition." International Journal of Electrochemical Science 6, no. 12 (2011): 6094-6104.

62. Serin N., T. Serin, Ş. Horzum, and Y. Celik. "Annealing effects on the properties of copper oxide thin films prepared by chemical deposition." Semiconductor science and technology 20, no. 5 (2005): 398.

63. Tahir D., and S. Tougaard. "Electronic and optical properties of Cu, CuO and Cu_2O studied by electron spectroscopy." Journal of physics: Condensed matter 24, no. 17 (2012): 175002.

64. Liu Y. L., Y. C. Liu, R. Mu, H. Yang, C. L. Shao, J. Y. Zhang, Y. M. Lu, D. Z. Shen, and X. W. Fan. "The structural and optical properties of Cu_2O films electrodeposited on different substrates." Semiconductor science and technology 20, no. 1 (2004): 44.

65. Lee S., C.-W. Liang, and L. W. Martin. "Synthesis, control, and characterization of surface properties of Cu_2O nanostructures." American Chemical Society (ACS) nano 5, no. 5 (2011): 3736-3743.

66. Xiong L., S. Huang, X. Yang, M. Qiu, Z. Chen, and Y. Yu. "p-Type and n-type Cu_2O semiconductor thin films: Controllable preparation by simple solvothermal method and photoelectrochemical properties." Electrochimica Acta 56, no. 6 (2011): 2735-2739.

67. Farhad, S. F. Uddin, D. Cherns, J. A. Smith, N. A. Fox, and D. J. Fermin. "Pulsed laser deposition of single phase n-and p-type Cu_2O thin films with low resistivity." Materials & Design 193, (2020): 108848.

68. Akimoto K., S. Ishizuka, M. Yanagita, Y. Nawa, G. K. Paul, and T. Sakurai. "Thin film deposition of Cu_2O and application for solar cells." Solar energy 80, no. 6 (2006): 715-722.

69. Chen A., H. Long, X. Li, Y. Li, G. Yang, and P. Lu. "Controlled growth and characteristics of single-phase Cu_2O and CuO films by pulsed laser deposition." Vacuum 83, no. 6 (2009): 927-930.

70. Ishizuka S., T. Maruyama, and K. Akimoto. "Thin-film deposition of Cu_2O by reactive radio-frequency magnetron sputtering." Japanese Journal of Applied Physics 39, no. 8A (2000): L786.

71. Grozdanov I. "Electroless chemical deposition technique for Cu_2O thin films." Materials Letters 19, no. 5-6 (1994): 281-285.

72. Subramaniyan A., J. D. Perkins, R. P. O'Hayre, S. Lany, V. Stevanovic, D. S. Ginley, and A. Zakutayev. "Non-equilibrium deposition of phase pure Cu_2O thin films at reduced growth temperature." APL Materials 2, no. 2 (2014): 022105.

73. Dhakal D., T. Waechtler, S. E. Schulz, T. Gessner, H. Lang, R. Mothes, and A. Tuchscherer. "Surface chemistry of a Cu (I) beta-diketonate precursor and the atomic layer deposition of Cu_2O on SiO_2 studied by x-ray photoelectron spectroscopy." Journal of Vacuum Science & Technology A: Vacuum, Surfaces, and Films 32, no. 4 (2014): 041505.

74. Iivonen T., M. J. Heikkilä, G. Popov, H.-E. Nieminen, M. Kaipio, M. Kemell, M. Mattinen et al. "Atomic layer deposition of photoconductive Cu_2O thin films." American Chemical Society (ACS) omega 4, no. 6 (2019): 11205-11214.

75. Geng J., J. Ma, F. Li, S. Ma, D. Zhang, and X. Ning. "Atomic layer deposition of Cu_2O on NH_2-MIL-101(Fe) for enhanced photocatalytic performance and decreased electron/hole recombination." Ceramics International 47, no. 10 (2021): 13291-13300.

76. Chu Y. S., I. K. Robinson, and A. A. Gewirth. "Comparison of aqueous and native oxide formation on Cu (111)." The Journal of chemical physics 110, no. 12 (1999): 5952-5959.

77. Raebiger H., S. Lany, and A. Zunger. "Origins of the p-type nature and cation deficiency in Cu_2O and related materials." Physical Review *B* 76, no. 4 (2007): 045209.

78. Laidoudi S., A. Y. Bioud, A. Azizi, G. Schmerber, J. Bartringer, S. Barre, and A. Dinia. "Growth and characterization of electrodeposited Cu_2O thin films." Semiconductor science and technology 28, no. 11 (2013): 115005.

79. Dhakal D., K. Assim, H. Lang, P. Bruener, T. Grehl, C. Georgi, T. Waechtler, R. Ecke, S. E. Schulz, and T. Gessner. "Atomic layer deposition of ultrathin Cu_2O and subsequent reduction to Cu studied by in situ x-ray photoelectron spectroscopy." Journal of Vacuum Science & Technology A: Vacuum, Surfaces, and Films 34, no. 1 (2016): 01A111.

80. Wang Y., J. Ghanbaja, F. Soldera, S. Migot, P. Boulet, D. Horwat, F. Mücklich, and J.-F. Pierson. "Tuning the structure and preferred orientation in reactively sputtered copper oxide thin films." Applied Surface Science 335 (2015): 85-91.

81. de Melo C., M. Jullien, Y. Battie, A. E. Naciri, J. Ghanbaja, F. Montaigne, J.-F. Pierson et al. "Semi-transparent p-Cu_2O/n-ZnO nanoscale-film heterojunctions for photodetection and photovoltaic applications." American Chemical Society (ACS) Applied Nano Materials 2, no. 7 (2019): 4358-4366.

82. Shubbak M. H. "Advances in solar photovoltaics: Technology review and patent trends." Renewable and Sustainable Energy Reviews 115 (2019): 109383.

83. Huber H. P., F. Herrnberger, S. Kery, and S. Zoppel. "Selective structuring of thin-film solar cells by ultrafast laser ablation." Commercial and Biomedical Applications of Ultrafast Lasers VIII 6881, International Society for Optics and Photonics, (2008): 688117.

84. Ernst K., A. Belaidi, and R. Könenkamp. "Solar cell with extremely thin absorber on highly structured substrate." Semiconductor science and technology 18, no. 6 (2003): 475.

85. Soldera M., K. Taretto, J. Berger, and A. F. Lasagni. "Potential of Photocurrent Improvement in μc-Si: H Solar Cells with TCO Substrates Structured by Direct Laser Interference Patterning." Advanced Engineering Materials 18, no. 9 (2016): 1674-1682.

86. Jandeleit J., A. Horn, R. Weichenhain, E. W. Kreutz, and R. Poprawe. "Fundamental investigations of micromachining by nano-and picosecond laser radiation." Applied Surface Science 127 (1998): 885-891.

87. "Structuring and texturing". LightPulse. https://www.light-pulse.de/en-gb/laserstructuring.

88. "Laser Structuring". Mks. https://www.spectra-physics.com/n/laser-structuring.

89. https://www.epic-assoc.com/wp-content/uploads/2015/09/Published-ManufacturingTechnologies-Benefits.pdf.

90. Jean J., P. R. Brown, R. L. Jaffe, T. Buonassisi, and V. Bulović. "Pathways for solar photovoltaics." Energy & Environmental Science 8, no. 4 (2015): 1200-1219.

91. Rosas-Laverde, N. Maria, A. Pruna, J. Cembrero, J. Orozco-Messana, and F. J. Manjón. "Performance of graphene oxide-modified electrodeposited ZnO/Cu_2O heterojunction solar cells." boletín de la sociedad española de cerámica y vidrio 58, no. 6 (2019): 263-273.

92. Jeong S. S., A. Mittiga, E. Salza, A. Masci, and S. Passerini. "Electrodeposited ZnO/Cu_2O heterojunction solar cells." Electrochimica Acta 53, no. 5 (2008): 2226-2231.

93. Minami T., Y. Nishi, T. Miyata, and J.-i. Nomoto. "High-efficiency oxide solar cells with ZnO/Cu_2O heterojunction fabricated on thermally oxidized Cu_2O sheets." Applied physics express 4, no. 6 (2011): 062301.

94. Guerguerian G., F. Elhordoy, C. J. Pereyra, R. E. Marotti, F. Martín, D. Leinen, J. R. Ramos-Barrado, and E. A. Dalchiele. "ZnO/Cu_2O heterostructure nanopillar arrays: synthesis, structural and optical properties." Journal of Physics D: Applied Physics 45, no. 24 (2012): 245301.

95. Chou S.-M., M.-H. Hon, C. Leu, and Y.-H. Lee. "Al-Doped ZnO/Cu_2O heterojunction fabricated on (200) and (111)-orientated Cu_2O substrates." Journal of the Electrochemical Society 155, no. 11 (2008): H923.

96. Yang M., L. Zhu, Y. Li, L. Cao, and Y. Guo. "Asymmetric interface band alignments of Cu_2O/ZnO and ZnO/Cu_2O heterojunctions." Journal of alloys and compounds 578 (2013): 143-147.

97. Lindig S. "Performance evaluation towards optimal Building Integrated Photovoltaic Systems Simulation of BiPV systems using dynamic simulations." Master diss., University of Applied Science HTWK Leipzig, (2014).

98. Morales-Aragonés, J. Ignacio, M. del C. Alonso-García, S. Gallardo-Saavedra, V. Alonso-Gómez, J. L. Balenzategui, A. Redondo-Plaza, and L. Hernández-Callejo. "Online Distributed Measurement of Dark I–V Curves in Photovoltaic Plants." Applied Sciences 11, no. 4 (2021): 1924.

99. Naghdi Sa. "Thin films- definition, deposition techniques, and applications". Research Gate, (February, 2021).https://www.researchgate.net/publication/349494202_Thin_films_definition_deposition_techniques_and_applications.

100. "What is Thin Film Deposition?". Denton Vacuum. https://www.dentonvacuum.com/what- is-%20%20%20%20%20%20%20%20%20%20%20%20thin-film-deposition/.

101. Hughes M. "What Is Thin Film Deposition ?". Semicore, (November 21, 2014). http://www.semicore.com/news/81-what-is-thin-film-deposition.

102. Mattox D. M. "Physical vapor deposition (PVD) processes." Metal Finishing 100 (2002):394-408.

103. « PVD – Pressure Vapour Deposition Techniques and Advantages ». CM Group. https://www.cmgroupsrl.eu/en/pvd-pressure-vapour-deposition-techniques-and-advantages.

104. Makhlouf A. S. H. "Current and advanced coating technologies for industrial applications." Nanocoatings and ultra-thin films, (2011): 3-23.

105. "Plasma, the fourth state of matter". Pie Scientific. https://piescientific.com/resource_pages/resource_introduction_to_plasma/.

106. "Sputtering: Process, Types, and Uses". Nanografi. https://nanografi.com/blog/sputtering-process types-and-uses/.

107. Fager H. "Growth and Characterization of Amorphous TiAlSiN and HfAlSiN Thin Films." PhD diss., Linköping University Electronic Press, (2012).

108. Gudmundsson J. T. "Physics and technology of magnetron sputtering discharges." Plasma Sources Science and Technology 29, no. 11 (2020): 113001.

109. "Magnetron Sputtering". Materials Science. http://www.msipse.com/PDF/Technical%20Notes/TN%20000%20100%2002_03.pdf.

110. Kelly P. J., and R. Derek Arnell. "Magnetron sputtering: a review of recent developments and applications." Vacuum 56, no. 3 (2000): 159-172.

111. Olaya J. J., S. E. Rodil, and S. Muhl. "Comparative study of niobium nitride coatings deposited unbalanced and balanced magnetron sputtering." Thin Solid Films 516, no. 23 (2008): 8319-8326.

112. Shanker G., P. Prathap, K. M. K. Srivatsa, and P. Singh. "Effect of balanced and unbalanced magnetron sputtering processes on the properties of SnO_2 thin films." Current Applied Physics 19, no. 6 (2019): 697-703.

113. Safi I. "Recent aspects concerning DC reactive magnetron sputtering of thin films: a review." Surface and Coatings Technology 127, no. 2-3 (2000): 203-218.

114. Musil J., P. Baroch, J. Vlček, K. H. Nam, and J. G. Han. "Reactive magnetron sputtering of thin films:
present status and trends." Thin solid films 475, no. 1-2 (2005): 208-218.

115. Danisman K., S. Danisman, S. Savas, and I. Dalkiran. "Modelling of the hysteresis effect of target voltage in reactive magnetron sputtering process by using neural networks." Surface and Coatings Technology 204, no. 5 (2009): 610-614.

116. Strijckmans K., R. Schelfhout, and D. Depla. "Tutorial: Hysteresis during the reactive magnetron sputtering process." Journal of Applied Physics 124, no. 24 (2018): 241101.

117. Chamorro W., D. Horwat, P. Pigeat, P. Miska, S. Migot, F. Soldera, P. Boulet, and F. Mücklich. "Near-
room temperature single-domain epitaxy of reactively sputtered ZnO films." Journal of Physics D: Applied Physics 46, no. 23 (2013): 235107.

118. Horwat D., and A. Billard. "Effects of substrate position and oxygen gas flow rate on the properties of
ZnO: Al films prepared by reactive co-sputtering." Thin solid films 515, no. 13 (2007): 5444-5448.

119. Maud J. "Synthèse et caractérisation de films minces d'oxydes pour le développement d'un système électrochrome tout céramique"." PhD diss., Institut National Polytechnique de Lorraine, (2011).

120. Gudmundsson J. T., and D. Lundin. "Introduction to magnetron sputtering." High Power Impulse Magnetron Sputtering, (2020): 1-48.

121. Ellmer K. "Magnetron sputtering of transparent conductive zinc oxide: relation between the sputtering
parameters and the electronic properties." Journal of Physics D: Applied Physics 33, no. 4 (2000): R17.

122. Le M.-T., Y.-U. Sohn, J.-W. Lim, and G.-S. Choi. "Effect of sputtering power on the nucleation and growth of Cu films deposited by magnetron sputtering." Materials transactions 51, no. 1 (2010): 116-120.

123. Hughes M. "What is HIPIMS? High Power Impulse Magnetron Sputtering". Semicore, (October 28, 2016). http://www.semicore.com/news/93-what-is-hipims.

124. Ganesan R., B. J. Murdoch, B. Treverrow, A. E. Ross, I. S. Falconer, A. Kondyurin, D. G. McCulloch,
J. G. Partridge, D. R. McKenzie, and M. M. M. Bilek. "The role of pulse length in target poisoning during reactive HiPIMS: application to amorphous HfO_2." Plasma Sources Science and Technology 24, no. 3 (2015): 035015.

125. Wallin E., and U. Helmersson. "Hysteresis-free reactive high power impulse magnetron sputtering." Thin Solid Films 516, no. 18 (2008): 6398-6401.

126. Dr. W. Gajewski. "HiPIMS new possibilities for industry". TRUMPF Hüttinger White Paper, (2017).

127. Mahieu S., W. P. Leroy, K. Van Aeken, and D. Depla. "Modeling the flux of high energy negative ions during reactive magnetron sputtering." Journal of Applied Physics 106, no.9 (2009): 093302.

128. Welzel T., and K. Ellmer. "The influence of the target age on laterally resolved ion distributions in reactive planar magnetron sputtering." Surface and Coatings technology 205 (2011): S294-S298.

129. T-Thienprasert, J., S. Rujirawat, W. Klysubun, J. N. Duenow, T. J. Coutts, S. B. Zhang, D. C. Look, and S. J. P. R. L. Limpijumnong. "Compensation in Al-doped ZnO by Al-related acceptor complexes:
synchrotron X-ray absorption spectroscopy and theory." Physical review letters 110, no. 5 (2013): 055502.

130. Gilbert B. "Synthèse de films nanocomposites Ag/YSZ, Ag/CGO & Ag(Cu)/CGO par pulvérisation cathodique magnétron réactive pour l'électrocatalyse de l'éthylène en oxyde d'éthylène." PhD diss., Université de Lorraine, 2020.

131. de Melo C., M. Jullien, J. Ghanbaja, F. Montaigne, J.-F. Pierson, F. Soldera, F. Rigoni et al. "Local structure and point-defect-dependent area-selective atomic layer deposition approach for facile synthesis of p-Cu_2O/n-ZnO segmented nanojunctions." American Chemical Society (ACS) applied materials & interfaces 10, no. 43 (2018): 37671-37678.

132. Elam J. W., N. P. Dasgupta, and F. B. Prinz. "ALD for clean energy conversion, utilization, and storage." Materials Research Society (MRS) bulletin 36, no. 11 (2011): 899-906.

133. Johnson R. W., A. Hultqvist, and S. F. Bent. "A brief review of atomic layer deposition: from fundamentals to applications." Materials today 17, no. 5 (2014): 236-246.

134. Moshe H., and Y. Mastai. "Atomic layer deposition on self-assembled-monolayers." Materials Science-Advanced Topics (2013): 63-84.

135. Cremers V., R. L. Puurunen, and J. Dendooven. "Conformality in atomic layer deposition: Current status overview of analysis and modelling." Applied Physics Reviews 6, no. 2 (2019): 021302.

136. Lee S. W., Y. S. Lee, J. Heo, S. C. Siah, D. Chua, R. E. Brandt, S. B. Kim, J. P. Mailoa, T. Buonassisi,
and R. G. Gordon. "Improved Cu_2O-based solar cells using atomic layer deposition to control the Cu oxidation state at the p-n junction." Advanced Energy Materials 4, no. 11 (2014): 1301916.

137. Kim H., M. Y. Lee, S.-H. Kim, S. I. Bae, K. Y. Ko, H. Kim, K.-W. Kwon, J.-H. Hwang, and D.-J. Lee.
"Highly-conformal p-type copper (I) oxide (Cu_2O) thin films by atomic layer deposition using a fluorine-free amino-alkoxide precursor." Applied Surface Science 349 (2015): 673-682.

138. Sundberg P., and M. Karppinen. "Organic and inorganic–organic thin film structures by molecular layer deposition: A review." Beilstein journal of nanotechnology 5, no. 1 (2014):1104-1136.

139. Asim N., S. Ahmadi, M. A. Alghoul, F. Y. Hammadi, K. Saeedfar, and K. Sopian. "Research and development aspects on chemical preparation techniques of photoanodes for dye sensitized solar cells." International Journal of Photoenergy 2014 (2014).

140. Lim J., S.-M. Lee, H.-Y. Jang, and S.-M. Kim. "Fabrication of an antireflective nanodome array with high packing density for photovoltaic applications." Journal of Nanomaterials 2015, no. 6 (2015).

141. Eisenhauer D., C. T. Trinh, D. Amkreutz, and C. Becker. "Light management in crystalline silicon thin-film solar cells with imprint-textured glass superstrate." Solar Energy Materials and Solar Cells 200 (2019): 109928.

142. Müller-Meskamp L., Y. H. Kim, T. Roch, S. Hofmann, R. Scholz, S. Eckardt, K. Leo, and A. F. Lasagni. "Efficiency enhancement of organic solar cells by fabricating periodic surface textures using direct laser interference patterning." Advanced Materials 24, no. 7 (2012): 906-910.

143. Balakrisnan B., S. Patil, and E. Smela. "Patterning PDMS using a combination of wet and dry etching." Journal of Micromechanics and Microengineering 19, no. 4 (2009):047002.

144. Khademhosseini A., and R. Langer. "Microengineered hydrogels for tissue engineering." Biomaterials 28, no. 34 (2007): 5087-5092.

145. Preissler N. "Front-side interface engineering for liquid-phase crystallized silicon solar cells on glass". PhD diss., Technische Universitaet Berlin (Germany), 2018.

146. Amkreutz D., J. Haschke, T. Häring, F. Ruske, and B. Rech. "Conversion efficiency and process stability improvement of electron beam crystallized thin film silicon solar cells on glass." Solar Energy Materials and Solar Cells 123 (2014): 13-16.

147. Canteli D., I. Torres, S. Fernández, J. D. Santos, M. Morales, and C. Molpeceres. "Photon-collection improvement from laser-textured AZO front-contact in thin-film solar cells." Applied Surface Science 463 (2019): 775-780.

148. "Laser Structuring and Selective Ablation". 3D Micromac. https://3d-micromac.com/laser%20micromachining/applications/laser-structuring/#flexible-thin-films.

149. Wang L., Z.-H. Wang, Y.-H. Yu, and H.-B. Sun. "Laser interference fabrication of large-area functional periodic structure surface." Frontiers of Mechanical Engineering 13, no. 4 (2018): 493-503.

150. Bieda M., M. Siebold, and A. F. Lasagni. "Fabrication of sub-micron surface structures on copper, stainless steel and titanium using picosecond laser interference patterning." Applied Surface Science 387 (2016): 175-182.

151. Lasagni A. F., D. F. Acevedo, C. A. Barbero, and F. Mücklich. "One-Step Production of Organized Surface Architectures on Polymeric Materials by Direct Laser Interference Patterning." Advanced Engineering Materials 9, no. 1-2 (2007): 99-103.

152. Voisiat B., A. I. Aguilar-Morales, T. Kunze, and A. F. Lasagni. "Development of an analytical model for optimization of direct laser interference patterning." Materials 13, no. 1 (2020): 200.

153. Catrin R., T. Gries, B. Raillard, F. Mücklich, S. Migot, and D. Horwat. "Influence of laser interference patterning on microstructure and friction behavior of gold/yttria-stabilized zirconia nanocomposite thin films." Journal of Materials Research 27, no.6 (2012): 879-885.

154. Yang Y.-K., Y.-X. Wu, T.-H. Lin, C.-W. Yu, and C.-C. Fu. "Improve large area uniformity and production capacity of laser interference lithography with beam flattening device." Laser-based Micro- and Nanoprocessing X 9736. International Society for Optics and Photonics (2016): 97360Y.

155. Voisiat B., S. Milles, and A. F. Lasagni. "Impact of Molten Pool Dynamics on Resultant Surface Structures During Direct Laser Interference Patterning." Journal of Laser Micro Nanoengineering 16, no. 1 (2021): 30-35.

156. Rosenkranz A., M. Hans, C. Gachot, A. Thome, S. Bonk, and F. Mücklich. "Direct laser interference patterning: Tailoring of contact area for frictional and antibacterial properties." Lubricants 4, no. 1 (2016): 2.

157. Aguilar-Morales A. I., S. Alamri, and A. F. Lasagni. "Micro-fabrication of high aspect ratio periodic structures on stainless steel by picosecond direct laser interference patterning." Journal of Materials Processing Technology 252 (2018): 313-321.

158. Milles S., J. Dahms, B. Voisiat, S. Indrišiunas, G. Raciukaitis, and A. F. Lasagni. "Wetting Properties of Aluminium Surface Structures Fabricated Using Direct Laser Interference Patterning with Picosecond and Femtosecond Pulses." Journal of Laser Micro Nanoengineering 16, no. 1 (2021): 74-79.

159. Sever M., B. Lipovšek, J. Krč, A. Čampa, G. S. Plaza, F.-J. Haug, M. Duchamp, W. Soppe, and M. Topič. "Combined model of non-conformal layer growth for accurate optical simulation of thin-film silicon solar cells." Solar Energy Materials and Solar Cells 119 (2013): 59-66.

160. Campa A., and J. Krc. "Two approaches for incoherent propagation of light in rigorous numerical simulations." Progress In Electromagnetics Research 137 (2013).

161. Sau S., S. Chakraborty, T. Das, and M. Pal. "Ethanol sensing properties of nanocrystalline α-MoO_3." Frontiers in Materials 6 (2019): 285.

162. Zhou W., R. Apkarian, Z. L. Wang, and D. Joy. "Fundamentals of scanning electron microscopy (SEM)." Scanning microscopy for nanotechnology, (2006): 1-40.

163. Sharma S. K., D. S. Verma, L. U. Khan, S. Kumar, and S. B. Khan, “Handbook of materials Characterization”. Springer International Publishing, (2018).

164. Tagliente M. A., M. Penza, M. Gusso, and A. Quirini. "Characterisation of ZnS: Mn thin films by Rietveld refinement of Bragg–Brentano X-ray diffraction patterns." Thin Solid Films 353, no. 1-2 (1999): 129-136.

165. “Chapter 3 - Methods for Assessing Surface Cleanliness”. Developments in Surface Contamination and Cleaning 12, (2019): 23-105.

166. Epp J. "X-ray diffraction (XRD) techniques for materials characterization." Materials characterization using nondestructive evaluation (NDE) methods, (2016): 81-124.

167. “2.11.6 X-Ray Diffraction”. Openstax CNX. https://cnx.org/contents/uNNozUZi@1.377:7rP98uDK@2/X-Ray-Diffraction.

168. Monshi A., M. R. Foroughi, and M. R. Monshi. "Modified Scherrer equation to estimate more accurately nano-crystallite size using XRD." World Journal of Nano Science and Engineering 2, no. 3 (2012): 154-160.

169. Muniz F. T. L., MA R. Miranda, C. M. dos Santos, and J. M. Sasaki. "The Scherrer equation and the dynamical theory of X-ray diffraction." Acta Crystallographica Section A: Foundations and Advances 72, no. 3 (2016): 385-390.

170. Orloff J., L. Swanson, and M. Utlaut. “High resolution focused ion beams: FIB and its applications: The physics of liquid metal ion sources and ion optics and their application to focused ion beam technology”. Springer Science & Business Media, 2003.

171. Bollmeyer M. and L. Boxi. “Transmission electron microscopy (TEM): TEM versus STEM and HAADF”. Chemistry LibreTexts, (November 29, 2020). https://chem.libretexts.org/Courses/Franklin_and_Marshall_College/Introduction_to_Materials_Characterization__CHM_412_Collaborative_Text/Electron_and_Probe_Microscopy/Transmission_electron_microscopy_(TEM)%3A_TEM_versus_STEM_and_HAADF#:~:text=While%20in%20TEM%20parallel%20electron,is%20rastered%20across%20the%20sample.

172. Goo N. H. "Formation of hard magnetic L10-FePt/FePd monolayers from elemental multilayers." PhD diss., Max-Planck-Institut für Metallforschung Stuttgart, 2007.

173. Davis B. “What is the difference between TEM and STEM?”. (July 29, 2019).

174. Keast V. J., A. J. Scott, R. Brydson, D. B. Williams, and J. Bruley. "Electron energy-loss near-edge structure–a tool for the investigation of electronic structure on the nanometer scale." Journal of Microscopy 203, no. 2 (2001): 135-175.

175. https://eels.info/about/overview.

176. Technique sheet of the Olympus® 3D Measuring Laser Microscope OLS4100 LEXT.

177. Uchqun M., and T. Jahongir. "The Research of the VI Characteristics of a Solar Panel Using a Computerized Measuring Bench “EPH 2 Advanced Photovoltaics Trainer”." International Journal of Academic and Applied Research (IJAAR) 3, no. 4 (2019).

178. Ravichandran K., N. Jabena Begum, S. Snega, and B. Sakthivel. "Properties of sprayed aluminum-

doped zinc oxide films—a review." Materials and Manufacturing Processes 31, no. 11 (2016): 1411-1423.

179. Jeong S. H., and J. H. Boo. "Influence of target-to-substrate distance on the properties of AZO films grown by RF magnetron sputtering." Thin Solid Films 447 (2004): 105-110.

180. Li M., X. Qian, A.-D. Li, Y.-Q. Cao, H.-F. Zhai, and D. Wu. "A comparative study of growth and properties of atomic layer deposited transparent conductive oxide of Al doped ZnO films from different Al precursors." Thin solid films 646 (2018): 126-131.

181. Singh S., and S.-H. Park. "Effect of post deposition annealing treatments on properties of AZO thin films for Schottky diode applications." Journal of Nanoscience and Nanotechnology 16, no. 1 (2016):
861-866.

182. Uthanna S., T. K. Subramanyam, B. Srinivasulu Naidu, and G. Mohan Rao. "Structure-composition-property dependence in reactive magnetron sputtered ZnO thin films." Optical Materials 19, no. 4 (2002): 461-469.

183. Horwat D., and A. Anders. "Compression and strong rarefaction in high power impulse magnetron sputtering discharges." Journal of Applied Physics 108, no. 12 (2010): 123306.

184. Sittinger V., O. Lenck, M. Vergöhl, B. Szyszka, and G. Bräuer. "Applications of HiPIMS metal oxides." Thin Solid Films 548 (2013): 18-26.

185. Aiempanakit M., A. Aijaz, D. Lundin, U. Helmersson, and T. Kubart. "Understanding the discharge current behavior in reactive high power impulse magnetron sputtering of oxides." Journal of Applied Physics 113, no. 13 (2013): 133302.

186. Reed A. N., P. J. Shamberger, J. J. Hu, C. Muratore, J. E. Bultman, and A. A. Voevodin. "Microstructure of ZnO thin films deposited by high power impulse magnetron sputtering." Thin Solid
Films 579 (2015): 30-37.

187. Poolcharuansin P., and J. W. Bradley. "Short-and long-term plasma phenomena in a HiPIMS discharge." Plasma Sources Science and Technology 19, no. 2 (2010): 025010.

188. Corbella C., A. Marcak, T. de los Arcos, and A. von Keudell. "Revising secondary electron yields of ion-sputtered metal oxides." Journal of Physics D: Applied Physics 49, no. 16 (2016): 16LT01.

189. Straňák V., M. Quaas, H. Wulff, Z. Hubička, S. Wrehde, M. Tichý, and R. Hippler. "Formation of TiO_x films produced by high-power pulsed magnetron sputtering." Journal of Physics D: Applied Physics 41, no. 5 (2008): 055202.

190. Kappertz O. "Atomistic effects in reactive direct current sputter deposition." PhD diss., Bibliothek der
Rheinisch-Westf¨alischen Technischen Hochschule (RWTH) Aachen, 2003.

191. Cornelius S., M. Vinnichenko, N. Shevchenko, A. Rogozin, A. Kolitsch, and W. Möller. "Achieving high free electron mobility in ZnO: Al thin films grown by reactive pulsed magnetron sputtering."

Applied Physics Letters 94, no. 4 (2009): 042103.

192. Lu J. G., Z. Z. Ye, Y. J. Zeng, L. P. Zhu, L. Wang, J. Yuan, B. H. Zhao, and Q. L. Liang. "Structural,
optical, and electrical properties of (Zn, Al) O films over a wide range of compositions." Journal of Applied Physics 100, no. 7 (2006): 073714.

193. Jullien M., D. Horwat, F. Manzeh, R. Escobar Galindo, Ph Bauer, J. F. Pierson, and J. L. Endrino. "Influence of the nanoscale structural features on the properties and electronic structure of Al-doped ZnO thin films: An X-ray absorption study." Solar Energy Materials and Solar Cells 95, no. 8 (2011):
2341-2346.

194. Rambu A. P., L. Ursu, N. Iftimie, V. Nica, M. Dobromir, and F. Iacomi. "Study on Ni-doped ZnO films as gas sensors." Applied Surface Science 280 (2013): 598-604.

195. Lee K. E., M. Wang, E. J. Kim, and S. H. Hahn. "Structural, electrical and optical properties of sol–gel AZO thin films." Current Applied Physics 9, no. 3 (2009): 683-687.

196. Claeyssens F., C. L. Freeman, N. L. Allan, Y. Sun, M. NR Ashfold, and J. H. Harding. "Growth of ZnO thin films—experiment and theory." Journal of Materials Chemistry 15, no. 1 (2005): 139-148.

197. Tu Z. C., and X. Hu. "Elasticity and piezoelectricity of zinc oxide crystals, single layers, and possible single-walled nanotubes." Physical Review B 74, no. 3 (2006): 035434.

198. Tusche C., H. L. Meyerheim, and J. Kirschner. "Observation of depolarized ZnO (0001) monolayers: formation of unreconstructed planar sheets." Physical review letters 99, no. 2 (2007): 026102.

199. Quang H. T., A. Bachmatiuk, A. Dianat, F. Ortmann, J. Zhao, J. H. Warner, J. Eckert, G. Cunniberti, and M. H. Rümmeli. "In situ observations of free-standing graphene-like mono-and bilayer ZnO membranes." American Chemical Society (ACS) nano 9, no. 11 (2015): 11408-11413.

200. Sang H., Y. Zeng, and L. Sun. "Stability of graphite-like ZnO film with Cu doping: First principle study." The European Physical Journal Plus 134, no. 1 (2019): 24.

201. Mun Wong K., S. M. Alay-e-Abbas, A. Shaukat, Y. Fang, and Y. Lei. "First-principles investigation of the size-dependent structural stability and electronic properties of O-vacancies at the ZnO polar and
non-polar surfaces." Journal of Applied Physics 113, no. 1 (2013): 014304.

202. Liu H., V. Avrutin, N. Izyumskaya, Ü. Özgür, and H. Morkoç. "Transparent conducting oxides for electrode applications in light emitting and absorbing devices." Superlattices and Microstructures 48, no. 5 (2010): 458-484.

203. Nian Q., M. Y. Zhang, B. D. Schwartz, and G. J. Cheng. "Ultraviolet laser crystallized ZnO: Al films on sapphire with high Hall mobility for simultaneous enhancement of conductivity and transparency."
Applied Physics Letters 104, no. 20 (2014): 201907.

204. Dhakal T., A. S. Nandur, R. Christian, P. Vasekar, S. Desu, C. Westgate, D. I. Koukis, D. J. Arenas,

and D. B. Tanner. "Transmittance from visible to mid infra-red in AZO films grown by atomic layer deposition system." Solar Energy 86, no. 5 (2012): 1306-1312.

205. Bikowski A., and K. Ellmer. "Analytical model of electron transport in polycrystalline, degenerately doped ZnO films." Journal of Applied Physics 116, no. 14 (2014): 143704.

206. Lin T.-C., W.-C. Huang, and F.-C. Tsai. "The electro-optical characteristics of AZO/Mo/AZO transparent conductive film." Journal of Materials Science: Materials in Electronics 26, no. 6 (2015): 3685-3690.

207. Lin T.-C., W.-C. Huang, and F.-C. Tsai. "The structural and electro-optical characteristics of AZO/Cr:
Cu/AZO transparent conductive film." Thin Solid Films 589 (2015): 446-450.

208. Wang J., Z. Wang, B. Huang, Y. Ma, Y. Liu, X. Qin, X. Zhang, and Y. Dai. "Oxygen vacancy induced
band-gap narrowing and enhanced visible light photocatalytic activity of ZnO." American Chemical Society (ACS) applied materials & interfaces 4, no. 8 (2012): 4024-4030.

209. Mugwang'a F. K., P. K. Karimi, W. K. Njoroge, and O. Omayio. "Characterization of aluminum doped
zinc oxide (Azo) thin films prepared by reactive thermal evaporation for solar cell applications." Journal of Fundamentals of Renewable Energy and Applications 5, no. 170 (2015): 2.

210. Turkoglu F., H. Koseoglu, S. Zeybek, M. Ozdemir, G. Aygun, and L. Ozyuzer. "Effect of substrate rotation speed and off-center deposition on the structural, optical, and electrical properties of AZO thin films fabricated by DC magnetron sputtering." Journal of Applied Physics 123, no. 16 (2018): 165104.

211. Bikowski A., T. Welzel, and K. Ellmer. "The correlation between the radial distribution of high-energetic ions and the structural as well as electrical properties of magnetron sputtered ZnO: Al films."
Journal of Applied Physics 114, no. 22 (2013): 223716.

212. Stamate E. "Spatially resolved optoelectronic properties of Al-Doped zinc oxide thin films deposited by radio-frequency magnetron plasma sputtering without substrate heating." Nanomaterials 10, no. 1 (2019): 14.

213. Paul B., B. Singh, S. Ghosh, and A. Roy. "A comparative study on electrical and optical properties of group III (Al, Ga, In) doped ZnO." Thin Solid Films 603 (2016): 21-28.

214. Das A. K., P. Misra, R. S. Ajimsha, D. M. Phase, and L. M. Kukreja. "Metal to semiconductor transition in lightly Al doped ZnO thin films grown by sequential pulsed laser deposition." Laser Materials Processsing Division, Raja Ramanna Center for Advanced Technology, Indore–452 13.

215. Tominaga K., T. Yuasa, M. Kume, and O. Tada. "Influence of energetic oxygen bombardment on conductive ZnO films." Japanese journal of applied physics 24, no. 8R (1985): 944.

216. Wang Z., Q. Li, Y. Yuan, L. Yang, H. Zhang, Z. Liu, J. Ouyang, and Q. Chen. "The semi-conductor

of ZnO deposited in reactive HiPIMS." Applied Surface Science 494 (2019): 384-390.

217. Sarma B. K., and P. Rajkumar. "Al-doped ZnO transparent conducting oxide with appealing electro-optical properties–Realization of indium free transparent conductors from sputtering targets with varying dopant concentrations." Materials Today Communications 23 (2020): 100870.

218. Gordon R. G. "Criteria for choosing transparent conductors." Materials Research Society (MRS) bulletin 25, no. 8 (2000): 52-57.

219. Huang L.-j., B.-j. Li, H.-d. Cao, W. Zu, N.-f. Ren, and H. Ding. "Influence of annealing temperature on formation and photoelectric properties of AZO nanosheet-coated FTO-based films." Journal of materials Science: Materials in Electronics 28, no. 6 (2017): 4706-4712.

220. Meljanac D., K. Juraić, V. Mandić, H. Skenderović, S. Bernstorff, J. R. Plaisier, A. Šantić, A. Gajović,

B. Šantić, and D. Gracin. "The influence of thermal annealing on the structural, optical and electrical properties of AZO thin films deposited by magnetron sputtering." Surface and Coatings Technology 321 (2017): 292-299.

221. Li M., Y. Wang, Y. Wang, and X. Wei. "AZO/Ag/AZO transparent flexible electrodes on mica substrates for high temperature application." Ceramics International 43, no. 17 (2017): 15442-15446.

222. Fang G., D. Li, and B.-L. Yao. "Fabrication and vacuum annealing of transparent conductive AZO thin films prepared by DC magnetron sputtering." Vacuum 68, no. 4 (2002): 363-372.

223. Chen T.-H., T.-C. Cheng, and Z.-R. Hu. "The electrical and optical properties of AZO thin film under

different post-annealing temperatures." Microsystem technologies 19, no. 11 (2013): 1787-1790.

224. Tseng S.-F. "Investigation of post-annealing aluminum-doped zinc oxide (AZO) thin films by a graphene-based heater." Applied Surface Science 448 (2018): 163-167.

225. Chaves M., R. Ramos, E. Martins, E. Cipriano Rangel, N. Cristino da Cruz, S. Frederick Durrant, and

J. R. R. Bortoleto. "Al-doping and properties of AZO thin films grown at room temperature: sputtering

pressure effect." Materials Research 22, no. 2 (2019).

226. Tahar R. B. H. "Structural and electrical properties of aluminum-doped zinc oxide films prepared by sol–gel process." Journal of the European Ceramic Society 25, no. 14 (2005): 3301-3306.

227. Yoshioka S., K. Toyoura, F. Oba, A. Kuwabara, K. Matsunaga, and I. Tanaka. "First-principles investigation of $R_2O_3(ZnO)_3$ (R= Al, Ga, and In) in homologous series of compounds." Journal of Solid State Chemistry 181, no. 1 (2008): 137-142.

228. Yoshioka S., F. Oba, R. Huang, I. Tanaka, T. Mizoguchi, and T. Yamamoto. "Atomic structures of supersaturated ZnO–Al_2O_3 solid solutions." Journal of Applied Physics 103, no. 1 (2008): 014309.

229. Bikowski A., D. A. Zajac, M. Vinnichenko, and K. Ellmer. "Evidence for the Al_{Zn}-O_i defect-complex model for magnetron-sputtered aluminum-doped zinc oxide: A combined X-ray absorption near edge

spectroscopy, X-ray diffraction and electronic transport study." Journal of Applied Physics 126, no. 4
(2019): 045106.

230. Rijpstra K., S. Cottenier, M. Waroquier, and V. Van Speybroeck. "Crystal structure prediction for supersaturated AZO: the case of $Zn_3Al_2O_6$." CrystEngComm 15, no. 48 (2013): 10440-10444.

231. Filatova E. O., and A. S. Konashuk. "Interpretation of the changing the band gap of Al_2O_3 depending on its crystalline form: connection with different local symmetries." The Journal of Physical Chemistry
C 119, no. 35 (2015): 20755-20761.

232. Costina I., and R. Franchy. "Band gap of amorphous and well-ordered Al_2O_3 on Ni3Al(100)." Applied physics letters 78, no. 26 (2001): 4139-4141.

233. Sampath S. K., and J. F. Cordaro. "Optical properties of zinc aluminate, zinc gallate, and zinc aluminogallate spinels." Journal of the American Ceramic Society 81, no. 3 (1998): 649-654.

234. Belyaev A. V., I. I. Evdokimov, V. V. Drobotenko, and A. A. Sorokin. "A new approach to producing
transparent $ZnAl_2O_4$ ceramics." Journal of the European Ceramic Society 37, no. 7 (2017): 2747-2751.

235. Sommer S., E. D. Bøjesen, A. B. Blichfeld, and B. B. Iversen. "Tailoring band gap and thermal diffusivity of nanostructured phase-pure $ZnAl_2O_4$ by direct spark plasma sintering synthesis." Journal of Solid State Chemistry 256 (2017): 45-52.

236. Cho D.-Y., J. H. Kim, K. D. Na, J. Song, C. S. Hwang, B.-G. Park, J.-Y. Kim, C.-H. Min, and S.-J. Oh. "Spectroscopic evidence for limited carrier hopping interaction in amorphous ZnO thin film." Applied Physics Letters 95, no. 26 (2009): 261903.

237. Mizoguchi T. "Overlap population diagram for ELNES and XANES: peak assignment and interpretation." Journal of Physics: Condensed Matter 21, no. 10 (2009): 104215.

238. Gilbert B., B. H. Frazer, H. Zhang, F. Huang, J. F. Banfield, D. Haskel, J. C. Lang, G. Srajer, and G. De Stasio. "X-ray absorption spectroscopy of the cubic and hexagonal polytypes of zinc sulfide." Physical Review B 66, no. 24 (2002): 245205.

239. Cong G. W., W. Q. Peng, H. Y. Wei, X. L. Liu, J. J. Wu, X. X. Han, Q. S. Zhu et al. "Aluminium doping induced enhancement of p–d coupling in ZnO." Journal of Physics: Condensed Matter 18, no.
11 (2006): 3081.

240. Yuste M., R. Escobar Galindo, I. Caretti, R. Torres, and O. Sánchez. "Influence of the oxygen partial pressure and post-deposition annealing on the structure and optical properties of ZnO films grown by dc magnetron sputtering at room temperature." Journal of Physics D: Applied Physics 45, no. 2 (2011):
025303.

241. Etinger-Geller Y., I. Polishchuk, E. Seknazi, A. Livne, G. Ciatto, and B. Pokroy. "Surface reconstruction causes structural variations in nanometric amorphous Al_2O_3." Physical Chemistry Chemical Physics 21, no. 27 (2019): 14887-14891.

242. Bouchet D., and C. Colliex. "Experimental study of ELNES at grain boundaries in alumina: intergranular radiation damage effects on Al-L_{23} and OK edges." Ultramicroscopy 96, no. 2 (2003): 139-152.

243. Imai Y., and A. Watanabe. "Comparison of electronic structures of doped ZnO by various impurity elements calculated by a first-principle pseudopotential method." Journal of Materials Science: Materials in electronics 15, no. 11 (2004): 743-749.

244. Wang C., Y. Wang, G. Zhang, C. Peng, and G. Yang. "Theoretical investigation of the effects of doping on the electronic structure and thermoelectric properties of ZnO nanowires." Physical Chemistry Chemical Physics 16, no. 8 (2014): 3771-3776.

245. van Bokhoven J. A., T. Nabi, H. Sambe, D. E. Ramaker, and D. C. Koningsberger. "Interpretation of the Al K-and $L_{II/III}$-edges of aluminium oxides: differences between tetrahedral and octahedral Al explained by different local symmetries." Journal of physics: Condensed matter 13, no. 45 (2001): 10247.

246. Wehrspohn R. B., and J. Üpping. "3D photonic crystals for photon management in solar cells." Journal of Optics 14, no. 2 (2012): 024003.

247. Wang D. L., H. Cui, and G. Su. "A modeling method to enhance the conversion efficiency by optimizing light trapping structure in thin-film solar cells." Solar Energy 120 (2015): 505-513.

248. Jiang T., T. Xie, Y. Zhang, L. Chen, L. Peng, H. Li, and D. Wang. "Photoinduced charge transfer in ZnO/Cu_2O heterostructure films studied by surface photovoltage technique." Physical Chemistry Chemical Physics 12, no. 47 (2010): 15476-15481.

249. Gorai P., E. G. Seebauer, and E. Ertekin. "Mechanism and energetics of O and O_2 adsorption on polar and non-polar ZnO surfaces." The Journal of Chemical Physics 144, no. 18 (2016): 184708.

250. Laffont L., M. Y. Wu, F. Chevallier, P. Poizot, M. Morcrette, and J. M. Tarascon. "High resolution EELS of Cu–V oxides: Application to batteries materials." Micron 37, no. 5 (2006): 459-464.

251. Yang G., S. Cheng, C. Li, J. Zhong, C. Ma, Z. Wang, and W. Xiang. "Investigation of the oxidation states of Cu additive in colored borosilicate glasses by electron energy loss spectroscopy." Journal of Applied Physics 116, no. 22 (2014): 223707.

252. Wang Y., S. Lany, J. Ghanbaja, Y. Fagot-Revurat, Y. P. Chen, F. Soldera, D. Horwat, F. Mücklich, and J. F. Pierson. "Electronic structures of Cu_2O, Cu_4O_3, and CuO: A joint experimental and theoretical study." Physical Review B 94, no. 24 (2016): 245418.

253. Ngantcha J. P., M. Gerland, Y. Kihn, and A. Rivière. "Correlation between microstructure and

mechanical spectroscopy of a Cu-Cu_2O alloy between 290 K and 873 K." The European Physical Journal-Applied Physics 29, no. 1 (2005): 83-89.